A Lattice QCD Determination of Potentials between Pairs of Static-Light Mesons

Dissertation

zur Erlangung des Doktorgrades
der Naturwissenschaften (Dr. rer. nat.)
der Fakultät für Physik
der Universität Regensburg

vorgelegt von

Martin Hetzenegger

aus Regensburg

Juli 2011

Promotionsgesuch eingereicht am: 13.07.2011
Die Arbeit wurde angeleitet von: Prof. Dr. G. Bali
Das Kolloquium fand am 04.07.2012 statt.

Prüfungsausschuss:	Vorsitzender:	Prof. Dr. C. Back
	1. Gutachter:	Prof. Dr. G. Bali
	2. Gutachter:	Prof. Dr. V. Braun
	weiterer Prüfer:	Prof. Dr. J. Fabian

Contents

"Ich möchte wissen, wie Gott diese Welt erschaffen hat. Ich bin nicht an dem einen oder anderen Phänomen interessiert, an dem Spektrum des einen oder anderen Elements. Ich möchte seine Gedanken kennen, alles Übrige sind nur Einzelheiten."

Albert Einstein

1 Prologue

What keeps the World together?

Since the beginning of time people have been overwhelmed and intrigued by nature. But it is not only the fascination for natural spectacles or phenomena that is burning in ourselves. It is the question of origin, or, in other words: "What keeps the world together at its innermost?"[1].

The status quo for describing physics at the entire range of the energy regime is given by four elementary theories. *Gravitation* acts on all particles having mass. A comprehensive and revolutionary geometrical interpretation of four dimensional space-time was introduced by Einstein in his general theory of relativity. Also well known is *electromagnetism* whose exploitation provides most technical products nowadays. In contrast to these two forces, which have an infinite range, the *weak force* acts on very tiny length scales and is responsible for some nuclear processes like beta decays. The fourth force, the *strong force*, is effective inside atomic nuclei, keeps them together and binds quarks into hadrons. The corresponding theory is the subject of this thesis and is described in the following chapters.

Electromagnetism, the weak interactions and the strong interactions could

[1] According to Johann Wolfgang von Goethe, "Faust - Der Tragödie erster Teil"

be formulated as local gauge theories and put together in the *Standard Model (SM)* of particle physics, which is remarkably successful. Twelve fundamental fermionic particles of matter, six quarks and six leptons within three particle-generations and the corresponding gauge bosons of the three gauge theories, are enough to confirm all experimental results of particle physics. However, there are several reasons that this model is not the final word.

For instance, any 4D renormalizable local gauge theory introduces a gauge field whose gauge bosons are massless and mediate the interactions. In contrast to these predictions, the Z and W bosons of the weak theory carry non vanishing masses. In order to preserve gauge invariance and let the gauge theories unchanged, masses have to be generated by spontaneous symmetry breaking of some scalar field. The preferred candidate is the *Higgs-field* that acquires a non-vanishing ground state. The discovery of the corresponding Higgs-boson at the *Large Hadron Collider (LHC)*[2] would further strengthen the SM. And indeed weak signals that have to be verified were already announced in December 2011. Also a very philosophical question is a subject of research. Why do we exist? Or more physically: Why is there so much more matter than anti-matter in our universe? Is the violation of parity and charge conjugation the responsible mechanism or does the Standard Model need to be expanded? Quite exciting is also the exploration of new physics like *Supersymmetry (SUSY)* and the search for supersymmetric particles that could explain the "dark matter" which constitutes the main part of the matter in the universe[3].

All these intriguing questions bring me back to the quotation at the beginning, the fascination by nature. This drives my interest and motivates me to contribute to the understanding of our universe. For this purpose I investigate potentials between pairs of static-light mesons numerically to see whether they are attractive or repulsive. The underlying theory is *Quantum Chromodynamics (QCD)*, the theory of quarks and gluons, the fundamental constituents of matter, and their interactions. In the following I will motivate this topic and provide the necessary theoretical background before I present our results and conclude.

[2]The LHC near Geneva is the largest machine scientists ever built, where e.g., in proton-proton collisions up to aspired energy scales of 14 TeV the interactions between the proton's fundamental particles, the quarks and gluons, are investigated.

[3]For more details on the mentioned topics we refer the reader to the popular science articles [1] and [2].

"Ich erinnere mich an viele Diskussionen mit Bohr, die bis spät in die Nacht dauerten und fast in Verzweiflung endeten. Und wenn ich am Ende solcher Diskussionen allein einen Spaziergang im benachbarten Park unternahm, wiederholte ich immer und immer wieder die Frage, ob die Natur wirklich so absurd sein könne, wie sie uns in diesen Atomexperimenten erschien."

Werner Heisenberg

2 Introduction

Quantum Chromodynamics

When Rutherford discovered the atomic nucleus in his scattering experiments at the beginning of the 20th century a new field of research, nuclear physics, opened up. Soon the number of strongly interacting elementary particles, now called hadrons, increased. By putting new high energy accelerators into operation in the 1950s, the "hadronic zoo" began to fill. In order to understand the spectrum and to terminate the almost biological classification scientists were searching for a deeper physical insight. The answer was given by the development of the *quark model* in 1963 by M. Gell-Mann [3] and G. Zweig [4, 5]. In this model every hadron consists of two or three quarks which are the real fundamental particles[1]. They have spin $\frac{1}{2}$, carry fractional electric charges and come in different flavors, namely *up*, *down*, *strange*, *charm*, *bottom* and *top*[2]:

$$\begin{pmatrix} u \\ d \end{pmatrix} \quad \begin{pmatrix} c \\ s \end{pmatrix} \quad \begin{pmatrix} t \\ b \end{pmatrix} \qquad \begin{matrix} +\frac{2}{3}e \\ -\frac{1}{3}e \end{matrix}$$

This model has been confirmed (indirectly) by several experiments, such as deep inelastic scattering or the discovery of the famous J/ψ-meson in 1974 at

[1] The following part is mainly based on the introduction in reference [6].

[2] The original model contained only three quark flavors, namely up, down and strange.

SLAC [7] and at the Brookhaven National Laboratory [8].

Furthermore, theoretical predictions have shown that quarks should have an additional $SU(3)$ gauge degree of freedom, called *color charge*. The reason was the existence of the Δ^{++} hadron which consists of three up quarks with parallel spin. For the Pauli exclusion principle to take effect, the additional quantum number was necessary. For quarks there are three types of color labeled as blue, green and red. Due to the eight generators of the corresponding group $SU(3)$ it was proposed that there are eight massless vector bosons, the gluons, which also carry color charge and mediate the strong interactions between the quarks. This theory of strong interactions is flavor blind but sensitive to color (*Greek: chroma*) and is therefore called *Quantum Chromodynamics (QCD)*. It is a non-Abelian gauge theory, also called Yang-Mills theory, with gauge group $SU(3)$.

As mentioned above, the gauge fields also carry color charge. This is a very crucial property, since this leads to self-interactions between the gluons which make QCD a highly nonlinear theory and induce many new phenomena. Most prominent here is *asymptotic freedom*. Its discoverers, Gross, Wilczek [9] and Politzer [10], received the Nobel Price in 2004. They found out that the force between quarks becomes weak for large momentum transfers corresponding to short distances. For this reason perturbation theory is successful in the high energy regime of QCD. At the other end of the energy scale however, there is *confinement*, i.e., quarks and gluons can never be liberated from hadrons which have to be color-neutral. Quark confinement has not been proven yet, but one believes that the self-interactions are responsible for a growing coupling strength with increasing quark separation. Therefore, perturbation theory breaks down at low energies.

Lattice Quantum Chromodynamics

For a complete understanding of the nature of strong interactions however, one also needs to understand this strong-coupled region, i.e., how hadrons are built up from quarks and gluons and how they interact with each other. Non-perturbative methods are needed and *Lattice QCD* is the most promising path method to gain access to the low energy regime of QCD. It is a theory from first principles as the quark masses and the coupling strength are its only input parameters. The idea is to map the continuum theory onto a hypercubic lattice by discretizing the four-dimensional space-time. The main virtue of the

resulting lattice gauge theory is that expectation values of observables can be evaluated numerically on a computer by applying Monte Carlo methods. Great successes have already been achieved in such lattice simulations. Very popular, for instance, is the evidence for quark confinement [11] or for chiral symmetry breaking.

One of the biggest drawbacks is the immense amount of computing power to perform such calculations. Therefore, one mainly studied numerically cheap quenched simulations[3] in the past. But with increasing computational resources, also dynamical simulations became possible. Systematic errors like discretization effects or finite volume effects have been reduced by using larger lattices with finer lattice spacings. However, most crucial are the quantities in which one is interested. While the reproduction of ground state hadron masses is well understood, calculating the spectrum of excited and multiquark states is still a challenge. For instance, nucleon-nucleon interactions have been described by effective theories, like meson-exchange models, for several decades. An access from first principles is desirable and the aim of today's efforts. The insights from those calculations would also reveal what parts of such models are of real fundamental nature.

Static-Light Meson-Meson Potentials

In this thesis we discuss multiquark systems consisting of two heavy-light mesons ($\mathcal{B} = Q\bar{q}$) or a heavy-light meson-antimeson pair. While the light quarks can be described fully relativistically, the heavy quark masses are too large for common lattices and one needs special techniques. Therefore, one removes the dominant scale, the heavy quark mass m_Q, and works with an effective Lagrangian. Combinations with light quarks and one heavy quark are governed by *Heavy Quark Effective Theory (HQET)* [12, 13] which is an expansion in $1/m_Q$. We work with the lowest order of HQET, called the static limit, where the heavy quark mass is sent to infinity. Thus, propagation in space is not possible for the static quarks and we are able to investigate potentials between pairs of static light mesons at well defined static quark-quark or quark-antiquark separations. Our main focus lies on the question of attraction and repulsion with respect to the separation between the static-light mesons and within different spin and isospin channels.

These potentials between static-light mesons are also interesting in a sense

[3]These are simulations without quark loops.

that they give insights to the nature of strong interactions from first principles for multiquark systems. Such multiquark systems are possible candidates for the X, Y and Z resonances and intensely debated in charm physics. We mainly follow the explanations in the references [14, 15, 16].

The $X(3872)$ is the figurehead for a non-$q\bar{q}$ particle and was first discovered by Belle in 2003 [17] in $\mathcal{B}$ meson decays. Soon this state was confirmed in high energy proton-antiproton collisions by the CDF [18] and DO [19] groups at Fermilab and in $\mathcal{B}$ meson decays by BaBar [20][4]. Arguments as, e.g., isospin violation in charmonium decay channels, speak against a charmonium explanation for this state (see, e.g., [15] and the references therein). Thus, several models are discussed to explain the $X(3872)$ resonance. Since its mass is very close to the sum of the D^0 and the D^{*0} meson masses, the interpretation of a molecular $D^{*0}\overline{D}^0$ state [21, 22, 23, 24, 25] is the favored candidate. The binding can be explained by pion exchange and quark-level interactions. The model of a tetraquark molecule, built up from diquark-antidiquark pairs and bound by QCD forces, was proposed by Maiani *et. al* [26, 27]. However, this model predicts the existence of charged partners of the $X(3872)$ that have not been found yet[5]. Additional models are, e.g., $c\bar{c}g$ hybrid mesons [28] consisting of a charm-anticharm quark pair and a gluonic excitation.

Another quite interesting state is the $Z^+(4430)$ resonance which was detected by the Belle group in 2007 [29] which, however, could not be confirmed by other groups. Its distinctive feature is, that it is the only observed electrically charged state among the XYZ mesons. Since $c\bar{c}$ charmonium states and $c\bar{c}g$ hybrid mesons cannot carry electrical charge, the $Z^+(4430)$ is strongly supposed to be a multiquark state. Most likely it is either a molecule [30, 31, 32] or a tetraquark [33] state.

These speculations about the nature of the XYZ exotic meson resonances motivate us to study potentials between pairs of static-light mesons within the theoretical background of Lattice QCD. For large heavy quark masses, the spectra of heavy-light mesons are determined by excitations of the light quark and gluonic degrees of freedom. In particular, the vector-pseudoscalar splitting vanishes and the static-light meson $\mathcal{B}$ can be interpreted as either a $\overline{B}$, a $\overline{B}^*$, a D or a D^* heavy-light meson. Calculating potentials between two $\mathcal{B}$ mesons then will also enable investigations of possible bound molecules and tetraquark

[4] Taken from reference [15].
[5] We refer to chapter II of [14]

states or for particles that are close to the meson-antimeson threshold, such as the $X(3872)$ or the $Z^+(4430)$ [6].

Outline of this Work

This thesis is organized as follows:

In chapter 2 we give a short introduction to Quantum Chromodynamics. In addition we briefly explain the inner structure of mesons and their quantum numbers. Prepared with these insights into the nature of strong interactions we map the continuum theory onto a four dimensional lattice. The procedure of this discretization, the upcoming issues and their solutions are discussed in chapter 4. Furthermore we provide the theoretical background for calculating observables using Monte Carlo techniques. In chapter 5 we present a very effective technique to extract masses from the asymptotic behavior of Euclidean-time correlation functions not only for ground states but also for excited states. We focus on static-light meson correlators and discuss several techniques to increase statistics and the signal over noise ratio. In chapter 6 we explicitly calculate the static-light meson correlators for $\mathcal{B}$, $\mathcal{B}\mathcal{B}$ and $\mathcal{B}\overline{\mathcal{B}}$ states. We display their graphical interpretation and discuss their relation to different isospin channels. In order to generate $\mathcal{B}$ mesons and pairs of $\mathcal{B}$ mesons with different quantum numbers for total angular momentum J, parity P and charge conjugation C we use different operators and operator combinations. An overview of these representations and also the used lattice simulation parameters is listed. Before we conclude in chapter 8 we present and discuss our results for for $\mathcal{B}$, $\mathcal{B}\mathcal{B}$ and $\mathcal{B}\overline{\mathcal{B}}$ states in chapter 7.

[6] We refer to our Lattice 2011 proceedings [34] where this last part is taken from.

"QCD, ah ja, und was sagt etz diese QCD?
- QCD beschäftigt sich mit dem Weg der
quantenfeldtheoretischen Beschreibung stark
wechselwirkender Teilchen. Die ihr zu Grunde
liegende Eichtheorie ist unitär, wie diejenige
der QED, aber ich würde doch sagen in einer
etwas mehr spezielleren und nicht-abelschen
Art und Weise. - Ahhh ja, da werdens aber
spitzen ..."
- Im Buchladen -

Gerhard Polt & Martin Hetzenegger

3

QCD in the Continuum

Quantum Chromodynamics (QCD) is the most widely used theory of the strong (color) force describing the interactions between quarks and gluons. This non-Abelian gauge field theory, with $SU(3)$ being its gauge group, is an important part of the *Standard Model of Particle Physics* and yields deep insights in the nature of matter. All hadronic particles consist of quarks and gluons, the gauge bosons of QCD. In order to maintain the Pauli exclusion principle an additional quantum number for the quarks was postulated, the so-called color charge. However, not only the quarks but also the gluons which mediate the strong interactions between the quarks carry color charge. The resulting self-interactions make QCD a highly nonlinear theory and lead to new phenomena like asymptotic freedom and confinement. One consequence is that there is no single method to solve QCD at all energy scales of interest. Perturbation theory works effectively for high momentum transfers but cannot cover the low energy spectrum. The most promising method is *Lattice QCD* with benefits and drawbacks.

Before going to the lattice we give a short overview of the continuum formulation. We will introduce the fermion and the gauge fields to construct the QCD action. One of its most fundamental properties is invariance under local $SU(3)$ gauge transformations. This background knowledge of the continuum formalism will prepare us for the subsequent challenge to map the theory onto

a four dimensional lattice. At the end of this chapter we will give an overview of the inner structure of mesons.

All formulations will be done in Euclidean space (A.2) because it is most suitable for lattice calculations. Furthermore, throughout the whole thesis we will use natural units ($\hbar = c = 1$) and the Einstein summation convention (A.1).

More detailed discussions can be found in standard textbooks like [35, 36, 37, 38]. Also [39, 40, 41, 42] provide short introductions. We mainly follow the work of [37].

3.1 The QCD Action

The starting point is the QCD action S_{QCD}. It is invariant under local $SU(3)$ color transformations and defined by the space-time integral over the QCD Lagrange density $\mathcal{L}_{\mathrm{QCD}}$:

$$S_{\mathrm{QCD}} = \int d^4x \, \mathcal{L}_{\mathrm{QCD}} = S_{\mathrm{ferm}} + S_{\mathrm{gauge}} \,. \tag{3.1}$$

The fermionic part of the action S_{ferm} describes the propagation of quarks and their interaction with gauge fields whereas the gluonic part S_{gauge} specifies the self-interaction of the gluons and their propagation. Before discussing these two terms we introduce the quark and gluon fields.

3.1.1 Quark and Gluon Fields

Quarks and antiquarks are massive fermions and therefore described by Dirac 4-spinors

$$\psi^f_{\alpha,a}(x),\ \bar{\psi}^f_{\alpha,a}(x), \tag{3.2}$$

that carry several indices and arguments,

x	space-time position,
α	Dirac index (1,...,4),
a	color index (blue, green, red),
f	flavor index (1,...,N_f).

Hence every quark field $\psi^f(x)$ has 12 independent complex components at each space-time point. N_f labels the number of flavors included in the theory. In

most cases, however, it is sufficient to consider only the light quarks, which means up, down and strange.

Quantum field theories contain another kind of particles, the gauge bosons that act as carriers of the fundamental forces of nature and describe the interactions between the fermions. The corresponding field reads

$$A_\mu^{ab}(x), \tag{3.3}$$

with the indices

x	space-time position,
μ	Lorentz index (1,...,4),
a, b	color indices (blue, green, red).

The gluon fields are traceless, hermitian 3×3 color matrices which obviously carry color charge, too. Consequently there are not only interactions between the quarks but also self-interactions between the gluons. The Lorentz index μ labels the direction of the different components in space-time of this vector field.

The gauge fields $A_\mu(x)$ are elements of the Lie algebra $su(3)$ and we can write them as

$$A_\mu(x) = \tilde{A}_\mu^c(x)t^c = gA_\mu^c(x)t^c, \tag{3.4}$$

where the factor g is the strong coupling constant. The components $A_\mu^c, c = 1, 2, \ldots 8$, are real-valued fields, the so-called color components and the t^c denote the generators of the $SU(3)$ group.

For brevity, we will often use matrix/vector notation in the following.

3.1.2 The Fermion Action

Now we can write down the fermion action which is a bilinear functional in the quark fields ψ and $\bar{\psi}$. It is given by

$$S_{\text{ferm}}[\psi, \bar{\psi}, A] = \sum_f \int d^4x \; \bar{\psi}^f(x) \left[\gamma_\mu D_\mu(x) + m^f\right] \psi^f(x), \tag{3.5}$$

where the Dirac matrices γ_μ are defined in appendix A.1 and m^f is the mass of a quark with flavor f described by ψ^f. The term in brackets can be identified as the Dirac operator

$$\gamma_\mu D_\mu(x) + m \equiv D_m(x). \tag{3.6}$$

In order to guarantee local gauge invariance the ordinary derivative ∂_μ was replaced by the covariant derivative $D_\mu(x)$:

$$D_\mu(x) = \partial_\mu + iA_\mu(x). \tag{3.7}$$

As required, the fermion action $S_{\text{ferm}}[\psi, \bar{\psi}, A]$ is invariant under a local gauge transformation, which is described by $SU(3)$ matrices $\Lambda(x)$. Usually one writes them as exponentials of the generators of the group t^a:

$$\Lambda(x) = e^{i\theta(x)^a t^a}, \tag{3.8}$$

where $\theta(x)$ lies in the parameter space of the group and is space-time dependent. The fields transform as:

$$\psi(x) \longrightarrow \psi'(x) = \Lambda(x)\psi(x), \tag{3.9}$$

$$\bar{\psi}(x) \longrightarrow \bar{\psi}'(x) = \bar{\psi}(x)\Lambda^{-1}(x), \tag{3.10}$$

$$A_\mu(x) \longrightarrow A'_\mu(x) = \Lambda(x)A_\mu(x)\Lambda^{-1}(x) + i\left(\partial_\mu\Lambda(x)\right)\Lambda^{-1}(x). \tag{3.11}$$

3.1.3 The Gauge Field Action

The gauge action describing the interactions between the gluons and their propagation reads:

$$\begin{aligned} S_{\text{gauge}}[A] &= \frac{1}{2g^2}\int d^4x\, \text{Tr}\left[F_{\mu\nu}(x)\, F_{\mu\nu}(x)\right] \\ &= \frac{1}{4g^2}\int d^4x\, F^a_{\mu\nu}(x)\, F^a_{\mu\nu}(x). \end{aligned} \tag{3.12}$$

$F_{\mu\nu}(x)$ is the field strength tensor of QCD and in analogy to *Quantum Electrodynamics* (QED) it is given by,

$$F_{\mu\nu}(x) = -i\left[D_\mu(x), D_\nu(x)\right] \tag{3.13}$$

$$= \partial_\mu A_\nu(x) - \partial_\nu A_\mu(x) + i[A_\mu(x), A_\nu(x)] \tag{3.14}$$

$$= [\partial_\mu \tilde{A}^a_\nu(x) - \partial_\nu \tilde{A}^a_\mu(x) - f^{abc}\tilde{A}^b_\mu(x)\tilde{A}^c_\nu(x)]t^a. \tag{3.15}$$

$$= F^a_{\mu\nu}(x)t^a\,, \tag{3.16}$$

where the structure functions f^{abc} are defined in appendix A.2. Up to the third term in (3.14) the field strength tensor $F_{\mu\nu}(x)$ has the same form as the field strength in QED. The additional term leads to three and four gluon interactions. These self-interactions are a consequence of QCD being a non-Abelian gauge theory and very important, since they cause many interesting phenomena which do not exist in QED, like confinement and asymptotic freedom.

Gauge invariance of (3.12) under a local SU(3) gauge transformation $\Lambda(x)$ follows directly from (3.16) in combination with the invariance of the trace under cyclic permutations, since the field strength tensor transforms as follows,

$$F_{\mu\nu}(x) \longrightarrow F'_{\mu\nu}(x) = \Lambda(x)\, F_{\mu\nu}(x)\, \Lambda^{-1}(x). \tag{3.17}$$

3.2 Chiral Symmetry

Another crucial part of our understanding of QCD is chiral symmetry and its spontaneous breaking, which explains for example the small masses of pions and why we observe large mass differences between the nucleon N and its parity partner N^* instead of degenerate masses.

Chiral symmetry means, that for massless quarks the fermion action (3.5) is invariant under the transformations,

$$\psi_f(x) \to \psi'_f(x) = e^{i\gamma_5 \epsilon^c t^c_{ff'}} \psi_{f'}(x), \quad \bar{\psi}_f(x) \to \bar{\psi}'_f(x) = \bar{\psi}_{f'}(x) e^{i\gamma_5 \epsilon^c t^c_{f'f}}, \tag{3.18}$$

$$\psi_f(x) \to \psi'_f(x) = e^{i\gamma_5 \epsilon^0 \mathbb{1}_{ff'}} \psi_{f'}(x), \quad \bar{\psi}_f(x) \to \bar{\psi}'_f(x) = \bar{\psi}_{f'}(x) e^{i\gamma_5 \epsilon^0 \mathbb{1}_{f'f}}, \tag{3.19}$$

where $\mathbb{1}$ denotes the $N_f \times N_f$ unit matrix and the coefficients ϵ^c are arbitrary real numbers. This holds because the massless Dirac operator $D_{m=0}(x) = \gamma_\mu D_\mu(x)$ anti-commutes with γ_5,

$$\left\{ D(x)\Big|_{m=0}, \gamma_5 \right\} = 0. \tag{3.20}$$

However, chiral symmetry is spontaneously broken. While the massless action is invariant under global chiral rotation, the ground state is not. This spontaneous breaking of chiral symmetry manifests itself in a non-vanishing expectation value of the so-called chiral condensate [37],

$$\langle \bar{\psi}\psi \rangle \neq 0\,, \tag{3.21}$$

which acts like a mass term and is consequently not invariant under chiral transformation.

Furthermore, the *Goldstone theorem* postulates one massless *Nambu Goldstone Boson* for each generator of a spontaneous broken continuous and global symmetry [43]. In our case, the spontaneous broken subgroup can be reduced to $SU(N_f)$. Thus, for $N_f = 2$ the three corresponding Goldstone particles are identified with the pion triplet. Although their masses are non-zero, they are significantly smaller than those of other mesons. Hence, the pions are also

called *Pseudo-Goldstone Bosons*. Their small but finite masses originate from an explicit breaking of chiral symmetry due to the non-zero quark masses in the action.

Chiral symmetry and its spontanous breaking is a crucial property of QCD. However, implementing chiral symmetry on the lattice is a challenge, since discretizing QCD in a simple and computationally cheap way will explicitly break this symmetry, even for zero quark masses (see section 4.1.4).

3.3 An Excursion to Mesons

Since we are mainly studying mesons and their interactions in this thesis we give a short overview of the internal structure of light mesons and their quantum numbers which is based on [44, 45, 41, 46].

As we have seen in the previous sections, QCD describes the interaction between quarks and gluons as well as their propagation. Due to confinement only color singlets can be observed in nature, because they are the only finite energy states. So let us have a look at the possible combinations of the colored fields.

The simplest case is the combination of a quark and an antiquark $(q\bar{q})$[1]. In the language of group theory one couples an $SU(3)$ triplet with an $SU(3)$ antitriplet in order to reduce this tensor product to irreducible multiplets:

$$3 \otimes \bar{3} = \mathbf{1} \oplus 8. \tag{3.22}$$

The resulting representations are a color singlet contributing to a meson state and a color octet meson, not observable as a free particle. Combining this octet with a gluon, which can also be represented as an octet, one obtains

$$8 \otimes 8 = \mathbf{1} \oplus 8 \oplus 8 \oplus 10 \oplus \overline{10} \oplus 27, \tag{3.23}$$

which again contains a color singlet. By adding successively color octets to (3.22),

$$3 \otimes \bar{3} \otimes 8 \otimes \ldots \otimes 8 = \mathbf{1} \oplus \ldots \quad , \tag{3.24}$$

one can always form a color singlet. So this has to be considered as a possible finite energy state. States like these, consisting of a quark-antiquark pair and

[1] We will use ψ and q as synonyms for the fermion fields.

a valence gluon excitation ($q\bar{q}g$), represent possible configurations of a physical meson state. Whenever this valence component ($q\bar{q}g$) dominates the meson state, it is usually called *hybrid meson*[2]. This deliberately vague statement arises from the issue of defining the difference between valence and sea gluons. Since all mesons contain a gluonic component, the definition of a hybrid meson has been studied mainly within various models like bag models [47, 48], the flux tube model [49] or the strong coupling lattice model [50, 51] whereas each one exhibits a particular description of gluonic excitation [52, 53].

However, this is only the tip of the iceberg. Also higher Fock states, e.g. four-quark states, are possible contributions to a physical meson state. One can even think of states without any valence quark content, the so-called glueballs only consisting of gluonic excitations.

In general a physical meson state is characterized by its quantum numbers $J^{P(C)}$, isospin, strangness, charm, topness and bottomness. Now the crucial point is that all these possible different configurations exhibiting the required quantum numbers of a given meson state contribute to this meson state.

An expansion of a meson state $|\mathcal{M}\rangle$ in a basis of different configurations of the constituents is given by,

$$|\mathcal{M}\rangle = A_0|q\bar{q}\rangle + A_1|q\bar{q}\rangle' + \ldots + B_0|q\bar{q}g\rangle + B_1|q\bar{q}g\rangle' + \ldots + \text{higher Fock states}, \tag{3.25}$$

where $|q\bar{q}\rangle$ labels a quark-antiquark combination in a color singlet, $|q\bar{q}g\rangle$ denotes a quark-antiquark combination in a relative color octet with a valence gluonic content. The prime stands for excitations, and "higher Fock states" include for example four-quark states like $|q\bar{q}q\bar{q}\rangle$. The amplitudes are given by $A_0 = \langle q\bar{q}|\mathcal{M}\rangle, \ldots$ and denote the overlap with the physical state.

Meson states with the desired quantum numbers $J^{P(C)}$ can be generated by so-called interpolators. In general they read

$$\bar{\psi}^f(y)_{\;a}^{\;\alpha}\,\Gamma_{\alpha\beta}\,\mathcal{D}(A)_{ab}\,\psi^f(x)_{\;b}^{\;\beta}, \quad a,b = 1,2,3, \tag{3.26}$$

where Γ is a combination of Dirac-γ matrices and the operator $\mathcal{D}(A)$ provides a gauge covariant connection of the quark and antiquark fields. Both objects combined determine the quantum numbers $J^{P(C)}$ of the meson state, with spin J, parity P and charge conjugation C.

[2]Strictly speaking this only holds in the heavy-quark limit.

"Wia mach mas, also rein stilistisch von der Topologie? Kontinuierlich oder ... - Du bist der Künstler. Der Gestalter und Kreateur bist du, aber wennst mich fragst, mir is da aus so einer Divergenz noch a Gitter geblieben. Vielleicht wenn mas integrieren könnten..."
- Die Garage -

Gerhard Polt & Martin Hetzenegger

4
QCD on the Lattice

Calculating observables in quantum field theories like QCD is a challenging task, since divergences are appearing and one has to renormalize the theory. First a regularization scheme has to be introduced, for example a momentum cut-off, *Pauli-Villars regularization* [54] or *dimensional regularization* [55, 56, 57]. Finally, the resulting regularization parameters can be absorbed by redefining the physical parameters of the theory which are known from experiments. But all these regularization schemes are based on the Feynman diagram expansion of a given process. In the case of QCD this is only useful in the high energy regime. However, many interesting phenomena of QCD appear at low energies. Herein lies the big advantage of the lattice which acts like a momentum cutoff before any perturbation theory was done.

In this chapter, we will show how our theory is mapped on a four dimensional lattice and prepared for computational simulations. We start with the naive discretization of the fermion action. Thereby, we will get additional unphysical poles, called *doublers*. Removing these doublers by introducing the so-called *Wilson term* yields other issues since this term explicitly breaks chiral symmetry.

Afterwards we discuss the representation of the gluon fields on the lattice, which differs from the continuum form. Instead of elements of the algebra, gluons now have to be introduced as elements of the gauge group. Therefore,

we introduce *link variables* which are located between the lattice sites. Then we show how to construct a lattice gauge action depending on these link variables.

Finally, one needs a suitable formalism to numerically evaluate expectation values of observables. This formalism is *Feynman's path integral formalism* in Euclidean spacetime where one has to integrate over all possible field configurations, of the quark, antiquark and gauge fields. Since the fermion fields are anticommuting we will introduce *Grassman numbers* and their properties. Equipped with this knowledge one can solve the integral over the quark fields analytically and is left with an integral over the gauge fields only. But the number of degrees of freedom one has to integrate over is still much too high. At this point we make use of the great benefit of the path integral formalism which allows us to implement methods of statistical mechanics to quantum field theory. After all, by applying *Monte Carlo methods*, the integral can be reduced to a finite sum over a small set of independent gauge configurations and a computational determination of expectation values becomes feasible.

The discussions of these topics are mainly based on textbooks like [37] and [6, 58, 59, 60]. Also the explanations in [39, 40, 41, 61, 62, 63] provide an adequate overview.

4.1 Discretization of the Fermion Action

To map the continuum theory to a hypercubic lattice, we start with the discretization of the continuous spacetime, i.e.

$$x = a \begin{pmatrix} n_1 \\ n_2 \\ n_3 \\ n_4 \end{pmatrix}, \quad \text{with} \quad n_\mu \in \{0, \ldots, L_\mu - 1\}, \tag{4.1}$$

where a is the lattice spacing and aL_μ is the extension of the lattice in μ-direction. The fermion fields ψ and $\bar{\psi}$ live on the lattice points, which are called *sites*,

$$\psi(x) \equiv \psi(na), \tag{4.2}$$

labeled by the vectors n. To conserve gauge invariance we introduce the gauge fields U_μ which are elements of the group $SU(3)$. They are orientated quantities and live on the *links* connecting the sites. A more detailed discussion of this

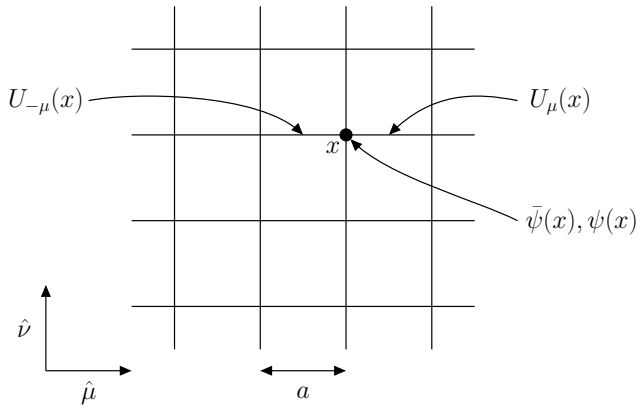

Figure 4.1: The μ-ν-plane of the hypercubic lattice. The fermion fields $\bar{\psi}(x)$ and $\psi(x)$ live on the lattice sites and the gauge fields U_μ live on the links between them.

subject will follow in section 4.2. In figure 4.1, we visualize the μ-ν-plane of the hypercubic lattice.

To maintain translation invariance, we impose (anti)periodic boundary conditions in all four directions effectively obtaining a 4-torus. To satisfy the anticommuting nature of fermions the boundary conditions for fermions are periodic in spatial direction

$$\psi(aL_1 + x_1, x_2, x_3, x_4) = \psi(x_1, x_2, x_3, x_4) \quad \text{etc.}, \tag{4.3}$$

but antiperiodic in time direction

$$\psi(x_1, x_2, x_3, aL_4 + x_4) = -\psi(x_1, x_2, x_3, x_4), \tag{4.4}$$

while the gluon fields are periodic in all four dimensions.

4.1.1 Naive Fermions

First of all we start discretizing the Euclidean continuum action for free fermions, i.e., $D_\mu \to \partial_\mu$. To keep it simple we consider the case of only one quark flavor:

$$S^{\text{free}}_{\text{ferm}}[\psi, \bar{\psi}] = \int d^4x \bar{\psi}(x) \left[\gamma_\mu \partial_\mu(x) + m\mathbb{1}\right] \psi(x). \tag{4.5}$$

To formulate this action on the lattice, integrals are replaced by sums

$$\int d^4x \longrightarrow a^4 \sum_x \tag{4.6}$$

and, by the naive discretization procedure, derivatives are replaced by the symmetric nearest neighbor differences

$$\partial_\mu \psi(x) \longrightarrow \frac{\psi(x + a\hat{\mu}) - \psi(x - a\hat{\mu})}{2a}, \tag{4.7}$$

where $\hat{\mu}$ is the unit vector in μ-direction.

These substitutions then lead to the following naive fermion action on the lattice:

$$S_{\text{ferm}}^{\text{naive}}[\psi, \bar{\psi}] = a^4 \sum_x \bar{\psi}(x) \left[\sum_{\mu=1}^{4} \gamma_\mu \frac{\psi(x + a\hat{\mu}) - \psi(x - a\hat{\mu})}{2a} + m\mathbb{1}\, \psi(x) \right]$$

$$= a^4 \sum_{x,y} \bar{\psi}(x) D_{\text{naive}}(x, y) \psi(y), \tag{4.8}$$

with the naive Dirac operator

$$D_{\text{naive}}(x, y) = \sum_{\mu=1}^{4} \gamma_\mu \frac{\delta_{x+a\hat{\mu},y} - \delta_{x-a\hat{\mu},y}}{2a} + m\mathbb{1}\delta_{x,y}. \tag{4.9}$$

The sums $\sum_{x,y}$ are over all lattice points and $\mathbb{1}$ denotes the unit matrix in Dirac space.

We obtain the correct continuum action for free fermions when taking the limit $a \to 0$ and we are already able to express expectation values of observables as path integrals, as we will see later. However, within this naive discretization the so-called *fermion doubling problem* occurs.

4.1.2 The Fermion Doubling Problem

An important quantity in QCD is the quark propagator. It is a two-point function and according to Wick's theorem the inverse of the Dirac operator:

$$\langle\, \psi(x)\, \bar{\psi}(y)\, \rangle = D_{\text{naive}}^{-1}(x, y). \tag{4.10}$$

Calculations are often easier in momentum space, as it is the case for the naive Dirac operator, which then becomes

$$\tilde{D}'_{\text{naive}}(p, q) = a^8 \sum_{x,y} e^{-ip\cdot x} D_{\text{naive}}(x, y) e^{iq\cdot y}$$

$$= a^4 \sum_x e^{-i(p-q)\cdot x} \left(\sum_{\mu=1}^{4} \gamma_\mu \frac{e^{iq_\mu a} - e^{-iq_\mu a}}{2a} + m\mathbb{1} \right)$$

$$= a^4\,\delta_{p,q}\,V\,\left(\frac{i}{a}\sum_{\mu=1}^{4}\gamma_\mu \sin(q_\mu a) + m\mathbb{1}\right), \tag{4.11}$$

where $V = L_1L_2L_3L_4$ denotes the volume of the 4-dimensional lattice.

We introduce the following notation:

$$\tilde{D}'_{\text{naive}}(p,q) = a^4\,\delta_{p,q}\,V\,\tilde{D}_{\text{naive}}(q), \tag{4.12}$$

$$\tilde{D}_{\text{naive}}(q) = m\mathbb{1} + \frac{i}{a}\sum_{\mu=1}^{4}\gamma_\mu \sin(q_\mu a). \tag{4.13}$$

Now the inversion is trivial and we get the quark propagator in momentum space:

$$\begin{aligned}\tilde{D}^{-1}_{\text{naive}}(q) &= \frac{m\mathbb{1} - ia^{-1}\sum_\mu \gamma_\mu \sin(q_\mu a)}{m^2 + a^{-2}\sum_\mu \sin(q_\mu a)^2} \\ &\xrightarrow{a\to 0} \quad \frac{m\mathbb{1} - i\sum_\mu \gamma_\mu q_\mu}{m^2+q^2}.\end{aligned} \tag{4.14}$$

Let us have a look at the case of massless fermions which is of particular interest:

$$\tilde{D}^{-1}_{\text{naive}}(q)|_{m=0} = \frac{-ia^{-1}\sum_\mu \gamma_\mu \sin(q_\mu a)}{a^{-2}\sum_\mu \sin(q_\mu a)^2} \quad \xrightarrow{a\to 0} \quad \frac{-i\sum_\mu \gamma_\mu q_\mu}{q^2}. \tag{4.15}$$

At the first sight everything seems to be fine, because the naive lattice quark propagator has the correct continuum limit. We see, that in the continuum the propagator has one pole at $q = (0,0,0,0)$ corresponding to a single fermion which is described by the continuum Dirac operator. But for finite a we find 15 additional poles on the lattice, namely:

$$\begin{aligned} q = &(\frac{\pi}{a},0,0,0),(0,\frac{\pi}{a},0,0),\ldots,\\ &(\frac{\pi}{a},\frac{\pi}{a},0,0),\ldots,\\ &(\frac{\pi}{a},\frac{\pi}{a},\frac{\pi}{a},0),\ldots,\\ &(\frac{\pi}{a},\frac{\pi}{a},\frac{\pi}{a},\frac{\pi}{a}).\end{aligned} \tag{4.16}$$

These extra poles are not the result of a mistake we made, but a consequence of the lattice. Since we discretized spacetime with periodic boundary conditions, also the momenta became discrete with a periodicity of $\frac{2\pi}{a}$. But every pole of the propagator corresponds to a real particle. And so we obtain 15 unphysical quarks, which are called *fermion doublers*. For physical calculations, they have to be removed.

4.1.3 Wilson Fermions

A possible solution was proposed by Wilson [64]. He added a new term, the Wilson term, that removes the doublers by giving them an infinite mass in the continuum limit. The Wilson fermion action is then given by

$$S_W[\psi,\bar{\psi}] = S^{\text{naive}}_{\text{ferm}}[\psi,\bar{\psi}] - S_{\text{new}}[\psi,\bar{\psi}] \tag{4.17}$$

with the new term

$$\begin{aligned} S_{\text{new}}[\psi,\bar{\psi}] &= a^4 \sum_x \sum_{\mu=1}^{4} \mathbb{1}\bar{\psi}(x)\, \frac{\psi(x+a\hat{\mu}) - 2\psi(x) + \psi(x-a\hat{\mu})}{2a} \\ &\longrightarrow \frac{a}{2}\int d^4x\, \bar{\psi}(x)\Delta\psi(x) \quad \overset{a\to 0}{\longrightarrow} \quad 0. \end{aligned} \tag{4.18}$$

The subscript W stands for "Wilson" and in the limit $a \to 0$ the additional Wilson term vanishes. So we still have the correct continuum limit. Let us now have a closer look at the new Wilson fermion action:

$$\begin{aligned} S_W[\psi,\bar{\psi}] &= a^4 \sum_x \bar{\psi}(x) \left[\sum_{\mu=1}^{4} \gamma_\mu \frac{\psi(x+a\hat{\mu}) - \psi(x-a\hat{\mu})}{2a} + m\mathbb{1}\,\psi(x) \right. \\ &\qquad \left. - \sum_{\mu=1}^{4} \mathbb{1}\, \frac{\psi(x+a\hat{\mu}) - 2\psi(x) + \psi(x-a\hat{\mu})}{2a} \right] \\ &= a^4 \sum_{x,y} \bar{\psi}(x)\, D_W(x,y)\psi(y), \end{aligned} \tag{4.19}$$

Using a particularly compact notation the new Dirac operator for Wilson fermions reads

$$D_W(x,y) = \left(m + \frac{4}{a}\right) \mathbb{1}\delta_{x,y} - \frac{1}{2a} \sum_{\mu=\pm 1}^{\pm 4} (\mathbb{1} - \text{sign}(\mu)\gamma_\mu)\, \delta_{x+a\hat{\mu},y}, \tag{4.20}$$

where we have defined

$$\gamma_{-\mu} = -\gamma_\mu\ , \qquad \mu = 1,2,3,4. \tag{4.21}$$

Next we perform a Fourier transformation of the lattice Dirac operator D_W, as we did for our naive ansatz and obtain

$$\tilde{D}'_W(p,q) = V\, \delta_{p,q}\ a^4\, \tilde{D}_W(q), \tag{4.22}$$

with

$$\tilde{D}_W(q) = \frac{i}{a} \sum_{\mu=1}^{4} \gamma_\mu \sin(aq_\mu) + \frac{1}{a} \sum_{\mu=1}^{4} \mathbb{1}(1 - \cos(aq_\mu)) + m\mathbb{1}. \tag{4.23}$$

Expanding $\tilde{D}_W(q)$ for small q_μ we obtain $\tilde{D}_W = m\mathbb{1} + i\gamma_\mu q_\mu + \mathcal{O}(a)$, as it should be. In the limit $q_\mu \to \frac{\pi}{a}$, for l components μ, we get

$$\tilde{D}_W(q) = \frac{2l}{a} + \mathcal{O}(a^0) \quad \overset{a\to 0}{\longrightarrow} \quad \infty. \tag{4.24}$$

Thus, we have managed that the unphysical doublers get an infinite mass in the continuum limit, such that they decouple and get removed from the theory.

The drawback of the additional Wilson term is however that it breaks chiral symmetry explicitly, even for zero quark masses,

$$\left\{ D_W\Big|_{m=0}, \gamma_5 \right\} \neq 0. \tag{4.25}$$

This is due to the diagonal part of the Wilson term and can be seen directly from equation (4.20).

4.1.4 The Nielsen-Ninomiya No-Go-Theorem

Roughly speaking explicit breaking of chiral symmetry is closely related to the removing of the doublers. A more general formulation of this statement is given by the *Nielsen-Ninomiya no-go-theorem* [65, 66]. It states that the following four conditions cannot hold simultaneously for a Dirac operator[1]:

1. Locality: $D(x)$ is local and bound by $Ce^{-\gamma|x|}$, i.e., it vanishes fast enough for $|x| \to \infty$.
2. Correct continuum limit: The Fourier transform $\tilde{D}(p)$ for small momenta $p \ll \frac{\pi}{a}$ is: $\tilde{D}(p) = i\gamma_\mu p_\mu + \mathcal{O}(a^2 p^2)$.
3. No doublers: $\tilde{D}(p) \neq 0$ for $p \neq 0$.
4. Naive chiral symmetry: $\{\gamma_5, D\} = 0$.

Of course, it would be desirable to have a Dirac operator fulfilling all these requested properties. But as this is not possible and violating one of the first three conditions causes severe theoretical problems like the unphysical doublers, one often accepts the explicit breaking of chiral symmetry. However, this also causes some issues:

- Chiral symmetry is broken by discretization errors of the order $\mathcal{O}(a)$.
- Operators of different chiral representations mix.

[1] This section is partly taken from chapter 1.6.1 of [61] and chapter 6.1 of [40].

- The bare quark mass has to be fine tuned to acquire chiral symmetry in the continuum limit, because quark masses have to be renormalized additive.

- Fluctuations of the eigenvalues of the Dirac operator make the computation of the Dirac propagator very expensive for small quark masses like those of up and down.

In spite of the Nielsen-Ninomiya no-go-theorem, there is a way out of this dilemma, which was proposed by Ginsparg and Wilson [67] in 1982. They suggested to replace the relation (3.20) by a weaker condition for chiral symmetry on the lattice, the so-called Ginsparg-Wilson equation:

$$\gamma_5 D + D\gamma_5 = aD2R\gamma_5 D \qquad \text{for} \quad m = 0, \tag{4.26}$$

which gives the correct continuum limit (3.20). Thereby, a is the lattice spacing and R is a local operator which commutes with γ_5. An exact solution for (4.26) are, e.g., *domain wall fermions* [68, 69], when the fifth dimension is taken to infinity, and *overlap fermions* [70, 71]. However, simulations with overlap fermions are very expensive in terms of computer resources. Therefore, other possibilities have been investigated which are approximate solutions like, e.g., *fixed point fermions* [72] or *chirally improved fermions* [73, 74].

4.2 Gauge Fields on the Lattice

After having removed unphysical artefacts from our lattice fermion action a much more essential issue is arising again. It is the question of invariance under local $SU(3)$ gauge transformations which was one of the fundamental requirements for the QCD action. Or more precisely, the Wilson fermion action (4.19) has to be invariant under the transformations (3.9) and (3.10). However, due to the non-local discrete derivatives in (4.19) this is not the case. One may look, e.g., at the transformation behavior of terms like

$$\begin{aligned} \bar{\psi}(x)\psi(x+a\hat{\mu}) &\to \bar{\psi}'(x)\psi'(x+a\hat{\mu}) \\ &= \bar{\psi}(x)\Lambda^{-1}(x)\Lambda(x+a\hat{\mu})\psi(x+a\hat{\mu}) \end{aligned} \tag{4.27}$$

which is apparently not gauge invariant. The solution to maintain gauge invariance in discrete spacetime is to implement a gauge covariant connection of the lattice sites. Therefore, one introduces the so-called *link variables* $U_\mu(x)$.

These vector fields are elements of the group $SU(3)$, have an orientation and live on the links between the lattice sites. They can be interpreted as gauge transporters connecting adjacent lattice sites and are given by

$$U_\mu(x) \approx e^{iaA^b_\mu(x)t^b} \in SU(3). \tag{4.28}$$

where the $A_\mu(x)$ label the continuum gauge fields and the t^b are the generators of the $su(3)$-algebra.

For negative indices the link variables are defined by

$$U_{-\mu}(x) = U_\mu(x - a\hat{\mu})^\dagger \tag{4.29}$$

and under a local gauge transformation $\Lambda(x)$ the link variables transform as:

$$U_\mu(x) \to U'_\mu(x) = \Lambda(x)U_\mu(x)\Lambda^{-1}(x + a\hat{\mu}). \tag{4.30}$$

As already mentioned, on the lattice we have periodic boundary conditions for gauge fields in space as well as in time direction:

$$U_\mu(x + L_\nu) = U_\mu(x), \quad \nu = 1, 2, 3, 4. \tag{4.31}$$

Now gauge invariance is obvious when we consider, e.g., terms like

$$\begin{aligned}\bar{\psi}(x)U_\mu(x)\psi(x + a\hat{\mu}) &\to \bar{\psi}'(x)U'_\mu(x)\psi'(x + a\hat{\mu}) \\ &= \bar{\psi}(x)\Lambda^{-1}(x)\Lambda(x)U_\mu(x)\Lambda^{-1}(x + a\hat{\mu})\Lambda(x + a\hat{\mu})\psi(x + a\hat{\mu}).\end{aligned} \tag{4.32}$$

4.2.1 Coupling of Fermion and Gauge Fields

Equipped with these basics we are able to couple the gauge fields to the Wilson action (4.19). In order to reconstruct gauge invariance we insert the link variables between all diagonal fermionic products. Then our action reads

$$\begin{aligned}S_W[\psi, \bar{\psi}] = a^4 \sum_x \bar{\psi}(x) \Bigg[&\sum_{\mu=1}^{4} \gamma_\mu \frac{U_\mu(x)\psi(x + a\hat{\mu}) - U_{-\mu}(x)\psi(x - a\hat{\mu})}{2a} + m\mathbb{1}\psi(x) \\ &- \sum_{\mu=1}^{4} \mathbb{1} \, \frac{U_\mu(x)\psi(x + a\hat{\mu}) - 2\psi(x) + U_{-\mu}(x)\psi(x - a\hat{\mu})}{2a} \Bigg].\end{aligned} \tag{4.33}$$

In terms of our compact notation we obtain:

$$S_W[\psi, \bar{\psi}] = a^4 \sum_x \bar{\psi}(x) \, D_W(x, y)\psi(y), \tag{4.34}$$

$$D_W(x,y) = \left(m + \frac{4}{a}\right) \mathbb{1}\delta_{x,y} - \frac{1}{2a} \sum_{\mu=\pm 1}^{\pm 4} (\mathbb{1} - \text{sign}(\mu)\gamma_\mu)\, U_\mu(x)\delta_{x+a\hat{\mu},y}. \quad (4.35)$$

Gauge invariance of $S_W[\psi, \bar{\psi}]$ follows directly from equation (3.9), (3.10) and (4.30). We note that this action yields the correct continuum form (3.5) in the limit $a \to 0$.

4.2.2 The Wilson Gauge Action

We also want to describe the interactions between the gluons and their propagation on the lattice. Therefore, we have to discretize the gauge action as we did it for the fermion action. The main challenge is again to conserve gauge invariance and to obtain the correct continuum limit when sending a to zero.

In the last section we introduced the link variables U_μ as the fundamental quantities for putting the gluon fields on the lattice. From the transformation behavior (4.30) it can be seen that the trace over closed loops is gauge invariant. The shortes closed loops are squares of length a, which are called *plaquettes* (see figure 4.2) and defined by:

$$U^P_{\mu\nu}(x) = U_\mu(x) U_\nu(x + a\hat{\mu}) U_{-\mu}(x + a\hat{\mu} + a\hat{\nu}) U_{-\nu}(x + a\hat{\nu}). \quad (4.36)$$

From these objects Wilson developed the *Wilson gauge action* [75], the first formulation for a lattice gauge theory, which is a sum over all plaquettes, with each plaquette counted with only one orientation:

$$S_{\text{gauge}} = \sum_P S_P[U] = \beta \sum_x \sum_{1 \le \mu < \nu \le 4} \left\{ 1 - \frac{1}{N} \text{Re}\left[\text{Tr}(U^P_{\mu\nu}(x))\right] \right\}. \quad (4.37)$$

This is a gauge action for a general $SU(N)$ theory, where $N = 3$ in the case of QCD and $\text{Re}[\text{Tr}(U^P_{\mu\nu}(x))]$ is the real part of the trace over the plaquette. Gauge invariance can be seen easily from (4.30).

To show that equation (4.37) has the correct continuum limit, we expand the links U_μ for small a. In first order in a we obtain

$$S_{\text{gauge}} = \frac{\beta}{4N} \int d^4x \text{Tr}[F_{\mu\nu}(x)\, F_{\mu\nu}(x)] + O(a^2), \quad (4.38)$$

which leads to a relation between the coupling constant g of the continuum action (3.12) and β in the Wilson action:

$$\beta = \frac{2N}{g^2}. \quad (4.39)$$

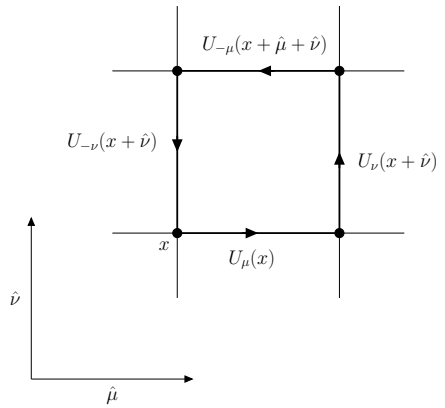

Figure 4.2: Here the plaquette $U^P_{\mu\nu}(x)$ is plotted in the μ-ν-plane.

We also note that the Wilson gauge action (4.37) has discretization errors of $\mathcal{O}(a^2)$. Since the discretization of the action is arbitrary as long as it has the correct continuum limit, one can also use more complicated loops to improve the situation. See e.g., [76, 77], where the *Lüscher-Weisz gauge action* is presented.

4.3 Clover-Wilson Fermions

As one can see, there are many possible choices for actions as long as the correct continuum limit and local gauge invariance are maintained. In order to choose an action for a lattice simulation one should always keep the cost-benefit ratio in mind. As chirality is not expected to be of major importance for our determination of static-light meson-meson potentials, the Wilson action is an adequate choice for us.

While the discretization errors of the Wilson gauge action are of the order $\mathcal{O}(a^2)$, the Wilson fermion action is afflicted with errors of order $\mathcal{O}(a)$. A systematic improvement scheme to reduce discretization errors by adding irrelevant terms to the gauge action has been proposed by Symanzik [78]. The generalization of this improvement scheme also to fermion actions is done by adding the following term to the Wilson fermion action, according to Sheikholeslami and Wohlert [79]:

$$S^{SW}_{\text{ferm}} = S_W + c_{SW}\frac{i}{4}a^5\sum_x \bar{\psi}(x)\sigma_{\mu\nu}F_{\mu\nu}\psi(x). \tag{4.40}$$

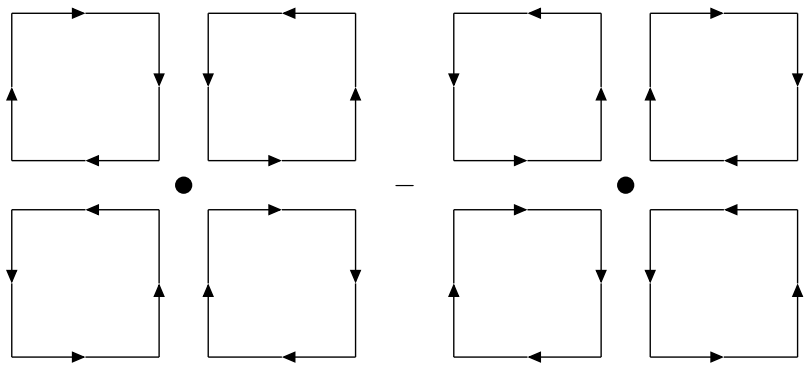

Figure 4.3: Picture of the simplest formulation of the field strength tensor on the lattice. The clover-like shapes are responsible for the name of the clover improved Wilson action. Taken from chapter 2.2.4 of [39].

For $F_{\mu\nu}$ one usually chooses the simplest lattice realization which is given by

$$F_{\mu\nu}(x) = \frac{1}{8a^2}\left[Q_{\mu\nu}(x) - Q_{\nu\mu}(x)\right], \tag{4.41}$$

with

$$\begin{aligned} Q_{\mu\nu}(x) = {} & U_\mu(x)U_\nu(x+a\hat{\mu})U_{-\mu}(x+a\hat{\mu}+a\hat{\nu})U_{-\nu}(x+a\hat{\nu}) \\ & + U_\mu(x)U_{-\nu}(x+a\hat{\mu})U_{-\mu}(x+a\hat{\mu}-a\hat{\nu})U_\nu(x-a\hat{\nu}) \\ & + U_{-\mu}(x)U_{-\nu}(x-a\hat{\mu})U_\mu(x-a\hat{\mu}-a\hat{\nu})U_\nu(x-a\hat{\nu}) \\ & + U_{-\mu}(x)U_\nu(x-a\hat{\mu})U_\mu(x-a\hat{\mu}+a\hat{\nu})U_{-\nu}(x+a\hat{\nu}). \end{aligned} \tag{4.42}$$

In a common discretization the field strength tensor $F_{\mu\nu}$ has the form of a clover leaf and thus is responsible for the name of this term. It includes the plaquettes from the Wilson action, that attach to the point x in the μ-ν-plane. A visualization is given in figure 4.3[2]. After this improvement errors induced by the finite lattice spacing are reduced to $\mathcal{O}(a^2)$, if the clover coefficient c_{sw} is determined non-perturbatively. This has been done for a set of lattice spacings, e.g., in [80, 81, 82, 83].

A general introduction to non-perturbative improvement can be found in [84].

[2]Taken from chapter 2.2.4 of [39].

4.4 Calculating Observables on the Lattice

4.4.1 The Feynman Path Integral

Having constructed the fermion and gauge action on the lattice, we want to show how expectation values of observables can be computed. Since we need a suitable formalism for numerical calculations we use *Feynman's path integral*:

$$\langle \mathcal{O}[\psi, \bar{\psi}, U] \rangle = \frac{1}{Z} \int [d\psi]\, [d\bar{\psi}]\, [dU]\, \mathcal{O}[\psi, \bar{\psi}, U]\, e^{-S_{\mathrm{QCD}}} \tag{4.43}$$

with the partition function

$$Z = \int [d\psi]\, [d\bar{\psi}]\, [dU]\, e^{-S_{\mathrm{QCD}}}. \tag{4.44}$$

In this process our observable $\mathcal{O}[\psi, \bar{\psi}, U]$ is a functional of the fermion and gauge fields. It is calculated for each field configuration, weighted with the exponent of the negative action and then integrated over all possible field configurations. Consequently, configurations with minimal action contribute most to the path integral. The partition function Z in the denominator of (4.43) is for normalization, such that $\langle \mathbb{1} \rangle = 1$.

We have to integrate over all degrees of freedom and the corresponding measures are given by:

$$[d\psi] = \prod_x \prod_{\alpha,a,f} d\psi^f_{\alpha,a}(x), \quad a = 1, 2, 3, \tag{4.45}$$

$$[d\bar{\psi}] = \prod_x \prod_{\alpha,a,f} d\bar{\psi}^f_{\alpha,a}(x), \tag{4.46}$$

$$[dU] = \prod_x \prod_{\mu} dU_\mu(x). \tag{4.47}$$

They are all well defined on the lattice, where in the last expression each individual measure $dU_\mu(x)$ is the measure invariant under group transformations, the so-called *Haar measure*.

The Euclidean path integral expression (4.43) of an observable has an obvious similarity to statistical mechanics. So we are able to apply the techniques developed in that field for numerical calculations. The most important one is the *Monte Carlo method* (see section 4.5), since a full evaluation of this integral is not feasible.

Sampling the gauge fields can be implemented easily. The fermion fields however are anticommuting and described by Grassman variables, which makes

a numerical treatment difficult. But the integration over the fermion fields can be done analytically[3] and we are left with an integral over the gauge fields only and an effective action for the gluons. By separating the QCD action in a fermionic part, which depends on fermion fields as well as on gauge fields, and a gauge field part, which depends only on the gauge fields, we can write the path integral as follows:

$$\langle \mathcal{O}[\psi,\bar{\psi},U]\rangle = \frac{\int [dU]\, e^{-S_{\text{gauge}}[U]}\,(\int\,[d\psi]\,[d\bar{\psi}]\, e^{-S_{\text{ferm}}[\psi,\bar{\psi},U]}\,\mathcal{O}[\psi,\bar{\psi},U])}{\int [dU]\, e^{-S_{\text{gauge}}[U]}(\int [d\psi]\,[d\bar{\psi}]\, e^{-S_{\text{ferm}}[\psi,\bar{\psi},U]})}. \quad (4.48)$$

The integration over the fermion fields is often referred to as *fermion contraction* and explained in the next section.

4.4.2 Fermion Contraction

To integrate the fermionic part of (4.48) we take a look at the integral over the fermionic degrees of freedom in the numerator of (4.48)[4]:

$$\int [d\psi]\,[d\bar{\psi}]\, e^{-S_{\text{ferm}}[\psi,\bar{\psi},U]}\mathcal{O}[\psi,\bar{\psi},U]. \quad (4.49)$$

With the results of Appendix B we can solve this integral. First we write down the *generating functional* W of the fermions:

$$W[\eta,\bar{\eta}] = \prod_{k=1}^{N_f} \int (d\psi_k\, d\bar{\psi}_k)\, \exp\left\{ -\sum_f \bar{\psi}_f\, D\, \psi_f + \bar{\psi}_f \eta_f + \bar{\eta}_f \psi_f \right\}, \quad (4.50)$$

where f labels the different quark flavors and N_f is the number of quark masses. By applying *Wick's theorem* we can express (4.49) as

$$\begin{aligned}\int [d\psi]\,[d\bar{\psi}]\, e^{-S_{\text{ferm}}[\psi,\bar{\psi},U]}\mathcal{O}[\psi,\bar{\psi},U] &= \mathcal{O}[\frac{\partial}{\partial\bar{\eta}},\frac{\partial}{\partial\eta},U]\, W[\eta,\bar{\eta}]\Big|_{\eta=0,\bar{\eta}=0} \\ &= \left(\prod_f \det D_f[U]\right)\, \mathcal{O}[D_f^{-1},U]) \quad (4.51)\end{aligned}$$

and (4.48) simplifies to:

$$\langle \mathcal{O}[U]\rangle_U = \frac{\int [dU]\, e^{-S_{\text{gauge}}[U]}\, \prod_f \det D_f[U]\, \mathcal{O}[D_f^{-1},U])}{\int [dU]\, e^{-S_{\text{gauge}}[U]}\, \prod_f \det D_f[U]}. \quad (4.52)$$

The determinant $\det D_f[U]$ is called fermion determinant and $\mathcal{O}[D_f^{-1},U]$ is now a functional of the quark propagator and link variables.

[3] More details can be found in Appendix B.

[4] The term in the denominator of (4.48) can be treated the same way by setting $\mathcal{O} = \mathbb{1}$.

4.5 Monte Carlo Methods

Our observable is now given by an integral over the gauge fields only (4.52). But a complete numerical integration is impossible, because the number of degrees of freedom one has to integrate out is much too large[5]. Hence, we use Monte Carlo techniques, which are often the only possibility to evaluate such high-dimensional integrals. Thereby, we do not take the whole condition space into account, but generate a small subset of N independent gauge field configurations U_i with a certain probability $P[U_i]$. Then the average of the observable $\mathcal{O}$ evaluated on these gauge configurations is an approximation to the expectation value.

4.5.1 Simple Sampling and Importance Sampling

In the *simple sampling method*, which is the easiest case, all possible gauge configurations U_i appear with the same probability and one chooses N configurations randomly. Then the expectation value of the observable $\mathcal{O}$ is given by:

$$\langle \mathcal{O} \rangle_N = \frac{\sum_{i=1}^{N} e^{-S_{\text{gauge}}[U_i]} \prod_f \det D_f[U_i]\, \mathcal{O}[D_f^{-1}, U])}{\sum_{i=1}^{N} e^{-S_{\text{gauge}}[U_i]} \prod_f \det D_f[U_i]}, \tag{4.53}$$

where the integral of (4.52) has been replaced by a sum over the gauge fields.

The main disadvantage of this method is that relevant configurations, which contribute most to the path integral, are rarely generated. For this reason one applies the *importance sampling method*, where the gauge configurations are generated with an appropriate probability distribution $P[U_i]$. In order to pick those configurations contributing most we use the following distribution:

$$P[U_i] = \frac{e^{-S_{\text{gauge}}[U_i]} \prod_f \det D_f[U_i]}{\sum_{j=1}^{N} e^{-S_{\text{gauge}}[U_j]} \prod_f \det D_f[U_j]}. \tag{4.54}$$

With this choice we obtain for the expectation value:

$$\langle \mathcal{O} \rangle_N = \frac{\sum_{i=1}^{N} e^{-S_{\text{gauge}}[U_i]} \prod_f \det D_f[U_i]\, \mathcal{O}[D_f^{-1}, U]) \frac{1}{P[U_i]}}{\sum_{i=1}^{N} e^{-S_{\text{gauge}}[U_i]} \prod_f \det D_f[U_i] \frac{1}{P[U_i]}}$$

[5]For a lattice with 10^4 sites (which is very small), there are 4×10^4 link variables. Each of them can be parameterized by 8 real parameters in the case of $SU(3)$, hence 320000 integrations have to be done. If one evaluates each integrand at only 10 points, this means that the full integral over gauge fields has to be approximated by a sum over 10^{320000} terms (Example taken from [6] and chapter 2.5.3 of [39] respectively).

$$= \frac{1}{N} \sum_{i=1}^{N} \mathcal{O}[D_f^{-1}, U], \tag{4.55}$$

which is now given by the average of the observable on a finite number N of configurations. The weighting factor $e^{-S_{\text{gauge}}} \prod_f \det D_f$ has disappeared, because it is already included by the way the configurations have been generated.

According to the central limit theorem the sample average becomes the expectation value $\langle \mathcal{O}[U] \rangle_U$ in the limit of infinitely many configurations

$$\langle \mathcal{O}[U] \rangle_U = \lim_{N \to \infty} \langle \mathcal{O} \rangle_N. \tag{4.56}$$

4.5.2 Markov Chains

To generate the gauge configurations with the probability (4.54), one starts with an arbitrary configuration and constructs a so-called *Markov chain* of subsequent configurations:

$$U_0 \longrightarrow U_1 \longrightarrow U_2 \longrightarrow \ldots, \tag{4.57}$$

where the change of a field configuration to a new one is called *update* or *Monte Carlo step*. The key quantity here is the transition probability $w(U \to U')$ to get from a configuration U to a new configuration U'. The transition probabilities $w(U \to U')$ obey

$$0 \leq w(U \to U') \leq 1 \qquad \forall \; U, U', \tag{4.58}$$

with the normalization

$$\sum_{U'} w(U \to U') = 1. \tag{4.59}$$

In order for the configurations to appear with the probability distribution (4.54) we have to properly choose the transition probability $w(U \to U')$. Once the Markov process is in equilibrium it cannot have sources or sinks of probability. This property is characterized by the balance equation

$$\sum_{U} w(U \to U') P[U] \stackrel{!}{=} \sum_{U} w(U' \to U) P[U']. \tag{4.60}$$

A sufficient solution for this equation (4.60) is the *detailed balance* condition

$$w(U \to U') P[U] = w(U' \to U) P[U']. \tag{4.61}$$

4.5.3 The Metropolis Algorithm

A suitable and popular algorithm that fulfills the detailed balance condition is the *Metropolis algorithm* [85]. This algorithm advances the Markov chain from a configuration U to a new configuration U' by an update step as follows.

First a new configuration U', called offer, is generated by the updating process from the configuration U. In the next step this offer is accepted immediately if the new configuration U' has a higher probability $P[U'] > P[U]$ than the old configuration $P[U]$. But if $P[U'] < P[U]$, then the new configuration is only accepted with the probability $P[U']/P[U]$:

$$w_A(U \to U') = \min\left(1,\, \frac{P[U']}{P[U]}\right). \tag{4.62}$$

This transition property fulfills equation 4.61.

If we start the Monte Carlo simulation with a random configuration U_0, we are generally not yet in the equilibrium. Therefore, one discards the first *sweeps* ($\mathcal{O}(1000)$). One Metropolis sweep consists of Metropolis steps for all links of the lattice. And since one also wants to obtain independent configurations, one has to iterate this sweep again several times ($\mathcal{O}(100)$) between the single measurements to minimize correlation.

Since Monte Carlo is very expensive for dynamical fermions, one usually uses an improved algorithm, the *Hybrid Monte Carlo (HMC) algorithm* [86], which increases the acceptance rate and lowers the autocorrelation. Thus, the equilibrium distribution can be reached sooner and less sweeps are necessary.

4.5.4 Quenched Approximation versus Dynamical Simulations

For generating the gauge configurations with the probability distribution (4.54) one has to compute the fermion determinant for each non-degenerated quark flavor. Including this determinant in the probability is called a simulation with *dynamical quarks*. But the numerical effort of Monte Carlo simulations can be reduced drastically by using the *quenched approximation*, where one assumes

$$\det D_f[U] = \text{constant} \tag{4.63}$$

such that equation (4.52) simplifies to

$$\langle \mathcal{O}[U] \rangle_U = \frac{\int [dU]\, e^{-S_{\text{gauge}}[U]}\, \mathcal{O}[D_f^{-1}, U])}{\int [dU]\, e^{-S_{\text{gauge}}[U]}}. \tag{4.64}$$

One reason for this is that a numerical evaluation of the fermion determinant is a complicated and extremely expensive task, since $D[U]$ is a very huge matrix. For a lattice with 20 sites in each direction the dimension of $D[U]$ is $12 \cdot 20^4 \sim O(10^6)$. Furthermore, the updating step of the Metropolis algorithm is local in the quenched approximation. As the gauge action (4.37) is a sum of local terms the weighting factor reduces to

$$e^{-\sum_P S_P[U]} = \prod_P e^{-S_P[U]} \,, \tag{4.65}$$

which is now a product of local terms. For a new link variable $U_\mu(x)$ only a few of the factors change and the new weight can be computed very quickly. When including the fermion determinant the situation becomes more difficult, since it connects the link variables in a non-local way.

On the other hand, putting the fermion determinant to a constant factor means to omit closed fermion loops. So one is neglecting the fermionic vacuum where virtual pairs of quarks and antiquarks are created and annihilated. This is equivalent to shifting the mass of the sea quarks to infinity, so that they cannot propagate. Nevertheless, this approximation works surprisingly well and the systematic error caused by the quenched approximation is only in the order of 10% to 20%.

In this work however, all our configurations have been generated with dynamical quarks.

4.6 Setting the Scale

The lattice spacing a is not a parameter of Lattice QCD. Besides the Lattice QCD action does not contain any dimensional parameters, only the dimensional coupling β (4.39) and the quark masses which always appear in the combination am. Therefore, to connect lattice quantities to the real world one has to "set the scale", by determing the physical length of the lattice spacing a. One possibility is to compare observables obtained from lattice simulations to the experimental values, e.g., the mass of the vector meson ρ.

For our calculations, however, we use the method introduced by Sommer [87, 88]. This method involves the computation of the *static quark potential* $V_{Q\overline{Q}}(r)$ which can be parameterized by

$$V_{Q\overline{Q}}(r) = A + \frac{B}{r} + \sigma r. \tag{4.66}$$

The parameter A is some irrelevant normalization of the energy, B denotes the strength of the Coulomb part of the potential and σ is the so-called "string tension". From QCD phenomenology one expects a value of $\sigma \approx 800\,\mathrm{MeV/fm}$. There is a characteristic length scale r_0 related to the shape of the static quark potential, the so-called Sommer parameter r_0 which is based on the force $F(r)$ between two static quarks. From experimental data for the $\bar{b}b$ and $\bar{c}c$ one obtains the following relation:

$$r_0^2\, F(r) = r_0^2\, \frac{\partial}{\partial r} V_{Q\overline{Q}}(r)\Big|_{r_0} = 1.65 \qquad \text{where} \quad r_0 \approx 0.5\,\mathrm{fm}. \tag{4.67}$$

In lattice units this term can be expressed as

$$\frac{r_0}{a} = \sqrt{\frac{1.65 + B}{a^2\sigma}}\,. \tag{4.68}$$

We are able to determine the static quark potential in lattice simulations by calculating Wilson loops (4.72). The numbers B and $a^2\sigma$ can then be obtained by fits of $V_{Q\overline{Q}}(r)$ to the computed potential. Finally one gains the lattice spacing a in physical units from the physical value of r_0.

The ratios $\frac{r_0}{a}$ for the lattice sets we are using for our simulations have been determined in the framework of [89][6]. They have used the Sommer parameter with $r_0 = 0.5$ fm. The data for the Wilson loops we need to analyze our results in chapter 7.3 have been calculated by Najjar [92].

The Wilson Loop

What remains is the definition of the Wilson loop $W_{\mathcal{L}}$[7]. In section 4.2.2 we have seen that a trace of a product of link variables along a closed loop is a gauge covariant object.

Based on this behavior one constructs the Wilson loop from four pieces, two so-called "Wilson lines" $S(\mathbf{m}, \mathbf{n}, n_t)$, $S(\mathbf{m}, \mathbf{n}, n_{t_0})$ and two temporal transporters $T(\mathbf{n}, n_t)$, $T(\mathbf{m}, n_t)$. The Wilson line connects two spatial points $\mathbf{m}$ and $\mathbf{n}$ along some path $\mathcal{C}_{\mathbf{m},\mathbf{n}}$ at a fixed time:

$$S(\mathbf{m}, \mathbf{n}, n_t) = \prod_{(\mathbf{k},j)\in\mathcal{C}_{\mathbf{m},\mathbf{n}}} U_j(\mathbf{k}, n_t). \tag{4.69}$$

[6]Since this paper is not published yet, we also cite the QCDSF database [90] which however is an internal website for QCDSF members only. Within previous studies the Sommer parameter with $r_0 = 0.467$ fm was used to set the physical scale and we refer to [91].

[7]We take the explanations from chapter 3.3.1 of [37].

The temporal transporter is a straight line of n_t link variables in time direction which are bound to a fixed spatial position,

$$T(\mathbf{n}, n_t) = \prod_{j=0}^{n_t-1} U_4(\mathbf{n}, j). \tag{4.70}$$

Next, one composes the pieces in such a way that a closed Loop $\mathcal{L}$ is formed,

$$\mathcal{L}: \quad (\mathbf{m}, n_t) \overset{S}{\to} (\mathbf{n}, n_t) \overset{T^\dagger}{\to} (\mathbf{n}, n_{t_0}) \overset{S^\dagger}{\to} (\mathbf{m}, n_{t_0}) \overset{T}{\to} (\mathbf{m}, n_t). \tag{4.71}$$

Finally one ends up with the Wilson loop by taking the trace:

$$\begin{aligned} W_{\mathcal{L}}[U] &= \mathrm{Tr}\left[S(\mathbf{m}, \mathbf{n}, n_t) T(\mathbf{n}, n_t)^\dagger S(\mathbf{m}, \mathbf{n}, n_{t_0})^\dagger T(\mathbf{m}, n_t)\right] \\ &= \mathrm{Tr} \prod_{(k,\mu)\in\mathcal{L}} U_\mu(k). \end{aligned} \tag{4.72}$$

We note that there exist two different types of Wilson loops depending on the path of the Wilson line given by $S(\mathbf{m}, \mathbf{n}, n_t)$. If the lattice sites $\mathbf{n}$ and $\mathbf{m}$ have spatial coordinates in common coordinate axis, the loop of a rectangle, one speaks of a "planar Wilson loop". Otherwise it is called non-planar.

"Is schon schön, oder? Klar, also rein numerisch, nicht wahr, war's eine Herausforderung für den Physiker an dieser Stelle ein Masse zu extrahieren, wo man mit Fug und Recht sagen kann: Jawohl, DAS ist eine Masse."
- Die Garage -

Gerhard Polt & Martin Hetzenegger

5
Spectroscopy Techniques

Once a large enough number of independent gauge configuration is generated one can start calculating observables in Lattice QCD. It is a theory from first principles with the coupling strength β and N_f quark masses m_i being its only parameters. Reproducing the mass spectrum of hadrons is one of the most important subjects in Lattice QCD. One reason is that the comparison to experiments provides a deeper understanding of the hadron spectrum and resonances. Furthermore one is able to study the influence of systematic effects like quenching, finite volume errors or discretization errors to the measured quantities. To go one step further, within Lattice QCD also the investigation of experimentally unknown resonances becomes feasible. This leads to the prediction of new particles or characteristics like string breaking [93] to state only one example.

This chapter gives an overview of how to determine mass spectra in general, but especially for *static-light mesons* which we also call $\mathcal{B}$ mesons. Our explanation of the necessary steps and the applied improvement schemes is mainly based on [37, 58] or the references given in the text. We also follow the work of [39, 40, 41, 92].

Euclidean correlation functions are central objects in lattice simulations. On the one hand they can be expressed as Feynman path integral expectation values and on the other hand they can be interpreted in Hilbert space. Comparing

the result from Hilbert space to the lattice data allows us to extract matrix elements or energy levels. In order to obtain meson masses we specialize on meson correlators. Appropriate interpolating fields yield the desired quantum numbers. Since propagations in space are forbidden for static quarks the static-light meson correlator is automatically zero-momentum projected $\mathbf{p} = \mathbf{0}$.

In principle these are the ingredients for mass spectroscopy. However, due to restricted computer resources signals from lattice simulations are often weak. Limiting factors are for example finite lattice volumes or finite lattice spacings. In particular, the full calculation of the light quark propagator is not realizable on common lattices[1]. The full propagator describes the propagation from all sources to all sinks and is therefore also called all-to-all propagator. A very simple and often sufficient approach is to calculate only one column of the full propagator, so-called point-to-all propagators. However, if one needs larger statistics as in our case one has to estimate the all-to-all propagator. For this purpose we use stochastic estimates to reconstruct the full propagator. In addition we use several different improvement techniques. The *Hopping Parameter Acceleration* (HPA), see e.g. [93], cancels nearest neighbor noise. Fermion field smearing and link fuzzing techniques improve the overlap with the physical state and the signal to noise ratio. For our data analysis finally, we use a whole matrix of correlators instead of single correlators only. This *variational method* [94, 95] further improves our signal and enables us to extract also excited states.

5.1 Euclidean Correlators

The most important tools in lattice QCD are *Euclidean correlation functions*. For two operators $\hat{O}_1$ and $\hat{O}_2$ the Euclidean correlator is defined by

$$\langle \hat{O}_2(t)\, \hat{O}_1(0) \rangle_T \equiv \frac{1}{Z_T} \mathrm{Tr} \left[e^{-(T-t)\hat{H}} \hat{O}_2 e^{-t\hat{H}} \hat{O}_1 \right], \tag{5.1}$$

with the normalization factor

$$Z_T = \mathrm{Tr} \left[e^{-T\hat{H}} \right]. \tag{5.2}$$

The operators $\hat{O}_1$ and $\hat{O}_2$ can be particle creators or annihilators, or operators that measure observables or combinations of all of these. $\hat{H}$ labels the Hamiltonian of the system which governs the time evolution and measures the energy

[1] Common lattices are of volume $V = 16^3 \times 32$ or even larger.

of the system. The arguments t and T denote Euclidean time and in discretized space-time they are given by $t = an_4$ and $T = aL_4$ which labels the extension of the lattice in time direction, see also section 4.1.

On the one hand one can show that for infinite T the Euclidean correlator (5.1) is just the vacuum expectation value of the product of $\hat{O}_1$ and $\hat{O}_2$ separated in time, which can be expressed in the path integral formalism (4.43):

$$\begin{aligned} \langle \hat{O}_2(t)\, \hat{O}_1(0) \rangle_T \quad &\overset{T\to\infty}{\longrightarrow} \quad \langle \hat{O}_2(t)\, \hat{O}_1(0) \rangle \equiv C(\hat{O}_1, \hat{O}_2, t) \\ &= \quad \frac{1}{Z} \int [d\psi]\, [d\overline{\psi}]\, [dU]\, \hat{O}_2[\psi, \overline{\psi}, U]\, \hat{O}_1[\psi, \overline{\psi}, U]\, e^{-S_{\mathrm{QCD}}}. \end{aligned} \tag{5.3}$$

This two point correlation function $C(\hat{O}_1, \hat{O}_2, t)$ can be evaluated in numerical simulations as we have shown in the last sections. Therefore, equation (5.3) is our first key formula.

On the other hand the Euclidean correlator (5.1) can be interpreted in Hilbert space. Therefore we use the eigenstates $|n\rangle$ of the Hamiltonian that are yet unknown but obey

$$\hat{H}|n\rangle = E_n|n\rangle, \qquad \mathbb{1} = \sum_n |n\rangle\langle n|. \tag{5.4}$$

Then we can evaluate (5.1) as follows:

$$\begin{aligned} \langle \hat{O}_2(t)\, \hat{O}_1(0) \rangle_T &= \frac{\sum_{m,n} \langle m|e^{-(T-t)\hat{H}} \hat{O}_2 |n\rangle \langle n|e^{-t\hat{H}} \hat{O}_1 |m\rangle}{\sum_n \langle n|e^{-T\hat{H}}|n\rangle} \\ &= \frac{\sum_{m,n} e^{-(T-t)E_m} \langle m|\hat{O}_2|n\rangle e^{-tE_n} \langle n|\hat{O}_1|m\rangle}{\sum_n e^{-TE_n}} \\ &= \frac{\sum_{m,n} \langle m|\hat{O}_2|n\rangle \langle n|\hat{O}_1|m\rangle e^{-t\Delta E_n} e^{-(T-t)\Delta E_m}}{1 + e^{-T\Delta E_1} + e^{-T\Delta E_2} + \dots}, \end{aligned} \tag{5.5}$$

where we defined

$$E_0 \le E_1 \le E_2 \le E_3 \dots, \qquad \Delta E_n = E_n - E_0. \tag{5.6}$$

Thus the Euclidean correlator depends only on the energy differences ΔE_n which can be measured in experiments. For convenience we denote these energy differences to the vacuum simply with E_n instead of ΔE_n, which means that the energy of the vacuum state $|0\rangle$ is normalized to zero.

We are again interested in the limit $T \to \infty$ for equation (5.5). For $E_1 > 0$ and an unique vacuum one obtains:

$$\langle \hat{O}_2(t)\, \hat{O}_1(0) \rangle_T \quad \overset{T\to\infty}{\longrightarrow} \quad \langle \hat{O}_2(t)\, \hat{O}_1(0) \rangle = \sum_n \langle 0|\hat{O}_2|n\rangle \langle n|\hat{O}_1|0\rangle\, e^{-tE_n}\,. \tag{5.7}$$

This result is central for any Lattice QCD calculation and our second key equation. It is a sum over energy eigenstates, where the summands are products of amplitudes and exponential functions governed by the corresponding energy level. The amplitudes determine the overlap of the interpolators[2] with the physical states. Obviously these matrix elements are only non-vanishing for states $|n\rangle$ with the same quantum numbers as the operators $\hat{O}_1$ and $\hat{O}_2$ respectively.

Equipped with our two key equations we are now able to extract energies by numerically calculating (5.3) and comparing it to the right hand side of (5.7). For example by fitting exponentials to the correlator[3]. This approach is, e.g., applicable in groundstate spectroscopy for interpolators providing a large overlap with the physical state. In most cases however, more sophisticated techniques are necessary (see section 5.3.1).

For a better conception to the quantities we calculate in our work let us now assume that operator $\hat{O}_1$ is a meson creation operator $\mathcal{B}^\dagger$ and operator $\hat{O}_2$ is the corresponding annihilation operator $\mathcal{B}$. Consequently all matrix elements $\langle n|\mathcal{B}^\dagger|0\rangle$ will vanish for states $|n\rangle$ that do not have the quantum numbers of the meson state. Only the groundstate $\langle B|$ and the excited states $\langle B'|, \langle B''|, \ldots$ describing the meson will have overlap with $\mathcal{B}^\dagger|0\rangle$. Therefore (5.7) reduces to

$$\langle \mathcal{B}(t)\, \mathcal{B}^\dagger(0)\rangle = |\langle B|\mathcal{B}^\dagger|0\rangle|^2\, e^{-tE_B} + |\langle B'|\mathcal{B}^\dagger|0\rangle|^2\, e^{-tE_{B'}} + \ldots \quad . \tag{5.8}$$

where we used

$$\langle u|\mathcal{B}|v\rangle = \langle v|\mathcal{B}^\dagger|u\rangle^* \tag{5.9}$$

We stress that the operators $\mathcal{B}^\dagger, \mathcal{B}$ can also be products of several operators, e.g., two-particle operators in the case of our meson-meson potentials. These states consist of two meson creators and two meson annihilators altogether (see section 6.1).

5.2 Momentum Projection

The states $\langle B|, \langle B'|, \langle B''|, \ldots$ still contain any momenta, but we want them to have definite spatial momentum. To project the meson interpolator to definite

[2] We use interpolator and operator as synonyms.
[3] This paragraph is based on chapter 4.1 of [41].

momentum we apply the Fourier transformation

$$\mathcal{B}(\mathbf{p},t) = L^{-\frac{3}{2}} \sum_{\mathbf{y}} e^{-i\mathbf{p}\mathbf{y}} \mathcal{B}(\mathbf{y},t). \tag{5.10}$$

It is sufficient to project only one of the two interpolators to definite spatial momentum, because of momentum conservation. We choose the interpolator $\mathcal{B}^\dagger(\mathbf{x},0)$ in real space which creates a meson with arbitrary momentum and the interpolator $\mathcal{B}(\mathbf{p},t)$ in momentum space which annihilates the state only if it has the definite momentum $\mathbf{p}$. Thus, our correlation function will only have contributions with a total momentum $\mathbf{p}$.

To obtain the masses of the meson states we have to project to zero momentum $\mathbf{p} = \mathbf{0}$, since the energy $E(\mathbf{p})$ is related to the meson mass m through the relativistic dispersion relation

$$E(\mathbf{p}) = \sqrt{m^2 + \mathbf{p}^2}. \tag{5.11}$$

Then our Euclidean correlation function (5.8) reads

$$\langle \mathcal{B}(\mathbf{p}=\mathbf{0},t)\, \mathcal{B}^\dagger(\mathbf{x},0) \rangle = A_0\, e^{-tm} + A_1\, e^{-tm'} + \dots \tag{5.12}$$

where the constant factor $L^{-\frac{3}{2}}$ is absorbed in the amplitudes and the prime denotes excitations.

For our case of static light mesons the momentum is automatically projected to zero. This is due to the delta function $\delta_{\mathbf{xy}}$ in the static light propagator, see equation (5.20), that anticipates propagations in space and consequently yields $\mathbf{p} = \mathbf{0}$.

5.3 Extracting Masses

The equations (5.7) and (5.12) show that also all excited and higher Fock states[4] contribute to the correlation function. Hence, it is a challenge to extract masses. For ground state spectroscopy, one assumes that the excited states become sufficiently suppressed for large enough times and only the groundstate survives. This however is only the case for interpolators which exhibit a large overlap with the groundstate. Also the fitting ranges have to be selected very carefully. Even more uncertain is the extraction of excited states. The naive ansatz of multi-exponential fits would formally work but often fails in the evaluation

[4] See also section 3.3 and equation (3.25).

of real lattice data. This is for instance due to a short Euclidean lifetime of excited states. Also the statistical errors are often too large to disentangle excited states. Other alternatives are for example *Bayesian priors* [96] or the *maximum entropy method* [97]. A improved and very powerful technique that we use for our analysis is presented in the next section.

5.3.1 The Variational Method

In our work we apply the *variational method* which was first proposed by C. Michael [94], see also Lüscher and Wolff [95]. It has already successfully been applied in many lattice simulations, for instance in the quenched studies of excited mesons [98] and baryons [99], the dynamical simulations of low and high spin mesons [100, 101] and even to separate ghost states [102]. The variational method is a very effective technique to disentangle states and therefore to obtain clearer signals and less noise for both, ground and excited states. The main idea is to use a basis of several different meson interpolators $\mathcal{B}_i$, $i = 1, \dots N$, all with the quantum numbers of the desired state, and to compute all possible cross correlations

$$C_{\mathcal{B}}(t)_{ij} = \sum_{\mathbf{x}} \langle \mathcal{B}(\mathbf{x}, t)_i \, \mathcal{B}^\dagger(\mathbf{x_0}, 0)_j \rangle \tag{5.13}$$

$$= \sum_{\mathbf{x}} \sum_{n} \langle 0|\mathcal{B}(\mathbf{x}, t)_i|n\rangle\langle n|\mathcal{B}^\dagger(\mathbf{x_0}, 0)_j|0\rangle \, e^{-tm_n} \, . \tag{5.14}$$

While the correlator $C_{\mathcal{B}}$ is defined on the infinite dimensional Hilbert space $C_{\mathcal{B}}(t)_{ij}$ is only a small part of the Hilbert space. It is the projection onto the subspace which is spanned by the finite interpolator basis $\mathcal{B}_i$. Thus the choice of the basis operators is important for the success of this variational approach. Linear independence, orthogonality and a good overlap with the physical state of interest are just a few of the desired properties. One way to construct interpolators $\mathcal{B} = \bar{q}\mathcal{O}Q$ (see section 5.4.2) with the same quantum numbers is to use operators $\mathcal{O}$ of different Dirac structures. However, interpolators with different Dirac structure alone may not lead to a good overlap with excited states and thus they do not provide a suitable basis (see, e.g., [103, 104]). Therefore, we generate a basis of extended interpolators by different amounts of smearing steps to the fermion fields (see section 5.7.1). This proceeding has also been very successful in the study of static-static-light baryons [105].

Having chosen a suitable basis of interpolators one can extract the eigenval-

ues $\lambda^{(k)}(t, t_0)$ by solving the generalized eigenvalue problem

$$C_{\mathcal{B}}(t)\,\mathbf{v}_k = \lambda_k(t, t_0)\,C_{\mathcal{B}}(t_0)\,\mathbf{v}_k\,. \tag{5.15}$$

Then the eigenvalues behave as

$$\lambda_k(t, t_0) \propto e^{-(t-t_0)\,m_k}[1 + \mathcal{O}(e^{-(t-t_0)\,\Delta m_k})]\,, \tag{5.16}$$

where m_k is the mass of the k-th state and Δm_k is the difference to the first mass which is not contained in the operator basis. This holds at least for the first order in perturbation theory. For higher orders also states within the interpolator basis can contribute to the error. The normalization at some time slice $t_0 < t$ suppresses the contributions from higher states already before diagonalizing and solving the generalized eigenvalue problem. The benefits are improved signals and a more stable diagonalization process.

For our analysis we apply the rewritten generalized eigenvalue problem

$$C_{\mathcal{B}}^{-\frac{1}{2}}(t_0)\,C_{\mathcal{B}}(t)\,C_{\mathcal{B}}^{-\frac{1}{2}}(t_0)\,\mathbf{u}_k = \lambda_k(t, t_0)\,\mathbf{u}_k\,. \tag{5.17}$$

Solving this symmetric form yields exactly the same eigenvalues $\lambda_k(t, t_0)$ as equation (5.15). However, while the eigenvectors $\mathbf{v}_k$ in (5.15) are only orthogonal in the metric $C(t_0)$, the eigenvalues $\mathbf{u}_k$ of the symmetric generalized eigenvalue problem (5.17) fulfill the same orthogonality condition as the physical states.

5.3.2 Effective Mass Curves

The next thing to do is to extract the masses from the eigenvalues $\lambda_k(t, t_0)$ of the cross-correlation matrix. Due to their exponential behavior (5.16) they can be fitted[5] to the function

$$\lambda_k(t, t_0) = A_k\,e^{-m_k(t-t_0)}\,, \tag{5.18}$$

However, the eigenvalues are still polluted by contributions from higher lying states. Fitting ranges $[t_{\min}, t_{\max}]$ have to be selected carefully. Reliable fits can only be obtained for large enough $t_{\min}$ when the higher excited states are sufficiently suppressed and the exponential is dominated by the mass m_k. On the other hand $t_{\min}$ should not be chosen to large because useful information

[5]We use the method of least squares fitting which is explained in appendix C.2.

could be lost and the signal to noise ratio decreases for increasing Euclidean time[6].

A good way to find appropriate fitting ranges is to determine *effective masses* from ratios of adjacent timeslices

$$M^k_{\mathrm{eff},t_0}\left(t+\frac{a}{2}\right) = a^{-1}\ln\left(\frac{\lambda_k(t,t_0)}{\lambda_k(t+a,t_0)}\right). \tag{5.19}$$

Once the eigenvalue is dominated by the lowest lying state, M_{eff} becomes approximately constant and the curve forms an *effective mass plateau*. The quality of the plateau is the criterion for selecting the fitting range with the lowest possible t_{min}.

We note that we use the effective mass only as an estimation to select fitting ranges. Since it contains only the information from adjacent timeslices effective masses are no alternative to a fully correlated fit.

5.4 Meson Interpolators and Correlators

In order to be able to extract masses for static-light mesons we have to construct appropriate interpolators and calculate the correlation functions. The expression static-light already describes the essential properties of our states. They consist of a light quark q and a heavy quark Q in the "static limit" $m_Q \to \infty$. Therefore, we continue with some words on heavy quarks, mainly following [37, 58, 12, 13].

5.4.1 Heavy Quarks

Heavy quarks, such as the charm c or the bottom b quark, are characterized by a very large mass $m_Q \gg \Lambda_{\mathrm{QCD}}$, where Λ_{QCD} is the scale of QCD at which perturbation theory breaks down and nonperturbative effects dominate. Indeed for most lattices the mass of these heavy quarks is in the range of the cutoff or even larger $m_Q > 1/a$. Also discretization effects get out of hand when the product $m_Q a$ becomes large. Furthermore, the extension of the lattice would have to be large enough to accommodate hadrons including heavy quarks and to allow their propagation. Therefore, lattice investigations of states which include heavy quarks require special techniques. The main idea is to remove the dominant scale, the mass m_Q of the heavy quark, and to derive an effective

[6] More details can be found in chapter 9.3 of [58]

action. One ansatz for states with two heavy quarks (QQ and $\overline{Q}Q$ respectively) is *nonrelativistic QCD (NRQCD)*. The expansion parameter of this effective field theory is the relative velocity between the two quarks. For an introduction we recommend the references [106, 107]. In the case of states with light quarks and only one heavy quark one can assume that the center of mass is centered in the heavy quark. The expansion parameter is given by $1/m_Q$ and the theory describing these systems is called *Heavy Quark Effective Theory (HQET)*. We refer the reader to [12]. See also [108, 109, 110, 111]. Taking just this lowest order, where the heavy quark has an infinite mass $m_Q \to \infty$, is called the "static limit". Then the heavy quark behaves like a static color source of zero velocity. We note that this behavior is important for our calculation of meson-meson potentials since static color sources guarantee well defined distances. Moreover, the static limit also provides some new symmetries[7].

- *Heavy quark flavor symmetry*: Since QCD is flavor blind the quarks are only distinguished by their different masses. Thus, in the limit $m_Q \to \infty$ the quark dynamics remain unchanged under flavor rotations.

- *Heavy quark spin symmetry*: In lowest order HQET and NRQCD heavy quarks can only interact via gluons which are spin independent. Thus, the dynamics of heavy quarks is unchanged under spin transformations [112, 113].

Let us come to the crucial quantity for us, the static quark propagator, which was derived from lowest order HQET, see e.g. [108]. For times $t > t_0$, it is given by

$$D^{-1}_{\text{static}}(\mathbf{x}, t|\mathbf{y}, t_0) = P_+ \, \delta_{\mathbf{xy}} \prod_{k=0}^{t_0+t-1} U_4^\dagger(\mathbf{x},\ t_0 + ka\hat{4}), \tag{5.20}$$

$$D^{-1}_{\text{static}}(\mathbf{y}, t_0|\mathbf{x}, t) = P_- \, \delta_{\mathbf{xy}} \prod_{k=0}^{t_0+t-1} U_{-4}(\mathbf{x},\ t - ka\hat{4}), \tag{5.21}$$

where $U_\mu(x)$ is the gauge link connecting the lattice site x with $x + a\hat{\mu}$. In (5.20) the heavy quark propagates forward in time and in (5.21) it propagates backward. The absence of the spin in the static propagator necessitates the $P_\pm$ Dirac projection of the (fermionic) static-light "meson" to fix the parity P.

$$P_\pm = \frac{\mathbb{1} \pm \gamma_4}{2}\,. \tag{5.22}$$

[7] See also section 2.1.1 of [92], where parts of this paragraph are taken from.

This is very similar to baryonic correlation functions where a spin $\frac{1}{2}$ source is created by three (rather than one) light quarks.

As the static propagator is just a spin projected product of temporal links we note that it is very cheap and easy to calculate in terms of computer resources. Simulating light quark propagators is much more expensive which will be discussed in section 5.5.

5.4.2 Meson Interpolators

In order to measure states with the desired quantum numbers we need appropriate interpolating fields $\mathcal{B}$. Meson interpolators are certain combinations of quark fields, Dirac γ-matrices and lattice derivative operators having the same quantum numbers as the considered particles to get a non-zero overlap with the physical states. In order to construct such interpolators one has to analyze the properties of the particles, like isospin, spin and the behavior under parity transformation and charge conjugation[8]. We will follow the explanations given in [37] and the paper of X. Liao and T. Manke [44].

The general form of a meson interpolator (3.26) may be written as

$$\mathcal{B}(x) = \overline{q}^{f_1}_{\alpha,a}(x)\, \mathcal{O}_{\substack{\alpha\beta \\ ab}}\, q^{f_2}_{\beta,b}(x), \tag{5.23}$$

where the indices f_1, f_2 denote different quark flavors, the indices α, β are spinor indices and a, b are color indices. The quantum numbers for spin J, parity $P = \pm 1$ and charge conjugation $C = \pm 1$ are governed by the operators $\mathcal{O}$. Their structure can denote a monomial of Dirac-γ matrices Γ that are elements of the Clifford-algebra, see equation (A.9), a symmetric spatial lattice derivative operator $\nabla[U]$ or a combination of these objects. The $\nabla[U]$ depend on the gauge fields U_μ and provide a gauge covariant connection of the quark and antiquark fields:

$$\nabla_j[U]q(x) = \frac{U_j(x)q(x + a\hat{j}) - U_{-j}(x)q(x - a\hat{j})}{2a} \tag{5.24}$$

For our calculation of static-light meson correlators we have a couple of requirements to the interpolators. To guarantee confinement any physical particle has to be a color singlet. Then, as the notation static-light tells us, our meson state has to consist of a static color source Q and a light quark q, namely up or

[8]The behavior of lattice fields under parity transformations and charge conjugation is given in Appendix A.

down which are mass degenerated in our simulations ($m_q = m_u = m_d$). Then our static-light meson interpolator generally reads

$$\mathcal{B}(x) = \delta_{ab}\, \overline{q}(x)_{\,a}^{\,\alpha}\; \mathcal{O}_{\alpha,\beta}\; Q(x)_{\,b}^{\,\beta}\,. \tag{5.25}$$

Especially the requirement of a static quark leads to several restrictions. Due to the infinite heavy mass of the static quark, propagations in space are not allowed. For this reason disconnected pieces which transport the static quark from a space-time point back to the same point do not appear in our simulations. Since the static quark is flavor blind charge conjugation is no quantum number for static-light mesons. Finally, only the light quark contributes to the spin. Therefore, we will observe half-integer spin quantum numbers for static-light mesons and integer spin quantum numbers in the case of static-light meson-meson potentials.

A more detailed discussion on the interpolators we use in our work, their corresponding symmetries and quantum numbers will follow in section 6.2.

5.4.3 The Static-Light Correlator

Having constructed the meson interpolators, we are now able to write down the two-meson correlator in the path integral formalism. We introduce the following notation

$$\langle\!\langle \ldots \rangle\!\rangle_U = \frac{\int [dU]\, e^{-S_{\text{gauge}}[U]} \prod_f \det D_f[U] \ \ldots}{\int [dU]\, e^{-S_{\text{gauge}}[U]} \prod_f \det D_f[U]}\,, \tag{5.26}$$

where N_f is the number of the degenerated quark flavors and $\langle\!\langle \ldots \rangle\!\rangle_U$ indicates the expectation value over gauge configurations. Let $\mathcal{B}^\dagger(\mathbf{x_0}, 0)$ create a meson at space-time point $(\mathbf{x_0}, 0)$ which is measured by $\mathcal{B}(\mathbf{x}, t)$ at $(\mathbf{x}, t)$. Then the path integral representation of the static-light meson correlation function is given by

$$\begin{aligned} C_{\mathcal{B}}(t) &= \sum_{\mathbf{x}} \langle 0|\mathcal{B}(\mathbf{x}, t)\, \mathcal{B}^\dagger(\mathbf{x_0}, 0)|0\rangle \\ &= \pm \sum_{\mathbf{x}} \left\langle\!\!\left\langle \mathrm{Tr}\left[M^{-1}(\mathbf{x_0}, 0|\mathbf{x}, t)\; \mathcal{O}\; D^{-1}_{\text{static}}(\mathbf{x}, t|\mathbf{x_0}, 0)\; \mathcal{O}\, \right] \right\rangle\!\!\right\rangle_U\,. \end{aligned} \tag{5.27}$$

The $\pm$ in the second step depends on the exchange of quark fields and the γ-structure of $\mathcal{O}$. One gets one minus sign for each quark exchange and maybe an additional minus sign from the commutation of γ-matrices. The trace is over color and Dirac indices (not displayed) and $M^{-1}(y|x) = \langle q(y)\bar{q}(x)\rangle$ is the

propagator[9] from x to y for the light quark q on a given gauge configuration. $D^{-1}_{\text{static}}(\mathbf{x}, t|\mathbf{x_0}, 0)$ labels the static propagator from equation (5.20). A more detailed evaluation of static-light correlation functions will follow in section 6.1.

We note that it is possible to calculate correlators from different source and sink interpolators. They can be constructed from different structures of Dirac γ-matrices and/or derivative operators within the operators $\mathcal{O}$. But to measure a signal they have to carry the same quantum numbers J^{PC}. Alternatively one can generate interpolators of different spatial extension originating from different smearing. This is for example done when applying the variational method to extract not only masses of ground states but also masses of excited states (see section 5.3.1).

Meson-meson $\mathcal{B}\mathcal{B}$ and meson-antimeson $\mathcal{B}\overline{\mathcal{B}}$ correlation functions can be obtained by combining the above correlator with another one that is spatially shifted by a distance $\mathbf{r}$, before taking the gauge average.

5.5 The Light Quark Propagator

From (5.27) we see that the static light correlator $C_{\mathcal{B}}(t)$ requires the determination of quark propagators. As already mentioned in section 5.4.1 the static propagator is cheap and easy to evaluate. Calculating the light quark propagator M^{-1} however means inverting the Dirac operator which is of size $12V$, where V denotes the number of lattice points. Hence, the complete propagator is a matrix consisting of $\mathcal{O}(10^{12})$ complex numbers for usual lattices. To determine all these (highly correlated) entries would not be feasible and the amount of data one had to store would be enormous.

5.5.1 Point-to-All Propagators

Fortunately in many cases the complete quark propagator is not necessary, and it is enough to evaluate it on some source $\eta_{x_0,\alpha_0,a_0} \equiv \eta_{k_0}$

$$\psi_{k_0 j} = \sum_l M^{-1}_{jl}\, \eta_{k_0 l}, \tag{5.28}$$

where one usually chooses a *point source*

$$\eta_{k_0 l} = \delta_{k_0 l} = \delta_{x_0 x}\delta_{\alpha_0 \alpha}\delta_{a_0 a}. \tag{5.29}$$

[9] In the following M^{-1} labels the massive light quark propagator.

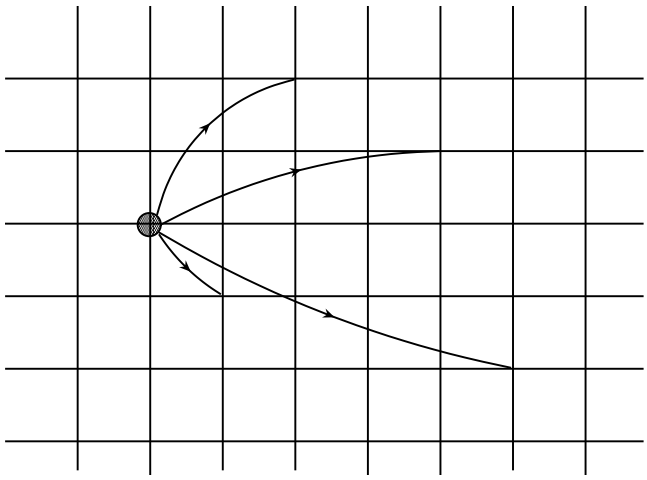

Figure 5.1: A two-dimensional visualization of a point-to-all propagator. Taken from chapter 4.4 of [41].

$\psi_{k_0 j}$ is the propagator from a fixed site x_0, a fixed Dirac-index α_0 and a fixed color-index a_0 to all lattice sites, i.e., one column of the inverse Dirac operator. For a short notation we use multi-indices k_0, l and j. Typically one evaluates (5.28) at the same site x_0 for all 12 combinations of Dirac and color indices α_0, a_0 and gains a propagator from one to any site of the lattice. A sketch is given in figure 5.1[10]. These so-called point-to-all propagators are sufficient for many lattice simulations without disconnected loops, see e.g. [100, 101].

Inverting the Dirac operator on some source (5.28) is equivalent to solving the linear equation

$$\sum_j M_{jl}\, \psi_{k_0 j} = \eta_{k_0 l}. \tag{5.30}$$

This can be accomplished by iterative methods like *conjugate gradient (CG)* [114, 115] or the improved *Bi-Conjugate Gradient Stabilized (Bi-CGStab)* [116, 117] which enables also the evaluation of non symmetric matrices[11].

5.5.2 All-to-All Propagators

In our case of the static light correlator however, point-to-all propagators would lead to very poor signals. Due to the delta function $\delta_{\mathbf{xy}}$ of the static propagator

[10] Taken from chapter 4.4 of [41].
[11] See also chapter 4.4. of [41]

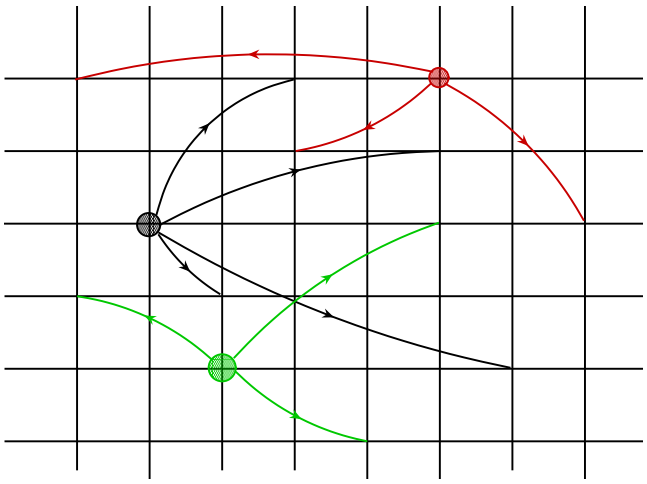

Figure 5.2: A two-dimensional visualization of an all-to-all propagator. The three source points are plotted of all the other points. Taken from chapter 4.5 of [41].

only a single term would contribute to the correlator. Instead of that we want to average over propagators starting at each lattice site[12]. Therefore, we have to implement so-called *all-to-all propagator* techniques and refer to, e.g., [93, 118, 119, 120, 121]. Figure 5.2[13] displays a two dimensional sketch of an all-to-all propagator.

An approximation of the full quark propagator M^{-1} can be reached by a stochastic estimation. Therefore, one generates an ensemble of N independent random noise vectors η_j^n where $n = 1, \ldots, N$. The multi-index $j \equiv (x_0, \alpha_0, a_0)$ again includes the indices for space-time, Dirac and color. These vectors have to obey the following properties

$$\frac{1}{N} \sum_{n=1}^{N} \eta_i^n = \mathcal{O}\left(\frac{1}{\sqrt{N}}\right), \tag{5.31}$$

$$\frac{1}{N} \sum_{n=1}^{N} \eta_i^n \, \eta_j^{n*} = \delta_{ij} + \mathcal{O}\left(\frac{1}{\sqrt{N}}\right). \tag{5.32}$$

For our simulations it is suitable to fill the components with complex $\mathbb{Z}_2$ noise [122,

[12] See also chapter 4.2.1 of [39].
[13] Taken from chapter 4.5 of [41].

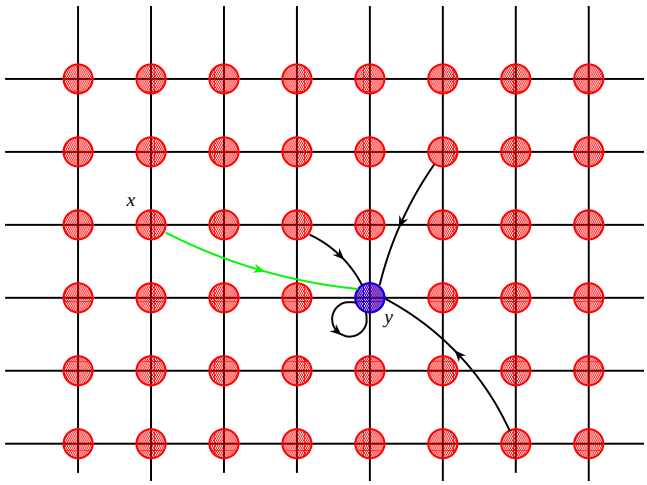

Figure 5.3: Two-dimensional sketch of our random noise source. For the propagator from x to y only the green curve contributes to the signal, the black ones are pure noise. Taken from chapter 4.6 of [41].

123, 124]:

$$\eta_j^n = \frac{1}{\sqrt{2}}(\nu + i\omega), \qquad \nu, \omega \in \pm 1. \tag{5.33}$$

The route is to invert the full propagator on all sources η_j^n, $n = 1, \ldots, N$

$$\psi_i^n = M_{ij}^{-1}\, \eta_j^n. \tag{5.34}$$

With the obtained solution vectors ψ_i^n one is now able to estimate the the full quark propagator from all sources to all sinks

$$\begin{aligned} \frac{1}{N}\sum_n \psi_i^n \eta_k^{n*} &= \frac{1}{N}\sum_n M_{ij}^{-1}\, \eta_j^n \eta_k^{n*} \\ &= M_{ij}^{-1}\left(\mathbb{1} + \mathcal{O}\left(\frac{1}{\sqrt{N}}\right)\right). \end{aligned} \tag{5.35}$$

Thus we have found a way to estimate the full propagator M^{-1}. In terms of computer time and memory this approach reduces the problem from $\mathcal{O}(12V \times 12V)$ to $\mathcal{O}(N \times 12V)$. However, signals are additionally polluted by errors of $\mathcal{O}(\frac{1}{\sqrt{N}})$ due to the stochastic estimation.

5.6 The Hopping Parameter Acceleration

By our way of constructing all to all propagators $M^{-1}(y|x)$, see equation (5.35), we get the desired exact propagator contaminated by noise terms from all source

sites $z \neq x$. This noise comes especially from source points near the sink (see figure 5.3[14]) since signals from correlation functions decrease exponentially with the distance[15], see e.g. (5.7),

$$M^{-1}(y|x) \propto e^{-|x-y|/a}. \tag{5.36}$$

In order to reduce this stochastic variance from nearest neighbors we apply a technique called *hopping parameter acceleration (HPA)* [93, 120, 125] which is based on the *hopping parameter expansion* of the Wilson Dirac operator. So let us have a closer look at equation (4.35) from section 4.2.1 again. In terms of the massive Wilson Dirac operator M it reads

$$M(x|y) = \left(m + \frac{4}{a}\right) \mathbb{1}\delta_{x,y} - \frac{1}{2a} \sum_{\mu=\pm 1}^{\pm 4} (\mathbb{1} - \mathrm{sign}(\mu)\gamma_\mu)\, U_\mu(x)\delta_{x+a\hat{\mu},y}. \tag{5.37}$$

As a first step we redefine the fermion fields by

$$\psi \to \sqrt{C}\,\psi, \quad \overline{\psi} \to \sqrt{C}\,\overline{\psi}, \tag{5.38}$$

$$C = m_0 + \frac{4}{a}, \quad m = m_0 + a^{-1}\mathcal{O}(g^2)\,. \tag{5.39}$$

Next we introduce the "hopping parameter" κ and the massless Dirac operator D, also referred to as "hopping matrix"

$$\kappa = \frac{1}{2(am_0 + 4)}, \quad D(x|y) = \sum_{\mu=\pm 1}^{\pm 4} (\mathbb{1} - \mathrm{sgn}(\mu)\gamma_\mu)\, U_\mu(x)\delta_{x+a\hat{\mu},y}. \tag{5.40}$$

With these definitions the Dirac operator in compact matrix/vector notation reads

$$M = \mathbb{1} - \kappa D. \tag{5.41}$$

The intention behind this formulation is that for sufficient small $\kappa < \kappa_c$ one can expand the propagator M^{-1} in powers of κ

$$M^{-1} = (\mathbb{1} - \kappa D)^{-1} = \sum_{j=0}^{\infty} (\kappa D)^j. \tag{5.42}$$

This geometrical series demonstrates that $M^{-1}(x|y)$ can be interpreted as a sum over all possible paths connecting the space-time points x and y. The longer the path the higher the order in κ and the stronger the suppression. Thus the leading term is given by the shortest path.

[14] Taken from chapter 4.6 of [41].
[15] See also chapter 4.6 of [41].

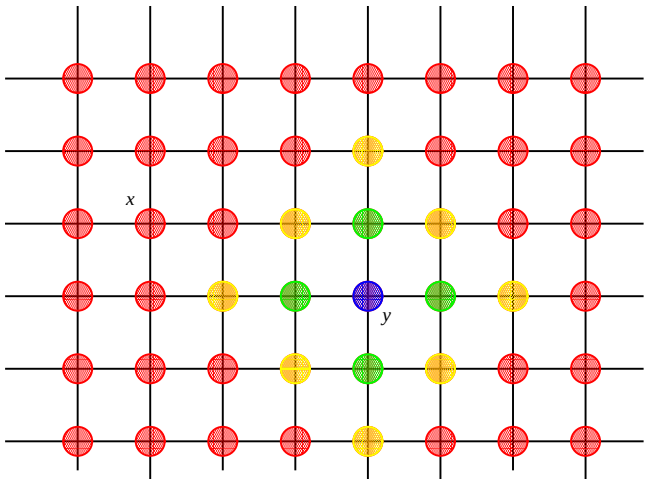

Figure 5.4: Visualization of the effect of HPA, where y indicates the sink and x some arbitrary source site. One application of κD removes the contributions from the blue sources, two applications the contributions from the green sources and three applications the contributions from the yellow sources. Taken from chapter 4.6.3 of [41].

Let us now consider a propagator $M^{-1}(x|y)$, $|x-y| = ka \geq 1$. Consequently all paths contributing to the exact propagator are longer then k lattice spacings. However, our estimated all-to-all propagator also contains shorter paths which only contribute to the noise. In order to get rid of these noise terms one derives

$$\begin{aligned} M^{-1} &= \sum_{j=0}^{k-1} (\kappa D)^j \; + \; (\kappa D)^k M^{-1} \\ &\Rightarrow (\kappa D)^k M^{-1} = M^{-1} - \sum_{j=0}^{k-1} (\kappa D)^j . \end{aligned} \tag{5.43}$$

This means applying $(\kappa D)^k$ to the estimated propagator yields the desired effect, i.e. we obtain the original propagator minus the contributions from all sources z $|z-y| < ka$. We note that contributions from these sources are not completely canceled since they can take a longer path to the sink. However, these noise terms are strongly suppressed due to (5.36). A visualization of this hopping parameter trick is shown in figure 5.4[16].

For our calculation of static light correlators we apply $\kappa^t D^t$, $ta = |x_4 - y_4|$

[16]Taken from chapter 4.6.3 of [41].

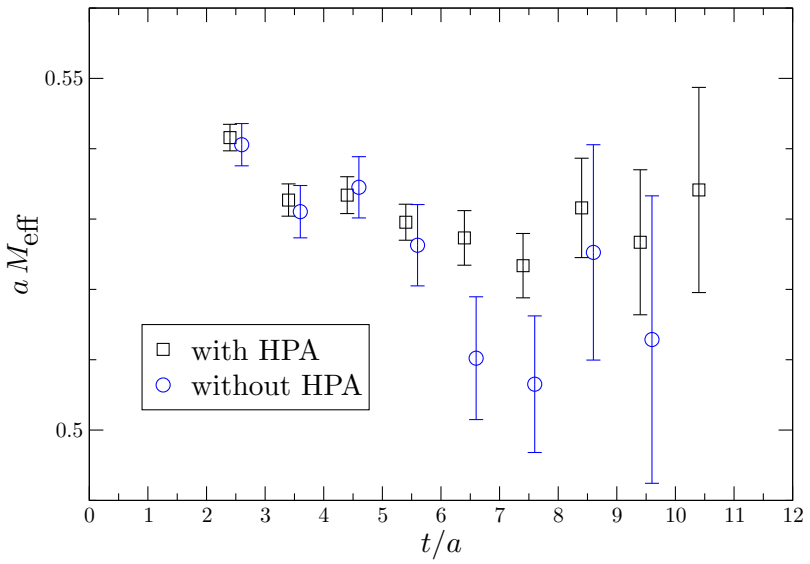

Figure 5.5: Effective masses of the pseudoscalar static-light meson from our coarse lattice ($16^3 \times 32$). The plot shows the groundstate with (black squares) and without (blue circles) applying the hopping parameter improvement. The missing point lies outside the plotted region. We used 50 estimates and averaged over 50 configurations.

to the random source vectors, where ta labels the separation from the source to the sink in time. The effect of this hopping parameter acceleration can be seen in figure 5.5. We display the effective groundstate masses for $t_0 = 2$ of the pseudoscalar static light meson with and without applying the hopping parameter acceleration. First one observes that the errors without HPA are much larger. But also the relative error without HPA increases with increasing time separation with respect to the improved case. A further benefit of canceling the noise from short distances is a general improvement of the signal to noise ratio. This results in a much better quality of the effective mass plateau of the improved correlator.

5.7 Smearing Techniques

5.7.1 Fermion Field Smearing - Extended Sources

Until now we have only considered source and sink vectors with local interpolators, i.e. all quark fields live on the same lattice site. But such interpolators

may have small overlap with the physical states and thus provide a weak signal. So instead of point-like fermion fields we use more realistic spatial wave functions, so-called *smeared* functions to improve the overlap. Furthermore, smearing quark fields is an established method to generate a basis of differently smeared source and sink operators. Such a basis allows us to use improved methods for extracting masses and we refer to section 5.3.1.

In our work we use *Wuppertal smearing* [126, 127, 128] which is gauge covariant and produces sources and sinks with a shape similar to a Gaussian. With this technique, the smeared field is generated iteratively via

$$\psi^{(n+1)}(x) = \frac{1}{1+6\kappa_{\mathrm{W}}} \left(\delta_{xy} + \kappa_{\mathrm{W}} H_{xy}\right) \psi^{(n)}(y)\,, \tag{5.44}$$

$$H_{xy} = \sum_{j=\pm 1}^{\pm 3} U_j^{\mathrm{APE}}(x) \delta_{x+a\hat{j},y}\,. \tag{5.45}$$

The operator H is the hopping term from the Dirac operator and describes the hopping in positive and negative spatial direction before time propagation starts and ends respectively. The free parameters are the number of iteration steps n and the positive real parameter κ_{W} which is proportional to the probability for hopping to a neighboring site. These two parameters can be used to adjust the width of the source and thus the overlap with the physical state. In our simulations we apply Wuppertal smearing to the source and sink interpolators with a hopping parameter value $\kappa_{\mathrm{w}} = 0.3$ and three iteration numbers

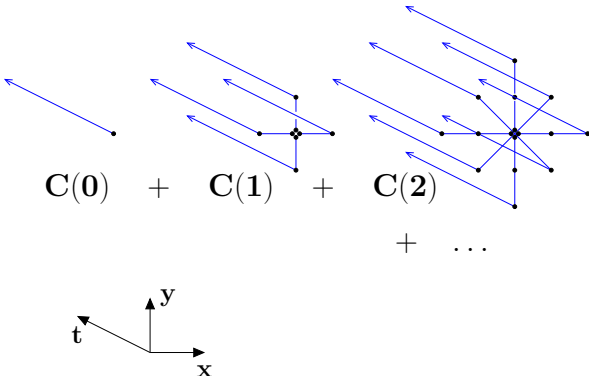

Figure 5.6: Visualization of the Wuppertal smearing process. $C(0)$ labels the propagator from a point-like source, $C(1)$ labels the propagator from a source where the quark jumps one step in each spatial direction with a certain probability before time-propagation starts, etc.

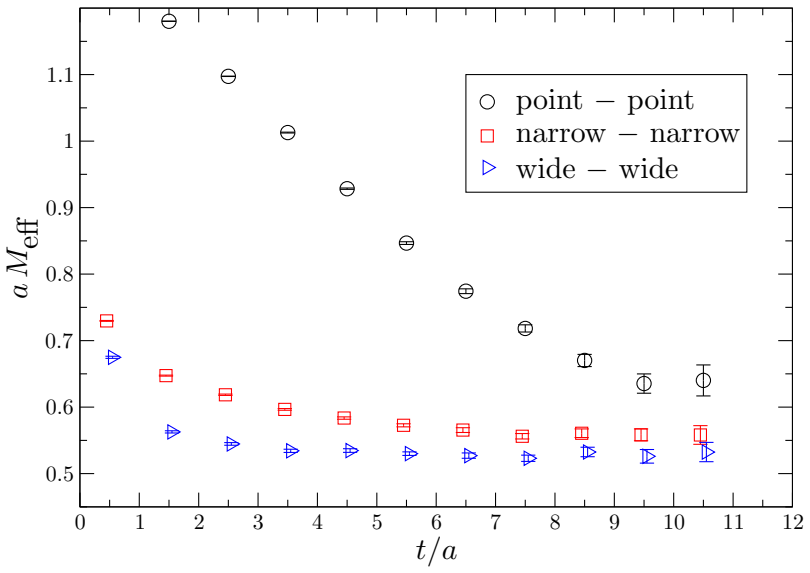

Figure 5.7: Effective masses of the pseudoscalar static-light meson from our coarse lattice ($16^3 \times 32$) for point, narrow and wide sources and sinks respectively. We used 50 estimates and averaged over 50 configurations.

$N_{\mathrm{iter}} \in \{16, 50, 100\}$ in order to generate a three by three cross-correlation matrix[17]. Instead of the original gauge fields U we employ APE smeared parallel transporters U^{APE} which are more suitable for generating extended sources[18]. A visualization of the Wuppertal smearing process is shown in figure 5.6.

In figure 5.7 we plotted the effective masses of our pseudoscalar static light meson correlator for different amounts of Wuppertal smearing. The masses labeled by black circles come from a correlator with point sources and sinks, the red squares from slightly smeared sources and sinks and the blue triangles from strongly smeared sources and sinks. While the black curve does not show a plateau at all, the red one shows a plateau from timeslice $t = 7$. The blue curve is even below the red one and shows a good plateau from timeslice $t = 6$. This means that also the correlator from the red curve is still contaminated by excited states. Moreover, for large enough times all three curves should agree within the errors. Since this is not the case up to $t/a = 11$, one even would have to go to larger times to observe the ground state for the unsmeared

[17] An overview of all our parameters is given in section 6.3.
[18] See next section.

and slightly smeared single correlator. However, one clearly finds that fermion field smearing increases the overlap with the physical state and thus the signal. Excitations are significantly suppressed, already for a few iteration steps. Also the errors for larger times are smaller than in the unsmeared case. Therefore, a plateau in the effective mass is reached earlier and also the quality of the plateau becomes better. Additionally this plot demonstrates the importance of applying the variational method which enables us to clearly disentangle ground and first excited states.

5.7.2 Gauge Field Smearing

Having seen how to improve the overlap with the use of smeared interpolators we will have a look at the gauge fields. It is typical for gauge theories that the gauge fields are fluctuating violently at short distances. Hence, it is sensible to *smoothen* or *smear* the gauge fields which can be performed in space and time. Thereby, one usually replaces the link variables by local averages over short paths connecting the link's endpoints. During this procedure one has to take care that gauge covariance and the continuum limit is maintained.

APE Smearing - Improving the Overlap

One way to smooth the fluctuations of the gauge fields is *APE-smearing* [129, 130, 131, 132]. Within this procedure we just smear the spatial link variables which are iteratively given by[19]

$$V_i^{(n+1)}(x) = U_i^{(n)}(x) + \alpha \sum_{j \neq i} C_{ij}^{(n)}(x)\,. \tag{5.46}$$

The average is over the original link variable U_i and the four perpendicular staples:

$$\begin{aligned} C_{ij}^{(n)}(x) = {} & U_j^{(n)}(x) U_i^{(n)}(x+\hat{j}) U_j^{(n)}(x+\hat{i})^\dagger \\ & + U_j^{(n)}(x-\hat{j})^\dagger U_i^{(n)}(x-\hat{j}) U_j^{(n)}(x-\hat{j}+\hat{i}). \end{aligned} \tag{5.47}$$

The parameter α is real and may be adjusted depending on the gauge coupling. For a $SU(2)$ theory the new link $V_i^{(n+1)}(x)$ is proportional to a group element. For $SU(3)$ however, this is not the case and one has to project the average

[19] We use the indices i, j for spatial directions only, while the indices μ, ν label space and time.

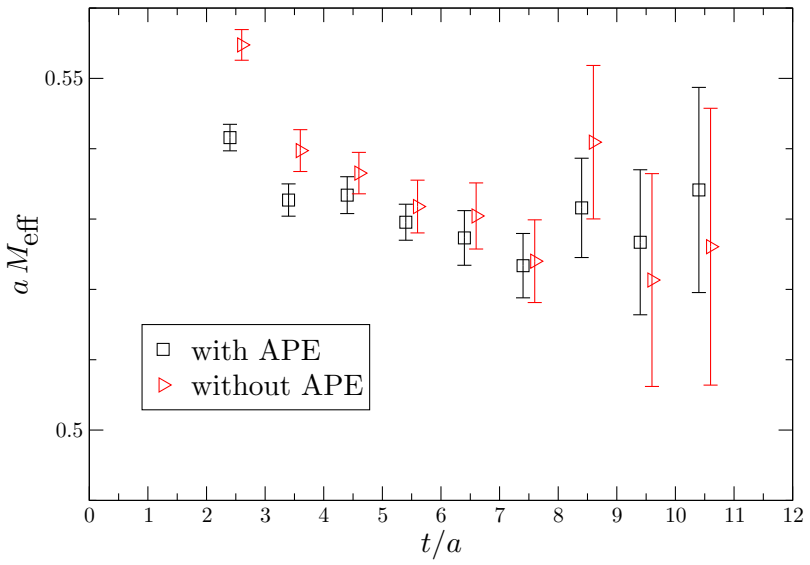

Figure 5.8: Effective masses of the pseudoscalar static-light meson from our coarse lattice ($16^3 \times 32$). The plot shows the groundstate with APE smearing (black squares) and without (red triangles). We used 50 estimates and averaged over 50 configurations.

back to the fundamental representation of $SU(3)$. This is usually done by maximizing $\mathrm{Re}\,\mathrm{Tr}[XV_i^{(n+1)}(x)^\dagger]$ for $X \in SU(3)$. Then one can use X as the new link variable $U_i^{(n+1)}(x)$

$$U_i^{(n+1)}(x) = P_{SU(3)} V_i^{(n+1)}(x)\,. \tag{5.48}$$

In our simulations we apply 15 smearing steps with a parameter $\alpha = 2.5$.

A crucial point to note is that all inversions are done on the original gauge fields to preserve the coupling strength and the fluctuations. APE smeared gauge fields are only used in the iterative process of generating the smeared quark fields (5.44). Thereby the overlap is increased and consequently the signal to noise ratio. This effect can be seen in figure 5.8 where we observe a better quality of the effective mass plateau and smaller errors for the APE smeared case.

Stout Smearing - Improving the Static Quark Action

A very similar technique to APE smearing is *stout smearing* [133]. This way of link smoothing is analytic and modifies the old link variable in such a manner

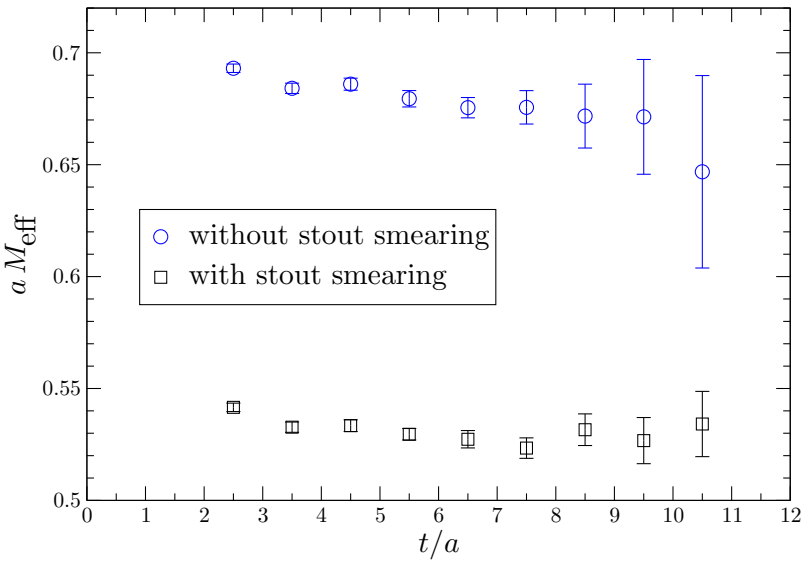

Figure 5.9: Effective masses of the pseudoscalar static-light meson from our coarse lattice ($16^3 \times 32$). The plot shows the groundstate with stout smearing (black squares) and without (blue circles). We used 50 estimates and averaged over 50 configurations.

that the new link variable remains within $SU(3)$. Hence there is no need for any projection back into the group. The new link after a smearing step is given by

$$U_\mu^{(n+1)}(x) = e^{iQ_\mu^{(n)}(x)}\, U_\mu^{(n)}(x)\,, \tag{5.49}$$

with

$$Q_\mu^{(n)}(x) = \frac{i}{2}\left(\Omega_\mu^{(n)}(x)^\dagger - \Omega_\mu^{(n)}(x) - \frac{\mathbb{1}}{3}\mathrm{Tr}\left[\Omega_\mu^{(n)}(x)^\dagger - \Omega_\mu^{(n)}(x)\right]\right)\,, \tag{5.50}$$

$$\Omega_\mu^{(n)}(x) = \left(\sum_{\nu\neq\mu} \rho_{\mu\nu}\, C_{\mu\nu}^{(n)}(x)\right) U_\mu^{(n)}(x)^\dagger\,. \tag{5.51}$$

The matrix $Q_\mu^{(n)}(x)$ is hermitian and traceless. Thus $e^{iQ_\mu^{(n)}(x)}$ is an element of $SU(3)$ and consequently also $U_\mu^{(n+1)}(x)$. The $\rho_{\mu\nu}$ define the weight of the perpendicular staples $C_{\mu\nu}^{(n)}(x)$ given in equation (5.47).

The staple weights are commonly chosen to be symmetric, $\rho_{\mu\nu} = \rho_{\nu\mu}$, or non-vanishing only for the spatial links, $\rho_{\mu 4} = \rho_{4\mu} = 0$. In our simulations however, we use stout smearing to improve the static action, i.e. the lattice

discretization of U_4 within (5.20). For this purpose we smear the temporal links and choose $\rho_{\mu 4} = \rho_{4\mu} = \frac{1}{6}$, $\rho_{\mu\nu} = 0$ for $\mu, \nu \neq 4$. This change of the lattice discretization of the action is possible since it does not change the continuum action in the limit $a \to 0$. To ensure that the action remains localized we perform only one smearing step.

The resulting so-called "fat" links reduce the self-energy of the static action and therefore enhances the signal to noise ratio [93]. Figure 5.9 shows the effective mass of a static light correlator with and without stout smearing. We find a significant mass reduction for the stout smeared case and smaller relative errors, especially for larger time separations. Since we are interested in energy differences, the self-energies cancel in the end and the physics for meson-meson and meson-antimeson potentials remain unaffected by this change of the self-energies.

We emphasize that only the combined effect of all these smearing techniques, applying the hopping parameter acceleration and the variational method allows us to measure signals and to extract meson states. Without all these noise reduction and signal enhancing techniques the signal would die from all the pollution from noise and excited states.

"Du wollt'st es doch wissen, oder? I kanns dir schon sagn wer aller dabei war, alle warns dabei: Die Baryonen, die Mesonen, die Exoten und, ah, ja klar, und die statisch Leichten. Freilich, die warn schon dabei. Wir habn ja noch gesagt, bringens ihre Signale noch rein in den Korrelator oder nicht? Aber die warn schon da, wia eine Brezn warn die da."
- Der Weber Max -

Gerhard Polt, Martin Hetzenegger & Sebi

6

Static-Light Meson-Meson Potentials

Static-light mesons represent the static limit $m_Q \to \infty$ of heavy-light mesons. In this limit the spectra of heavy-light mesons are characterized by excitations of the light quark and gluonic degrees of freedom. In particular, the vector-pseudoscalar splitting vanishes and the static-light meson $\mathcal{B}$ can be interpreted as either a $\overline{B}$, a $\overline{B}^*$, a D or a D^* heavy-light meson.

Static-light intermeson potentials were first evaluated on the lattice by Michael and Pennanen in the quenched approximation [134] and with $N_\mathrm{f} = 2$ Sheikholeslami-Wohlert sea quarks [135]. More detailed quenched studies can be found references [136, 137, 138, 139, 140, 141, 142]. For the computation of static-light meson-antimeson systems we refer to [93]. Recent dynamical simulations with twisted mass fermions were carried out by Wagner in references [143, 144]. Some descriptions of the following as well as preliminary results of our calculations with Sheikholeslami-Wohlert fermions were reported in our Lattice 2010 and Lattice 2011 proceedings [145, 34].

Equipped with the techniques from the previous chapters we are now able to investigate potentials between pairs of static-light mesons for different spin and isospin channels. Of special interest in our study is the question of attraction or repulsion and their dependence on the separation between the static quarks but also the possible mixing with other states. We numerically determine ground and excited states of $\mathcal{B}$ mesons as well as intermeson potentials between pairs

of static-light mesons, $\mathcal{B}(\mathbf{r})\mathcal{B}(\mathbf{0})$ and $\mathcal{B}(\mathbf{r})\overline{\mathcal{B}}(\mathbf{0})$. The static quark-quark (or quark-antiquark) separation is given by $r = |\mathbf{r}| = Ra, R \in \mathbb{N}_0$. a denotes the lattice spacing, Q a static color source and the positions of the mass-degenerate light quarks $q \in \{u, d\}$ are not fixed. Our calculations were performed on two lattices with the nonperturbatively improved Sheikholeslami-Wohlert fermion and the Wilson gauge actions with $N_\mathrm{f} = 2$ quark flavors at two lattice spacings $a \approx 0.084$ fm and $a \approx 0.077$ fm with a pseudoscalar mass of $m_{PS} \approx 770$ MeV and $m_{PS} \approx 400$ MeV, respectively.

We show how the correlation functions of our $\mathcal{B}$, $\mathcal{B}\mathcal{B}$ and $\mathcal{B}\overline{\mathcal{B}}$ states are calculated and how the different diagrams are related to the corresponding isospin channels. Next we present the interpolators and their combinations we use to obtain various quantum numbers for spin J, parity P and charge conjugation C. In the case of the intermeson potentials $\mathcal{B}\mathcal{B}$ and $\mathcal{B}\overline{\mathcal{B}}$ we distinguish the two cases $r = 0$ and distances $r > 0$. For our coarse lattice and the operator combinations that couple to total angular momentum $J = 0$ at vanishing distance we also perform a projection of the static-light meson spins into the direction $\hat{\mathbf{r}}$ of the static source distance. For the other combinations and our fine lattice different representations will mix. Finally we summarize the improvement methods we use and specify the details of our lattices and simulation parameters.

6.1 Calculation of the Correlators

6.1.1 Static-Light Mesons

The result for the static-light meson correlation function was already given in equation (5.27) of section 5.4.3. Now we want to show the evaluation and implementation of this two-point function in more detail:

$$\begin{aligned}
C_{\mathcal{B}}(t) &= \frac{1}{V_4} \sum_{\mathbf{x_0}} \sum_{\mathbf{x}} \langle 0 | \mathcal{B}(\mathbf{x}, t)\, \mathcal{B}^\dagger(\mathbf{x_0}, 0) | 0 \rangle \\
&= \pm \frac{1}{V_4} \sum_{\mathbf{x_0}} \sum_{\mathbf{x}} \left\langle\!\!\left\langle \overline{q}(\mathbf{x}, t)_{\,a}^{\,\alpha}\, \mathcal{O}_{\alpha,\beta}\, Q(\mathbf{x}, t)_{\,a}^{\,\beta}\, \overline{Q}(\mathbf{x_0}, 0)_{\,b}^{\,\gamma}\, \mathcal{O}_{\gamma,\delta}\, q(\mathbf{x_0}, 0)_{\,b}^{\,\delta} \right\rangle\!\!\right\rangle_U \\
&= \mp \frac{1}{V_4} \sum_{\mathbf{x_0}} \sum_{\mathbf{x}} \left\langle\!\!\left\langle M^{-1}(\mathbf{x_0}, 0 | \mathbf{x}, t)_{\,b,a}^{\,\delta,\alpha}\, \mathcal{O}_{\alpha,\beta}\, D^{-1}_{\mathrm{static}}(\mathbf{x}, t | \mathbf{x_0}, 0)_{\,a,b}^{\,\beta,\gamma}\, \mathcal{O}_{\gamma,\delta} \right\rangle\!\!\right\rangle_U \\
&= \mp \frac{1}{V_4} \sum_{\mathbf{x_0}} \left\langle\!\!\left\langle \mathrm{Tr} \left[M^{-1}(\mathbf{x_0}, 0 | \mathbf{x_0}, t)\, \mathcal{O}\, \frac{\mathbb{1} + \gamma_4}{2} \prod_{k=0}^{t-1} U_4^\dagger(\mathbf{x_0}, ka\hat{4})\, \mathcal{O} \right] \right\rangle\!\!\right\rangle_U .
\end{aligned} \tag{6.1}$$

$\mathcal{B}^\dagger(\mathbf{x_0}, 0)$ creates a static-light meson at space-time point $(\mathbf{x_0}, 0)$ which is annihilated by $\mathcal{B}(\mathbf{x}, t)$ at $(\mathbf{x}, t)$ on a given gauge configuration. Q labels the static color source, q the light quark and $\mathcal{O}$ a combination of lattice derivative operators and Dirac γ-matrices. In order to increase statistics and reduce statistical errors we additionally average over all possible source points $(\mathbf{x_0}, t_0) \in \{1, \ldots, L_\sigma\}^3 \times \{1, \ldots, L_\tau\}$ normalized by $V_4 = L_\sigma^3 L_\tau$ which labels the size of the lattice. The sum over $\mathbf{x}$ is due to the projection to definite momentum where we already set $\mathbf{p} = \mathbf{0}$, see section 5.2. The indices $\alpha, \beta, \gamma, \delta$ denote spinor indices and a, b represent color indices. The $\pm$ in the second step depends on the Γ-structure of $\mathcal{O}$. We get one minus sign from each exchange of fermion fields and maybe an additional minus sign from the commutation of Γ with γ_4 since

$$(\bar{q}\Gamma Q)^\dagger = (q^\dagger \gamma_4 \Gamma Q)^\dagger = -Q^\dagger \Gamma \gamma_4 q = \pm Q^\dagger \gamma_4 \Gamma q = \pm(\overline{Q}\Gamma q). \tag{6.2}$$

The change to $\mp$ in the third line of equation (6.1) is due to the permutation of the light quarks q in order to contract them to the light quark propagator $M^{-1}(y|x) = \langle q(y)\bar{q}(x)\rangle$. The static color sources Q have been contracted to the static propagator $D^{-1}_{\text{static}}(\mathbf{x}, t|\mathbf{x_0}, 0)$. In the last step we inserted the static propagator (5.20) where $U_\mu(x)$ is the gauge link connecting the lattice sites x and $x + a\hat{\mu}$, where $\hat{\mu}$ denotes a unit vector in μ-direction. Finally the trace is taken over color and Dirac indices.

Graphically, our static-light meson correlator can be depicted as

(6.3)

where the straight line represents the static quark propagator and the wiggly line the light quark propagator.

6.1.2 Static-Light Meson-Meson Potentials

With the experience from calculating the static-light correlation function we go one step further and determine also correlation functions between pairs of static-light mesons, namely $\mathcal{B}_{(\mathbf{r},t)}\mathcal{B}_{(\mathbf{0},t)}$[1] and $\mathcal{B}_{(\mathbf{r},t)}\overline{\mathcal{B}}_{(\mathbf{0},t)}$. Thereby the two $\mathcal{B}$ mesons are separated by the static quark-quark (or quark-antiquark) sources that guarantee definite spatial distance $r = |\mathbf{r}| = Ra$. a denotes the lattice

[1] In the following we use the more compact index-notation, i.e. we set $\mathcal{B}_x \equiv \mathcal{B}(x)$.

spacing, $R \in \mathbb{N}_0$ and the positions of the light quarks q are not fixed. In general, for n_f mass-degenerate flavors we denote $\mathcal{B}^i = \overline{q}^i \mathcal{O} Q$ as the static-light meson with light quark q^i where $i = 1, \ldots, n_f$ labels the quark flavor.

To keep formulas well-arranged we will not display the normalization factors, the sums for averaging over the whole lattice as well as the Fourier-transformations for momentum projection. Also Dirac and color indices will be omitted.

$\mathcal{BB}$ Meson Potentials

With these definitions the correlator of a potential between two static-light $\mathcal{B}^i$ mesons can be evaluated as:

$$\begin{aligned} C_{\mathcal{B}^i\mathcal{B}^j}(t) &= \langle 0 | \mathcal{B}^i_{(\mathbf{0},t)} \mathcal{B}^i_{(\mathbf{r},t)} \, (\mathcal{B}^j_{(\mathbf{0},0)} \mathcal{B}^j_{(\mathbf{r},0)})^\dagger | 0 \rangle \\ &= \pm \left\langle\!\!\left\langle \overline{q}^i_{(\mathbf{0},t)} \mathcal{O} \, Q_{(\mathbf{0},t)} \, \overline{q}^i_{(\mathbf{r},t)} \mathcal{O} \, Q_{(\mathbf{r},t)} \, \overline{Q}_{(\mathbf{r},0)} \mathcal{O} \, q^j_{(\mathbf{r},0)} \, \overline{Q}_{(\mathbf{0},0)} \mathcal{O} \, q^j_{(\mathbf{0},0)} \right\rangle\!\!\right\rangle_U \\ &= \pm \, \delta_{ij} \left\langle\!\!\left\langle \mathrm{Tr}\left[\mathcal{O} \, M^{-1}_{(\mathbf{0},0|\mathbf{0},t)} \mathcal{O} \, D^{-1}_{(\mathbf{0},t|\mathbf{0},0)} \right] \mathrm{Tr}\left[\mathcal{O} \, M^{-1}_{(\mathbf{r},0|\mathbf{r},t)} \mathcal{O} \, D^{-1}_{(\mathbf{r},t|\mathbf{r},0)} \right] \right\rangle\!\!\right\rangle_U \\ &\quad \mp \, \delta_{ij} \left\langle\!\!\left\langle \mathrm{Tr}\left[\mathcal{O} \, M^{-1}_{(\mathbf{r},0|\mathbf{0},t)} \mathcal{O} \, D^{-1}_{(\mathbf{0},t|\mathbf{0},0)} \mathcal{O} \, M^{-1}_{(\mathbf{0},0|\mathbf{r},t)} \mathcal{O} \, D^{-1}_{(\mathbf{r},t|\mathbf{r},0)} \right] \right\rangle\!\!\right\rangle_U \\ &= \pm \, \delta_{ij} \left(\right. \end{aligned} \quad - \quad \left. \right) \,, \tag{6.4}$$

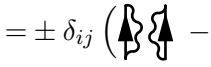

where the $\pm$ in the second step and the change to $\mp$ for the second term in the third step is of the same reasons as in the case of the static-light correlator, see equation (6.1). The traces are over Dirac and color indices again which are not displayed. One also observes that the correlation function is only non-zero for $i = j$.

Let us have a closer look at isospin. Since only the light quarks carry isospin it is convenient to classify $\mathcal{BB}$ mesons according to isospin. For our case of $n_f = 2$ light quark flavors the isospin singlet corresponds to the representation $\frac{1}{\sqrt{2}}(ud + du)$ and the isotriplet to (uu, dd, $\frac{1}{\sqrt{2}}(ud - du)$) . This means that for $I = 1$ both diagrams, the disconnected and the connected, contribute to the correlator. However, within the $I = 0$ sector the connected diagram does not appear and the correlator is only given by the disconnected diagram.

$\mathcal{B}\overline{\mathcal{B}}$ Meson Potentials

Next, we calculate the potential between a $\mathcal{B}^i$ and a $\overline{\mathcal{B}}^i$ meson. It is given by

$$C_{\mathcal{B}^i\overline{\mathcal{B}^j}}(t) = \langle 0 | \mathcal{B}^i_{(\mathbf{0},t)} \mathcal{B}^{i\,\dagger}_{(\mathbf{r},t)} \, (\mathcal{B}^j_{(\mathbf{0},0)} \mathcal{B}^{j\,\dagger}_{(\mathbf{r},0)})^\dagger | 0 \rangle$$

$$
\begin{aligned}
&= \pm \left\langle\!\!\left\langle \overline{q}^{\,i}_{(\mathbf{0},t)} \mathcal{O}\, Q_{(\mathbf{0},t)}\, \overline{Q}_{(\mathbf{r},t)} \mathcal{O}\, q^{i}_{(\mathbf{r},t)}\, \overline{q}^{\,j}_{(\mathbf{r},0)} \mathcal{O}\, Q_{(\mathbf{r},0)}\, \overline{Q}_{(\mathbf{0},0)} \mathcal{O}\, q^{j}_{(\mathbf{0},0)} \right\rangle\!\!\right\rangle_U \\
&= \pm\, \delta_{ij} \left\langle\!\!\left\langle \mathrm{Tr}\left[\mathcal{O}\, M^{-1}_{(\mathbf{0},0|\mathbf{0},t)} \mathcal{O}\, D^{-1}_{(\mathbf{0},t|\mathbf{0},0)}\right] \mathrm{Tr}\left[\mathcal{O}\, M^{-1}_{(\mathbf{r},t|\mathbf{r},0)} \mathcal{O}\, D^{-1}_{(\mathbf{r},0|\mathbf{r},t)}\right] \right\rangle\!\!\right\rangle_U \\
&\quad \mp \left\langle\!\!\left\langle \mathrm{Tr}\left[\mathcal{O}\, M^{-1}_{(\mathbf{r},t|\mathbf{0},t)} \mathcal{O}\, D^{-1}_{(\mathbf{0},t|\mathbf{0},0)} \mathcal{O}\, M^{-1}_{(\mathbf{0},0|\mathbf{r},0)} \mathcal{O}\, D^{-1}_{(\mathbf{r},0|\mathbf{r},t)}\right] \right\rangle\!\!\right\rangle_U \\
&= \pm\, \delta_{ij}
\end{aligned}
$$

$$
\mp
$$

$$
. \tag{6.5}
$$

The traces are over Dirac and color indices again and the evaluation is in analogy to equation (6.4). The corresponding isospin representations for the $\mathcal{B}\overline{\mathcal{B}}$ states are now given by ($\bar{d}u$, $\bar{u}d$, $\frac{1}{\sqrt{2}}(\bar{u}u - \bar{d}d)$) for $I = 1$ and $\frac{1}{\sqrt{2}}(\bar{u}u + \bar{d}d)$ for $I = 0$. For the isosinglet one receives contributions from the connected diagram in any case while the disconnected diagram only contributes for $i = j$. In contrast, for the isotriplet the connected diagram does not appear and the correlator is only given by the disconnected diagram.

Summary of our Calculations

Let us now sum over the flavor indices i and j for the correlators $C_{\mathcal{B}\mathcal{B}}(t)$ and $C_{\mathcal{B}\overline{\mathcal{B}}}(t)$. We define the (unnormalized) meson states,

$$
|B^i\rangle = \mathcal{B}^{i\,\dagger}\,|0\rangle \tag{6.6}
$$

and consider the case of $n_f = 2$ degenerate quark flavors[2]. We further define a symmetric meson state $|B_s\rangle$ and a antisymmetric meson state $|B_a\rangle$:

$$
|B_s\rangle = \frac{1}{\sqrt{2}}(|B^1\rangle + |B^2\rangle), \tag{6.7}
$$

$$
|B_a\rangle = \frac{1}{\sqrt{2}}(|B^1\rangle - |B^2\rangle). \tag{6.8}
$$

For instance, one finds that the antisymmetric combination decouples from the other states:

$$
C_{\mathcal{B}_s\overline{\mathcal{B}}_a}(t) = 0, \tag{6.9}
$$

$$
C_{\mathcal{B}_a\overline{\mathcal{B}}_a}(t) = \pm
$$

$$
. \tag{6.10}
$$

The generalization to $n_f > 2$ yields that only the completely symmetric combination of the states $|B^i\rangle$ has a nontrivial mixing. For each antisymmetric

[2]The following part is mainly based on chapter II.C of [93].

combination in two or more flavor indices the overlap with the $\overline{Q}Q$ states vanishes. Therefore, we define our general symmetric static-light meson state as

$$|B\rangle = \frac{1}{\sqrt{n_f}} \sum_{i}^{n_f} |B^i\rangle \,. \tag{6.11}$$

Then, for $n_f = 2$, the correlation functions for our meson-meson potentials classified due to isospin are given by (graphically and without irrelevant overall phases[3]):

- Isospin $I = 0$:

$C_{\mathcal{B}\mathcal{B}}(t) =$ 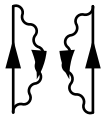 (6.12)

$C_{\mathcal{B}\overline{\mathcal{B}}}(t) =$ 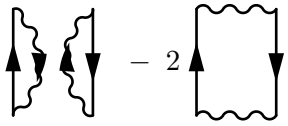 (6.13)

- Isospin $I = 1$:

$C_{\mathcal{B}\mathcal{B}}(t) =$ 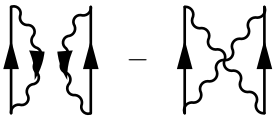 (6.14)

$C_{\mathcal{B}\overline{\mathcal{B}}}(t) =$ 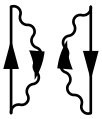 (6.15)

6.2 Representations and Classification of States

This section is mainly taken from our Lattice 2010 proceedings [145]. In addition we refer to [46]. In the continuum limit, the static-light states can be classified according to fermionic representations J^P of the rotation group O(3). At vanishing distance $\mathbf{r} = \mathbf{0}$ the $\mathcal{B}\mathcal{B}$ and $\mathcal{B}\overline{\mathcal{B}}$ states can be characterized by integer J^P and J^{PC} quantum numbers, respectively. However at $r = |\mathbf{r}| > 0$ the O(3) (or O(3) $\otimes\, \mathcal{C}$) symmetry is broken down to its cylindrical $\mathrm{D}_{\infty\mathrm{h}}$ subgroup. The irreducible representations of this are conventionally labeled by the

[3]Since we are only interested in energies and energy differences respectively, an overall sign or factor does not affect our calculations and results.

spin along the axis Λ, where Σ, Π, Δ refer to $\Lambda = 0, 1, 2$, respectively, with a subscript $\eta = g$ for gerade (even) $PC = +$ or $\eta = u$ for ungerade (odd) $PC = -$ transformation properties with respect to the midpoint. All $\Lambda \geq 1$ representations are two-dimensional. The one-dimensional Σ representations carry an additional $\sigma_v = \pm$ superscript for their reflection symmetry with respect to a plane that includes the two endpoints.

6.2.1 Operators and Quantum Numbers

To create states of different $J^{P(C)}$ we use operators $\mathcal{O}$ that contain combinations of Dirac γ-matrices and covariant lattice derivatives $\nabla[U]$ that act on a fermion spinor q as,

$$\nabla_\mu q_x = U_{x,\mu} q_{y+a\hat{\mu}} - U_{x,-\mu} q_{x-a\hat{\mu}}\,, \quad \text{where} \quad U_{x,-\mu} = U^\dagger_{x-a\hat{\mu},\mu}\,. \tag{6.16}$$

On the lattice the continuum rotational symmetry is broken and the groups O(3) and $\mathrm{D}_{\infty\mathrm{h}}$ need to be replaced by their finite dimensional subgroups $\mathrm{O_h}$ and $\mathrm{D_{4h}}$, respectively. We label fermionic representations of the octahedral group $\mathrm{O_h}$ as $\mathrm{O_h}'$. For fermionic representations of $\mathrm{D}_{\infty\mathrm{h}}$ that we do not need in the present context, see reference [105]. It is well known, see e.g. reference [46], that the assignment of a continuum spin to a lattice representation can be ambiguous, in particular for radial excitations because a given $\mathrm{O_h}$ representation can be subduced from several continuum Js. For instance,

$$\begin{aligned} G_1 &\leftarrow J = \frac{1}{2}, \frac{7}{2}, \ldots & A_1 &\leftarrow J = 0, 4, \ldots \\ H &\leftarrow J = \frac{3}{2}, \frac{5}{2}, \ldots & T_1 &\leftarrow J = 1, 3, 4, \ldots \end{aligned} \tag{6.17}$$

For $\Lambda \leq 2$ the mapping of continuum $\mathrm{D}_{\infty\mathrm{h}}$ onto discrete $\mathrm{D_{4h}}$ representations is more straight forward. Hence in this case we adopt the continuum notation only.

The operators that we used to create the static-light mesons are displayed in table 6.1 (see, e.g., reference [119]). The intermeson potentials were obtained by combining two static-light mesons of different (or the same) quantum numbers. This can be projected into an irreducible $\mathrm{D}_{\infty\mathrm{h}}$ representation, either by coupling the light quarks together in spinor space [143] or by projecting the static-light meson spins into the direction $\hat{\mathbf{r}}$ of the static source distance, by applying $\frac{1}{2}(\mathbb{1} \pm i\gamma_5 \boldsymbol{\gamma} \cdot \hat{\mathbf{r}})$, and taking appropriate symmetric ($S_z = 1$) or antisymmetric ($S_z = 0$) spin combinations. Both approaches can be related to each other via a Fierz transformation. For our coarse lattice and the operator combinations that

$\mathcal{O}$	wave [119]	O_h' rep.	continuum J^P	J^P (heavy-light)
γ_5	S	G_1^+	$\frac{1}{2}^+$	$0^-, 1^-$
$\mathbb{1}$	P_-	G_1^-	$\frac{1}{2}^-$	$0^+, 1^+$
$\gamma_i\nabla_i$	P_-	G_1^-	$\frac{1}{2}^-$	$0^+, 1^+$
$(\gamma_1\nabla_1 - \gamma_2\nabla_2)$ + cycl.	P_+	H^-	$\frac{3}{2}^-$	$1^+, 2^+$

Table 6.1: Operators and representations for static-light mesons. In the last column we display the J^P for a heavy-light meson, obtained by substituting the (spinless) static source by a heavy fermion.

$\mathcal{O} \otimes \mathcal{O}$	S_z	Isospin: $I = 1$		Isospin: $I = 0$	
		$r = 0$: J^P	$r > 0$: $\Lambda_\eta^{(\sigma_\nu)}$	$r = 0$: J^{PC}	$r > 0$: $\Lambda_\eta^{(\sigma_\nu)}$
$\gamma_5 \otimes \gamma_5$, $\mathbb{1} \otimes \mathbb{1}$	0	$0^+, 1^+$	Σ_g^+, Σ_g^+	$0^{++}, 1^{+-}$	Σ_g^+, Σ_u^-
	1	1^+	Π_g	1^{+-}	Π_u
$\gamma_5 \otimes \mathbb{1}$, $\gamma_5 \otimes \gamma_i\nabla_i$	0	$0^-, 1^-$	Σ_u^-, Σ_u^-	$0^{-+}, 1^{--}$	Σ_u^-, Σ_g^+
	1	1^-	Π_u	1^{--}	Π_g
$\gamma_5 \otimes (\gamma_1\nabla_1 - \gamma_2\nabla_2)$	/	$1^-, 2^-$	$\Sigma_u^+, \Pi_u, \Delta_u$	$1^{--}, 2^{-+}$	$\Sigma_g^+, \Pi_g, \Sigma_u^+$
$\gamma_i\nabla_i \otimes (\gamma_1\nabla_1 - \gamma_2\nabla_2)$	/	$1^+, 2^+$	$\Sigma_g^-, \Pi_g, \Delta_g$	$1^{+-}, 2^{++}$	$\Sigma_u^-, \Pi_u, \Sigma_g^+$

Table 6.2: Operators and continuum representations for the meson-meson ($\mathcal{BB}$) and meson-antimeson ($\mathcal{B}\overline{\mathcal{B}}$) states in the isosinglet as well as the isovector channel. The quantum numbers heavy-light mesons would carry are not displayed.

couple to total angular momentum $J = 0$ we have performed this spin projection which is discussed in more detail in the next subsection. For the other operator combinations on our coarse lattice and all operator combinations on our large lattice we have not performed this projection, due to limited computing time, and thus different representations will mix. The analyzed operators and the corresponding representations are listed in table 6.2. We note that the operator combinations $\gamma_5 \otimes \gamma_5$ and $\mathbb{1} \otimes \mathbb{1}$ carry the same quantum numbers as well as the combinations $\gamma_5 \otimes \mathbb{1}$ and $\gamma_5 \otimes \gamma_i\nabla_i$.

For $J > 0$ and $r > 0$ the irreducible representations of O(3) split up into two or more irreducible representations of $D_{\infty h}$. For instance the angular momentum of the P_+ wave operator within ($J^P = 1^-, 2^-$; $r = 0$) can be perpendicular or parallel to the intermeson axis. For the axis pointing into the $\hat{3}$-direction, we call the $S \otimes P_+$ operator $\gamma_5 \otimes (\gamma_1\nabla_1 - \gamma_2\nabla_2)$ "parallel" ($\gamma_5 \otimes P_\parallel$) and the other combinations "perpendicular" ($\gamma_5 \otimes P_\perp$). Equally, for our $P_- \otimes P_+$ operator $\gamma_i\nabla_i \otimes (\gamma_1\nabla_1 - \gamma_2\nabla_2)$ we label the "parallel" combination as $\gamma_i\nabla_i \otimes P_\parallel$ and the "perpendicular" combination as $\gamma_i\nabla_i \otimes P_\perp$.

The $P_\perp$ states have no angular momentum pointing into the direction of the

axis and hence only couple with the light quarks to the Σ and Π states. Vice versa, the $P_{\|}$ operators can only create Π and Δ states but not the Σ states.

6.2.2 The Coupling of two $\mathcal{B}$ Mesons – Spin Projection

As mentioned, the spin projection has only been performed on our coarse lattice and only for the operators that couple to spin $\frac{1}{2}$ (see table 6.1 and table 6.2). For all other combinations and the combinations on our fine lattice, different representations will mix. Because of the asymptotic behavior of the correlation function one then gets the lowest energy eigenstate in the limit $t \to \infty$. However, not all operators have good overlap with the ground state. Therefore an unambiguous determination of the spin states in these cases is difficult.

Building $\mathcal{B}\mathcal{B}$ and $\mathcal{B}\overline{\mathcal{B}}$ states by coupling two static-light mesons means coupling two half-integral spin states. In order to get meson-meson or meson-antimeson states of well defined spin quantum numbers $|S, S_z\rangle$ we first project the static-light meson spins into the direction $\hat{\mathbf{r}}$ of the static source distance. The projection operator $\mathcal{P}_\pm$ is given by

$$\mathcal{P}_\pm = \frac{1}{2}(\mathbb{1} \pm i\gamma_5 \boldsymbol{\gamma} \cdot \hat{\mathbf{r}})\,, \tag{6.18}$$

with properties

$$\mathcal{P}_\pm \mathcal{P}_\pm = \mathcal{P}_\pm \mathcal{P}_\pm^\dagger = \mathcal{P}_\pm^\dagger \mathcal{P}_\pm = \mathcal{P}_\pm\,, \tag{6.19}$$

$$\mathcal{P}_\pm \mathcal{P}_\mp = \mathcal{P}_\mp \mathcal{P}_\pm = \mathcal{P}_\pm \mathcal{P}_\mp^\dagger = 0\,. \tag{6.20}$$

Applying the projection operator to the static-light mesons we get

$$\mathcal{P}_+ \mathcal{B} = \mathcal{B}^\uparrow = \overline{q}\,\mathcal{O}\,\mathcal{P}_+ Q(x)\,, \tag{6.21}$$

$$\mathcal{P}_- \mathcal{B} = \mathcal{B}^\downarrow = \overline{q}\,\mathcal{O}\,\mathcal{P}_- Q(x)\,. \tag{6.22}$$

Now we can form well defined spin states $|S, S_z\rangle$ by taking appropriate symmetric or antisymmetric spin combinations. The antisymmetric singlet state is then given by

$$|0,0\rangle = \frac{1}{\sqrt{2}}(\mathcal{B}^\uparrow \mathcal{B}^\downarrow - \mathcal{B}^\downarrow \mathcal{B}^\uparrow) \tag{6.23}$$

and the symmetric triplet by

$$|1,1\rangle = \mathcal{B}^\uparrow \mathcal{B}^\uparrow, \quad |1,0\rangle = \frac{1}{\sqrt{2}}(\mathcal{B}^\uparrow \mathcal{B}^\downarrow + \mathcal{B}^\downarrow \mathcal{B}^\uparrow), \quad |1,-1\rangle = \mathcal{B}^\downarrow \mathcal{B}^\downarrow\,. \tag{6.24}$$

In our notation of table 6.2, Σ_g labels the antisymmetric $|0,0\rangle$ state, Σ_u the symmetric $|1,0\rangle$ state and $\Pi_{g/u}$ the linear combination $\frac{1}{2}(|1,1\rangle \pm i|1,-1\rangle)$.

Using the results of section 6.1.2 we evaluate the static-light meson-meson and meson-antimeson correlators for $\Sigma_{g/u}$ and $\Pi_{g/u}$ spin states. We start with the correlation function between two $\mathcal{B}$ mesons for the Σ_g state. Without irrelevant phases the correlator can be calculated as

$$\begin{aligned} C^{\Sigma_g}_{\mathcal{B}^i\mathcal{B}^j}(t) &= \langle 0| \left(\mathcal{B}^{\uparrow i}_{(\mathbf{0},t)}\mathcal{B}^{\downarrow i}_{(\mathbf{r},t)} - \mathcal{B}^{\downarrow i}_{(\mathbf{0},t)}\mathcal{B}^{\uparrow i}_{(\mathbf{r},t)}\right)\left(\mathcal{B}^{\uparrow j}_{(\mathbf{0},0)}\mathcal{B}^{\downarrow j}_{(\mathbf{r},0)} - \mathcal{B}^{\downarrow j}_{(\mathbf{0},0)}\mathcal{B}^{\uparrow j}_{(\mathbf{r},0)}\right)^\dagger |0\rangle \\ &= \langle 0| \mathcal{B}^{\uparrow i}_{(\mathbf{0},t)}\mathcal{B}^{\downarrow i}_{(\mathbf{r},t)}(\mathcal{B}^{\uparrow j}_{(\mathbf{0},0)}\mathcal{B}^{\downarrow j}_{(\mathbf{r},0)})^\dagger - \mathcal{B}^{\uparrow i}_{(\mathbf{0},t)}\mathcal{B}^{\downarrow i}_{(\mathbf{r},t)}(\mathcal{B}^{\downarrow j}_{(\mathbf{0},0)}\mathcal{B}^{\uparrow j}_{(\mathbf{r},0)})^\dagger \\ &\quad - \mathcal{B}^{\downarrow i}_{(\mathbf{0},t)}\mathcal{B}^{\uparrow i}_{(\mathbf{r},t)}(\mathcal{B}^{\uparrow j}_{(\mathbf{0},0)}\mathcal{B}^{\downarrow j}_{(\mathbf{r},0)})^\dagger + \mathcal{B}^{\downarrow i}_{(\mathbf{0},t)}\mathcal{B}^{\uparrow i}_{(\mathbf{r},t)})(\mathcal{B}^{\downarrow j}_{(\mathbf{0},0)}\mathcal{B}^{\uparrow j}_{(\mathbf{r},0)})^\dagger|0\rangle\,. \end{aligned} \tag{6.25}$$

By expanding these four terms the same way as in section 6.1.1 and using the commutation rules for γ-matrices and fermions as well as the properties of the spin projector (see eq. 6.19) we find that the second and third terms of equation (6.25) disappear. Thus, both states, Σ_g and Σ_u, are degenerated, since $C^{\Sigma_g}_{\mathcal{B}^i\mathcal{B}^j}(t)$ and $C^{\Sigma_u}_{\mathcal{B}^i\mathcal{B}^j}(t)$ only differ by the sign of the second and the third term (see, e.g., eq. 6.23 and eq. 6.24). The first and fourth terms finally yield

$$\begin{aligned} C^{\Sigma_{g/u}}_{\mathcal{B}^i\mathcal{B}^j}(t) &= \pm\,\delta_{ij}\left\langle\!\!\left\langle \mathrm{Tr}\left[\mathcal{P}_+\mathcal{O}\,M^{-1}_{(\mathbf{0},0|\mathbf{0},t)}\mathcal{O}\,D^{-1}_{(\mathbf{0},t|\mathbf{0},0)}\right]\mathrm{Tr}\left[\mathcal{P}_-\mathcal{O}\,M^{-1}_{(\mathbf{r},0|\mathbf{r},t)}\mathcal{O}\,D^{-1}_{(\mathbf{r},t|\mathbf{r},0)}\right]\right\rangle\!\!\right\rangle_U \\ &\quad \pm\,\delta_{ij}\left\langle\!\!\left\langle \mathrm{Tr}\left[\mathcal{P}_-\mathcal{O}\,M^{-1}_{(\mathbf{0},0|\mathbf{0},t)}\mathcal{O}\,D^{-1}_{(\mathbf{0},t|\mathbf{0},0)}\right]\mathrm{Tr}\left[\mathcal{P}_+\mathcal{O}\,M^{-1}_{(\mathbf{r},0|\mathbf{r},t)}\mathcal{O}\,D^{-1}_{(\mathbf{r},t|\mathbf{r},0)}\right]\right\rangle\!\!\right\rangle_U \\ &\quad \mp\,\delta_{ij}\left\langle\!\!\left\langle \mathrm{Tr}\left[\mathcal{P}_+\mathcal{O}\,M^{-1}_{(\mathbf{r},0|\mathbf{0},t)}\mathcal{O}\,D^{-1}_{(\mathbf{0},t|\mathbf{0},0)}\,\mathcal{P}_-\mathcal{O}\,M^{-1}_{(\mathbf{0},0|\mathbf{r},t)}\mathcal{O}\,D^{-1}_{(\mathbf{r},t|\mathbf{r},0)}\right]\right\rangle\!\!\right\rangle_U \\ &\quad \mp\,\delta_{ij}\left\langle\!\!\left\langle \mathrm{Tr}\left[\mathcal{P}_-\mathcal{O}\,M^{-1}_{(\mathbf{r},0|\mathbf{0},t)}\mathcal{O}\,D^{-1}_{(\mathbf{0},t|\mathbf{0},0)}\,\mathcal{P}_+\mathcal{O}\,M^{-1}_{(\mathbf{0},0|\mathbf{r},t)}\mathcal{O}\,D^{-1}_{(\mathbf{r},t|\mathbf{r},0)}\right]\right\rangle\!\!\right\rangle_U \\ &= \pm\,\delta_{ij}\Big[\Big(\underset{\mathcal{P}_+\ \mathcal{P}_-}{\quad} + \underset{\mathcal{P}_-\ \mathcal{P}_+}{\quad}\Big) - \Big(\underset{\mathcal{P}_+\ \mathcal{P}_-}{\quad} + \underset{\mathcal{P}_-\ \mathcal{P}_+}{\quad}\Big)\Big]\,. \end{aligned} \tag{6.26}$$

The correlator for the $\Pi_{g/u}$ states then is trivial and given by

$$C^{\Pi_{g/u}}_{\mathcal{B}^i\mathcal{B}^j}(t) = \pm\delta_{ij}\Big[\Big(\underset{\mathcal{P}_+\ \mathcal{P}_+}{\quad} + \underset{\mathcal{P}_-\ \mathcal{P}_-}{\quad}\Big) - \Big(\underset{\mathcal{P}_+\ \mathcal{P}_+}{\quad} + \underset{\mathcal{P}_-\ \mathcal{P}_-}{\quad}\Big)\Big]\,. \tag{6.27}$$

In analogy the correlation functions for static-light meson-antimeson states for $\Sigma_{g/u}$ reads

$$\begin{aligned} C^{\Sigma_{g/u}}_{\mathcal{B}^i\overline{\mathcal{B}}^j}(t) &= \pm\,\delta_{ij}\left\langle\!\!\left\langle \mathrm{Tr}\left[\mathcal{P}_+\mathcal{O}\,M^{-1}_{(\mathbf{0},0|\mathbf{0},t)}\mathcal{O}\,D^{-1}_{(\mathbf{0},t|\mathbf{0},0)}\right]\mathrm{Tr}\left[\mathcal{P}_-\mathcal{O}\,M^{-1}_{(\mathbf{r},t|\mathbf{r},0)}\mathcal{O}\,D^{-1}_{(\mathbf{r},0|\mathbf{r},t)}\right]\right\rangle\!\!\right\rangle_U \\ &\quad \pm\,\delta_{ij}\left\langle\!\!\left\langle \mathrm{Tr}\left[\mathcal{P}_-\mathcal{O}\,M^{-1}_{(\mathbf{0},0|\mathbf{0},t)}\mathcal{O}\,D^{-1}_{(\mathbf{0},t|\mathbf{0},0)}\right]\mathrm{Tr}\left[\mathcal{P}_+\mathcal{O}\,M^{-1}_{(\mathbf{r},t|\mathbf{r},0)}\mathcal{O}\,D^{-1}_{(\mathbf{r},0|\mathbf{r},t)}\right]\right\rangle\!\!\right\rangle_U \\ &\quad \mp\left\langle\!\!\left\langle \mathrm{Tr}\left[\mathcal{P}_+\mathcal{O}\,M^{-1}_{(\mathbf{r},t|\mathbf{0},t)}\mathcal{O}\,D^{-1}_{(\mathbf{0},t|\mathbf{0},0)}\mathcal{P}_-\mathcal{O}\,M^{-1}_{(\mathbf{0},0|\mathbf{r},0)}\mathcal{O}\,D^{-1}_{(\mathbf{r},0|\mathbf{r},t)}\right]\right\rangle\!\!\right\rangle_U \\ &\quad \mp\left\langle\!\!\left\langle \mathrm{Tr}\left[\mathcal{P}_-\mathcal{O}\,M^{-1}_{(\mathbf{r},t|\mathbf{0},t)}\mathcal{O}\,D^{-1}_{(\mathbf{0},t|\mathbf{0},0)}\mathcal{P}_+\mathcal{O}\,M^{-1}_{(\mathbf{0},0|\mathbf{r},0)}\mathcal{O}\,D^{-1}_{(\mathbf{r},0|\mathbf{r},t)}\right]\right\rangle\!\!\right\rangle_U \end{aligned}$$

$$= \pm\,\delta_{ij}\Big(\underset{\mathcal{P}_+\ \mathcal{P}_-}{\text{}} + \underset{\mathcal{P}_-\ \mathcal{P}_+}{\text{}}\Big) \mp \Big(\underset{\mathcal{P}_+\ \mathcal{P}_-}{\text{}} + \underset{\mathcal{P}_-\ \mathcal{P}_+}{\text{}}\Big)\,. \tag{6.28}$$

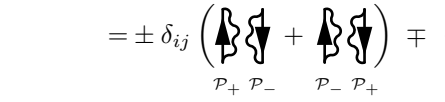

For the $\Pi_{g/u}$ state it is given by

$$C^{\Pi_{g/u}}_{\mathcal{B}^i\overline{\mathcal{B}}^j}(t) = \pm\delta_{ij}\Big(\underset{\mathcal{P}_+\ \mathcal{P}_+}{\text{}} + \underset{\mathcal{P}_-\ \mathcal{P}_-}{\text{}}\Big) \mp \Big(\underset{\mathcal{P}_+\ \mathcal{P}_+}{\text{}} + \underset{\mathcal{P}_-\ \mathcal{P}_-}{\text{}}\Big)\,. \tag{6.29}$$

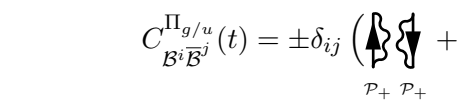

6.3 Simulation Details

For the numerical evaluation we employ two sets of $N_\mathrm{f} = 2$ Sheikholeslami-Wohlert configurations generated by the QCDSF Collaboration [146]. The parameter values for our small and our large lattice are listed in table 6.3 where the Sommer parameter with $r_0 = 0.5$ fm was used to set the physical scale [89] (see also section 4.6). The inversion of the Dirac operator is very expensive for the physical small up and down quark masses which are degenerate in our simulations, $m_u = m_d$. Thus, calculations are often performed at unphysically high quark masses m_q. They are related to the lattice parameter κ via

$$am_q = \frac{1}{2}\left(\frac{1}{\kappa} - \frac{1}{\kappa_\mathrm{crit}}\right). \tag{6.30}$$

On both lattices valence and sea quark masses are equal, $\kappa = \kappa_\mathrm{sea} = \kappa_\mathrm{val}$. However, our coarse lattice has a smaller κ value than our fine lattice. Hence the pseudoscalar mass is much higher on the $16^3 \times 32$ lattice (770 MeV) than on the $24^3 \times 48$ lattice (400 MeV). This might also yield interesting insights in the interactions between two $\mathcal{B}$ mesons and the question of attraction or repulsion. Finally, to obtain observables in physical units, the scale is set using the Sommer parameter $r_0(\beta, \kappa) = 0.5$ fm and the pseudoscalar mass corresponds to its infinite volume value.

In order to evaluate the correlation functions (6.1) and (6.12) - (6.15) for $\mathcal{B}, \mathcal{B}\mathcal{B}$ and $\mathcal{B}\overline{\mathcal{B}}$ mesons on the lattice we have written codes in C^{++} using the

volume $L_\sigma^3 \times L_\tau$	β	$\kappa_\mathrm{val} = \kappa_\mathrm{sea}$	c_SW	a [fm]	La [fm]	m_PS [MeV]	N_conf
$16^3 \times 32$	5.29	0.13550	1.9192	0.084	1.34	770(9)	180
$24^3 \times 48$	5.29	0.13620	1.9192	0.077	1.85	400(4)	200

Table 6.3: Lattice parameters.

Chroma software library [147, 148]. Thereby we apply the methods of chapter 5 and give a short summary and repeat[4].

To achieve high statistics all-to-all propagators need to be computed. This is done using stochastic estimator techniques. We generate 300 complex $\mathbb{Z}_2$ noise sources and apply the hopping parameter expansion to reduce the stochastic variance [125, 93, 120]. Furthermore we enhance the signal over noise ratio by employing a static action with reduced self-energy [93]. This is done by applying one stout smearing step [133] with the parameter $\rho = 1/6$ to the temporal links, used to calculate the static propagators. Wuppertal smearing [126] with a hopping parameter value $\kappa_{\mathrm{w}} = 0.3$ is applied to the source and sink operators, where we employ spatially smeared parallel transporters (APE smearing) [93] with the parameters $n_{\mathrm{iter}} = 15$, $\alpha = 2.5$. Wuppertal smearing changes the overlap of the interpolators with the physical states. Since we are not only interested in ground states but also in excited states, differently smeared interpolators are applied to get access to the desired states[5]. A very effective technique is the variational method. We generate a basis of three differently smeared source and sink interpolators with iteration numbers $N_{\mathrm{iter}} \in \{16, 50, 100\}$ for all our operators. Masses are then extracted from the resulting three by three cross-correlation matrices, solving a generalized eigenvalue problem as explained in section 5.3.1. Errors are calculated using the jackknife method (see appendix C.3).

Our computations were mainly performed on the high performance cluster *Athene* located at the computer center of the University of Regensburg [149].

[4] Taken from our Lattice 2010 proceedings [145]

[5] We explicitly make use of this property in section 7.3.3

"Das Schönste, was wir erleben können, ist das Geheimnisvolle. Es ist das Grundgefühl, das an der Wiege von wahrer Kunst und Wissenschaft steht. Wer es nicht kennt und sich nicht mehr wundern, nicht mehr staunen kann, der ist sozusagen tot und sein Auge ist erloschen."

Albert Einstein

7 Results

Using the methods detailed in the previous chapters, we now want to address the question of attraction or repulsion between two $\mathcal{B}$ mesons. Of special interest is the relation between the static-light meson-(anti)meson potential and the static quark-(anti)quark separation.

We start our discussion with the analysis of static-light mesons for both lattices. Using this example, we explain how we extract masses for ground and excited states using effective masses for selecting the fit ranges. Next, we move on to $\mathcal{B}\mathcal{B}$ meson-meson states and define the intermeson potential $V_{\mathcal{B}\mathcal{B}}(r)$ between pairs of static-light mesons. The results for both lattices, different operator combinations, different spin and isospin channels are discussed and compared.

Subsequently, we come to the $\mathcal{B}\overline{\mathcal{B}}$ meson-antimeson states which are also very interesting. In the isovector channel these states have the same quantum numbers as states consisting of a $Q\overline{Q}$ static potential and a scalar $I = 1$ particle. The isoscalar channel is even more complicated, since some operators in the $S_z = 0$ channel couple directly to the static quark potential or the vacuum state. Thus, at this background of multiparticle excitations, it is difficult to interpret the nature of the lowest few energy levels.

We note that the main results and explanations of the following were already reported in our Lattice 2010 and Lattice 2011 proceedings [145, 34].

7.1 Static-Light Mesons

In order to determine the energy levels of the static-light mesons, we calculate the static-light correlation function (6.1) for a three by three cross-correlation matrix. The meson interpolators differ by their amount of Wuppertal smearing steps given in section 6.3. Then, solving the generalized eigenvalue problem (5.15) yields the eigenvalues (5.16)

$$\lambda_k(t,t_0) \propto e^{-(t-t_0)\,m_k}[1+\mathcal{O}(e^{-(t-t_0)\,\Delta m_k})]\,, \tag{7.1}$$

as stated in section 5.3.1. Therefore, to extract the masses m_k by correlated fits (see appendix C.2) we use one- and also two-exponential ansätze of the form

$$C_{\lambda_k}(t) = A_1\, e^{-(t-t_0)\,m_k} \left[+A_2\, e^{-(t-t_0)\,m_k'}\right]. \tag{7.2}$$

Although the masses from higher excited states should die out for long time separations there are obvious reasons to additionally perform the four-parameter fits. In spite of using the variational method, signals are usually polluted at short time separations and for large times the signals might disappear in the noise. Thus, ranges for reliable one-exponential fits are often short and noisy, especially for the excited channels. Applying two-exponential fits enables us to start much earlier in time and thus to fit a larger range. We note that one has to include at least five data points as in this case there are four fit parameters. Contamination from excitations will then hopefully be absorbed in the second exponent m_k' and the mass m_k will be bared. However, two-exponential fits are more complicated to perform since these depend very sensitively on the four start parameters, the diagonalization-timeslice t_0 and the fit range. We therefore start with the one-exponential fit and use the result as input parameter for the two-exponential fit. The reliability of fits is characterized by the ratio χ^2/d.o.f. where d.o.f. labels the number of degrees of freedom. In addition we take care that fit parameters stay stable within errors against variation of fit ranges, i.e. the earliest timeslice t_{min} where we can start fitting is reached when the fit parameters agree within errors with the fit parameters obtained from fits starting at $t_{\mathrm{min}}+1$. A very small amplitude, a huge second mass or huge errors for amplitudes or masses,e.g., might indicate that the fitter does not "see" two exponents. In order to decide which fit we can trust most, we compare the results from one- and two-exponential fits in different fit ranges and choose the most reliable one.

To determine suitable fit ranges for the one-exponential fits, we calculate effective masses M_{eff} from ratios of adjacent timeslices and refer to section 5.3.2. It is given by

$$M^k_{\text{eff},t_0}\left(t+\frac{a}{2}\right) = a^{-1}\ln\left(\frac{\lambda_k(t,t_0)}{\lambda_k(t+a,t_0)}\right), \tag{7.3}$$

and will form a plateau as a function of t once the contributions of higher excited states are strongly suppressed. We note that the quality of the effective mass plateaus can depend upon the operators generating the desired quantum numbers as well as upon the chosen basis. The reason is, that the various interpolators have different overlap with ground and excited states.

In figure 7.1, we show the effective energy levels E_{eff} for $t_0 = 2a$ for all our static-light operators from table 6.1. On the left hand side we display the results from the coarse lattice and on the right hand side those from the fine lattice. In each channel all three eigenvalues are plotted. Black circles represent the ground state, blue squares the first excited state and green triangles the second excited one. The red horizontal lines mark our fit results plus and minus the error in the corresponding time interval $[t_{\min}, t_{\max}]$ from the single-exponential ansatz. In tables 7.1 to 7.4 we give the values of the fitted masses, together with t_0, the ratio χ^2/d.o.f. and the fit ranges for both, one- and two-exponential fits. The fit results we trust most, either from the single or from the double exponential fits, are printed bold.

The figure shows long and clear plateaus with small errors for all ground state masses, except for the $\nabla_i\gamma_i$ operator on the large lattice and the $(\nabla_1\gamma_1 - \nabla_2\gamma_2)\ P_+$ wave on our small lattice. First and second excited states are afflicted with larger errors and form shorter plateaus in most cases, since noise is swallowing the signal earlier. While the signals for the first excited state on our coarse lattice are quite good and form adequate plateaus the signals on the fine lattice are a bit weaker and the quality of the plateau is poorer. Also the time $t_{\min}$ where the plateaus start are larger on the fine lattice than on the coarse lattice. This is due to the smaller lattice spacing but also in debt of the much smaller quark mass on the fine lattice. Consequently the mass m_k of the eigenvalue λ_k governs the correlator only at larger time separations. For this reason also, the two-exponential ansatz mostly yields more reliable results on the fine lattice. The second excited state provides the weakest signals and the largest errors. Since it is the last state in our three by three operator basis, it is the state which is most contaminated by higher excitations. However, we also try to extract the masses of second excited states when possible, but enjoy the

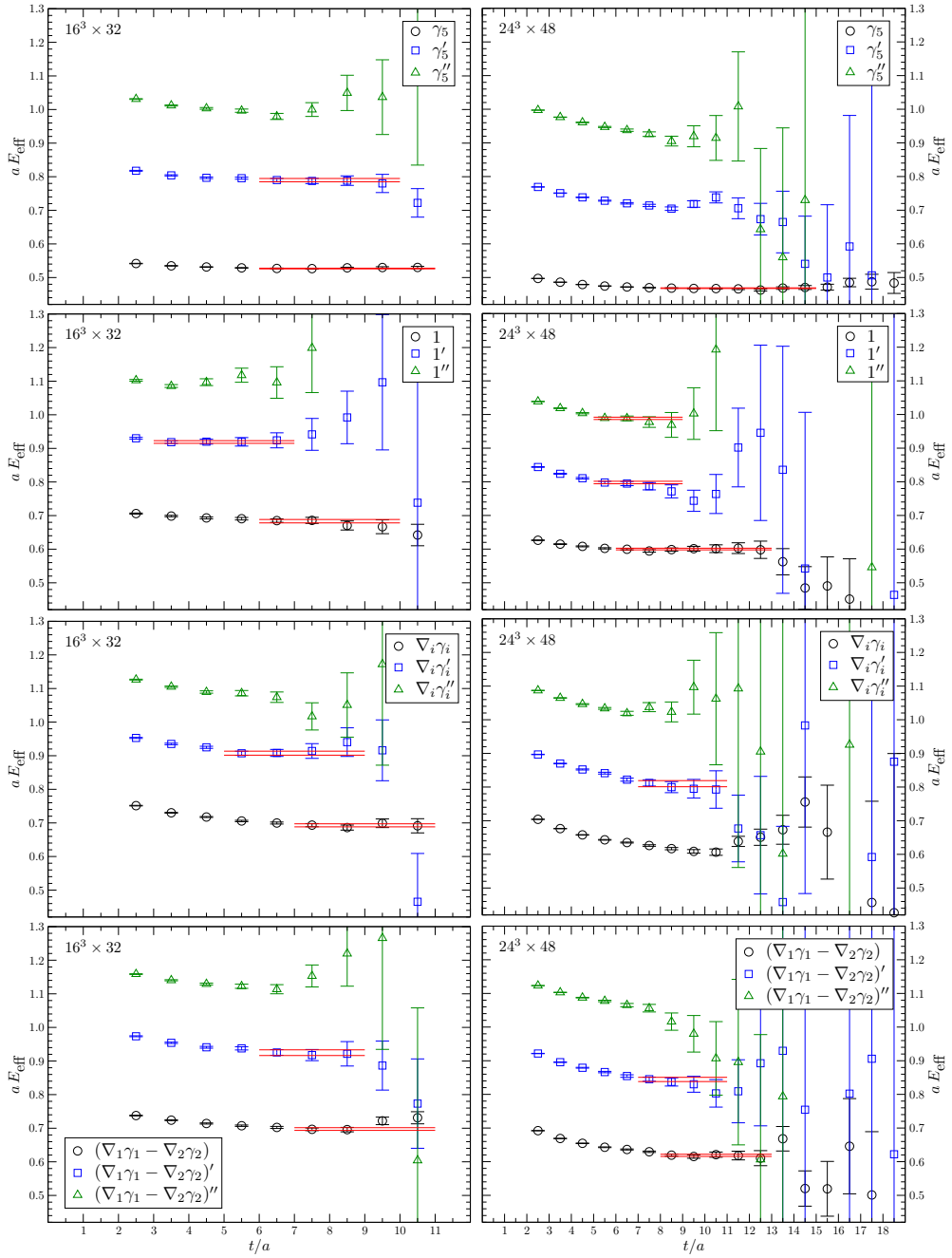

Figure 7.1: Effective mass plots for static-light mesons from our coarse (left column) and fine (right column) lattice. Both ground and excited states for all our operators are shown. The red horizontal lines indicate the $m \pm \sigma_m$ results from correlated single exponential fits to the corresponding time intervals which are also given in table 7.1 and 7.3.

$\mathcal{O}$	t_0	am_{λ_0}	χ^2/ν	$[t_{min}, t_{max}]$	t_0	am_{λ_1}	χ^2/ν	$[t_{min}, t_{max}]$	t_0	am_{λ_2}	χ^2/ν	$[t_{min}, t_{max}]$
γ_5	2	**0.5268(11)**	1.27	$[6, 11]$	2	**0.7899(49)**	0.10	$[6, 10]$	–	–	–	–
1	2	**0.6833(51)**	0.82	$[6, 10]$	2	**0.9190(40)**	0.39	$[3, 7]$	–	–	–	–
$\nabla_i\gamma_i$	2	0.6928(45)	0.67	$[7, 11]$	2	0.9076(60)	0.21	$[5, 9]$	–	–	–	–
$(\nabla_1\gamma_1 - \nabla_2\gamma_2)$	2	0.6976(40)	2.67	$[7, 11]$	2	0.9248(85)	0.14	$[6, 9]$	–	–	–	–

Table 7.1: Static-light meson masses from our $16^3 \times 32$ lattice obtained from single exponential fits.

$\mathcal{O}$	t_0	am_{λ_0}	χ^2/ν	$[t_{min}, t_{max}]$	t_0	am_{λ_1}	χ^2/ν	$[t_{min}, t_{max}]$	t_0	am_{λ_2}	χ^2/ν	$[t_{min}, t_{max}]$
γ_5	1	0.5262(14)	1.35	$[2, 11]$	1	0.7913(49)	0.33	$[2, 10]$	1	**0.9891(99)**	1.64	$[2, 8]$
1	–	–	–	–	–	–	–	–	–	–	–	–
$\nabla_i\gamma_i$	1	**0.6909(49)**	1.05	$[2, 11]$	1	**0.9006(148)**	1.21	$[2, 9]$	1	**1.0560(232)**	0.96	$[2, 8]$
$(\nabla_1\gamma_1 - \nabla_2\gamma_2)$	1	**0.6920(57)**	1.73	$[2, 11]$	1	**0.9198(114)**	0.60	$[2, 9]$	1	**1.1125(123)**	0.67	$[2, 8]$

Table 7.2: Static-light meson masses from our $16^3 \times 32$ lattice obtained from double exponential fits.

$\mathcal{O}$	t_0	am_{λ_0}	χ^2/ν	$[t_{min}, t_{max}]$	t_0	am_{λ_1}	χ^2/ν	$[t_{min}, t_{max}]$	t_0	am_{λ_2}	χ^2/ν	$[t_{min}, t_{max}]$
γ_5	2	0.4682(9)	1.01	$[8, 15]$	–	–	–	–	–	–	–	–
1	2	**0.6002(24)**	1.25	$[6, 13]$	2	**0.7978(37)**	0.78	$[5, 9]$	2	**0.9886(34)**	0.19	$[5, 9]$
$\nabla_i\gamma_i$	–	–	–	–	2	0.8100(91)	0.29	$[7, 11]$	–	–	–	–
$(\nabla_1\gamma_1 - \nabla_2\gamma_2)$	2	0.6188(32)	0.31	$[8, 13]$	2	0.8444(63)	0.45	$[7, 11]$	–	–	–	–

Table 7.3: Static-light meson masses from our $24^3 \times 48$ lattice obtained from single exponential fits.

$\mathcal{O}$	t_0	am_{λ_0}	χ^2/ν	$[t_{min}, t_{max}]$	t_0	am_{λ_1}	χ^2/ν	$[t_{min}, t_{max}]$	t_0	am_{λ_2}	χ^2/ν	$[t_{min}, t_{max}]$
γ_5	1	**0.4671(11)**	0.87	$[2, 15]$	1	**0.7056(52)**	1.07	$[2, 9]$	1	**0.9134(86)**	0.74	$[2, 12]$
1	2	0.5920(65)	1.04	$[3, 13]$	2	0.7561(420)	0.63	$[3, 11]$	2	0.9610(238)	0.79	$[3, 10]$
$\nabla_i\gamma_i$	1	**0.6074(52)**	1.22	$[3, 11]$	1	**0.8128(84)**	1.34	$[2, 11]$	1	**0.9941(116)**	1.35	$[2, 10]$
$(\nabla_1\gamma_1 - \nabla_2\gamma_2)$	1	**0.6134(53)**	1.22	$[3, 13]$	1	**0.8426(59)**	0.66	$[2, 12]$	1	**1.0471(82)**	0.95	$[2, 10]$

Table 7.4: Static-light meson masses from our $24^3 \times 48$ lattice obtained from double exponential fits.

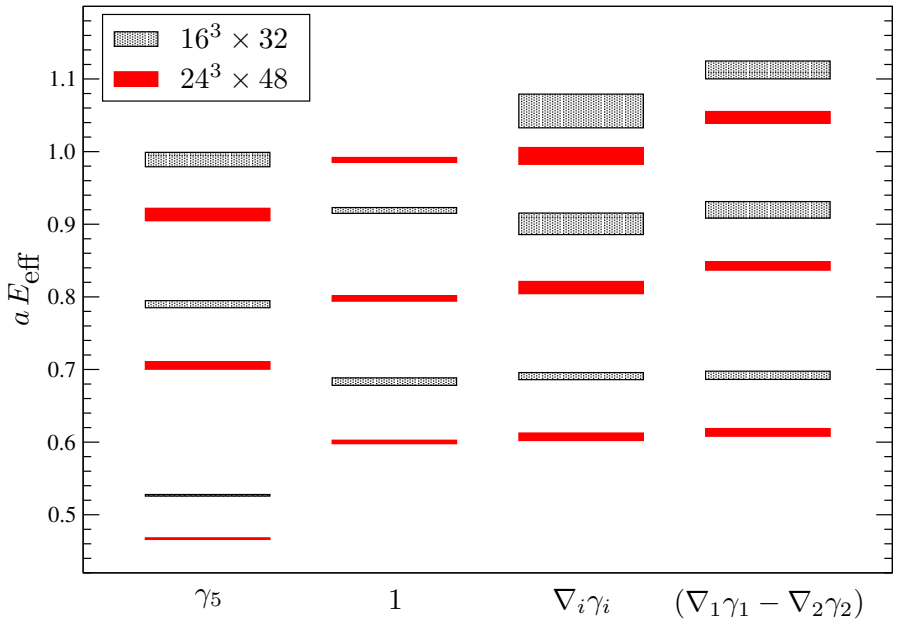

Figure 7.2: Summary plot of the static-light meson spectra. The black shaded rectangles represent our results from the coarse lattice and the red rectangles those from the fine lattice. Both ground and excited states for all our operators are shown.

results with caution. An overview of the effective static-light meson masses is displayed in figure 7.2.

7.2 $\mathcal{BB}$ Intermeson Potentials

In the following we present our results for the potentials between two mesons, $\mathcal{B}(\mathbf{r})\mathcal{B}(\mathbf{0})$, for different static quark-quark separations $r = |\mathbf{r}| = Ra$ with a being the lattice spacing. We show some effective mass plots and define the intermeson potential $V_{\mathcal{BB}}$. Next, we discuss our results and answer the question of attraction or repulsion. The different spin and isospin channels on our two lattice sets are compared and analyzed. Also the relation between the pion masses corresponding to a lattice set and the interaction strength between two $\mathcal{B}$ mesons is discussed.

We perform one and two exponential fits for all our computed potentials at each separation r. The fit results are compared and carefully checked with respect to the stability of the fit parameters by varying the fit ranges and with

respect to other parameters like the confidence of the fit or the ratio χ^2/d.o.f..

7.2.1 Effective Masses

In figure 7.3 we display the effective ground state energy levels E_{eff} for $t_0 = 2a$ of the $\gamma_5 \otimes \gamma_5$ $\mathcal{BB}$ system for different distances $R = r/a$. The upper plot shows the results obtained from the coarse lattice in the $I = S_z = 0$ channel and the lower one those from the fine lattice for $I = 0$. One should also keep in mind that on the $24^3 \times 48$ lattice we did not perform the spin projection and hence there will be additional pollution from the Π_u state, see table 6.2.

For both lattice sets we find that the quality of the effective mass plateaus deteriorates with decreasing distance. Since the two $\mathcal{B}$ mesons are interacting more strongly for short distance the wavefunction of such meson-meson states differs from the mere product of our two static-light meson interpolators. These interactions cause smaller effective masses at short distances. This is a first indicator for attraction at short static quark-quark separations in this channel. For increasing distances the effective masses of the $\mathcal{BB}$ state are increasing too and approach the sum of two $\frac{1}{2}^+$ static-light meson effective masses, the expected $r \to \infty$ limit, represented by the blue dotted curve.

For time separations $t > 9a$ on the $16^3 \times 32$ lattice signals become weak. Especially from the $24^3 \times 48$ lattice one sees that noise is gaining the upper hand for times $t > 11a$. Errors are comparable within lattice units. Due to the poor quality of many effective mass plateaus, two-exponential fits to the $t/a \in \{3, \ldots, 10/11\}$ data yield the most reliable masses for the displayed examples.

7.2.2 Potentials

Our aim is to clarify the question of attraction or repulsion between a pair of two $\mathcal{B}$ mesons as a function of their static quark separation. Monitoring effective mass curves however can only exhibit the rough trend and is basically used to choose appropriate fit ranges. Therefore, we define intermeson potentials as the difference between the meson-meson energy levels and the $r \to \infty$ two static-light meson limiting cases:

$$V_{\mathcal{B}_1\mathcal{B}_2}(r) = E_{\mathcal{B}_1\mathcal{B}_2}(r) - (m_{\mathcal{B}_1} + m_{\mathcal{B}_2}) \quad \stackrel{r\to\infty}{\longrightarrow} \quad 0\,. \tag{7.4}$$

The indices in $\mathcal{B}_1, \mathcal{B}_2$ represent the general case when we combine two static-light mesons of different (or the same) quantum numbers generated by the

corresponding operators given in table 6.1 and 6.2. For calculating the correlated difference between the $\mathcal{BB}$ meson energy levels and two static-light mesons we use the jackknife method.

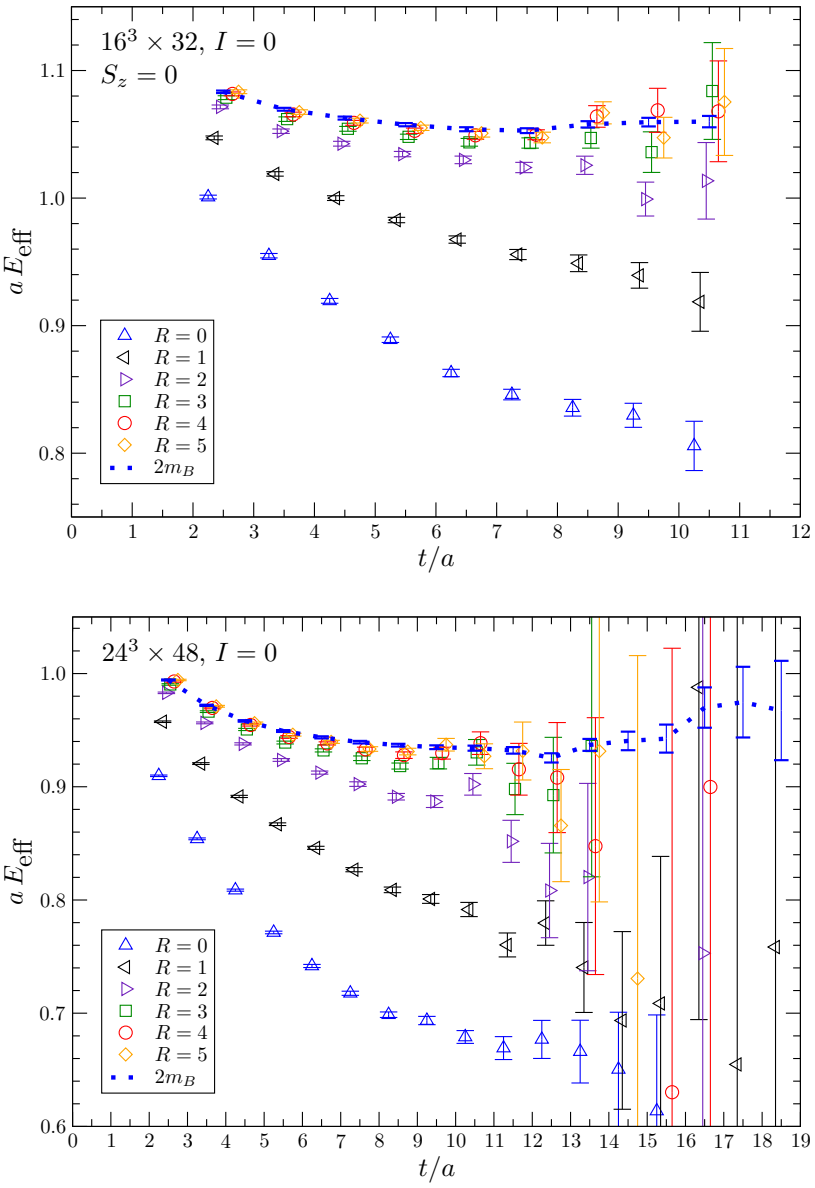

Figure 7.3: Effective groundstate masses of the $\gamma_5 \otimes \gamma_5$ (Σ_g^+) operator at different distances. The upper plot displays the $I = S_z = 0$ channel on the $16^3 \times 32$ lattice, the lower one the $I = 0$ channel without spin projection on the $24^3 \times 48$ lattice. The dotted line corresponds to twice the mass of a single $\frac{1}{2}^+$ static-light meson.

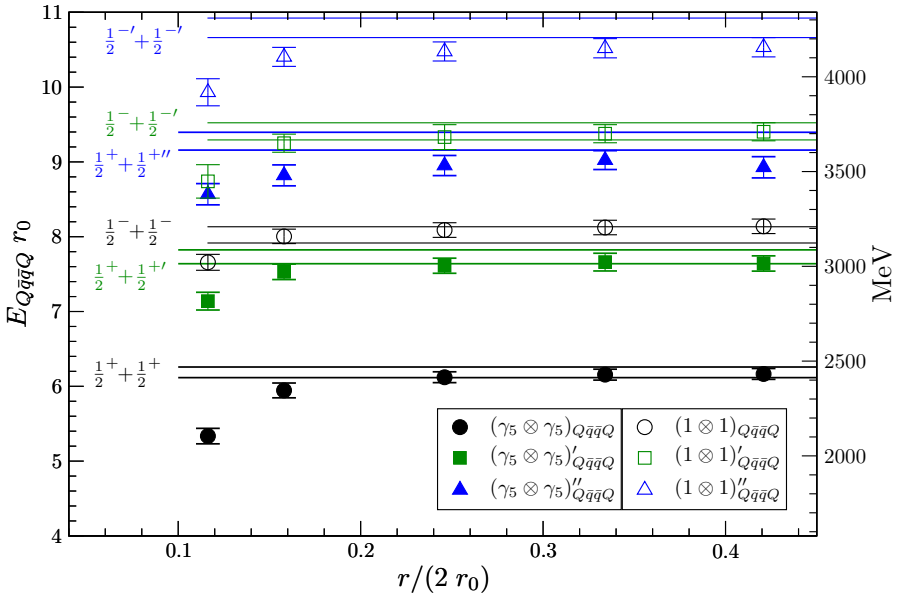

Figure 7.4: $\mathcal{BB}$ meson energy levels on the $16^3 \times 32$ lattice in the isoscalar Σ_g^+ channel for both operator combinations (see table 6.2), $\gamma_5 \otimes \gamma_5$ (full symbols) and $\mathbb{1} \otimes \mathbb{1}$ (open symbols). The horizontal lines mark the corresponding $m_{\mathcal{B}_1} + m_{\mathcal{B}_2}$ results from correlated fits, where their widths indicate the fit error.

Determining intermeson potentials eliminates a further issue. Energies evaluated in lattice simulations with static sources are afflicted with a large unphysical static self-energy contribution. By forming the difference these contributions cancel and we are able to concentrate on the binding energy between the states.

Before presenting the potentials we first have a look at $\mathcal{BB}$ meson energies. In figure 7.4 we compare the isoscalar Σ_g^+ channel for our two operator combinations $\gamma_5 \otimes \gamma_5$ and $\mathbb{1} \otimes \mathbb{1}$. We display ground, first and second excited states for both combinations and in addition the corresponding static-light meson masses $m_{\mathcal{B}_1} + m_{\mathcal{B}_2}$. On the x-axis one reads the separation r in fm and on the y-axis the energy levels both, in lattice units as well as in MeV.

Although both operator combinations generate the same quantum numbers we observe significant differences in the energies. The $\gamma_5 \otimes \gamma_5$ levels are lying much lower (of the order of 700 MeV) than the related $\mathbb{1} \otimes \mathbb{1}$ levels. The $\mathbb{1} \otimes \mathbb{1}$ ground state is lying slightly above the $\gamma_5 \otimes \gamma_5$ first excited state just like the ratio between the $\mathbb{1} \otimes \mathbb{1}$ first excited state and the $\gamma_5 \otimes \gamma_5$ second excited state. Both are of the order of 50 to 100 MeV. So this provides a good example that

operators with the same quantum numbers but different Dirac structures can couple to different sets of physical states. For this reason we determine the difference for the intermeson potentials only from meson-meson energies and static-light mesons with the corresponding operators of the same structure.

In this case we assume that the $\gamma_5 \otimes \gamma_5$ combination couples to the ground state Σ_g^+ whereas the $\mathbb{1}\otimes\mathbb{1}$ combination overlaps most with the first excited state $\Sigma_g^{+\prime}$. The marginal mass shift might arise from a small ground state contribution which pollutes the excitations. Similar observations were also found in [143].

7.2.3 Isoscalar Potentials

In this section we present intermeson potentials $V_{\mathcal{B}_1\mathcal{B}_2}(r)$ in the isoscalar channel of a selected operator combination. Our remaining results for $\mathcal{B}\mathcal{B}$ potentials with isospin $I = 0$ can be found in appendix D.1.

In figure 7.5 we display within three panels the operator combination $\gamma_5 \otimes \gamma_5$. On our coarse lattice we distinguish between the $S_z = 0$ (top panel) and the $S_z = 1$ (intermediate panel) spin channel while on our fine lattice both representations mix (bottom panel). For all plots we use black circles, red squares and blue triangles to mark the ground, the first excited and the second excited states respectively. The x-axis displays the separation r in fm and the y-axis the energy levels both, in lattice units as well as in MeV.

The first plot of this figure shows the ground state (Σ_g^+), the first excited state ($\Sigma_g^{+\prime}$) and the second excited state ($\Sigma_g^{+\prime\prime}$). In the last case the energetically most favorable $r \to \infty$ combination of states would be a $\frac{1}{2}^+$ (γ_5) ground state plus a radially excited $\frac{1}{2}^{+\prime\prime}$ state (γ_5). The next level would be the sum of two $\frac{1}{2}^{+\prime}$ states. It is not clear to which one of these states our creation operator has best overlap. In the figure we display both possibilities. The latter assignment however would mean that in the second excited state there is strong attraction of the order of 140 MeV at intermediate distances. Although the first excited state is attractive of the order of 50 MeV at the same distance, the ground state is not and approaches the expected limit. Thus we assume that also the intermeson potentials for the excited states should go to zero. At short distances we find strong attraction for all energy levels in a range of approximately 350 MeV to 100 MeV from the ground to the second excited state.

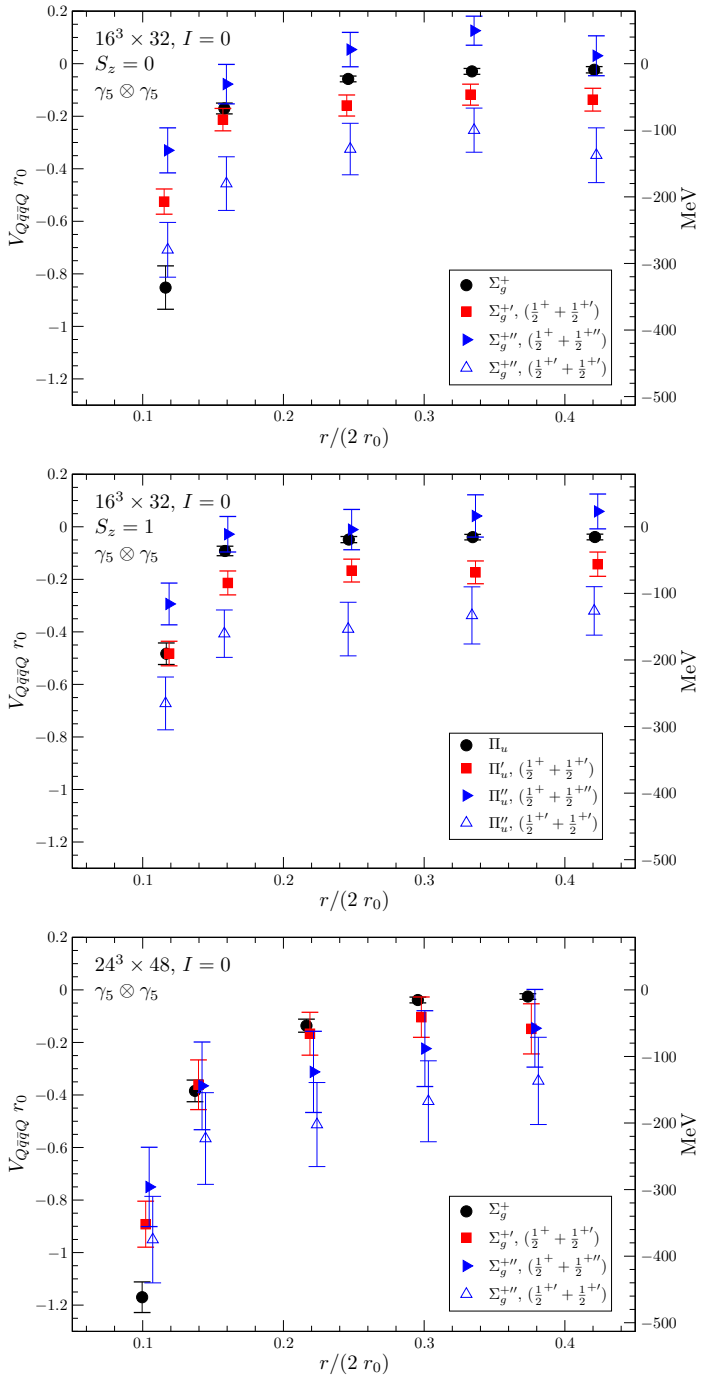

Figure 7.5: The intermeson potential $V_{\mathcal{B}_1\mathcal{B}_2}(r)$ in the isoscalar channel for the combination $\gamma_5 \otimes \gamma_5$. From top to bottom we show the coarse lattice for $S_z = 0$, $S_z = 1$ and the fine lattice. Black circles, red squares and blue triangles mark the ground, the first and the second excited states respectively. Full symbols indicate the chosen energy levels.

In the intermediate panel of the figure we display the potentials for spin $S_z = 1$ with quantum numbers Π_u, Π_u' and Π_u'' for ground state, first and second excitation. Also in this case the $(\frac{1}{2}^+ + \frac{1}{2}^{+\prime\prime})$ level is chosen to represent the Π_u'' state for the same reason. The attraction for short separations is a bit smaller in this spin channel. It is of the order of 200 MeV for ground and first excited state and of the order of 100 MeV for the second excited state. At intermediate distances of 0.4 fm the potentials for the Π_u and Π_u'' state approach zero while the Π_u' state is attractive and of the same order as the $\Sigma_g^{+\prime}$ state.

Finally, the bottom plot shows the results from our fine lattice. The states are represented by Σ_g^+, $\Sigma_g^{+\prime}$ and $\Sigma_g^{+\prime\prime}$ since they mark the lowest lying states. As on the coarse lattice we find attraction for short distances and the expected infinite distance limit at static quark separations of about 0.4 fm. The scaling seems to be a bit smoother and we will pick up on this point in section 7.2.6. The errors for the excited states are larger than in the two previous cases. We think this is due to the mixing of the different spin representations. While the ground state is still well resolved the excited states Σ_g^+ and $\Sigma_g^{+\prime}$ are significantly contaminated by the Π_u states.

7.2.4 Isovector Potentials

Next we pick one interesting example from the isovector channel and refer to appendix D.1 for the remaining $I = 1$ $\mathcal{BB}$ intermeson potentials. In figure 7.6 we show the operator combination $\gamma_5 \otimes \mathbb{1}$.

In the first plot we again depict the case where the spin component S_z is projected to zero. The Σ_u^- ground state is attractive at short distances of $O(100)$ MeV. At intermediate distances we observe evident repulsion of the order of 50 MeV in a range from $0.2 - 0.4$ fm. For the first excited state $(\Sigma_u^{-\prime})$ there are two possible combination of states, a radially excited $\frac{1}{2}^{+\prime}$ state (γ_5) plus a $\frac{1}{2}^-$ $(\mathbb{1})$ ground state or the reversed case, namely the sum of $\frac{1}{2}^+$ and $\frac{1}{2}^{-\prime}$. While the first assignment approaches the expected $r \to \infty$ limit at intermediate distances, the latter shows repulsion of $O(50)$ MeV. However, we think that this repulsive channel marks the correct first excited state. It is energetically most favorable and therefore our first choice. In addition, this is consistent with our ground state results. In analogy we choose the combination $(\frac{1}{2}^{+\prime\prime} + \frac{1}{2}^-)$ to represent the second excited state $\Sigma_u^{-\prime\prime}$ which also seems to be repulsive at distances of 0.35 fm. But errors are larger in this channel so that a clear statement is not possible.

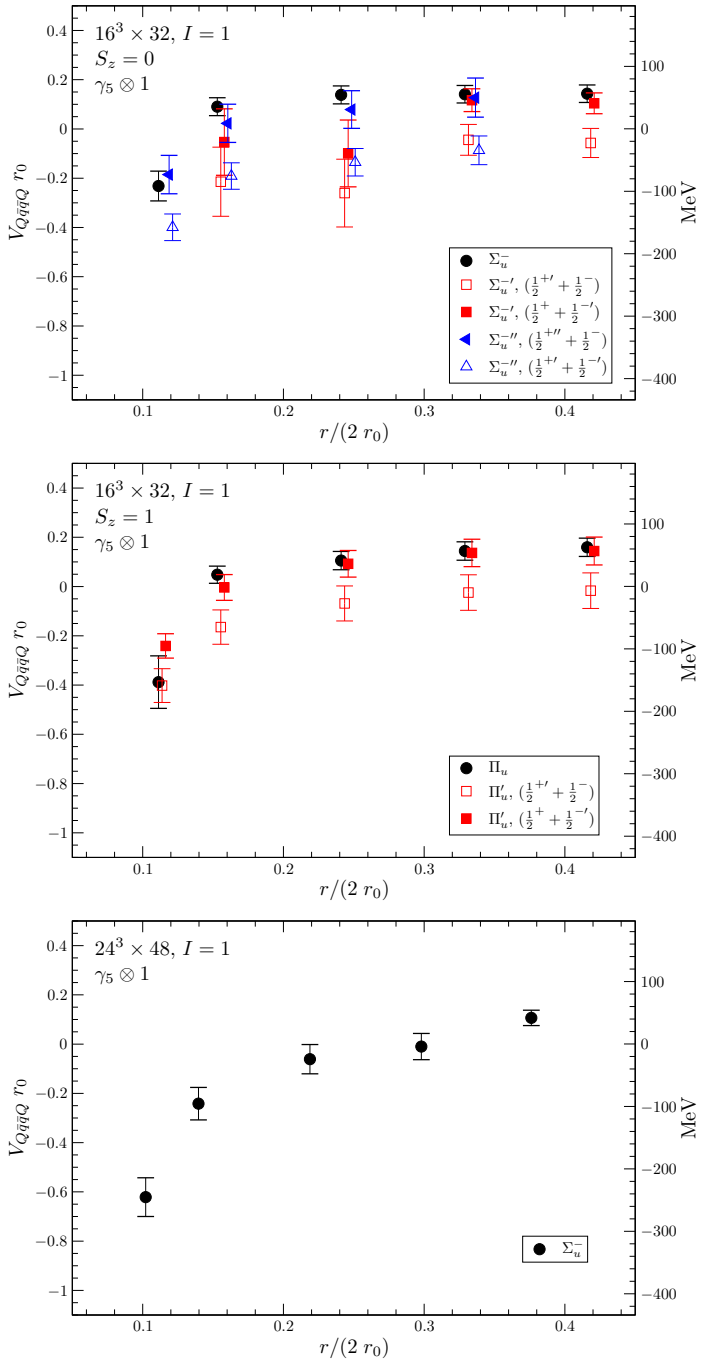

Figure 7.6: The intermeson potential $V_{\mathcal{B}_1\mathcal{B}_2}(r)$ in the isovector channel for the combination $\gamma_5 \otimes \mathbb{1}$. From top to bottom we show the coarse lattice for $S_z = 0$, $S_z = 1$ and the fine lattice. Black circles, red squares and blue triangles mark the ground, the first and the second excited states respectively. Full symbols indicate the chosen energy levels.

In the $S_z = 1$ channel we display the Π_g ground state and its first excitation Π_g' which is represented by the combination $(\frac{1}{2}^+ + \frac{1}{2}^{-\prime})$ like in the case of the $(\Sigma_u^{-\prime})$ state. The other possibility would be more attractive of the order of 70 MeV. But we think that our interpolators overlap most with the repulsive state. At short distances the intermeson potential is attractive for the Π_g and the selected Π_g' state. For intermediate separations then we find repulsion of the order of 60 MeV for the ground and the first excited state. The second excited state could not be extracted.

The last plot of the figure shows the Σ_u^- ground state potential on our fine lattice. At a distance of 0.1 fm the potential is attractive of $O(250)$ MeV and growing to a slight repulsion of the order of 40 MeV at 0.38 fm. The excited states could not be resolved since their signals are to weak and noisy.

7.2.5 Comparison of the different Spin and Isospin Channels

After this detailed discussion of the two examples we want to compare the various spin and isospin channels in order to clarify the differences between these channels and the different operator combinations [1]. From figure 7.7 to figure 7.10 we present the operator combinations $\gamma_5 \otimes \gamma_5$, $\mathbb{1} \otimes \mathbb{1}$, $\gamma_5 \otimes \mathbb{1}$ and $\gamma_5 \otimes \nabla_i \gamma_i$ on our coarse lattice, where we have performed the spin projection. The different spin $S_z = 0, 1$ and isospin $I = 0, 1$ channels are displayed in the upper plots for the ground state and in the lower plots for the first excited state. Thereby, full symbols represent isospin $I = 0$ and open symbols $I = 1$. The spin component $S_z = 0$ is visualized with black circles and spin $S_z = 1$ with green triangles. Again, on the x-axis one reads the separation r in fm and the y-axis display the energy levels both, in lattice units as well as in MeV.

In contrast to references [142, 143, 144] we observe attraction in all spin and isospin channels. Excepted is the operator combination $\mathbb{1} \otimes \mathbb{1}$ in the $I = 1, S_z = 0$ channel (see figure 7.8) where neither attraction nor repulsion could be detected at all computed separations. The ground state shows an attractive tendency at a distance of 0.12 fm and a possible repulsion for $r > 0.15$ fm. However, due to the large errors in this channel a definite confirmation lacks. Apart from this, at very short distances we in fact find attraction in all analyzed channels, see table 6.2, for ground and excited states. Our results from the fine lattice, displayed in figure 7.11 to figure 7.18, confirm these observations. This may not be too surprising as this is expected from gluon exchange in the 3^*

[1] A comparable overview can be found in our Lattice 2011 Proceedings [34].

channel between the two static sources.

When comparing the ground state of the $\gamma_5 \otimes \gamma_5$ operator in figure 7.7 for different spin and isospin channels we figure out that the $S_z = 0$ channel is more attractive than the $S_z = 1$ channel for isospin $I = 0$. For isospin $I = 1$ this pattern is reversed. In both cases the difference is of the order of 150 MeV at a distance of 0.11 fm. For the other spin-projected operator combinations ($\mathbb{1} \otimes \mathbb{1}$, $\gamma_5 \otimes \mathbb{1}$ and $\gamma_5 \otimes \gamma_i \nabla_i$ from figure 7.8 to 7.10) we find attractive forces of similar sizes for the $S_z = 0, 1$ and isospin $I = 0$ ground states in each case. For isospin $I = 1$ and for the operator combinations $\mathbb{1} \otimes \mathbb{1}$ and $\gamma_5 \otimes \mathbb{1}$ the $S_z = 1$ channel is more attractive than the $S_z = 0$ channel while the isovector $\gamma_5 \otimes \gamma_i \nabla_i$ ground state is more attractive for $S_z = 0$. For the first excited states we observe somewhat larger errors than for the ground states in most isoscalar channel. Much larger errors than for ground states are found in the excited isovector channels. A general decision whether the ground or the first excited state channels are more attractive is not feasible since this pattern varies for each operator combination. For instance for the combination $\gamma_5 \otimes \gamma_5$ the $I = S_z = 0$ ground state is much more attractive than the $I = S_z = 0$ excited state (of the order of 150 MeV) while for the $\mathbb{1} \otimes \mathbb{1}$ combination it is the other way around.

On our coarse lattice we observe repulsive potentials at distances between 0.3 fm and 0.45 fm for the $\gamma_5 \otimes \mathbb{1}$ operator in all spin and isospin channels. The repulsion is of the order of 50 MeV for the ground states as well as for the first excited states. In addition we find repulsion in the $I = 1, S_z = 1$ channel for the Π_g ground state of the $\gamma_5 \otimes \gamma_5$ operator for the same static quark separations between 0.3 fm and 0.45 fm. A tendency for a slight repulsive potential at intermediate distances can be observed for the Π_g' ($\gamma_5 \otimes \gamma_5$) excitation in the $I = S_z = 1$ channel, the $\mathbb{1} \otimes \mathbb{1}$ ground state for $S_z = 0, 1$ in the isoscalar channel and for $S_z = 0$ in the isovector channel, and finally for the $\gamma_5 \otimes \gamma_i \nabla_i$ first excited state for $I = 1, S_z = 0$. However, in these last cases errors are much larger and the expected infinite distance limit is within two sigma. Maybe higher statistics could clarify whether there is repulsion in these channels. In order to confirm or refute our results from the coarse lattice we present our findings from the fine lattice in the next section.

An overview of the potentials that are attractive, repulsive or have the expected continuum limit at intermediate distances between 0.3 fm and 0.45 fm is listed in table 7.5 at the end of this section.

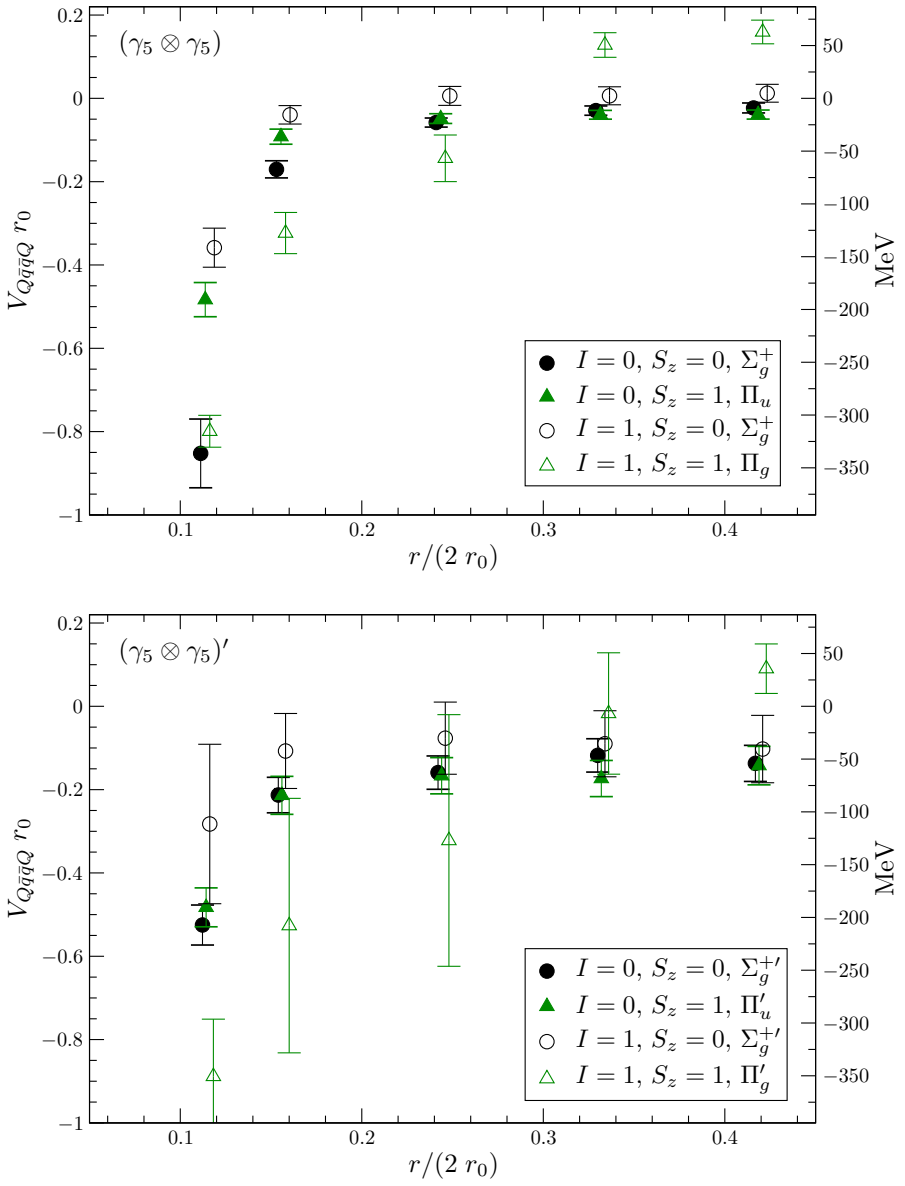

Figure 7.7: The intermeson potential $V_{\mathcal{B}_1\mathcal{B}_2}(r)$ in the different spin and isospin channels for the combination $\gamma_5 \otimes \gamma_5$. Ground state results are displayed in the upper plot and those for the first excited state in the lower plot. Full symbols indicate the isoscalar channel, open symbols the isovector channel. Black circles label spin $S_z = 0$, green triangles spin $S_z = 1$.

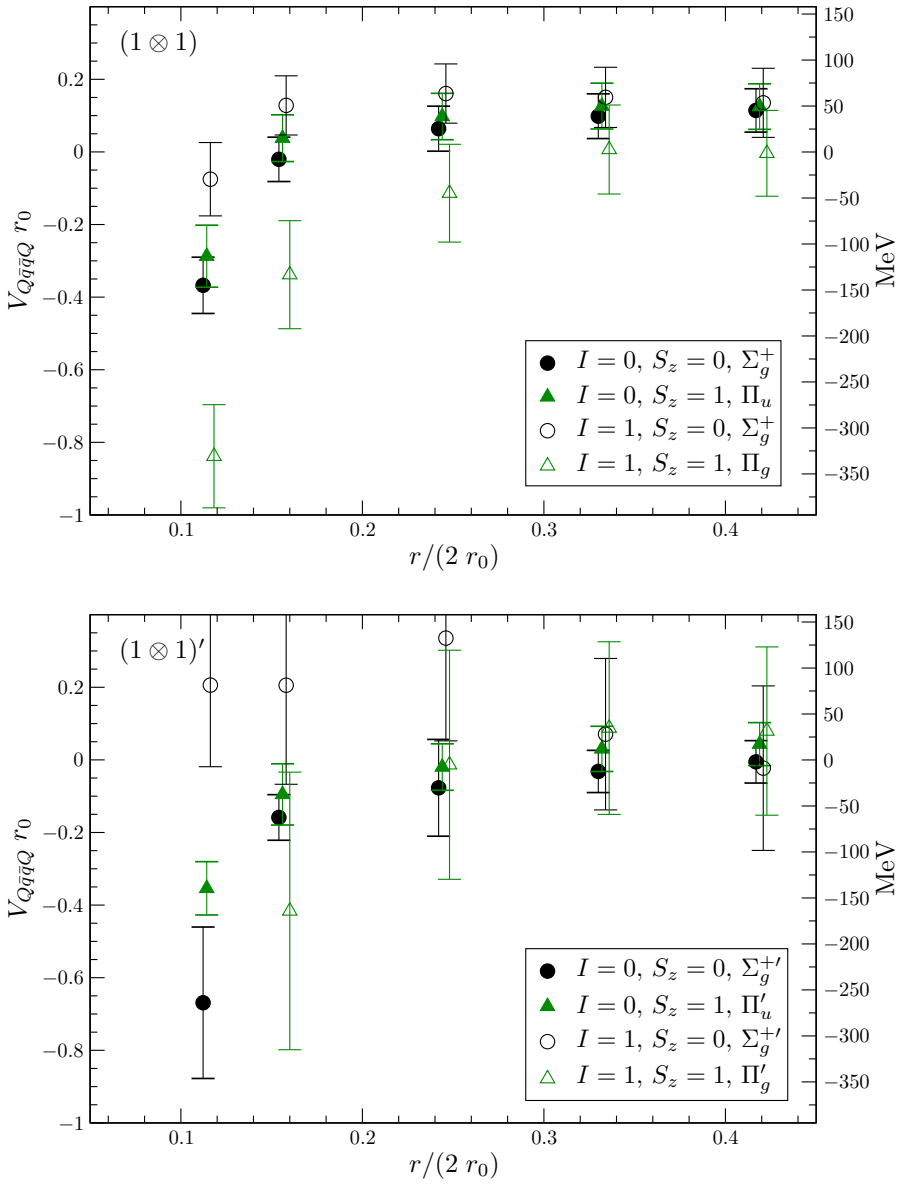

Figure 7.8: The intermeson potential $V_{\mathcal{B}_1\mathcal{B}_2}(r)$ in the different spin and isospin channels for the combination $\mathbb{1} \otimes \mathbb{1}$. Ground state results are displayed in the upper plot and those for the first excited state in the lower plot. Full symbols indicate the isoscalar channel, open symbols the isovector channel. Black circles label spin $S_z = 0$, green triangles spin $S_z = 1$.

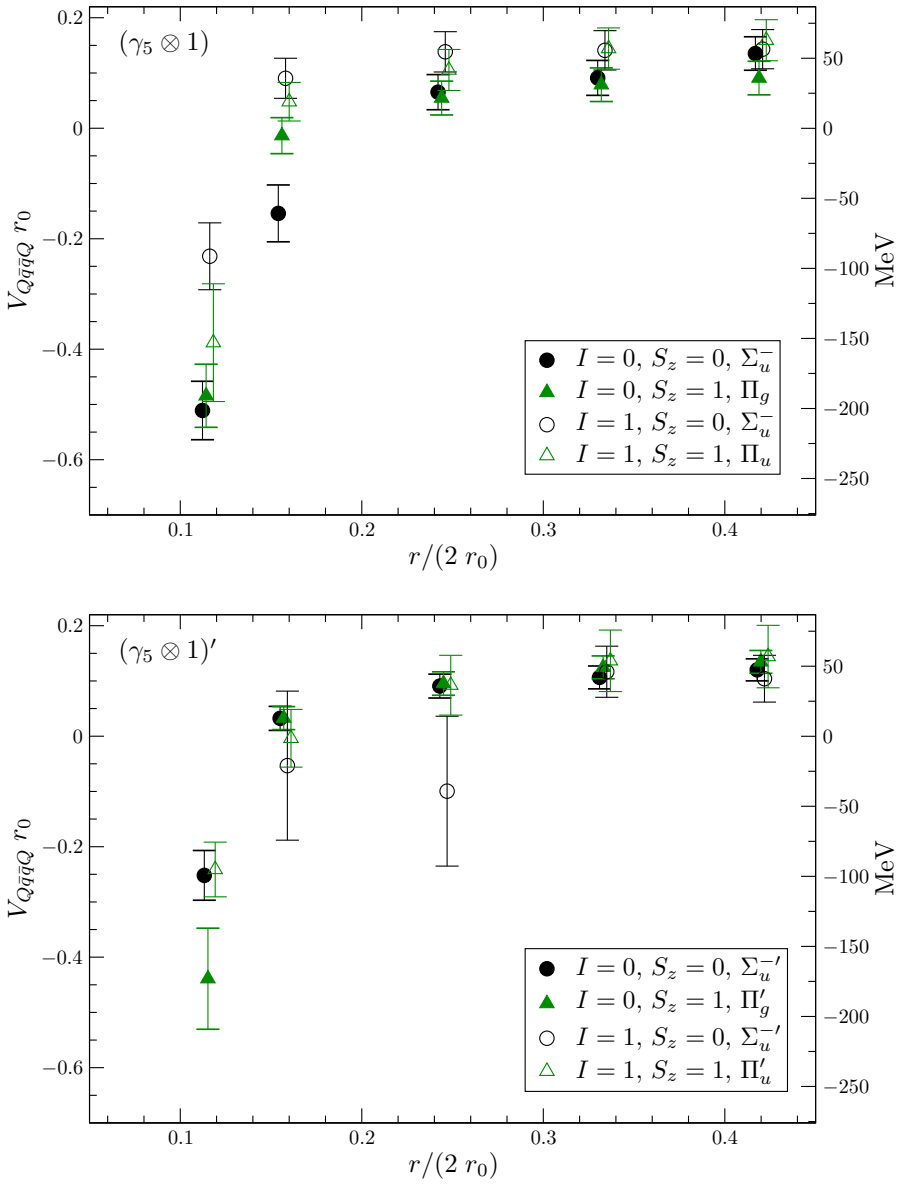

Figure 7.9: The intermeson potential $V_{\mathcal{B}_1\mathcal{B}_2}(r)$ in the different spin and isospin channels for the combination $\gamma_5 \otimes \mathbb{1}$. Ground state results are displayed in the upper plot and those for the first excited state in the lower plot. Full symbols indicate the isoscalar channel, open symbols the isovector channel. Black circles label spin $S_z = 0$, green triangles spin $S_z = 1$.

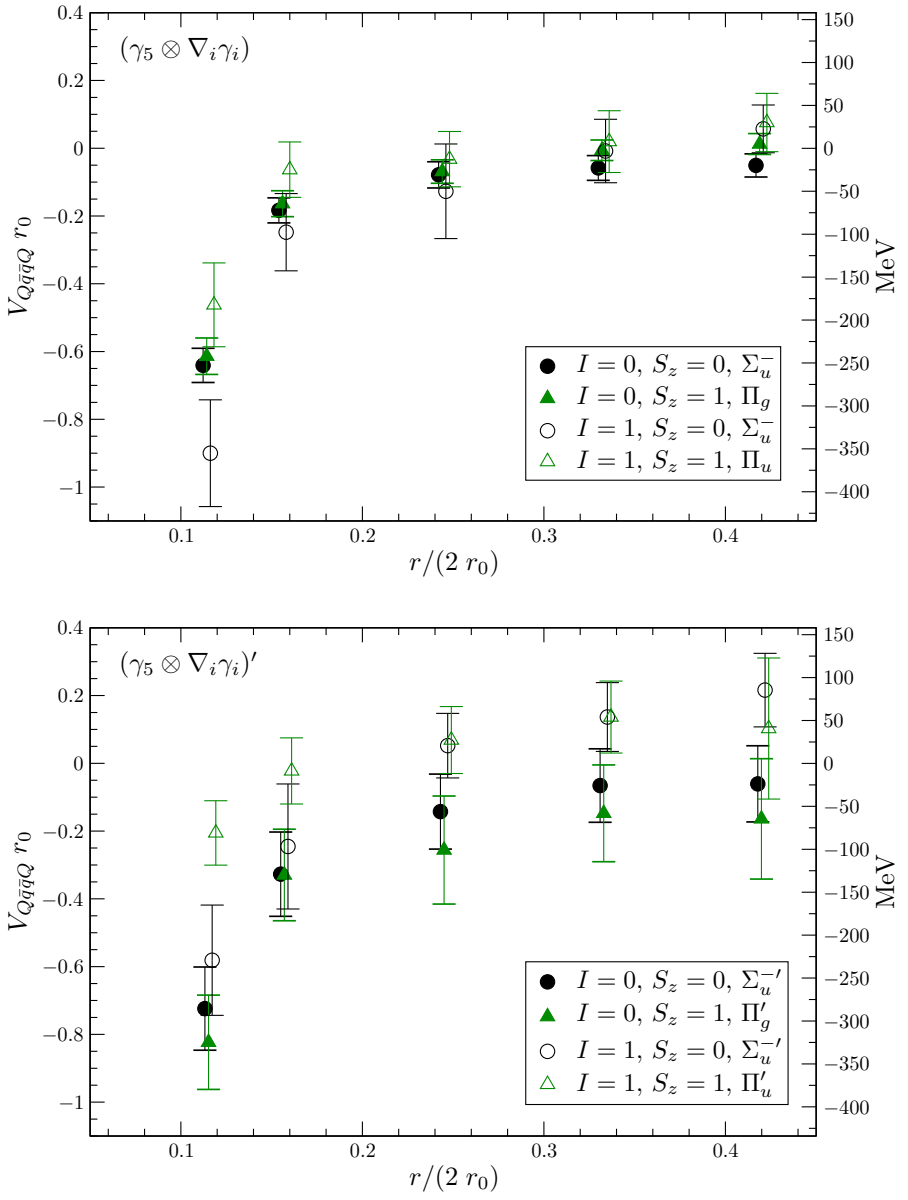

Figure 7.10: The intermeson potential $V_{\mathcal{B}_1\mathcal{B}_2}(r)$ in the different spin and isospin channels for the combination $\gamma_5 \otimes \nabla_i \gamma_i$. Ground state results are displayed in the upper plot and those for the first excited state in the lower plot. Full symbols indicate the isoscalar channel, open symbols the isovector channel. Black circles label spin $S_z = 0$, green triangles spin $S_z = 1$.

7.2.6 Comparison of the coarse and the fine Lattice

In this section we compare our intermeson potentials on the coarse lattice with those from the fine lattice. As we did not perform the spin projection for the fine lattice we cannot distinguish between Σ and Π states but between the isospin channels $I = 0$ and $I = 1$. In the cases where we performed the S_z projection on the coarse lattice we select the $I = 0, S_z = 0$ and the $I = 1, S_z = 0$ channels for the analysis as they access to the lowest lying states. In the following the spin quantum number S_z is omitted for simplicity.

From figure 7.11 to figure 7.18 we present the operator combinations $\gamma_5 \otimes \gamma_5$, $\mathbb{1} \otimes \mathbb{1}$, $\gamma_5 \otimes \mathbb{1}$, $\gamma_5 \otimes \nabla_i \gamma_i$, $\gamma_5 \otimes P_\perp$, $\gamma_5 \otimes P_\parallel$, $\nabla_i \gamma_i \otimes P_\perp$ and $\nabla_i \gamma_i \otimes P_\parallel$. The operators $P_\perp$ and $P_\parallel$ were defined in section 6.2.1. As previously we display ground states in the upper plots and first excited states in the lower plots. Now full symbols represent our results from the coarse $(16^3 \times 32)$ lattice and open symbols those from the fine lattice $(24^3 \times 48)$. Black circles indicate the isoscalar and red squares the isovector channel. The x-axis denotes the static quark separation in fm and the y-axis the intermeson potential both, in lattice units on the left and in MeV on the right.

In agreement with the coarse lattice results we obtain repulsion of $O(50$ MeV$)$ in the ground state Σ_u^- of the operator combination $\gamma_5 \otimes \mathbb{1}$ for isospin $I = 1$ at intermediate distances $r > 0.35$ fm. In the isoscalar ground state channel of the addressed operator the findings from the coarse lattice could not be reproduced on the fine lattice in this separation range. Anymore, slight repulsive potentials for the isovector $\gamma_5 \otimes \gamma_5, \mathbb{1} \otimes \mathbb{1}\,(\Sigma_g^+)$ and $\gamma_5 \otimes \nabla_i \gamma_i\,(\Sigma_u^-)$ ground states from the fine lattice confirm our coarse lattice results, where we refer to the $S_z = 1$ channel in case of the $\gamma_5 \otimes \gamma_5$ combination. Furthermore, we find repulsion of the order of 100 MeV in the first excitation of the combination $\nabla_i \gamma_i \otimes P_\perp$ for isospin $I = 1$ on the coarse lattice and $I = 0$ on the fine lattice. Finally, in the $I = 0$, $\nabla_i \gamma_i \otimes P_\parallel$ ground state (Σ_u^-) and first excited state $(\Sigma_u^{-\prime})$ channels we also observe a repulsive potential of $O(100)$ MeV on the fine lattice, while the corresponding potentials on the coarse lattice have the expected $r \to \infty$ limit.

In general we find that the intermeson potentials are either of the same order on both lattice sets or in many cases even more attractive on the fine lattice. For instance, for the operator combination $\gamma_5 \otimes \gamma_5$, we observe reasonable scaling while the fine lattice potentials, e.g. in the $\gamma_5 \otimes \mathbb{1}$ channel, behave more attractive and appear to rise slower with increasing distances. In the isoscalar ground state channel the difference is somewhat larger than 50 MeV

at intermediate distances. For the operator combination $\mathbb{1} \otimes \mathbb{1}$ we observe about 150 MeV more attractive fine lattice potentials for the isoscalar groundstate. The only exceptions are the Σ_u^- channels for the operators $\nabla_i \gamma_i \otimes P_\perp$ and $\nabla_i \gamma_i \otimes P_\parallel$.

These results may be related to the much lighter pion mass on the fine lattice. In addition to gluon exchange the interaction between two $\mathcal{B}$ mesons can also be mediated via meson-exchange, where the pion would be the lightest possible meson. This interaction behavior can be expressed as a Yukawa Potential

$$V(r) \sim \frac{e^{-mr}}{r}\,, \tag{7.5}$$

where r labels the separation and m the meson mass. The consequence is a larger interaction range on the fine lattice which could explain the stronger binding in some channels.

As already mentioned, for most channels the errors are larger on the fine than on the coarse lattice. This may be due to the missing spin projection and the mixing of Π- into Σ-states. For both lattice sets we in principle find larger errors in the isovector channel which includes the crossing diagrams. Since their computation is much more expensive than the calculation of the disconnected diagrams and our computer time was limited, we have used much less stochastic estimates. Thus, statistics are much lower for isospin $I = 1$ $\mathcal{BB}$ potentials which is incorporated in the error.

Finally, in table 7.5 at the end of this section we summarize and compare our results for the intermeson potentials $V_{\mathcal{B}_1\mathcal{B}_2}(r)$ from both lattices in different spin and isospin channels. The table gives an overview of the potentials that are attractive, repulsive or have the expected continuum limit at intermediate distances between 0.3 fm and 0.45 fm.

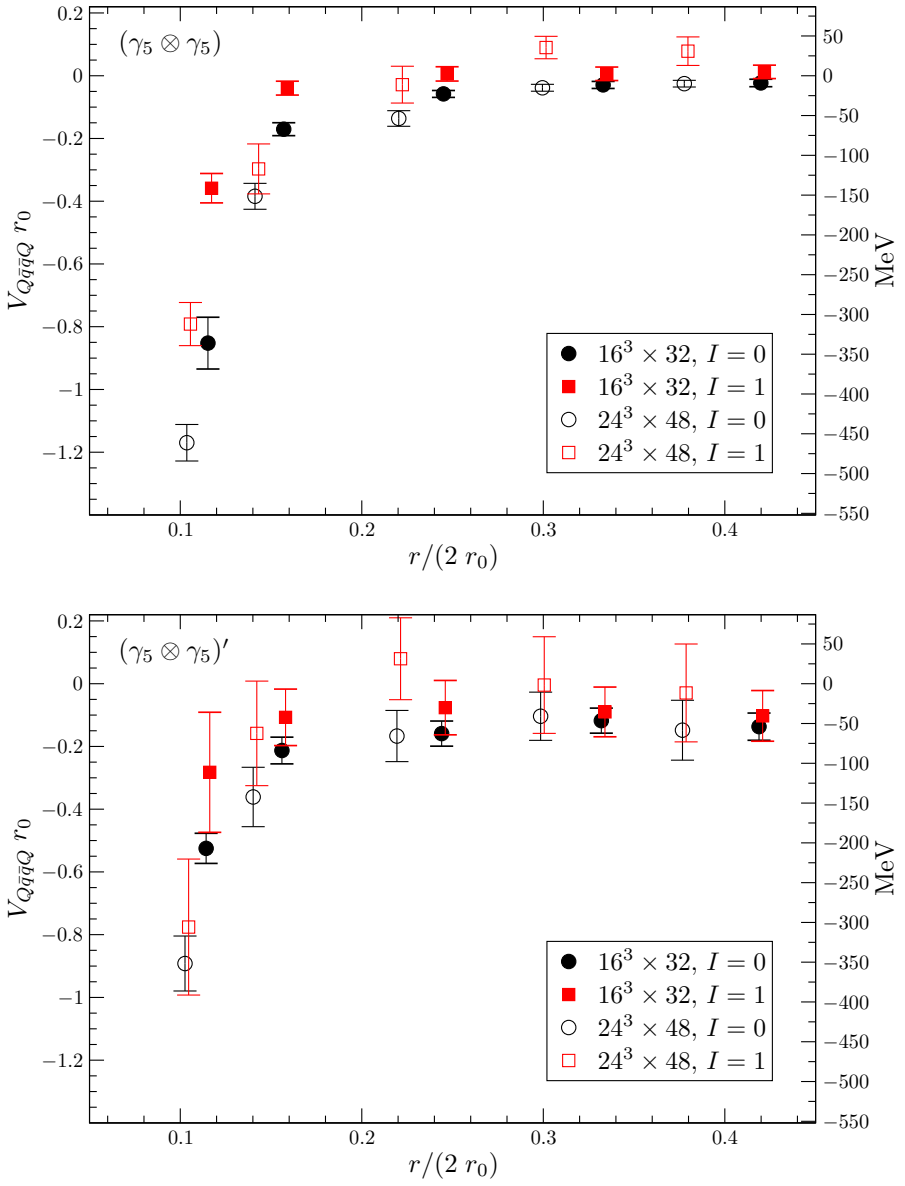

Figure 7.11: The intermeson potential $V_{\mathcal{B}_1\mathcal{B}_2}(r)$ for the combination $\gamma_5 \otimes \gamma_5$ on our coarse and fine lattice in different isospin channels. Ground state results are displayed in the upper plot and those for the first excited state in the lower plot. Full symbols indicate the $16^3 \times 32$ lattice results, open symbols the $24^3 \times 48$ lattice results. Black circles label isospin $I = 0$, red squares isospin $I = 1$.

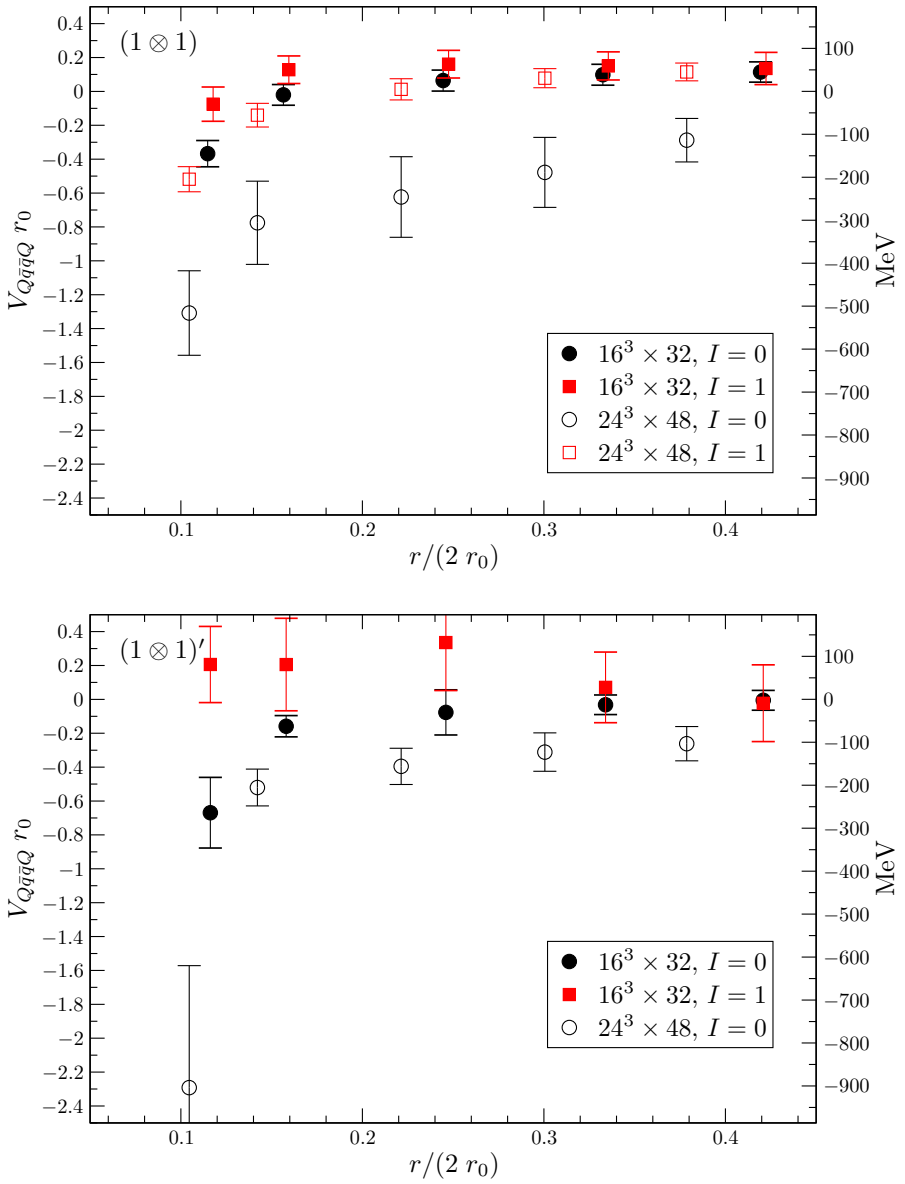

Figure 7.12: The intermeson potential $V_{\mathcal{B}_1\mathcal{B}_2}(r)$ for the combination $\mathbb{1} \otimes \mathbb{1}$ on our coarse and fine lattice in different isospin channels. Ground state results are displayed in the upper plot and those for the first excited state in the lower plot. Full symbols indicate the $16^3 \times 32$ lattice results, open symbols the $24^3 \times 48$ lattice results. Black circles label isospin $I = 0$, red squares isospin $I = 1$.

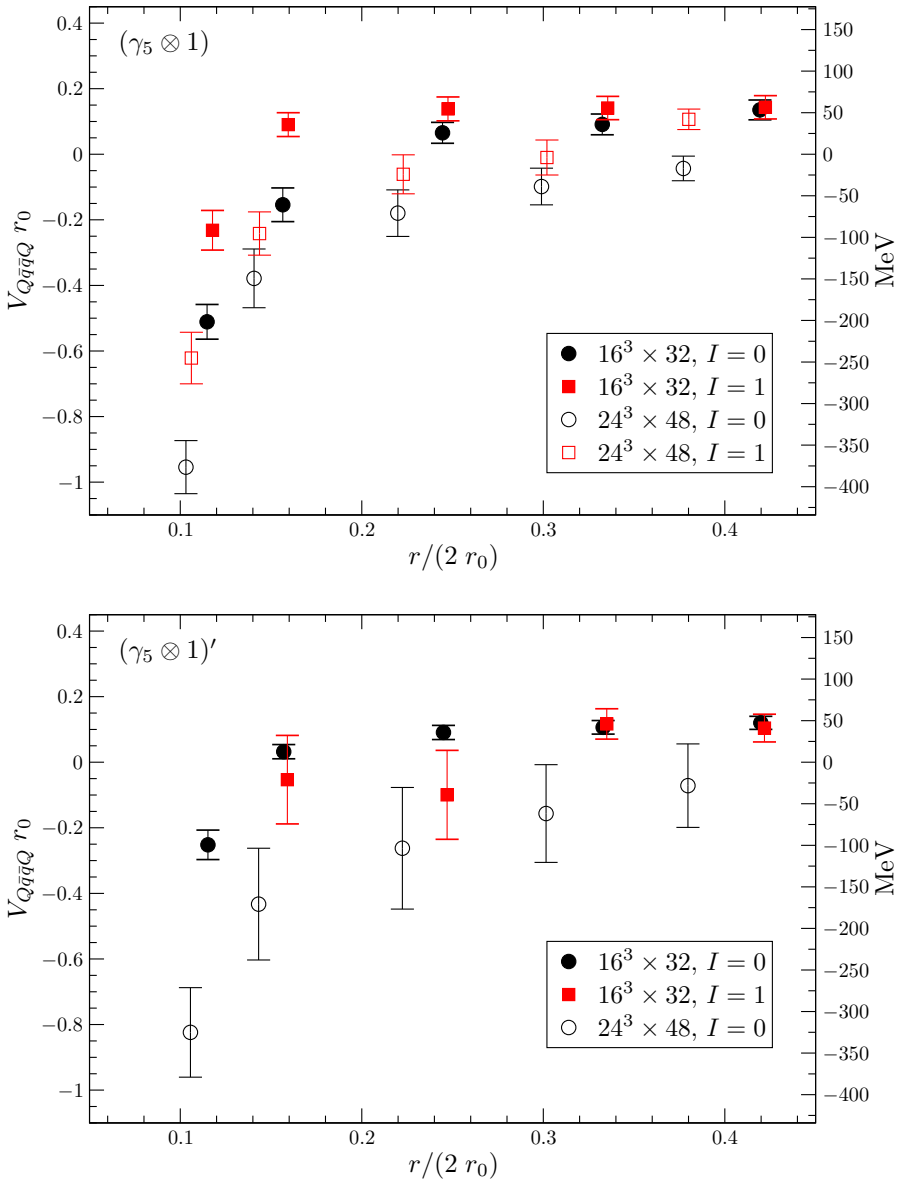

Figure 7.13: The intermeson potential $V_{\mathcal{B}_1\mathcal{B}_2}(r)$ for the combination $\gamma_5 \otimes \mathbb{1}$ on our coarse and fine lattice in different isospin channels. Ground state results are displayed in the upper plot and those for the first excited state in the lower plot. Full symbols indicate the $16^3 \times 32$ lattice results, open symbols the $24^3 \times 48$ lattice results. Black circles label isospin $I = 0$, red squares isospin $I = 1$.

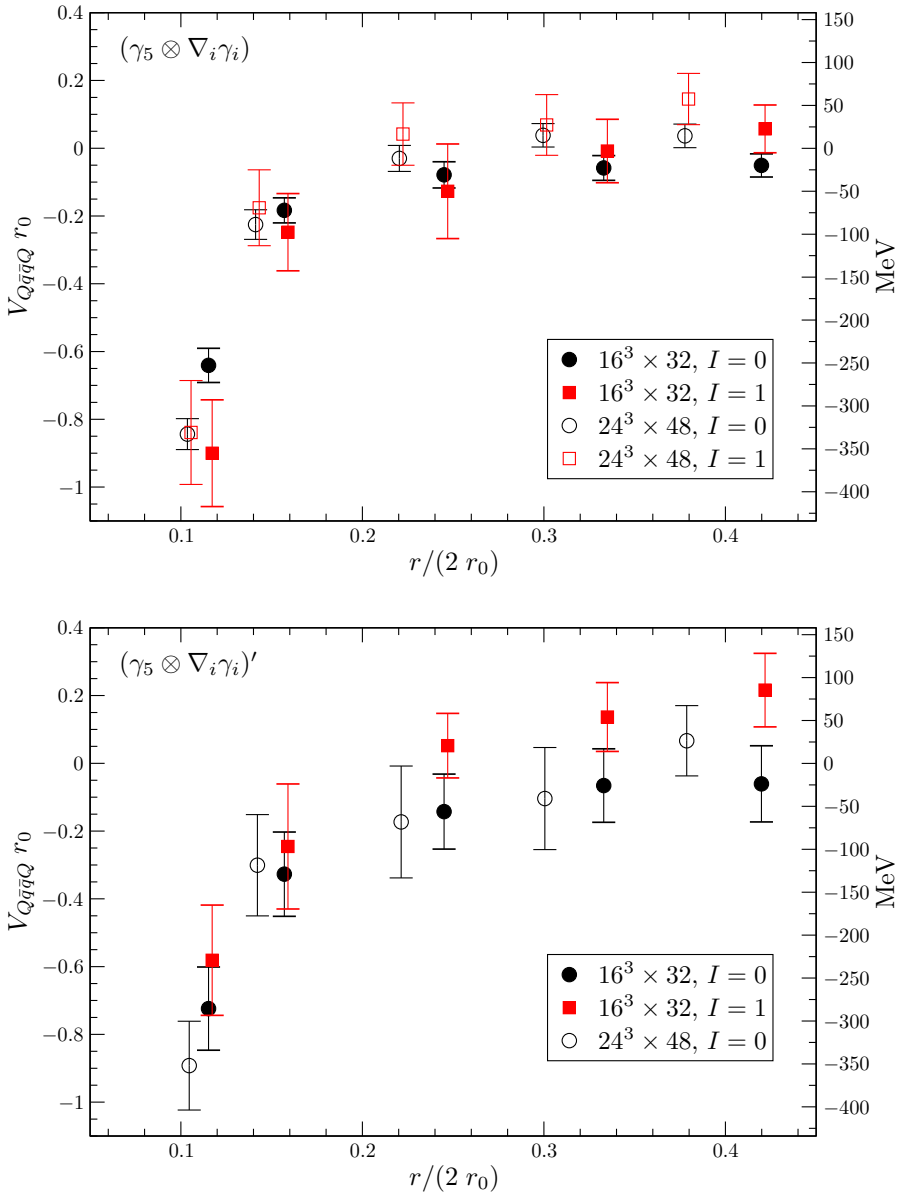

Figure 7.14: The intermeson potential $V_{\mathcal{B}_1\mathcal{B}_2}(r)$ for the combination $\gamma_5 \otimes \nabla_i \gamma_i$ on our coarse and fine lattice in different isospin channels. Ground state results are displayed in the upper plot and those for the first excited state in the lower plot. Full symbols indicate the $16^3 \times 32$ lattice results, open symbols the $24^3 \times 48$ lattice results. Black circles label isospin $I = 0$, red squares isospin $I = 1$.

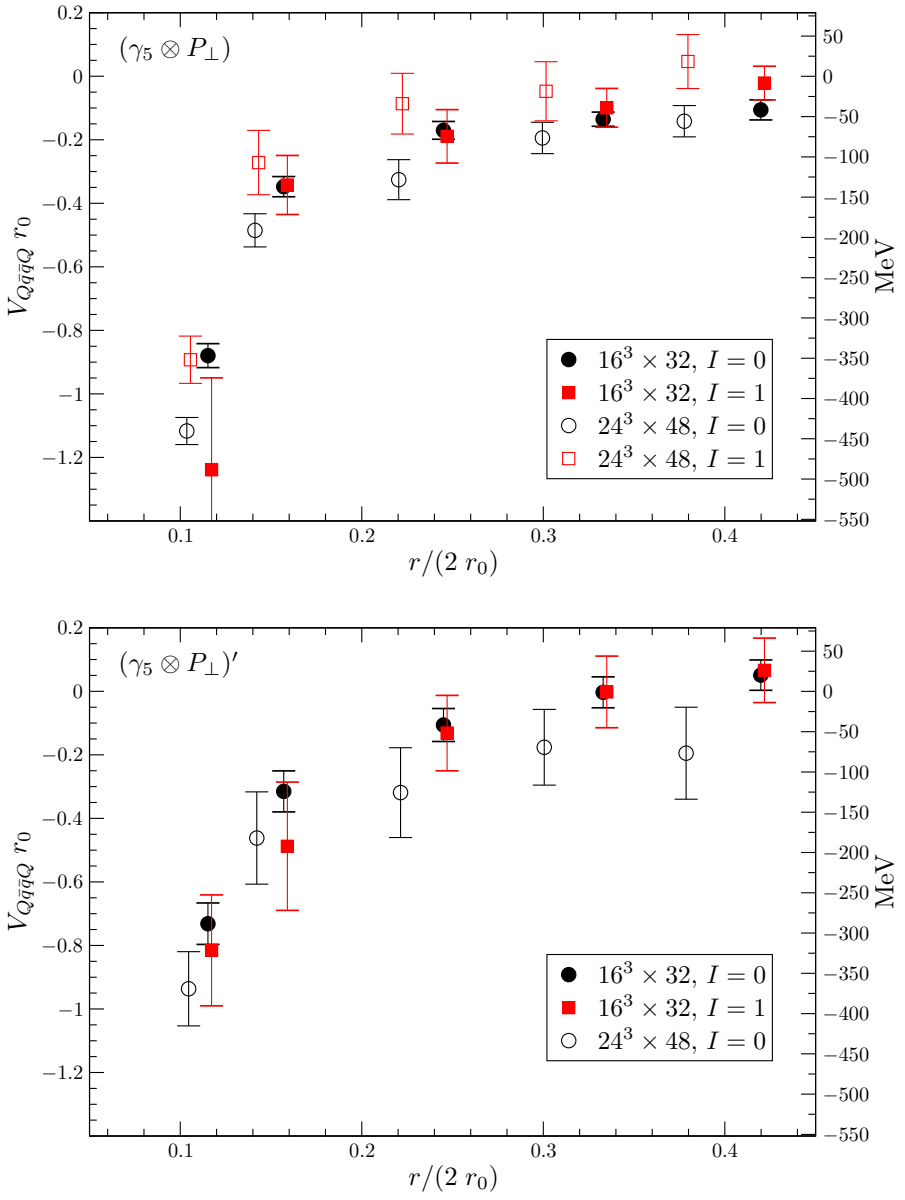

Figure 7.15: The intermeson potential $V_{\mathcal{B}_1\mathcal{B}_2}(r)$ for the combination $\gamma_5 \otimes P_\perp$ on our coarse and fine lattice in different isospin channels. Ground state results are displayed in the upper plot and those for the first excited state in the lower plot. Full symbols indicate the $16^3 \times 32$ lattice results, open symbols the $24^3 \times 48$ lattice results. Black circles label isospin $I = 0$, red squares isospin $I = 1$.

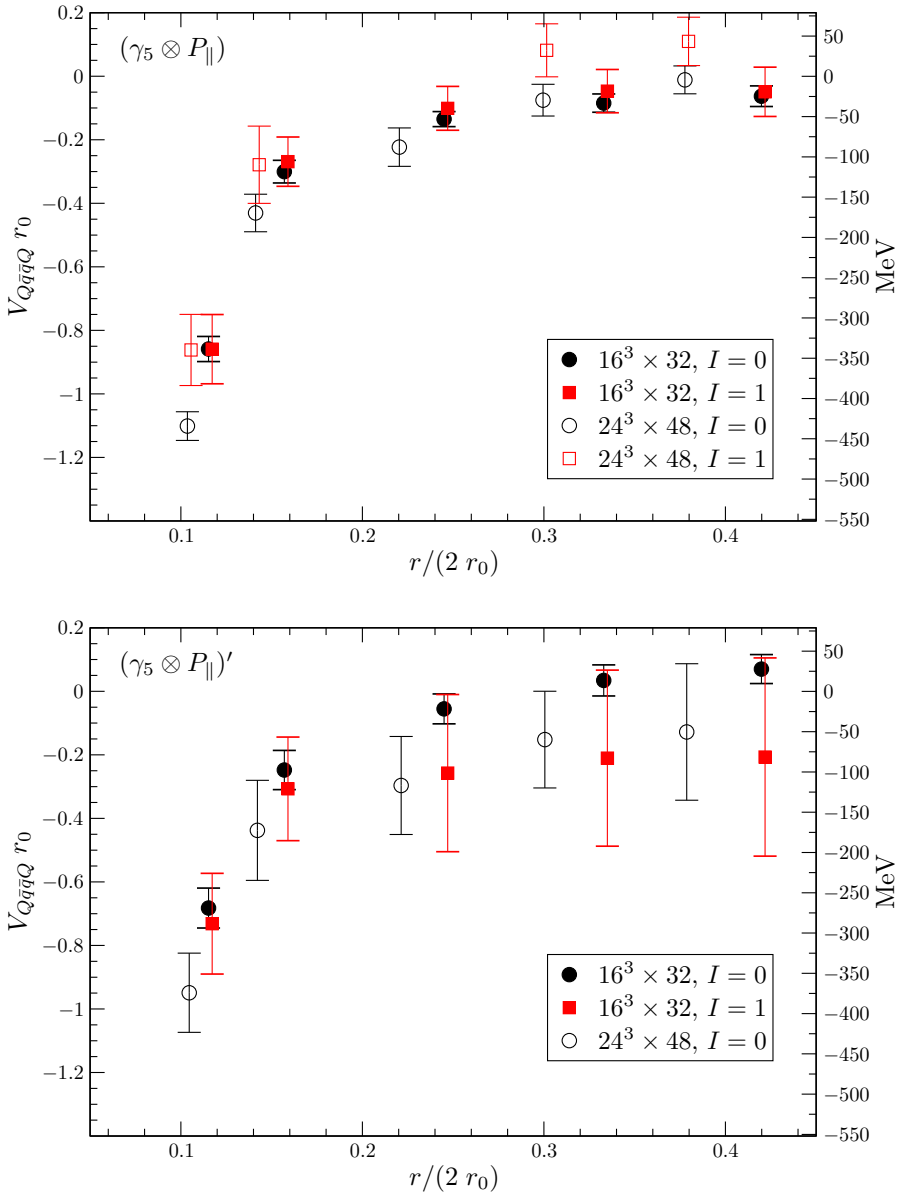

Figure 7.16: The intermeson potential $V_{\mathcal{B}_1\mathcal{B}_2}(r)$ for the combination $\gamma_5 \otimes P_\parallel$ on our coarse and fine lattice in different isospin channels. Ground state results are displayed in the upper plot and those for the first excited state in the lower plot. Full symbols indicate the $16^3 \times 32$ lattice results, open symbols the $24^3 \times 48$ lattice results. Black circles label isospin $I = 0$, red squares isospin $I = 1$.

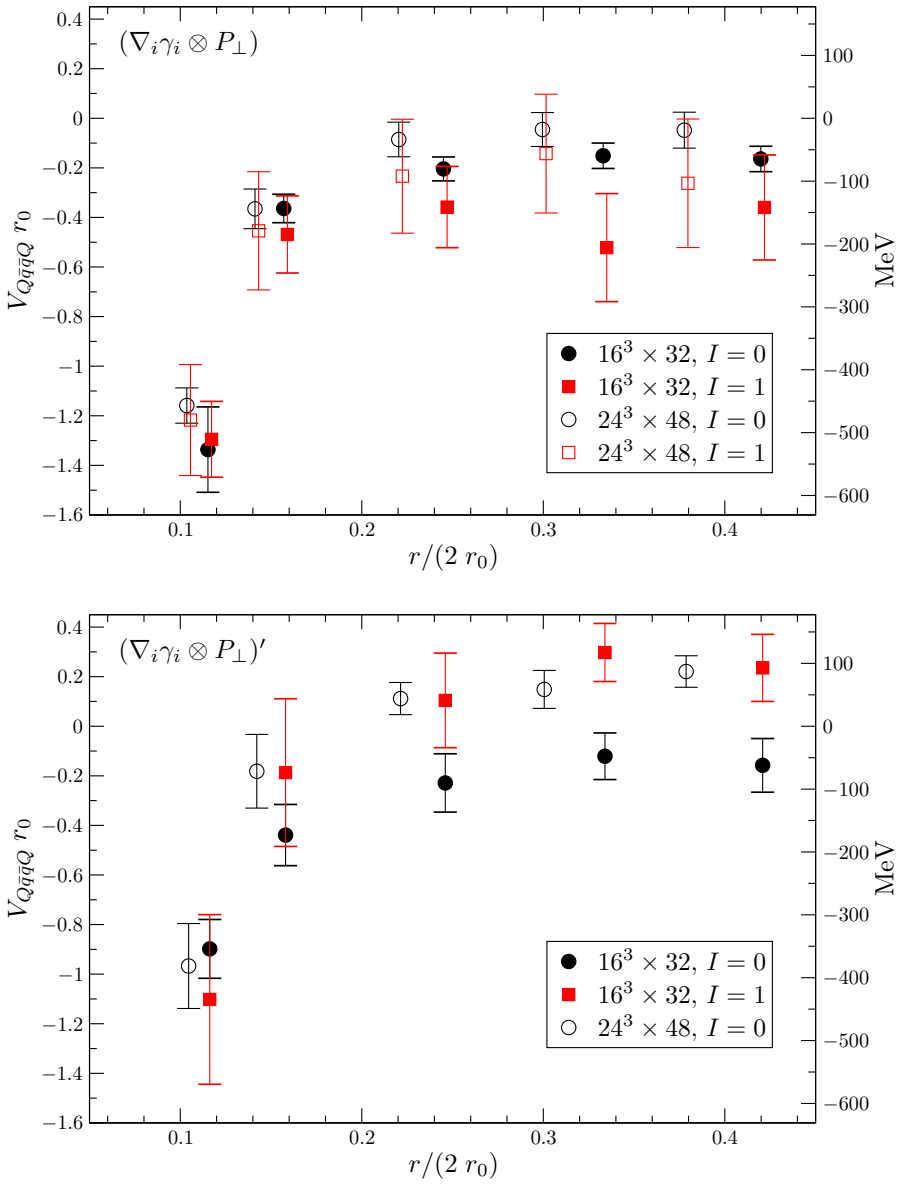

Figure 7.17: The intermeson potential $V_{\mathcal{B}_1\mathcal{B}_2}(r)$ for the combination $\nabla_i\gamma_i \otimes P_\perp$ on our coarse and fine lattice in different isospin channels. Ground state results are displayed in the upper plot and those for the first excited state in the lower plot. Full symbols indicate the $16^3\times32$ lattice results, open symbols the $24^3\times48$ lattice results. Black circles label isospin $I = 0$, red squares isospin $I = 1$.

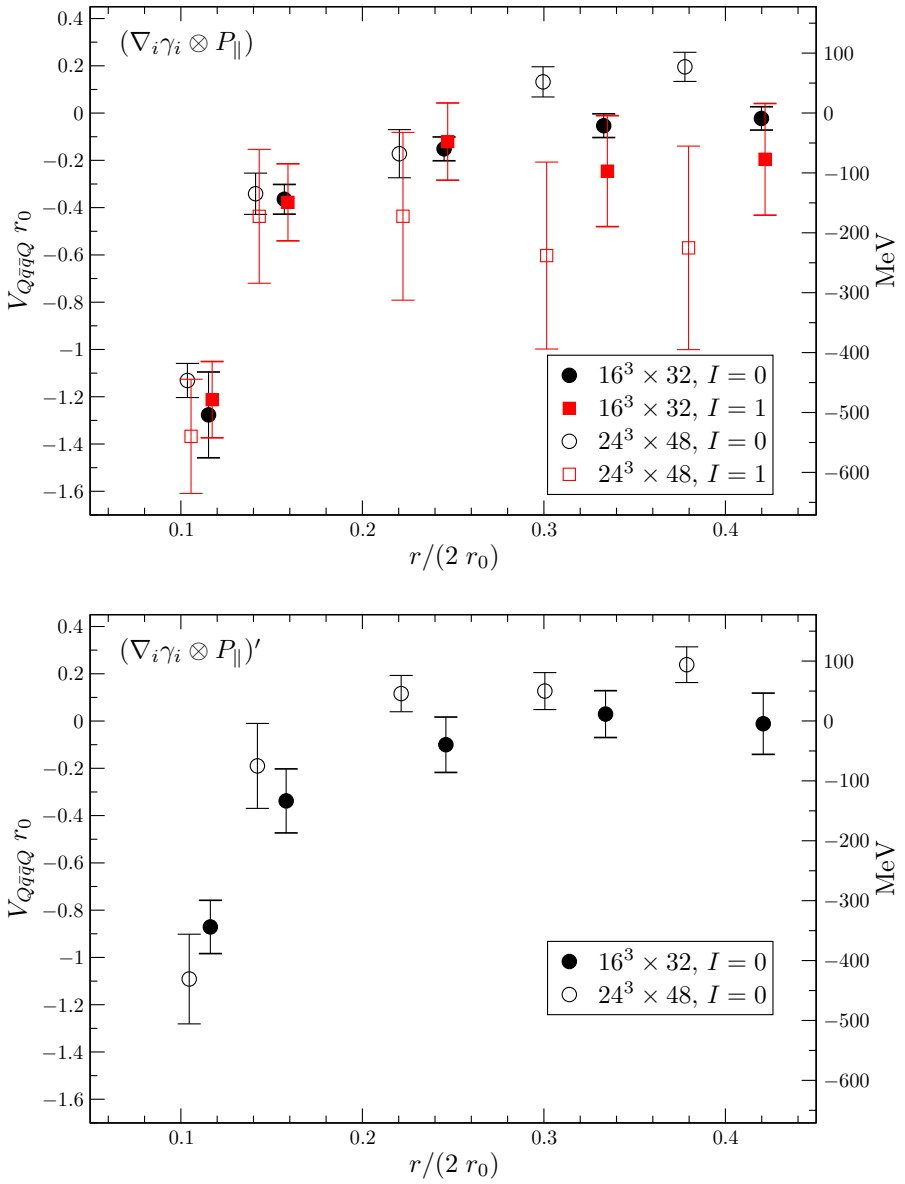

Figure 7.18: The intermeson potential $V_{\mathcal{B}_1\mathcal{B}_2}(r)$ for the combination $\nabla_i\gamma_i \otimes P_\parallel$ on our coarse and fine lattice in different isospin channels. Ground state results are displayed in the upper plot and those for the first excited state in the lower plot. Full symbols indicate the $16^3 \times 32$ lattice results, open symbols the $24^3 \times 48$ lattice results. Black circles label isospin $I = 0$, red squares isospin $I = 1$.

$\mathcal{O} \otimes \mathcal{O}$	$16^3 \times 32$					$24^3 \times 48$			
	I	S_z	$\Lambda_\eta^{(\sigma_\nu)}$	GS	FE	I	$\Lambda_\eta^{(\sigma_\nu)}$	GS	FE
$\gamma_5 \otimes \gamma_5$	0	0	Σ_g^+	CL	A	0	Σ_g^+	CL	CL
	0	1	Π_u	CL	A	/	/	/	/
	1	0	Σ_g^+	CL	A	1	Σ_g^+	R	CL
	1	1	Π_u	R	R	/	/	/	/
$\mathbb{1} \otimes \mathbb{1}$	0	0	Σ_g^+	R	CL	0	Σ_g^+	A	A
	0	1	Π_u	R	CL	/	/	/	/
	1	0	Σ_g^+	R	CL	1	Σ_g^+	R	/
	1	1	Π_u	CL	CL	/	/	/	/
$\gamma_5 \otimes \mathbb{1}$	0	0	Σ_u^-	R	R	0	Σ_u^-	CL	CL
	0	1	Π_g	R	R	/	/	/	/
	1	0	Σ_u^-	R	R	1	Σ_u^-	R	/
	1	1	Π_u	R	R	/	/	/	/
$\gamma_5 \otimes \gamma_i\nabla_i$	0	0	Σ_u^-	CL	CL	0	Σ_u^-	CL	CL
	0	1	Π_g	CL	CL	/	/	/	/
	1	0	Σ_u^-	CL	R	1	Σ_u^-	R	/
	1	1	Π_u	CL	CL	/	/	/	/
$\gamma_5 \otimes P_\perp$	0	/	Σ_g^+, Π_g	A	A	0	Σ_g^+, Π_g	CL	CL
	1	/	Σ_u^+, Π_u	CL	CL	1	Σ_u^+, Π_u	CL	/
$\gamma_5 \otimes P_\parallel$	0	/	Π_g	CL	CL	0	Π_g	CL	CL
	1	/	Π_u, Δ_u	CL	CL	1	Π_u, Δ_u	CL	/
$\gamma_i\nabla_i \otimes P_\perp$	0	/	Σ_u^-, Π_u	A	CL	0	Σ_u^-, Π_u	CL	R
	1	/	Σ_g^-, Π_g	A	R	1	Σ_g^-, Π_g	CL	/
$\gamma_i\nabla_i \otimes P_\parallel$	0	/	Π_u	CL	CL	0	Π_u	R	R
	1	/	Π_g, Δ_g	CL	/	1	Π_g, Δ_g	/	/

Table 7.5: Overview of all our determined intermeson potentials $V_{\mathcal{B}_1\mathcal{B}_2}(r)$ in different spin and isospin channels for groundstates (GS) and first excited states (FE). At intermediate static quark-quark separations between 0.3 fm and 0.45 fm we find potentials that are attractive (A), repulsive (R) or have the expected continuum limit (CL). We note that for the last four operator combinations and all operator combinations on the fine lattice we have not performed the spin projection.

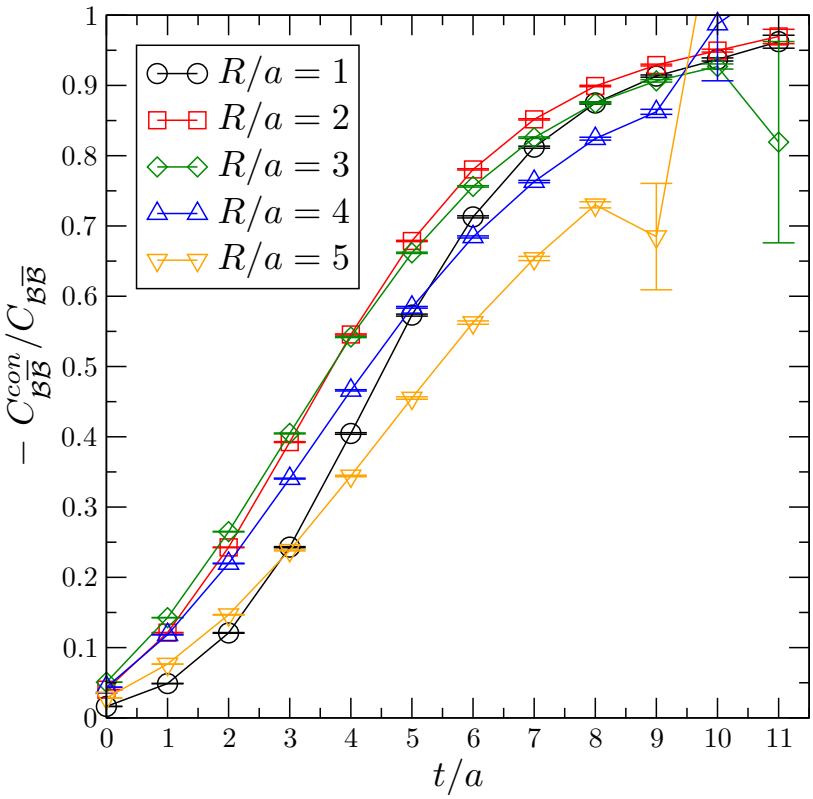

Figure 7.19: The ratio $-C^{\text{conn}}_{\mathcal{B}\overline{\mathcal{B}}}/C_{\mathcal{B}\overline{\mathcal{B}}}$ for the operator combination $\gamma_5 \otimes \gamma_5$ at different distances $r = R/a$ as a function of t.

7.3 $\mathcal{B}\overline{\mathcal{B}}$ Meson-Antimeson States

In this section we present the results for static-light $\mathcal{B}\overline{\mathcal{B}}$ meson-antimesons at various distances. A main characteristic of these states is their possible decay to the static quark potential $V_{Q\overline{Q}}$ plus scalar mesons which have the quantum numbers of the corresponding channel. Thus, we do not calculate intermeson potentials but show the meson-antimeson masses together with some possible decay states and the sum of the energy levels of the $r \to \infty$ limiting $\mathcal{B}$ meson masses.

7.3.1 Large Time Asymptotics

For a cross-check of our results we first determine the ration $-C^{\text{conn}}_{\mathcal{B}\overline{\mathcal{B}}}/C_{\mathcal{B}\overline{\mathcal{B}}}$ which was also computed in reference [93]. Thereby $C_{\mathcal{B}\overline{\mathcal{B}}}$ contains the disconnected and the connected contribution of the $\mathcal{B}\overline{\mathcal{B}}$ state. Graphically this is depicted

in equation (6.13) where the connected part alone $C^{\text{conn}}_{\mathcal{B}\overline{\mathcal{B}}}$ is given just the "loop diagram".

While the connected diagram is in the isoscalar channel, the disconnected part overlaps with the isovector channel. However, the states which couple to $I = 1$ are orthogonal to the isoscalar channel. For this reason any implicit mixing can only be mediated through $C^{\text{conn}}_{\mathcal{B}\overline{\mathcal{B}}}$. Consequently the connected diagram will dominate at asymptotically large time[2]:

$$C_{\mathcal{B}\overline{\mathcal{B}}} \overset{t\to\infty}{\longrightarrow} -C^{\text{conn}}_{\mathcal{B}\overline{\mathcal{B}}} \,. \tag{7.6}$$

To verify this anticipation we display the ratio $-C^{\text{conn}}_{\mathcal{B}\overline{\mathcal{B}}}/C_{\mathcal{B}\overline{\mathcal{B}}}$ as a function of t in figure 7.19. For large t this ratio indeed goes to one and for larger distances r the speed of convergence decreases a bit while at the same time errors increase at large times t. This is in agreement with the expectation of [93].

7.3.2 Isovector Meson-Antimesons

The simplest possibility to determine $\mathcal{B}\overline{\mathcal{B}}$ meson-antimeson masses is to evaluate the disconnected diagram alone which is drawn in figure 6.15. States generated this way have isospin $I = 1$ and we present a significant example in this section. For the remaining results of the other operator combinations we refer to appendix D.2. Previous results of the following, where we have not yet performed the projection to definite spin S_z can be found in our Lattice 2010 proceedings [145] where also parts of our explanations are taken from.

The layout for the following figures is quite similar as for the $\mathcal{B}\mathcal{B}$ potentials in the sections 7.2.3 and 7.2.4. In figure 7.20 we display the meson-antimeson masses of the operator combination $\gamma_5 \otimes \gamma_5$ as a function of the static quark-antiquark separation r in fm. Ground states are labeled as black circles, first excited states as red squares and second excited states as blue diamonds. For very large distances, the expected limit is given by the sum of the corresponding static-light $\mathcal{B}$ mesons. These are represented by the solid lines, where their widths indicate the jackknife errors. In addition green triangles denote the static quark potential $V_{Q\overline{Q}}$ plus various light mesons that have the appropriate quantum numbers. The values of the static quark potential $V_{Q\overline{Q}}$ have been calculated by Najjar [92].

[2] According to reference [93].

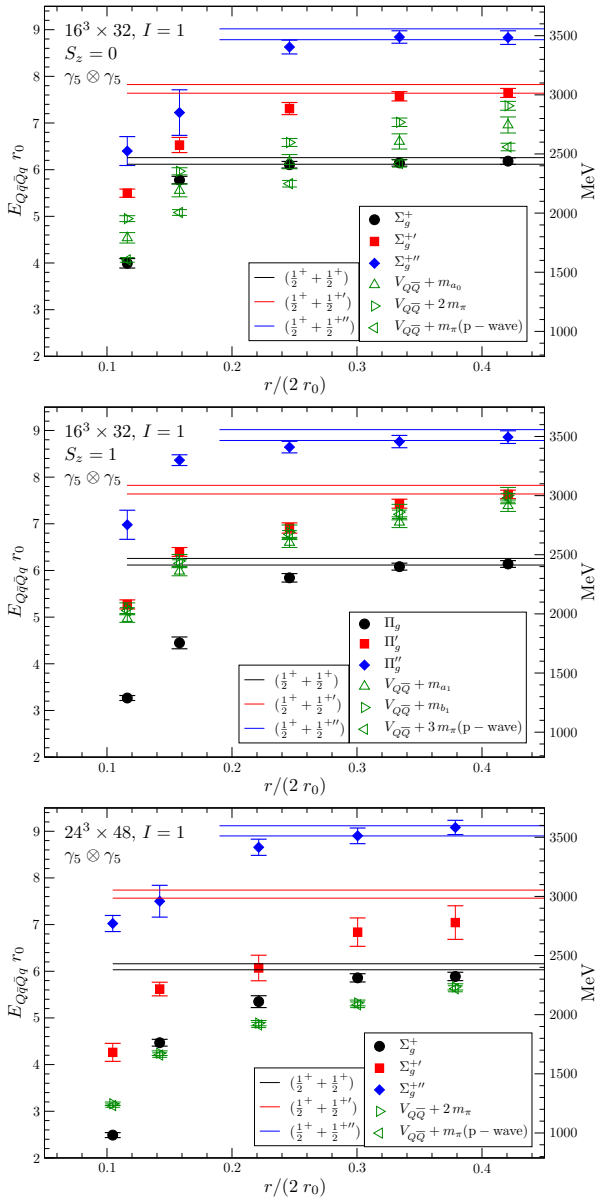

Figure 7.20: The $\mathcal{B}\overline{\mathcal{B}}$ meson-antimeson masses for the combination $\gamma_5 \otimes \gamma_5$ in the isovector channel. From top to bottom we show the coarse lattice for $S_z = 0$, $S_z = 1$ and the fine lattice. Black circles, red squares and blue diamonds mark the ground, the first and the second excited states respectively while the green triangles label the static $Q\overline{Q}$ potential plus various light mesons. The horizontal lines represent the sum of the corresponding static-light $\mathcal{B}$ mesons, the expected $r \to \infty$ limit, where their widths indicate the jackknife errors.

The upper plot of the figure shows the $\gamma_5 \otimes \gamma_5$ energy levels Σ_g^+, $\Sigma_g^{+\prime}$ and $\Sigma_g^{+\prime\prime}$ on our coarse lattice. The expected $r \to \infty$ limits correspond to twice the ground state mass of the $\frac{1}{2}^+$ static-light meson, its ground plus its first excited state masses and the sum of its ground and its second excited state masses respectively. These limits are approached for distances $r > 0.34$ fm in each case. At first sight there appear to be very substantial short distance attractive forces in this spin $S_z = 0$ channel. However, states consisting of a $Q\overline{Q}$ static potential and a scalar $I = 1$ particle will have the same quantum numbers. For our lattice parameters the pseudoscalar mass m_π within a P wave is the lowest such state, with masses of the a_0 meson as well as two pseudoscalars lying higher. We include the sum of these masses in the figure. The ground state $\mathcal{B}\overline{\mathcal{B}}$ energy lies between this levels. Thus it is hard to decide whether we find attraction at short distances or bound states between light mesons and the static quark potential[3].

A different situation can be observed in the intermediate plot, where the spin is projected to $S_z = 1$. In this channel the corresponding light mesons with the lowest mass are the a_1, the b_1 as well as $3\,\pi$ within a P wave. Their masses agree within the errors and for each we add the static quark potential. However, these masses are lying much higher, of the order of 500 MeV, than the Π_g ground state. Instead, the first excited state (Π_g') appears to overlap with the sum of these bound states. For this reason, we assume a significant ground state attraction of $O(1000)$ MeV at short distances while the first and second excited states are difficult to disentangle from bound states between the static quark potential and light mesons. At large distances, the expected limit is reached.

Quite similar to the upper plot on the figure is the lower one, where the results from the fine lattice are displayed. This is not too surprising since there we are dealing with the same quantum numbers. As for the $\mathcal{B}\mathcal{B}$ meson-meson states, we observe larger attraction at small distances and a slower rise of the meson-antimeson mass such that the limit is approached only for larger distances than on the coarse lattice. Responsible therefor may be the much lighter pion mass resulting in a different Yukawa potential. Due to the stronger attractive forces the Σ_g^+ ground state lies now somewhat below the bound states. Here the a_0 meson is missing, as its mass has not been calculated on this lattice. But generally, in order to decide whether we effectively see the sum of light

[3]We refer to our Lattice 2010 proceedings where this explanation is taken from.

mesons and the static potential and to disentangle which $I = 1$ Σ_g^+ (and $\Sigma_g^{+\prime}$ and $\Sigma_g^{+\prime\prime}$ respectively) energy level is the lowest one, interactions of the light mesons with the static potential will have to be taken into account.

7.3.3 Isoscalar Meson-Antimesons

As we also want to get access to to the isoscalar channel, we have to include box-diagrams which are numerically expensive. Graphically the whole term is depicted in equation 6.13. However, extracting $I = 0, S_z = 0$ $\mathcal{B}\overline{\mathcal{B}}$ states is quite difficult since for our operator combinations they couple either directly to the $Q\overline{Q}$ static potential or to the vacuum. In order to disentangle the meson-antimeson pairs from these states we would have to extend the operator basis to transition elements between $Q\overline{Q}$ and $B\overline{B}$ as it was done, e.g. in reference [93]. Since we only calculate $C_{\mathcal{B}\overline{\mathcal{B}}}$ correlators, we first analyze the $S_z = 1$ channel before we try to determine the $S_z = 0$ masses after all.

The $S_z = 1$ Spin Channel

On our coarse lattice we performed the projection of the static-light meson spins for some operators. Hence we are able to distinguish between appropriate antisymmetric ($S_z = 0$) or symmetric ($S_z = 1$) spin combinations. Our interpolator basis is suitable to evaluate the latter channel and we present a subset of our $I = 0$, $S_z = 1$ meson-antimeson analysis. The remaining results are shown in appendix D.2.

In figure 7.21 we see the meson-antimeson energy levels Π_u, Π_u' and Π_u'' of the operator combination $\gamma_5 \otimes \gamma_5$. Bound states between the static quark potential and the h_1 meson or three pseudoscalars within a P wave carry the same quantum numbers. We include their masses in the figure where we approximate m_{h_1} by m_{b_1}. Similar to the Π_g state in the $S_z = 1$ isovector channel in figure 7.20 also the Π_u ground state lies significantly below these sums, especially at very short distances of 0.12 fm. Thus, attraction is suspected in this channel. However, scaling is very strong and the expected infinite limit is approached at distances $r > 0.25$ fm. In contrast to the ground state, an overlap between the bound states and the excited $\mathcal{B}\overline{\mathcal{B}}$ meson-antimesons is very likely. The consequence is the obvious difficulty to distinguish between these states.

Next we have a look at the operator combination $\gamma_5 \otimes \mathbb{1}$ for $I = 0$ and $S_z = 1$. The Π_g ground state and its excitations Π_g' and Π_g'' are displayed in

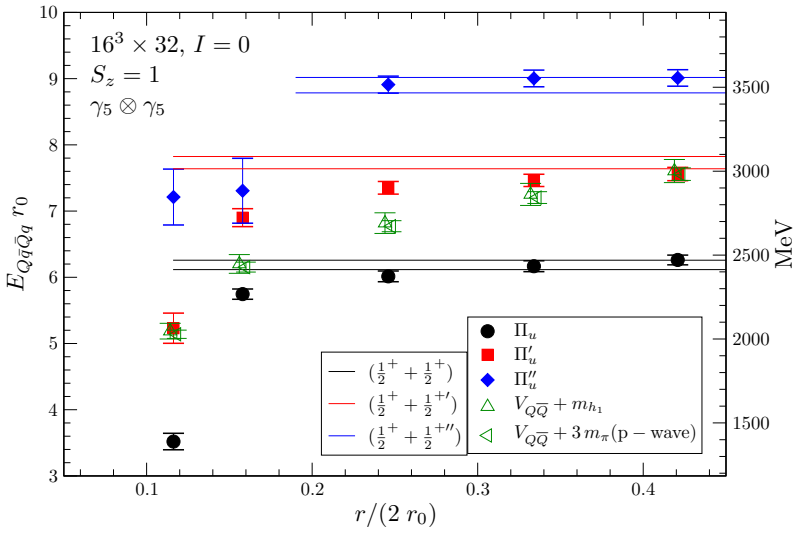

Figure 7.21: The $\mathcal{B}\overline{\mathcal{B}}$ meson-antimeson masses on our coarse lattice for the operator combination $\gamma_5 \otimes \gamma_5$ for $I = 0$ and $S_z = 1$. Black circles, red squares and blue diamonds mark the ground, the first and the second excited state respectively while the green triangles label the $Q\overline{Q}$ static potential plus various light mesons. The horizontal lines represent the sum of the corresponding static-light $\mathcal{B}$ mesons, where their widths indicate the jackknife errors.

figure 7.22 as well as the corresponding sums of the $Q\overline{Q}$ static potential and light mesons. In this case the ω meson which is approximated by the ρ meson is the lowest such state with the mass of three pseudoscalars within a P wave lying higher. For Π'_g the lowest lying $r \to \infty$ combination of states is given by a $\frac{1}{2}^+$ (γ_5) ground state plus a a radially excited $\frac{1}{2}^{-\prime}$ state ($\mathbb{1}$). For the second excited Π''_g the sum of a $\frac{1}{2}^{+\prime\prime}$ and a $\frac{1}{2}^-$ is the energetically favored possibility. These infinite distance limits are already reached at quite short distances r of about 0.15 fm in all channels. At very short distances of 0.11 fm there might be weak attractive ground state forces in the order of 200 MeV which is quite small in comparison to most other $\mathcal{B}\overline{\mathcal{B}}$ channels. The lowest lying bound states are much lighter of $O(1000)$ MeV and $O(500)$ MeV respectively. However, it is not clear whether the static-light meson-antimeson states decouple from bound states since there are several others lying higher that are not displayed in the figure.

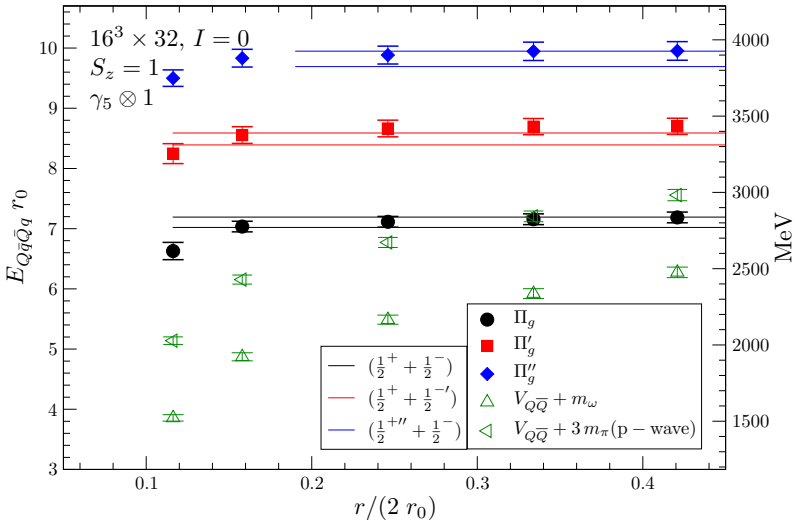

Figure 7.22: The $\mathcal{B}\overline{\mathcal{B}}$ meson-antimeson masses on our coarse lattice for the operator combination $\gamma_5 \otimes \mathbb{1}$ for $I = 0$ and $S_z = 1$. Black circles, red squares and blue diamonds mark the ground, the first and the second excited state respectively while the green triangles label the $Q\overline{Q}$ static potential plus various light mesons. The horizontal lines represent the sum of the corresponding static-light $\mathcal{B}$ mesons, where their widths indicate the jackknife errors.

Mixing within the $S_z = 0$ Spin Channel

As already stated, our $\mathcal{B}\overline{\mathcal{B}}$ operator combinations couple either to the $Q\overline{Q}$ static potential or to the vacuum in the $I = 0, S_z = 0$ channel. Nevertheless, with enormous effort we tried to extract the meson-antimeson energy levels. Some previous results of the following were already reported in our Lattice 2011 proceedings [34] where a large part of the discussion is taken from.

Coupling to the Static Quark Potential

The analysis in this section holds for our operator combinations $\mathbb{1} \otimes \mathbb{1}$ as well as for $\gamma_5 \otimes \gamma_5$ since both couple to the same state Σ_g^+. For this reason we just discuss the latter one in detail. At the end of this section we additionally present the final plots for the $\mathbb{1} \otimes \mathbb{1}$ operator.

In figure 7.23 we display the $I = 0$, $S_z = 0$ ground state for the $\mathcal{B}\overline{\mathcal{B}}$ meson-antimeson case in the $\gamma_5 \otimes \gamma_5\, (\Sigma_g^+)$ channel. We see the effective ground state energy levels E_{eff} for different t_0 of the $\gamma_5 \otimes \gamma_5$ operator combination at a distance of 0.11 fm. One finds a short plateau of poor quality in a range $t/a \in \{4, \ldots, 8\}$

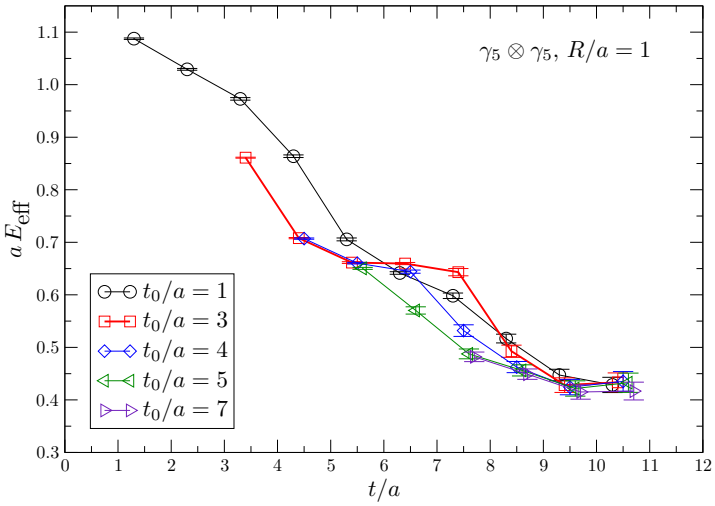

Figure 7.23: Effective masses for the $\gamma_5 \otimes \gamma_5$ $\mathcal{B}\overline{\mathcal{B}}$ isoscalar $S_z = 0$ ground state for different t_0 and a static quark-antiquark separation $R = a$. The splines are drawn to guide the eye.

for $t_0 > 2a$. Then the effective energy level decreases again and forms another plateau from $t/a = 8$ onwards. This can be explained by the observation that this state has the same quantum numbers as the $Q\overline{Q}$ static potential (and multiparticle states of the static potential plus a P wave η meson, the static potential plus two pions etc.). Our interpolator basis however, has very little overlap with these states. Therefore, we cannot easily disentangle the $Q\overline{Q}$ static potential and this background of multiparticle excitations from the lowest lying $\mathcal{B}\overline{\mathcal{B}}$ state that we are interested in.

As our meson-antimeson interpolator couples to all these states with different overlap we attempted to disentangle the $\mathcal{B}\overline{\mathcal{B}}$ state by splitting the correlation function in two parts:

$$C_{ij}(t) = C_{ij}^{\mathcal{B}\overline{\mathcal{B}}}(t) + d_{ij}\, e^{-V_{Q\overline{Q}}(t)\cdot t}\,. \tag{7.7}$$

In order to calculate the matrix d_{ij} we fitted the single correlators $C_i(t)$ to

$$C_i(t) = A_i\, e^{-V_{Q\overline{Q}}\cdot t)} + B_i \cdot e^{-mt} \tag{7.8}$$

and determined the fit parameters A_i, B_i and m. The matrix d_{ij} is then given by $\sqrt{A_i A_j}$. However, this ansatz to extract $C_{ij}^{\mathcal{B}\overline{\mathcal{B}}}(t)$ and apply the variational method failed as well.

So we tried to fit the ground state $\mathcal{B}\overline{\mathcal{B}}$ mass without using the variational approach, but from our single correlation function that has the largest overlap

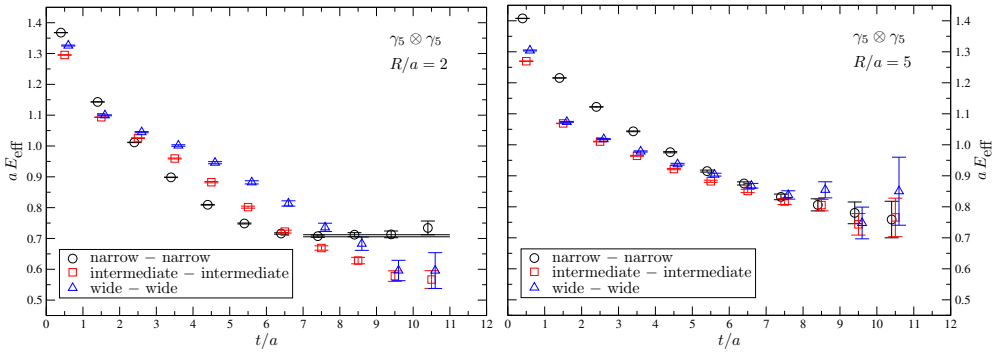

Figure 7.24: Effective $\mathcal{B}\overline{\mathcal{B}}$ masses from differently smeared single correlators in the $I = 0, S_z = 0$ channel for the operator combination $\gamma_5 \otimes \gamma_5$ at the distance $R = 2a$ (left plot) and $R = 5a$ (right plot). The horizontal lines in the left plot represent the result from the correlated fit in the displayed range. Their width indicates the jackknife error.

with the $\mathcal{B}\overline{\mathcal{B}}$ ground state. The effective energy levels for differently smeared source and sink interpolators are shown in figure 7.24, for a small static quark-antiquark separation ($R = 2a$) in the left panel and a large separation ($R = 5a$) in the right panel. At short distances, as in the left plot, we find clear effective mass plateaus for the correlator between a narrow smeared source and a narrow smeared sink. It decouples from the other masses and may overlap with he $\mathcal{B}\overline{\mathcal{B}}$ state. The black horizontal lines represent the fit results in the displayed range $[7, 11]$ and their width indicates the jackknife error. The effective masses of the other correlators decrease further such that plateaus can not be found. At larger quark-antiquark separations ($R > 3a$) the coupling to the $\mathcal{B}\overline{\mathcal{B}}$ state could not be resolved. This is depicted in the right panel of the figure where the effective masses from the different correlators overlap for times $t/a > 6$ and do not form plateaus. For our fine lattice we find the same behavior in this channel and we were also able to extract ground state $\mathcal{B}\overline{\mathcal{B}}$ masses in the same way.

The results from such single correlator fits are displayed in figure 7.25 for the combination $\gamma_5 \otimes \gamma_5$ and in figure 7.26 for the $\mathbb{1} \otimes \mathbb{1}$ operator. We keep the layout from previous result plots, such as figure 7.20 for example. Black circles mark the $\mathcal{B}\overline{\mathcal{B}}$ ground state and the two horizontal lines correspond to twice the ground state mass of the corresponding static-light meson, the expected $r \to \infty$ limit. In addition green triangles denote the static quark potential $V_{Q\overline{Q}}$ plus various light mesons that have the appropriate quantum numbers.

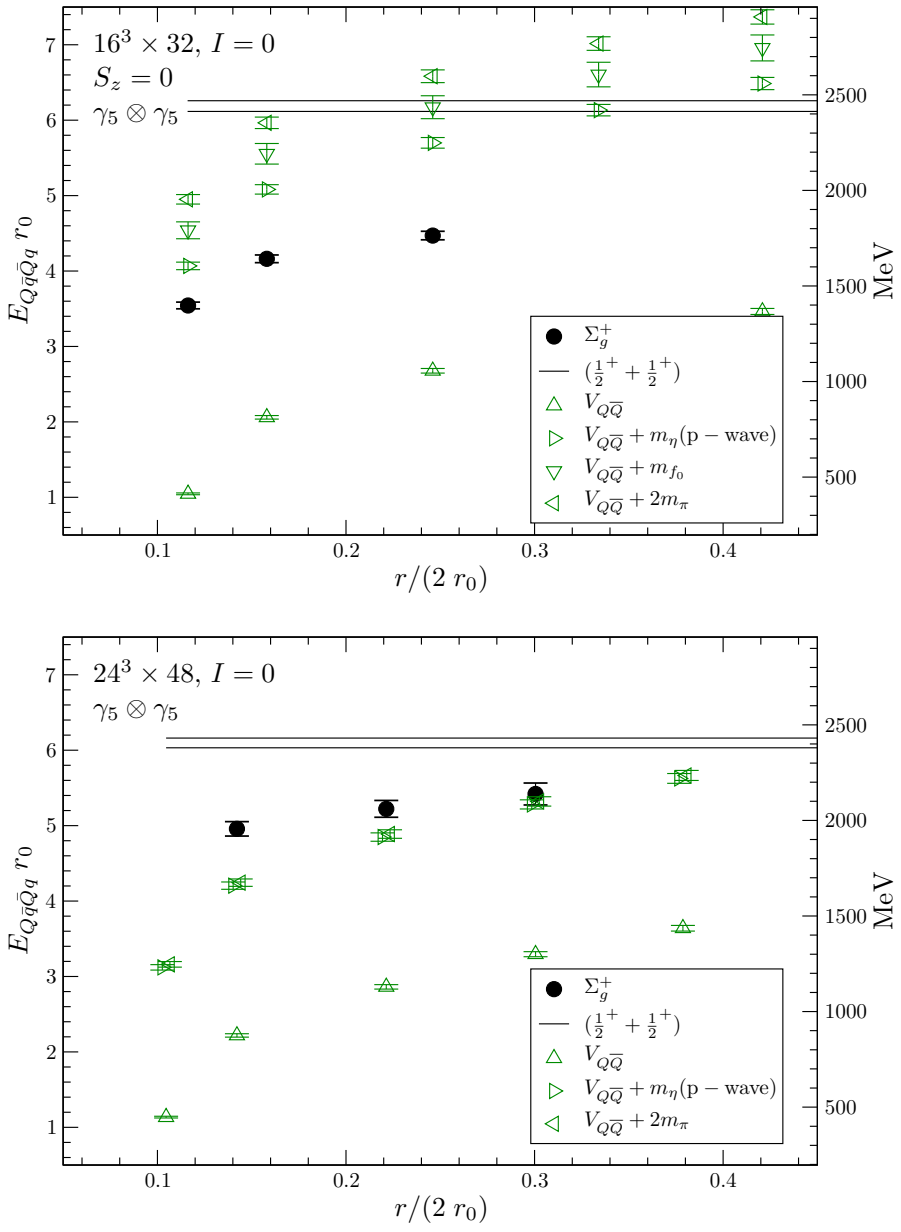

Figure 7.25: The $\mathcal{B}\overline{\mathcal{B}}$ meson-antimeson masses on our coarse (top) and fine lattice (bottom) for the operator combination $\gamma_5 \otimes \gamma_5$ in the $I = 0, S_z = 0$ channel. Black circles mark the ground state while the green triangles label the $Q\overline{Q}$ static potential plus various light mesons. The horizontal lines represent the sum of the corresponding static-light $\mathcal{B}$ mesons, where their widths indicate the jackknife errors.

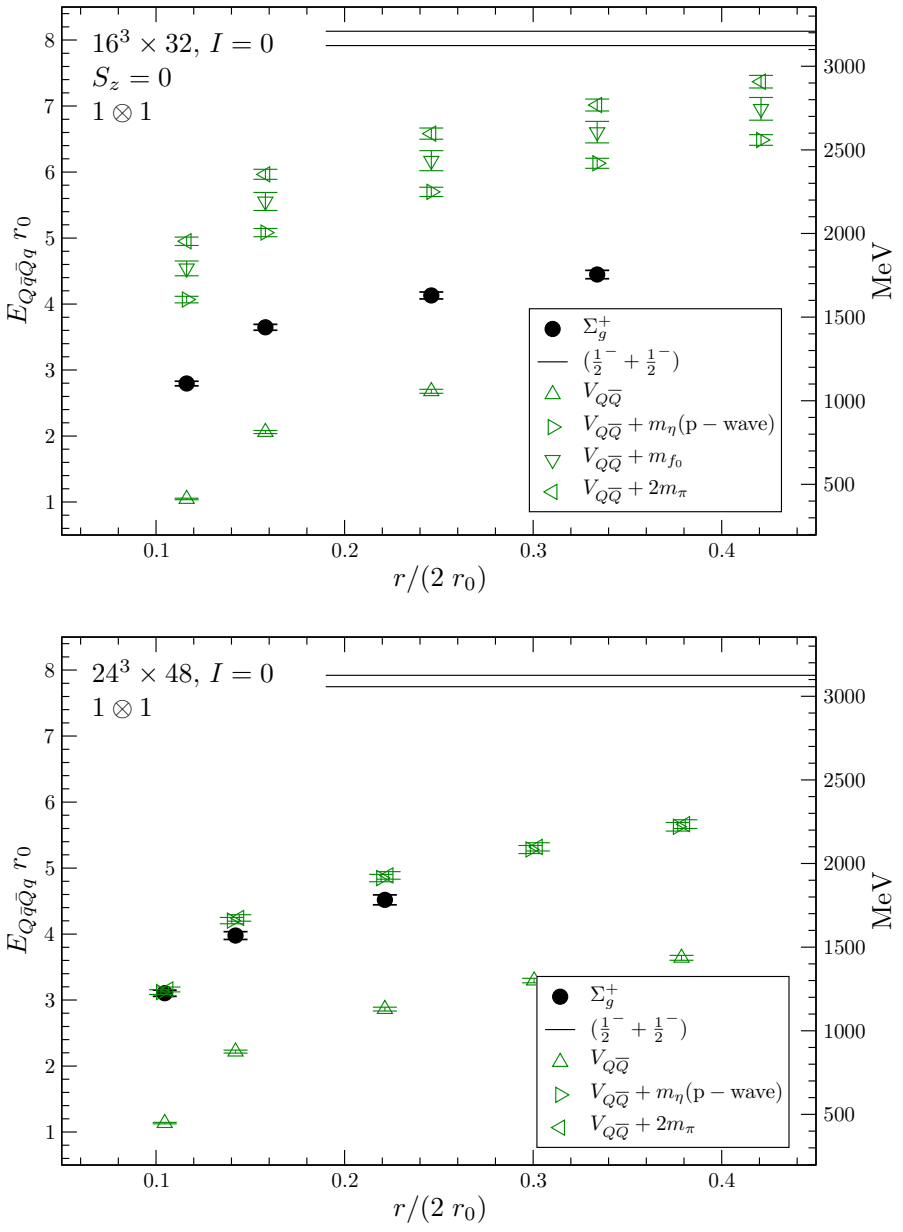

Figure 7.26: The $\mathcal{B}\overline{\mathcal{B}}$ meson-antimeson masses on our coarse (top) and fine lattice (bottom) for the operator combination $\mathbb{1} \otimes \mathbb{1}$ in the $I = 0, S_z = 0$ channel. Black circles mark the ground state while the green triangles label the $Q\overline{Q}$ static potential plus various light mesons. The horizontal lines represent the sum of the corresponding static-light $\mathcal{B}$ mesons, where their widths indicate the jackknife errors.

The upper plot of figure 7.25 shows the $\gamma_5 \otimes \gamma_5$ results from the coarse lattice. At first sight there appear to be very substantial short distance attractive forces in this channel. Also the static potential $V_{Q\overline{Q}}$ is lying much lower and can be disentangled. However, states consisting of a static potential and a scalar $I = 0$ particle will have the same quantum numbers. For our lattice parameters the P-wave pseudoscalar η meson (that at our quark mass will have a similar mass to the pion) is the lowest such state, with masses of a f_0 meson as well as two pseudoscalars lying higher. We include these sums in the figure where we approximate m_η by m_π and m_{f_0} by m_{a_0}. The ground state $\mathcal{B}\overline{\mathcal{B}}$ lies between these states and the static quark potential. So it is hard to decide whether we see a substantial attraction between the static-light meson-antimeson pair in this channel or bound states between the static quark potential and additional light mesons.

The results from our fine lattice are similar and depicted in the lower plot of figure 7.25. The meson-antimeson ground state energy is lying higher and closer to the expected infinite distance limit. Thus, either the attractive forces are smaller or the overlap with bound states between the $Q\overline{Q}$ static potential and light mesons is larger which is more probable.

Finally, figure 7.26 shows our findings for the $\mathbb{1} \otimes \mathbb{1}$ operator combination. The coarse and fine lattice results in this channel are in good agreement with those from the $\gamma_5 \otimes \gamma_5$ operator combination. The gap between the $\mathcal{B}\overline{\mathcal{B}}$ ground state and the $r \to \infty$ limit is much larger as in the previous case. However, as we are not able to distinguish between bound decay states and the $\mathcal{B}\overline{\mathcal{B}}$ meson-antimeson states further qualitative statements are not possible.

Coupling to the Vacuum

The operator combinations $\gamma_5 \otimes \mathbb{1}$ and $\gamma_5 \otimes \nabla_i \gamma_i$ couple to the Σ_u^- groundstate. In the isoscalar and spin $S_z = 0$ channel this state also overlaps with the vacuum which makes the extraction of $\mathcal{B}\overline{\mathcal{B}}$ energies quite complicated. For instance, this gets obvious when looking at figure 7.27 where we display the $\gamma_5 \otimes \mathbb{1}$ effective ground state masses at various distances R/a. Instead of forming plateaus with increasing time the effective mass curves tumble down to even negative values at times $t \sim 4$ before they rise again and may form plateaus. Especially for meson-antimeson pairs with a small static quark-antiquark separation, this behavior is particularly pronounced. Also the errors are really tiny in these cases. With increasing distances the minima of the effective mass curves move

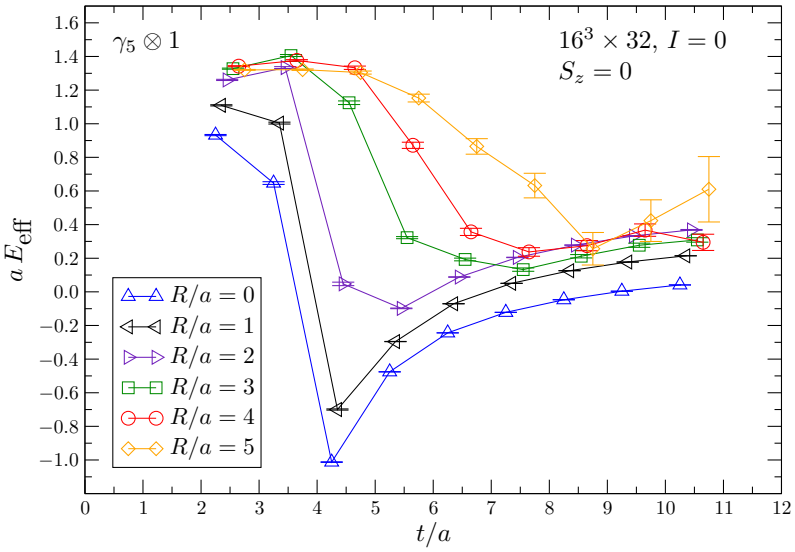

Figure 7.27: Effective masses for the $\gamma_5 \otimes \mathbb{1}$ $\mathcal{B}\overline{\mathcal{B}}$ isoscalar $S_z = 0$ ground state at various static quark-antiquark separation $R/a = 0, \ldots 5$. The splines are drawn to guide the eye.

to larger timeslices, the curve becomes smoother and the size of the errors gets believable. Thus, we assume that for larger static quark-antiquark separations our operator has more overlap with the $\mathcal{B}\overline{\mathcal{B}}$ states which are then consequently better resolved.

In order to get a clearer overall picture from this channel we observe the correlator itself, see e.g. figure 7.28 where we show the $\gamma_5 \otimes \mathbb{1}$ single correlation functions between differently smeared source and sink operators at a distance of $R = 2a$. For interpolators coupling to meson states one would expect an exponential decay resulting in a falling straight in the logarithmic plot. However, in this case we find a significant break for each correlator between $t \sim 4$ (for narrow smearing) to $t \sim 6$ (for wide smearing) for each correlator. After the break the curves seem to increase a bit before they get approximately constant.

A possible explanation for these findings is that in addition to the background of the static quark potential and multiparticle excitations this operator combinations also couples to the vacuum. So for short times the correlation function is governed by these multiparticle states which causes the exponential decay. At some intermediate time however, the constant vacuum energy dominates while the other masses get exponentially suppressed.

Nevertheless, we tried to get access to the lowest lying $\mathcal{B}\overline{\mathcal{B}}$ state that we

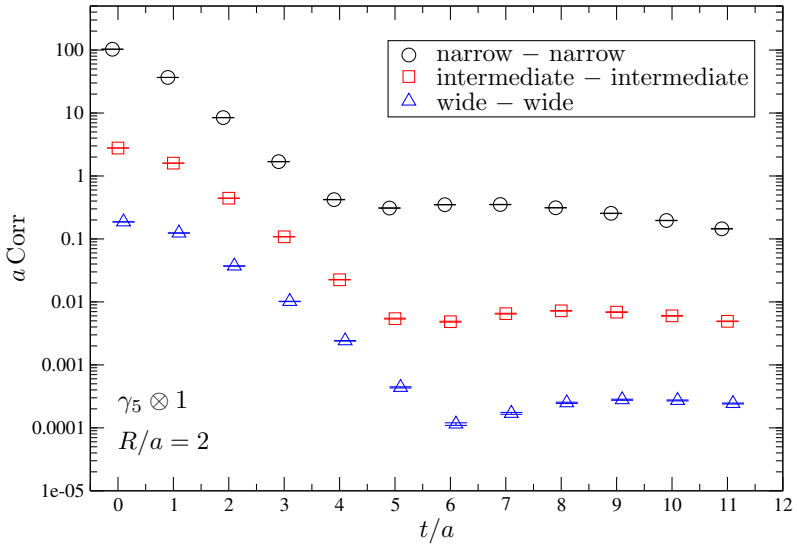

Figure 7.28: Single correlation functions between differently smeared source and sink operators for the $\mathcal{B}\overline{\mathcal{B}}$, $\gamma_5 \otimes \mathbb{1}$ combination in the $I = 0, S_z = 0$ channel at a static quark-antiquark separation of $R/a = 2$.

are interested in. The direct spectroscopy of single correlators as in the previous case is not feasible for this operator combination, since none of them decouples from the vacuum (see figure 7.28). Thus our intention was to separate $\mathcal{B}\overline{\mathcal{B}}$ meson-antimeson state from the vacuum energy and the multiparticle background. Thereby we fitted the single correlators $C_i(t)$ to

$$C_i(t) = f_i(t) + A_i\, e^{-mt} \tag{7.9}$$

and determined the parameters m, A_i as well as the sample function $f_i(t)$ for several ansätze, as for example a constant $f_i(t) = c_i$ or a time dependent function of the form $f_i(t) = c_i(1 - d_i/t)$. However, the effort to extract $C_{ij}^{\mathcal{B}\overline{\mathcal{B}}}(t)$ from a correlation function of the form

$$C_{ij}(t) = C_{ij}^{\mathcal{B}\overline{\mathcal{B}}}(t) + \sqrt{f_i(t) \cdot f_j(t)} \tag{7.10}$$

faild at each try.

On our fine lattice we find very similar results for the operator combination $\gamma_5 \otimes \mathbb{1}$. Thus, unfortunately we were not able to determine $\mathcal{B}\overline{\mathcal{B}}$ meson-antimeson energy levels for $I = 0, S_z = 0$ in this channel.

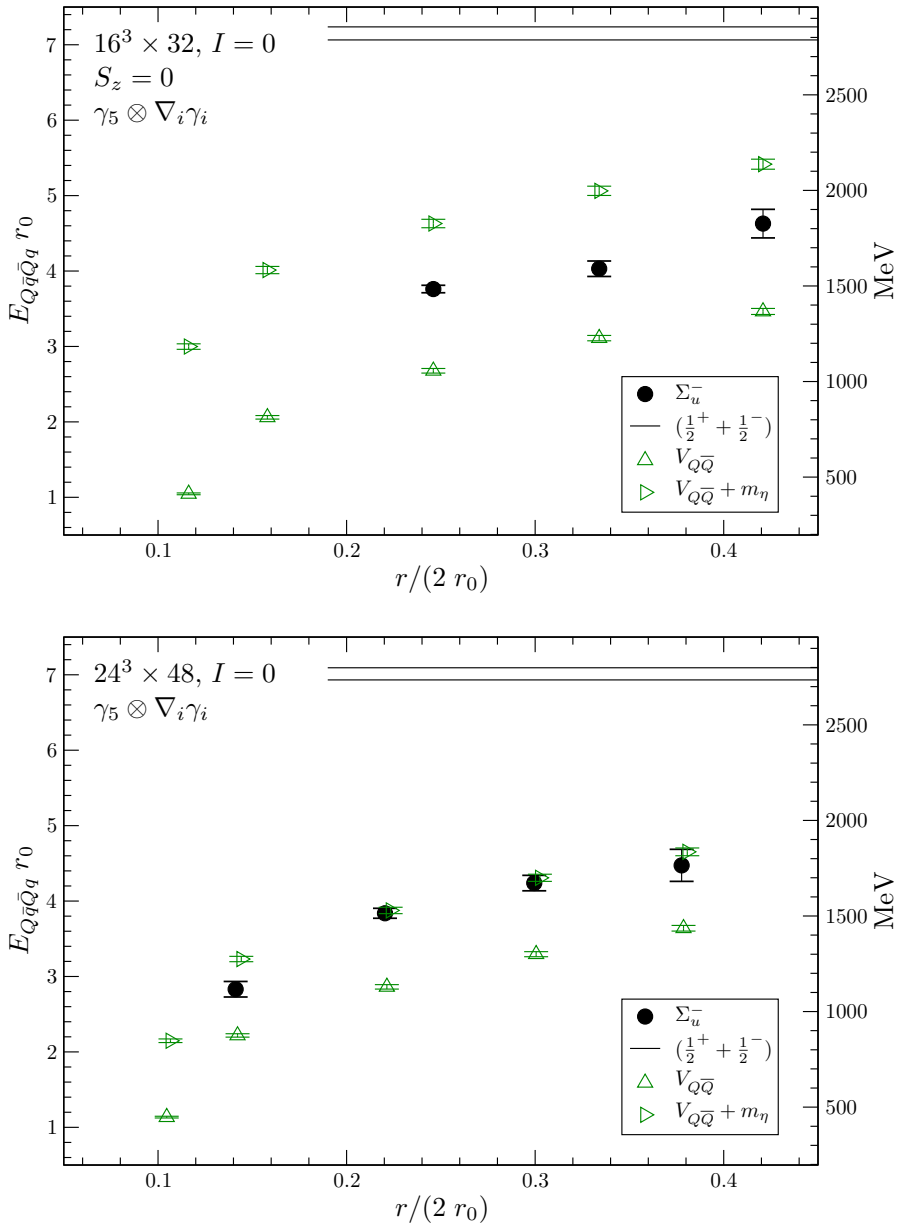

Figure 7.29: The $\mathcal{B}\overline{\mathcal{B}}$ meson-antimeson masses on our coarse (top) and fine lattice (bottom) for the operator combination $\gamma_5 \otimes \nabla_i \gamma_i$ in the $I = 0, S_z = 0$ channel. Black circles mark the ground state while the green triangles label the $Q\overline{Q}$ static potential plus various light mesons. The horizontal lines represent the sum of the corresponding static-light $\mathcal{B}$ mesons, where their widths indicate the jackknife errors.

Much better signals could be found for the $\gamma_5 \otimes \nabla_i \gamma_i$ operator in this $I = 0, S_z = 0$ channel. At short distances the correlator is still afflicted by the vacuum. At larger distances however, the overlap with $\mathcal{B}\overline{\mathcal{B}}$ states and/or the static quark potential $V_{Q\overline{Q}}$ and bound states of the potential plus light mesons increases and dominates the correlation function. By applying the variational approach we were able to extract ground state energies for distances $r > 24$ fm on our coarse lattice and for distances $r > 0.14$ fm on our fine lattice. The results are displayed in figure 7.29 where we keep our layout for final plots.

The lowest lying states with the same quantum numbers are the $Q\overline{Q}$ static potential and the sum of the static quark potential and the η meson which is approximated by the pseudoscalar. On the coarse lattice which is shown in the upper plot we find the extracted Σ_u^- ground state between these states. The lower plot displays the results from our fine lattice where the ground state $\mathcal{B}\overline{\mathcal{B}}$ agrees with the lowest lying bound state. For both lattice sets it is not possible to decide whether there is attraction in this channel or if the $\mathcal{B}\overline{\mathcal{B}}$ decays to some multiparticle state.

For our combinations where we coupled a S or a P_- wave with the P_+ wave the signals were much to weak in this channel. So an extraction of the $\mathcal{B}\overline{\mathcal{B}}$ energies for the operators $\gamma_5 \otimes P_\parallel$, $\gamma_5 \otimes P_\perp$, $\gamma_i \nabla_i \otimes P_\parallel$ and $\gamma_i \nabla_i \otimes P_\perp$ was not feasible.

7.4 Mass Splittings

As stated in section 6.2.1 the P_+ operator can be perpendicular or parallel to the intermeson axis. Hence we distinguish between "parallel" ($P_\parallel$) and "perpendicular" ($P_\perp$) states that couple to different quantum numbers. The $P_\parallel$ operators can only create Π and Δ states but not the Σ states while the $P_\perp$ operators only couple to the Σ and Π states. In order to check whether there is a mass splitting between these states we calculate the differences between the corresponding $P_\perp$ and $P_\parallel$ states. The errors are obtained using the jackknife method. However, serious results could only be found in the isoscalar $\mathcal{B}\mathcal{B}$ channel which are analyzed in the following.

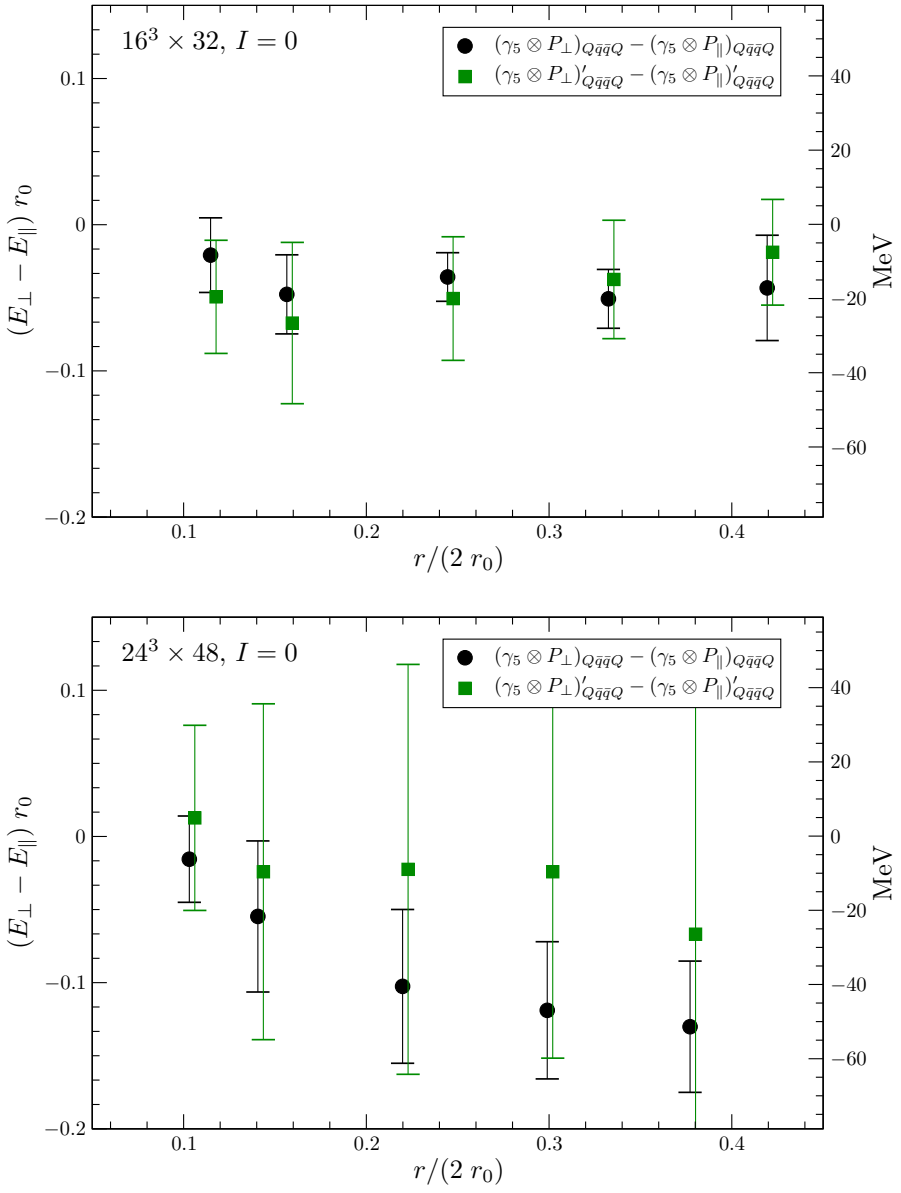

Figure 7.30: The $\mathcal{BB}$ meson-meson differences between the operator combinations $\gamma_5 \otimes P_\perp$ and $\gamma_5 \otimes P_\parallel$ in the isosinglet channel for ground (black circles) and first excited states (green squares). The upper plot shows the coarse lattice results and the lower one those of the fine lattice.

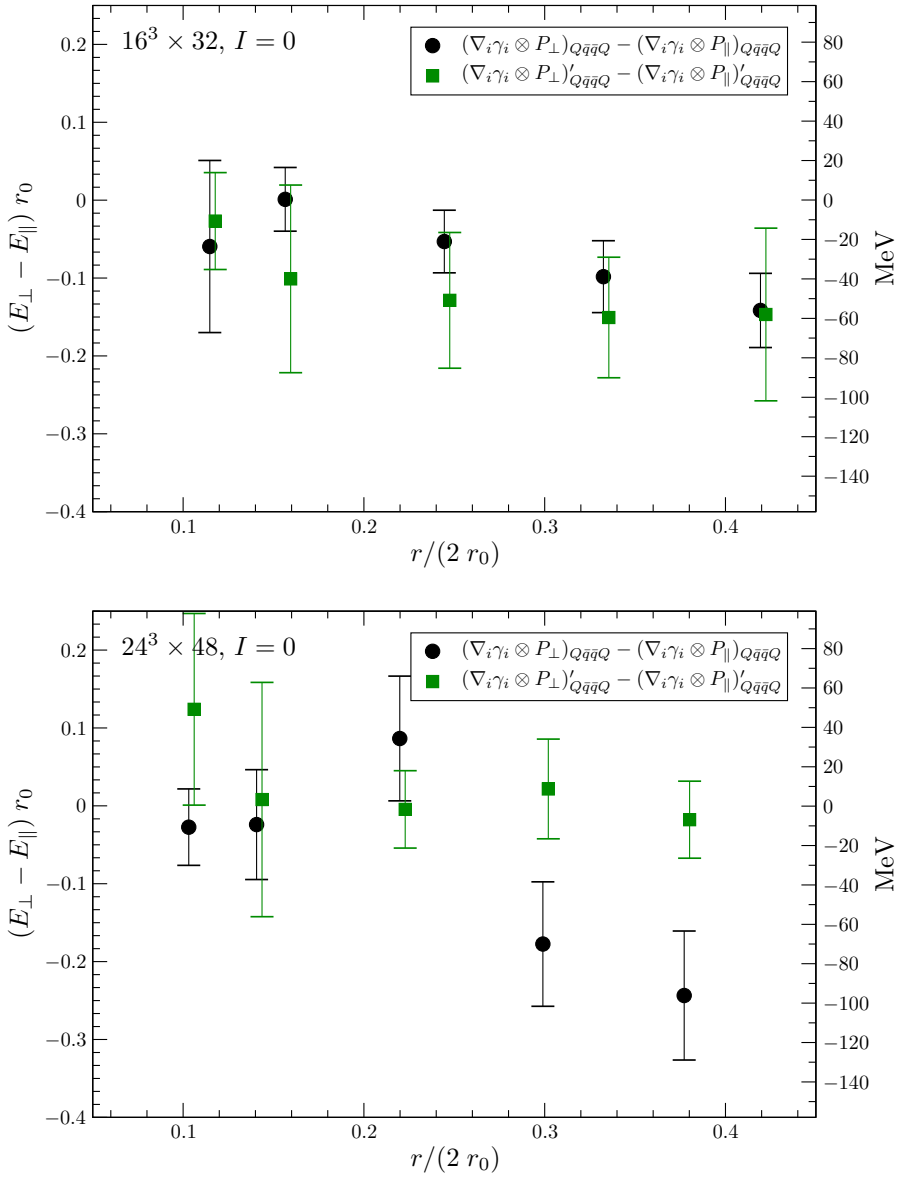

Figure 7.31: The $\mathcal{BB}$ meson-meson differences between the operator combinations $\nabla_i\gamma_i \otimes P_\perp$ and $\nabla_i\gamma_i \otimes P_\parallel$ in the isosinglet channel for ground (black circles) and first excited states (green squares). The upper plot shows the coarse lattice results and the lower one those of the fine lattice.

In figure 7.30 we display the $\mathcal{BB}$ meson-meson differences between the operator combinations $\gamma_5 \otimes P_\perp$ and $\gamma_5 \otimes P_\parallel$. On our coarse lattice which is shown in the upper plot we do not find mass splittings, neither for the ground nor for the first excited state. Although the trend goes to slightly heavier $\gamma_5 \otimes P_\parallel$ meson-meson energies the errors are to large to make a clear statement. On our fine lattice (lower plot) however, we observe a ground state splitting for intermediate distances $r > 0.22$ fm. Thereby the mass of the $\gamma_5 \otimes P_\parallel$ state is larger of the order of 50 MeV with an error of 20 MeV. Due to the large errors for the first excited state, splittings could not be resolved in this channel.

Next we look at the difference between $\nabla_i \gamma_i \otimes P_\perp$ and $\nabla_i \gamma_i \otimes P_\parallel$ states. Our coarse lattice results are shown in the upper plot of figure 7.31. In this channel the ground state difference between $P_\perp$ and $P_\parallel$ states is falling quite linear from zero at $r \approx 0.15$ fm to a splitting of the order of 60 MeV at $r \approx 0.42$ fm. Also in the first excited channel the $\nabla_i \gamma_i \otimes P_\parallel$ energies may lie somewhat higher. But errors are too large to resolve a splitting. In the lower plot of the figure we present the splittings on our fine lattice. The ground state errors are about twice as large as on the coarse lattice. We observe a splitting of the order of 100 MeV at distances $r \approx 0.4$ fm. Again the first excited channel shows no splitting.

In general, we find mass splittings between $P_\perp$ and $P_\parallel$ ground states of the order of $50 - 100$ MeV at intermediate distances. Thereby the difference between these states is more significant on the fine lattice. This might be due to the different Yukawa potential which has a longer interaction range on the fine lattice due to the much lighter pion mass. In contrast to the ground state, a mass splitting for the first excited states could not be resolved. We assume that that the $P_\perp$ operators tend to have more overlap with the Σ states than with the Π states while the $P_\parallel$ operators can not create the Σ states. But for the first excitation Π states might be created in both channels resulting in a vanishing mass splitting.

"Wissenschaft kann die letzten Rätsel der Natur nicht lösen. Sie kann es deswegen nicht, weil wir selbst ein Teil der Natur und damit auch ein Teil des Rätsels sind, das wir lösen wollen."

Max Planck

8 Conclusion

Summary

The central subject of this theses was the calculation of static-light $\mathcal{B}\mathcal{B}$ and $\mathcal{B}\overline{\mathcal{B}}$ meson-(anti)mesons in order to investigate potentials between pairs of static-light mesons and to clarify the question of attraction or repulsion depending on the static quark-quark or quark-antiquark separation.

After motivating this research project we gave a brief introduction to Quantum Chromodynamics. The distinctive feature of this theory is asymptotic freedom such that perturbation theory gets feasible for large momentum transfers and confinement that binds quarks and gluons to color neutral hadrons. So to get an access to this low energy sector and to calculate baryon or meson masses, as e.g. in our case, from first principles other methods have to be applied. Well established and very suitable is to map the continuum QCD action to discrete space-time. This Lattice QCD implementation was discussed in chapter four. We pointed out the occurring issues of additional unphysical poles as well as the explicit breaking of chiral symmetry and presented some solutions. Expressing observables as Feynman path integrals in Euclidean time allows us to evaluate them numerically by applying Monte Carlo methods.

The observables we are interested in are static-light $\mathcal{B}$ mesons and inter-meson potentials between pairs of static-light mesons, $\mathcal{B}(\mathbf{r})\mathcal{B}(\mathbf{0})$ and $\mathcal{B}(\mathbf{r})\overline{\mathcal{B}}(\mathbf{0})$,

as a function of the static quark-quark (or quark-antiquark) separation $\mathbf{r}$. In the fifth chapter we introduced the methods and improvement schemes to successfully evaluate these quantities. Central are Euclidean correlation functions which can be expressed as Feynman path integrals as well as in Hilbert space. Thus, comparing both results allows us to extract the desired energy levels. However, to obtain clear signals a couple of sophisticates techniques has to be applied. All-to-all propagators are needed to achieve high statistics. To approximate this numerical beast we used stochastic estimates, improved by a hopping parameter expansion to cancel the short distance noise. Furthermore, we applied several smearing techniques like Wuppertal smearing, APE link fuzzing and stout smearing to enhance the signal to noise ratio. For a analysis that enables us to determine not only ground stats but also excited states we calculated a whole matrix of differently smeared correlators. Masses were then extracted, by means of the variational method, solving a generalized eigenvalue problem.

In chapter six we explicitly evaluated the static-light meson correlators for $\mathcal{B}$, $\mathcal{B}\mathcal{B}$ and $\mathcal{B}\overline{\mathcal{B}}$ states. In addition we depicted the correlators graphically and showed how different isospin channels are related to the "crossing" and "box" diagrams. By using different operators and operator combinations we could generate various quantum numbers for spin, parity and charge conjugation. Thereby we had to distinguish between vanishing distance $\mathbf{r} = \mathbf{0}$ and distances $\mathbf{r} > \mathbf{0}$. For the latter case the O(3) (or $\mathrm{O}(3) \otimes \mathbb{C}$) symmetry is broken down to its cylindrical subgroup $\mathrm{D}_{\infty\mathrm{h}}$. Within this representation the states are labeled by the spin along the axis Λ, where Σ, Π, Δ refer to $0, 1, 2$ respectively. On our coarse lattice and for operator combinations that couple to total angular momentum $\Lambda = 0$ we additionally performed a projection of the static-light meson spins to a definite $S_z = 0$ or $S_z = 1$ spin quantum number. An overview of our lattices and simulation parameters was displayed before we analyzed our results in chapter seven.

Using the example of static-light $\mathcal{B}$ mesons we explained the extraction of masses where we determined appropriate ranges for one- and two-exponential fits by calculating effective masses from adjacent timeslices. Subsequently we moved on to $\mathcal{B}\mathcal{B}$ meson-meson states. Motivated by the examination of their effective masses for increasing distances, we defined the intermeson potentials $V_{\mathcal{B}\mathcal{B}}(r)$ as the difference between the meson-meson energy levels and the $r \to \infty$ two static-light meson limiting cases. we calculated these potentials for all our operator combinations and compared the different spin and isospin channels.

Main results

In contrast to references [142, 143, 144] we observe significant attraction for all our operator combinations in all spin and isospin channels at short distances of about 0.12 fm. Only for the $\mathbb{1} \otimes \mathbb{1}$ operator in the $I = 1$, $S_z = 0$ channel, neither attraction nor repulsion could be resolved. At intermediate distances of about 0.4 fm some operator combinations yield repulsion. On our coarse lattice we find repulsion for the $\gamma_5 \otimes \mathbb{1}$ operator in all spin and isospin channels for the ground and first excited states. Furthermore we observe repulsion in the $I = 1, S_z = 1$ ground state channel of the operator combination $\gamma_5 \otimes \gamma_5$ (Π_g) and for the $I = 1$ first excitation of the combination $\nabla_i \gamma_i \otimes P_\perp$. These findings could mostly be confirmed on our fine lattice. Excepted is the isoscalar ground state channel of the $\gamma_5 \otimes \mathbb{1}$ operator. In addition there is repulsion for the $I = 0$, $\nabla_i \gamma_i \otimes P_\parallel$ ground and first excited state as well as for the $I = 0$, $\nabla_i \gamma_i \otimes P_\perp$ ground state. While the attractive potentials at short distances were expected due to QCD forces, the repulsion in some channels at intermediate distances was not and should be investigated in future studies.

When comparing both lattice sets, we find that the intermeson potentials are either of the same order or in many cases even more attractive on the fine lattice. Also the increase of the potential appears to be "slower" and smoother in dependence of the distance than on the coarse lattice. This may be related to the much lighter pion mass on the fine lattice resulting in a larger interaction range due to a different Yukawa potential.

According to the introduction, $\mathcal{B}\overline{\mathcal{B}}$ meson-antimesons are also very interesting with respect to charmonium threshold states [150] ($D\overline{D}$ molecules or tetraquarks). However, mesons that are bound to the static quark potential (hadro-quarkonium [151]) will have the same quantum numbers as our calculated $\mathcal{B}\overline{\mathcal{B}}$ states. Since transition elements between $Q\overline{Q}$ and $\mathcal{B}\overline{\mathcal{B}}$ states were not taken into account within our simulations, it is very difficult to disentangle hadro-quarkonia and $\mathcal{B}\overline{\mathcal{B}}$ states and to decide whether there is attraction between static-light meson-antimeson pairs or if they couple to the $Q\overline{Q}$ static potential plus additional light mesons. There is only the spin $S_z = 1$ channel of the operator combination $\gamma_5 \otimes \gamma_5$ that decouples from the bound states because the ground state meson-antimeson energies Π_u in the isoscalar and Π_g in the isovector channel are lying much lower than the lightest hadro-quarkonium.

Analyzing $I = 0, S_z = 0$ $\mathcal{B}\overline{\mathcal{B}}$ states was a very challenging task since they couple directly to the $Q\overline{Q}$ static potential, e.g. in the case of the $\gamma_5 \otimes \gamma_5$

combination, or to the vacuum state, e.g. for the $\gamma_5 \otimes \mathbb{1}$ channel. With some effort we ware able to extract ground state energies in a few channels. However, also these states couple to bound hadro-quarkonia as well such that we could not disentangle the meson-antimeson energies from the bound states.

In general we found out, that $\mathcal{B}\mathcal{B}$ meson-mesons are stable at short distances due to significant attractive potentials in most channels. From our comparison of the light pion mass (fine) and the heavy pion mass (coarse) lattice we found indications that both, gluon and pion exchange contribute to this attraction. Although we were not able to clearly disentangle $\mathcal{B}\overline{\mathcal{B}}$ meson-antimesons from bound states between light mesons and the $Q\overline{Q}$ static quark potential, we assume that also the potentials between a $\overline{\mathcal{B}}$ antimeson and a $\mathcal{B}$ meson are attractive for small quark-antiquark separations. As one reason, we observe $\mathcal{B}\overline{\mathcal{B}}$ energies far below the threshold of the sum of the two static-light mesons. In many channels, as e.g. for the isotriplet $\gamma_5 \otimes \gamma_5$ combination, it is up to the order of $O(1000)$ MeV. In addition, the coupling to the static potential plus additional light mesons seems to be weak in some channels. Thus, our calculations support the molecule or tetraquark interpretation for the XYZ resonances, as for instance the $X(3872)$ and the $Z^+(4430)$.

Outlook

Our analysis of $\mathcal{B}\overline{\mathcal{B}}$ meson-antimesons is suffering from the mixing of these states with light mesons bound to the static quark potential that have the same quantum numbers. To get rid of this mixing problem, the next step would be to calculate not only $C_{\mathcal{B}\overline{\mathcal{B}}}(t)$ correlators, but also transition elements between $Q\overline{Q}$ and $\mathcal{B}\overline{\mathcal{B}}$, namely $C_{\mathcal{B}\overline{\mathcal{Q}}}(t), C_{\mathcal{Q}\overline{\mathcal{B}}}(t)$ correlators, and the Wilson loop $C_{\mathcal{Q}\overline{\mathcal{Q}}}(t)$ as it was done, e.g., in [93]. By reducing these four correlation functions to a two times two matrix the $\mathcal{B}\overline{\mathcal{B}}$ states can be extracted. This will enable further investigations about the attractive or repulsive nature of $\mathcal{B}\overline{\mathcal{B}}$ potentials. Also the $I = 0, S_z = 0$ channel will be accessible then.

Natural improvements are simulations on larger lattice volumes and using higher statistics. Especially the "box" and "cross" diagrams are numerically quite expensive, such that the number of stochastic estimates we could use for their calculation was severely limited by our computer time. By calculating potentials on a set of lattices with different pion masses towards the continuum pion mass one could further study the contribution of pion exchange to the potentials between pairs of static-light mesons.

A

Notations and Conventions

In this thesis we work with natural units, e.g., we set $\hbar = c = 1$.

Furthermore we mostly use the Einstein summation convention:

$$a_i b_i = \sum_i a_i b_i. \tag{A.1}$$

As common in lattice QCD all our calculations are performed in Euclidean space-time, which means substituting real time by imaginary time:

$$t \longrightarrow it. \tag{A.2}$$

The consequence of this is, that the metric tensor simplifies to the identity matrix, $g_{\mu\nu} = \delta_{\mu\nu}$, and time and space are treated the same way. Thus, we do not have to distinguish between covariant (lower) and contravariant (upper) indices.

The important advantage of this substitution is, that the exponential function in the Feynman path integral is not oscillating any more, but acts as an exponential suppression. For this reason a numerical evaluation of the path integral becomes feasible using Monte Carlo methods.

A.1 Conventions for the Gamma Matrices

The Euclidean gamma matrices have the following properties:

$$\gamma_\mu^\dagger = \gamma_\mu = \gamma_\mu^{-1}, \qquad \mu = 1, \ldots, 5 \tag{A.3}$$

$$\{\gamma_\mu, \gamma_\nu\} = 2\delta_{\mu\nu}\mathbb{1}. \qquad \mu, \nu = 1, \ldots, 4 \tag{A.4}$$

In the chiral representation they are given by

$$\gamma_1 = \begin{pmatrix} 0 & 0 & 0 & i \\ 0 & 0 & i & 0 \\ 0 & -i & 0 & 0 \\ -i & 0 & 0 & 0 \end{pmatrix} \qquad \gamma_2 = \begin{pmatrix} 0 & 0 & 0 & 1 \\ 0 & 0 & -1 & 0 \\ 0 & -1 & 0 & 0 \\ 1 & 0 & 0 & 0 \end{pmatrix}$$

$$\gamma_3 = \begin{pmatrix} 0 & 0 & i & 0 \\ 0 & 0 & 0 & -i \\ -i & 0 & 0 & 0 \\ 0 & i & 0 & 0 \end{pmatrix} \qquad \gamma_4 = \begin{pmatrix} 0 & 0 & 1 & 0 \\ 0 & 0 & 0 & 1 \\ 1 & 0 & 0 & 0 \\ 0 & 1 & 0 & 0 \end{pmatrix} \tag{A.5}$$

In addition we define γ_5 as the product

$$\gamma_5 = \gamma_1\gamma_2\gamma_3\gamma_4 = \begin{pmatrix} 1 & 0 & 0 & 0 \\ 0 & 1 & 0 & 0 \\ 0 & 0 & -1 & 0 \\ 0 & 0 & 0 & -1 \end{pmatrix}, \tag{A.6}$$

which anticommutes with all Dirac matrices:

$$\{\gamma_5, \gamma_\mu\} = 0. \qquad \mu = 1, \ldots, 4 \tag{A.7}$$

We define

$$\sigma_{\mu\nu} = \frac{1}{2i}[\gamma_\mu, \gamma_\nu]. \tag{A.8}$$

The $\sigma_{\mu\nu}$ are anti-symmetric in μ and ν. Consequently, they vanish if $\mu = \nu$ and one is left with 6 non-vanishing components.

A basis of complex 4×4 matrices over $\mathbb{C}$ is given by the following set of 16 matrices:

$$\Gamma \in \{\mathbb{1}_{4\times4}, \gamma_\mu, \sigma_{\mu\nu}, \gamma_5\gamma_\mu, \gamma_5\}. \tag{A.9}$$

These are the elements of the *Clifford-algebra*.

A.2 Gell-Mann Matrices

A $su(N)$ algebra is defined through its N^2-1 generators t^a. These are, in the fundamental representation, traceless and hermitian $N \times N$ matrices

$$\mathrm{Tr}[t^a] = 0 \quad \text{and} \quad (t^a)^\dagger = t^a \tag{A.10}$$

which are normalized by

$$\mathrm{Tr}[t^a t^b] = \frac{1}{2}\delta^{ab} \tag{A.11}$$

and fulfill the commutation relation

$$[t^a, t^b] = i f^{abc} t^c. \tag{A.12}$$

The f^{abc} are called *structure constants*. They are real numbers and completely antisymmetric in the indices.

For the $su(3)$ algebra in our case, the corresponding 8 generators are usually given by the *Gell-Mann* matrices λ^a:

$$t^a = \frac{\lambda^a}{2}, \qquad a = 1, 2, \ldots, 8 \tag{A.13}$$

where

$$\lambda^1 = \begin{pmatrix} 0 & 1 & 0 \\ 1 & 0 & 0 \\ 0 & 0 & 0 \end{pmatrix} \qquad \lambda^2 = \begin{pmatrix} 0 & -i & 0 \\ i & 0 & 0 \\ 0 & 0 & 0 \end{pmatrix}$$

$$\lambda^3 = \begin{pmatrix} 1 & 0 & 0 \\ 0 & -1 & 0 \\ 0 & 0 & 0 \end{pmatrix} \qquad \lambda^4 = \begin{pmatrix} 0 & 0 & 1 \\ 0 & 0 & 0 \\ 1 & 0 & 0 \end{pmatrix}$$

$$\lambda^5 = \begin{pmatrix} 0 & 0 & -i \\ 0 & 0 & 0 \\ i & 0 & 0 \end{pmatrix} \qquad \lambda^6 = \begin{pmatrix} 0 & 0 & 0 \\ 0 & 0 & 1 \\ 0 & 1 & 0 \end{pmatrix}$$

$$\lambda^7 = \begin{pmatrix} 0 & 0 & 0 \\ 0 & 0 & -i \\ 0 & i & 0 \end{pmatrix} \qquad \lambda^8 = \begin{pmatrix} \frac{1}{\sqrt{3}} & 0 & 0 \\ 0 & \frac{1}{\sqrt{3}} & 0 \\ 0 & 0 & \frac{-2}{\sqrt{3}} \end{pmatrix} \tag{A.14}$$

In the adjoint representation the generators can be represented through the structure constants:

$$(\lambda^a)_{bc} = -i f_{abc}. \tag{A.15}$$

A.3 Parity Transformations

A parity transformation $\mathcal{P}$ acts on our lattice fields as:

$$\psi(\vec{x},t) \xrightarrow{\mathcal{P}} \psi(\vec{x},t)^{\mathcal{P}} = \gamma_4\psi(-\vec{x},t), \tag{A.16}$$

$$\bar{\psi}(\vec{x},t) \xrightarrow{\mathcal{P}} \bar{\psi}(\vec{x},t)^{\mathcal{P}} = \bar{\psi}(-\vec{x},t)\gamma_4, \tag{A.17}$$

$$U_i(\vec{x},t) \xrightarrow{\mathcal{P}} U_i(\vec{x},t)^{\mathcal{P}} = U_i(-\vec{x}-a\hat{i},t)^\dagger, \quad i=1,2,3, \tag{A.18}$$

$$U_4(\vec{x},t) \xrightarrow{\mathcal{P}} U_4(\vec{x},t)^{\mathcal{P}} = U_4(-\vec{x},t). \tag{A.19}$$

A.4 Charge Conjugation

Charge conjugation transforms particles into anti-particles and is defined by

$$C\gamma_\mu C^{-1} = -\gamma_\mu^T. \tag{A.20}$$

In the chiral representation the charge-conjugation matrix is given by

$$C = i\gamma_2\gamma_4. \tag{A.21}$$

It obeys

$$C = C^{-1} = C^\dagger = -C^T \tag{A.22}$$

and acts on the lattice fields via

$$\psi(x) \xrightarrow{\mathcal{C}} \psi(x)^{\mathcal{C}} = C^{-1}\bar{\psi}(x)^T, \tag{A.23}$$

$$\bar{\psi}(x) \xrightarrow{\mathcal{C}} \bar{\psi}(x)^{\mathcal{C}} = -\psi(x)^T C, \tag{A.24}$$

$$U_\mu(x) \xrightarrow{\mathcal{C}} U_\mu(x)^{\mathcal{C}} = U_\mu(x)^* = \left(U_\mu(x)^\dagger\right)^T. \tag{A.25}$$

B

Grassmann Numbers

This Appendix gives a short overview of anticommuting numbers, also known as *Grassmann numbers*. They are necessary since we are dealing with fermion fields which have to be completely antisymmetric. This property cannot be fulfilled with ordinary numbers. A more detailed discussion of this topic may be found in chapter 5 of [37] and in chapter 2 of [6].

B.1 Definition

Grassmann numbers are anticommuting numbers that obey the following anticommutation relation for a set of numbers $\eta_i, i = 1, \ldots, N$:

$$\eta_i \eta_j + \eta_j \eta_i = 0 \qquad \forall\, i, j. \tag{B.1}$$

This equation implies that the η_i are *nilpotent*:

$$\eta_i^2 = 0. \tag{B.2}$$

Because of this nilpotency the power series expansion of any arbitrary Grassmann-valued function is given by a polynomial of the form

$$A = a + \sum_i a_i \eta_i + \frac{1}{2!} \sum_{i,j} a_{ij} \eta_i \eta_j + \ldots + \frac{1}{N!} \sum_{i_1,\ldots,i_N} a_{i_1 \ldots i_N} \eta_{i_1} \ldots \eta_{i_N} \tag{B.3}$$

with completely antisymmetric coefficients $a_{i_1 \dots i_N} \in \mathbb{C}$. These polynomials A form a *Grassmann algebra* of dimension N with generators $\eta_i, i = 1, \dots, N$.

B.2 Definition of Derivatives

For differentiating elements of the Grassman algebra with respect to the generators the following rules are found:

$$\frac{\partial}{\partial_{\eta_i}} 1 = 0, \tag{B.4}$$

$$\frac{\partial}{\partial_{\eta_i}} \eta_j = \delta_{ij}, \tag{B.5}$$

$$\frac{\partial}{\partial_{\eta_i}} \eta_j A = -\eta_j \frac{\partial}{\partial_{\eta_i}} A \qquad i \neq j, \tag{B.6}$$

$$\frac{\partial^2}{\partial_{\eta_i} \partial_{\eta_j}} A = -\frac{\partial^2}{\partial_{\eta_j} \partial_{\eta_i}} A \qquad \Longrightarrow \frac{\partial^2}{\partial_{\eta_i}^2} A = 0. \tag{B.7}$$

B.3 Integrals over Grassmann Numbers

Furthermore we need a consistent definition of integration over Grassmann numbers in analogy to the integral over the whole $\mathbb{C}^N$. From that we obtain three conditions [37]:

1. We require the integral to be a complex linear functional:

$$\int d^N \eta \, A \quad \in \mathbb{C}, \tag{B.8}$$

$$\int d^N \eta \, (\lambda_1 A_1 + \lambda_2 A_2) = \lambda_1 \int d^N \eta \, A_1 + \lambda_2 \int d^N \eta \, A_2, \tag{B.9}$$

$$\text{where} \quad d^N \eta = d\eta_N d\eta_{N-1} \dots d\eta_1. \tag{B.10}$$

2. The integral has to vanish at the boundary:

$$\int d^N \eta \, \frac{\partial}{\partial_{\eta_i}} A = 0. \tag{B.11}$$

3. It has to be normalized:

$$\int d^N \eta \, \eta_1 \eta_2 \dots \eta_N = 1. \tag{B.12}$$

This means that only expressions proportional to $\eta_1\eta_2\ldots\eta_N$ contribute to the integral:

$$\int d^N\eta\, A = a_{12\ldots N}, \tag{B.13}$$

These conditions lead to further definitions and conventions:

$$d\eta_i d\eta_j = -d\eta_j d\eta_i, \tag{B.14}$$

$$\int d\eta_i\, 1 = 0, \tag{B.15}$$

$$\int d\eta_i\, \eta_j = \delta_{ij}, \tag{B.16}$$

and we obtain the following identity:

$$\int d\eta_i\, \frac{\partial}{\partial\eta_i} A = 0. \tag{B.17}$$

B.4 Transformation of Variables in Grassmann Integrals

Performing a linear transformation via $\eta_i' = M_{ij}\eta_j$, where M_{ij} is a complex $N \times N$-matrix, the transformation properties of the measure is given by

$$d^N\eta = \det(M) d^N\eta', \tag{B.18}$$

in contrast to the „normal“ rule for transforming the integration measure for $\mathbb{R}^N$ with $\det(M)$ on the left-hand side. The determinant $\det(M)$ is referred to as *fermion determinant*.

B.5 Gaussian Integrals with Grassmann Numbers

Now we consider a Grassmann algebra with $2N$ generators $\eta_i, \bar\eta_i, i = 1, 2, \ldots, N$, where all these $2N$ generators anticommute with each other. Then we obtain for the simple Gaussian integral:

$$\begin{aligned}
\prod_{k=1}^{N} \int (d\eta_k\, d\bar\eta_k)\, e^{\sum_{i,j}\, \bar\eta_i M_{ij}\eta_j} &= \det(M) \prod_{k=1}^{N} \int (d\eta_k'\, d\bar\eta_k)\, e^{\sum_i\, \bar\eta_i\eta_i'} \\
&= \det(M) \prod_{k=1}^{N} \int (d\eta_k'\, d\bar\eta_k)\, (1 + \bar\eta_k\eta_k') \\
&= \det(M).
\end{aligned} \tag{B.19}$$

B.6 The Generating Functional

The *generating functional* contains Gaussian integrals over Grassman numbers. Gaussian integrals are needed to compute the generating functional

$$W[\Theta,\bar{\Theta}] = \prod_{i=1}^{N} \int (d\eta_i\, d\bar{\eta}_i)\, \exp\left\{ \sum_{k,l} \bar{\eta}_k M_{kl} \eta_l + \sum_k (\bar{\Theta}_k \eta_k + \bar{\eta}_k \Theta_k) \right\}. \quad \text{(B.20)}$$

First we rewrite the exponent in the following way (we use the Einstein summation convention for all indices):

$$\left(\bar{\eta}_i + \bar{\Theta}_j (M^{-1})_{ji}\right) M_{ik} \left(\eta_k + (M^{-1})_{kl}\Theta_l\right) - \bar{\Theta}_n (M^{-1})_{nm} \Theta_m. \quad \text{(B.21)}$$

After this we make a transformation of variables

$$\eta'_k = \eta_k + (M^{-1})_{kl}\Theta_l, \quad \text{(B.22)}$$

$$\bar{\eta}'_i = \bar{\eta}_i + \bar{\Theta}_j (M^{-1})_{ji}. \quad \text{(B.23)}$$

Because of (B.14, B.15, B.16) the integration measure remains invariant and the integral (B.20) reads

$$\begin{aligned} W[\Theta,\bar{\Theta}] &= e^{-\sum_{n,m} \bar{\Theta}_n M^{-1}_{nm} \Theta_m} \prod_i \int (d\eta'_i d\bar{\eta}'_i)\, e^{\sum_{k,l} \bar{\eta}'_k M^{-1}_{kl} \eta'_l} \\ &= \det(M) e^{-\sum_{n,m} \bar{\Theta}_n M^{-1}_{nm} \Theta_m}. \end{aligned} \quad \text{(B.24)}$$

For $\Theta = \bar{\Theta} = 0$, we obtain the previous result

$$W[0,0] = \det(M). \quad \text{(B.25)}$$

With the help of this functional we are now able to calculate so-called *n-point functions*:

$$\begin{aligned} \langle \eta_{i_1} \bar{\eta}_{j_1} \dots \eta_{i_n} \bar{\eta}_{j_n} \rangle &= \frac{1}{W[0,0]} \prod_{k=1}^{N} \int (d\eta_k d\bar{\eta}_k)\, \eta_{i_1} \bar{\eta}_{j_1} \dots \eta_{i_n} \bar{\eta}_{j_n} \exp\left(\sum_{l,m}^{N} \bar{\eta}_l M_{lm} \eta_m \right) \\ &= \frac{1}{W[0,0]} \prod_{k=1}^{N} \left(\frac{\partial}{\partial \bar{\Theta}_{j_k}}, \frac{\partial}{\partial \bar{\Theta}_{i_k}} \right) W[\Theta,\bar{\Theta}] \Big|_{\substack{\Theta=0 \\ \bar{\Theta}=0}} \\ &= (-1)^n \sum_{\mathcal{P}} \mathrm{sign}(\mathcal{P}) (M^{-1})_{i_1 j_{\mathcal{P}_1}} (M^{-1})_{i_2 j_{\mathcal{P}_2}} \dots (M^{-1})_{i_n j_{\mathcal{P}_n}}, \end{aligned} \quad \text{(B.26)}$$

where the sum runs over all permutations $\mathcal{P} \in \{1, 2, \dots, n\}$ and $\mathrm{sign}(\mathcal{P})$ determines the sign of the particular permutation.

We note that the formula (B.26) is also known as *Wick's theorem.*

C
Statistical Analysis

C.1 Statistical Errors

An introduction to error estimation and fitting techniques may be found in [152].

Performing N measurements on L quantities one obtains N data sets of the form

$$(x_i; y_i^n), \qquad i = 1, \ldots, L, \qquad n = 1, \ldots, N. \tag{C.1}$$

In our case we compute the correlator C_i^n on N gauge configurations for L timeslices t_i. Thus we get data sets $(t_i; C_i^n)$. The *sample mean value* of the quantities y_i^n is given by

$$\overline{y}_i = \frac{1}{N} \sum_{n=1}^{N} y_i^n \,. \tag{C.2}$$

For uncorrelated timeseries the *variance* reads

$$s_i^2 = \frac{1}{N-1} \sum_{n=1}^{N} (\overline{y}_i - y_i^n)^2 \tag{C.3}$$

$$= \frac{N}{N-1} (\overline{y_i^2} - \overline{y}_i^2) \,, \tag{C.4}$$

where s_i labels the standard deviation. According to the *central limit theorem* we obtain the statistical error

$$\sigma_i^2 = \frac{s_i^2}{N}[1 + O(\frac{1}{N})] \tag{C.5}$$

and our L quantities are then given by

$$(x_i, \overline{y}_i \pm \sigma_i). \tag{C.6}$$

Note that these formulae hold only if there is no correlation between the values y_i^n for different n.

C.2 Least Squares Fitting

Assuming Gaussian errors we use the method of *least squares fitting* to find a function $f(x_i, \boldsymbol{\theta})$ with parameters $\boldsymbol{\theta} = (\theta_1, \theta_2, \ldots, \theta_l)$ describing the data sets $(x_i, \overline{y}_i \pm \sigma_i)$ best. In the case of our correlator data sets $(t_i, \overline{C}_i)$ we have to fit a function $f(t; A, m) = Ae^{-mt}$ with parameters A, m. The starting point is the χ^2-functional:

$$\chi^2(\boldsymbol{\theta}) = \sum_{i,j=1}^{L} [\overline{y}_i - f(x_i, \boldsymbol{\theta})] S_{ij}^{-1} [\overline{y}_j - f(x_j, \boldsymbol{\theta})] \tag{C.7}$$

with the covariance matrix

$$S_{ij} = \frac{1}{N-1}(\overline{y_i y_j} - \overline{y}_i \overline{y}_j) \tag{C.8}$$

$$= \frac{1}{N(N-1)} \sum_{n=1}^{N} (y_i^n - \overline{y}_i)(y_j^n - \overline{y}_j), \tag{C.9}$$

that takes all correlations between the measured quantities into account.

For the case of uncorrelated measurements $\overline{y}_i$ the covariance matrix would reduce to $S_{ij} = \delta_{ij} \frac{s_i^2}{N}$ and (C.7) to

$$\chi^2(\boldsymbol{\theta}) = \sum_{i=1}^{L} \frac{(\overline{y}_i - f(x_i, \boldsymbol{\theta}))^2}{\sigma_i^2}. \tag{C.10}$$

However, we do not expect the propagators measured at different timeslices to be uncorrelated. Thus, we work with the general form (C.7) to find the optimal parameters. Therefore, we minimize the χ^2-functional with respect to the θ_k for the optimal values $\overline{\theta}_k$:

$$\left.\frac{\partial \chi^2}{\partial \theta_k}\right|_{\boldsymbol{\theta}=\bar{\boldsymbol{\theta}}} = 2 \sum_{i,j=1}^{L} \frac{\partial f(x_i, \bar{\boldsymbol{\theta}})}{\partial \theta_k} S_{ij}^{-1} [f(x_j, \bar{\boldsymbol{\theta}}) - \overline{y}_j] \stackrel{!}{=} 0\,, \tag{C.11}$$

which leads to a system of l equations.

To estimate the quality of the fit we have to consider the number of degrees of freedom (d.o.f.) ν, which is given by

$$\nu = L - l, \tag{C.12}$$

where l is the number of free parameters of the fit.

We assume, that the y_i^n are Gaussian distributed around $\overline{y}_i$ with a variance of σ_i^2:

$$P(y_i) = \frac{1}{\sqrt{2\pi}\sigma_i} e^{-\frac{(\overline{y}_i - y_i)^2}{2\sigma_i^2}}. \tag{C.13}$$

Then, for large ν, the expectation value of χ^2 reads

$$\overline{\chi^2} = \nu. \tag{C.14}$$

Thus a reliable fit should satisfy

$$\chi^2/d.o.f. = \frac{\chi^2}{\nu} \approx 1. \tag{C.15}$$

We note that if the number of measurements N (C.1) grows arbitrarily large, the validity of (C.13) holds and the function $f(x_i, \boldsymbol{\theta})$ was chosen right, then the ensemble average of the $\boldsymbol{\theta}$ gives the sample average of y_i by

$$\overline{y}_i = f(x_i, \overline{\boldsymbol{\theta}}). \tag{C.16}$$

In this case we obtain for the ensemble average of our fit parameters

$$\theta_k = \overline{\theta}_k \pm \sqrt{2(H^{-1})_{kk}} \qquad \forall\, k = 1, \ldots, l\ , \tag{C.17}$$

where H_{km} is the so-called *Hessian*:

$$H_{km} = \left.\frac{\partial^2 \chi^2}{\partial\theta_k \partial\theta_m}\right|_{\boldsymbol{\theta}=\bar{\boldsymbol{\theta}}}. \tag{C.18}$$

In most cases however, statistics are much to small and one has to calculate *secondary quantities*[1] separately, as we do in the next section.

[1]Secondary quantities are functional characteristics of directly measured averages of observables. These so called primary averages are the $\overline{y}_i$ in our calculations.

C.3 The Jackknife Method

For manageably large samples the *Jackknife method* is a useful way to estimate the errors of secondary observables. An example are fit parameters that we obtain by fitting correlation functions.

For a given set of data points $y_n,\ n = 1, \ldots, N$ with the sample average of equation (C.2), the best estimator for a secondary quantity $\boldsymbol{\theta}$ can be obtained by

$$\overline{\boldsymbol{\theta}} = \boldsymbol{\theta}(\overline{y}). \tag{C.19}$$

To estimate the error of this quantity $\boldsymbol{\theta}$ one creates N *Jackknife subsamples* $y_{(J)n}$ such that each subsample includes $N-1$ data points. In each case the nth data point is omitted. The sample mean value for each subsample is then given by

$$\overline{y}_{(J)n} = \frac{1}{N-1} \sum_{\substack{k=1 \\ k \neq n}}^{N} y_k. \tag{C.20}$$

Thereafter one calculates for each subsample, just as well as for the original sample, N *Jackknife estimators* of the secondary quantities

$$\boldsymbol{\theta}_{(J)n} = \boldsymbol{\theta}(y_{(J)n}) \tag{C.21}$$

which have the common sample average

$$\overline{\boldsymbol{\theta}_{(J)}} = \frac{1}{N} \sum_{n=1}^{N} \boldsymbol{\theta}_{(J)n}. \tag{C.22}$$

Therefrom one determines the variance of the jackknife estimators

$$\sigma^2_{(J)} = \frac{N-1}{N} \sum_{n=1}^{N} \left(\boldsymbol{\theta}_{(J)n} - \overline{\boldsymbol{\theta}_{(J)}} \right)^2. \tag{C.23}$$

and is finally left with the estimator of the ensemble average

$$\boldsymbol{\theta} = \overline{\boldsymbol{\theta}} \pm \sigma_{(J)}. \tag{C.24}$$

D
Result Plots

D.1 $\mathcal{BB}$ Potentials

In this section we present the intermeson potentials $V_{\mathcal{B}_1\mathcal{B}_2}(r)$ that were not discussed in section 7.2.3 and section 7.2.4 respectively. From figure D.1 to figure D.7 we display the operator combinations $\mathbb{1} \otimes \mathbb{1}$, $\gamma_5 \otimes \mathbb{1}$, $\gamma_5 \otimes \nabla_i\gamma_i$, $\gamma_5 \otimes P_\perp$, $\gamma_5 \otimes P_\parallel$, $\nabla_i\gamma_i \otimes P_\perp$ and $\nabla_i\gamma_i \otimes P_\parallel$ for isospin $I = 0$ and from figure D.8 to figure D.14 the operator combinations $\gamma_5 \otimes \gamma_5$, $\mathbb{1} \otimes \mathbb{1}$, $\gamma_5 \otimes \nabla_i\gamma_i$, $\gamma_5 \otimes P_\perp$, $\gamma_5 \otimes P_\parallel$, $\nabla_i\gamma_i \otimes P_\perp$ and $\nabla_i\gamma_i \otimes P_\parallel$ for isospin $I = 1$.

The layout is the same as in figure 7.5 of section 7.2.3 for instance. For the operator combinations where we performed the spin projection of the static-light meson spins we display the intermeson potentials on our coarse lattice for $S_z = 0$ in the upper plot and for $S_z = 1$ in the intermediate plot, while the lower plot shows our fine lattice results where both spin channels mix. For the combinations where we coupled a S or a P_- wave with the P_+ wave we did not perform the spin projection. Thus the different representations mix and we are not able to distinguish between Σ and Π states. In these cases the upper plot displays the coarse lattice potentials and the lower plot those from the fine lattice. For all plots we use black circles, red squares and blue triangles to mark the ground, the first excited and the second excited states respectively. The x-axis displays the separation r in fm and the y-axis the energy levels, both in

lattice units as well as in MeV.

The question of attraction or repulsion was already answered in detail in section 7.2.5 and 7.2.6. So we use this paragraph to discuss the ambiguity of first and second excited intermeson potentials with reference to some examples.

In figure D.2 we display the isoscalar channel for the operator combination $\gamma_5 \otimes \mathbb{1}$. The intermeson potential for the $S_z = 0$ ground state (Σ_u^-) is attractive at short distances and repulsive of the order of 50 MeV at intermediate distances. In case of the first excited level ($\Sigma_u^{-\prime}$) there are two possibilities to determine the potential. Either by subtracting the sum of a radially excited $\frac{1}{2}^{+\prime}$ state (γ_5) and a $\frac{1}{2}^-$ ($\mathbb{1}$) ground state or the reversed case, namely the sum of $\frac{1}{2}^+$ and $\frac{1}{2}^{-\prime}$. The latter assignment is energetically favorable and agrees with the repulsive ground state findings. For these reasons we have chosen this classification to represent the first excited state. Using the same arguments we appointed the second excited state of this channel as well as the excited states for spin $S_z = 1$ of the same operator combination.

The next example we want to address is the isosinglet $\gamma_5 \otimes P_\perp$ channel on the coarse lattice which is shown in the upper plot of figure D.4. For the first excited state $\Sigma_g^{+\prime}$ we have chosen the representation ($\frac{1}{2}^+ + \frac{3}{2}^{-\prime}$) since it is energetically favorable and approaches the expected $r \to \infty$ limit at intermediate distances. For the second excitation $\Sigma_g^{+\prime\prime}$ we find three levels. The combination $\frac{1}{2}^+$ plus $\frac{3}{2}^{-\prime\prime}$ would be energetically favorable. However, in contrast to ground and first excited state this representation would be repulsive of the order of 70 MeV. Thus, we see no clear evidence that our creation operator should overlap with this assignment. Remaining are the combinations ($\frac{1}{2}^{+\prime} + \frac{3}{2}^{-\prime}$) and ($\frac{1}{2}^{+\prime\prime} + \frac{3}{2}^-$). The first assignment would be very attractive at intermediate distances while the latter combination has the expected infinite distance limit and is energetically favorable. Therefore we choose this combination to represent the second excited state.

Finally, we look at the isovector $\gamma_5 \otimes \gamma_5$ channel on the coarse lattice in figure D.8. In both spin channels $S_z = 0$ and $S_z = 1$ the sum of a radial excited $\frac{1}{2}^{+\prime\prime}$ and a $\frac{1}{2}^+$ static-light would be the energetically most favorable second excited state. However, this representation is very repulsive of the order of 180 MeV and does not agree with ground and first excited states. Therefore, we see no evidence for this assignment and choose the combination ($\frac{1}{2}^{+\prime} + \frac{1}{2}^{+\prime}$).

In general we choose the energetically favored combination, except there is no evidence that our creation operator overlaps with this assignment, like in the last example.

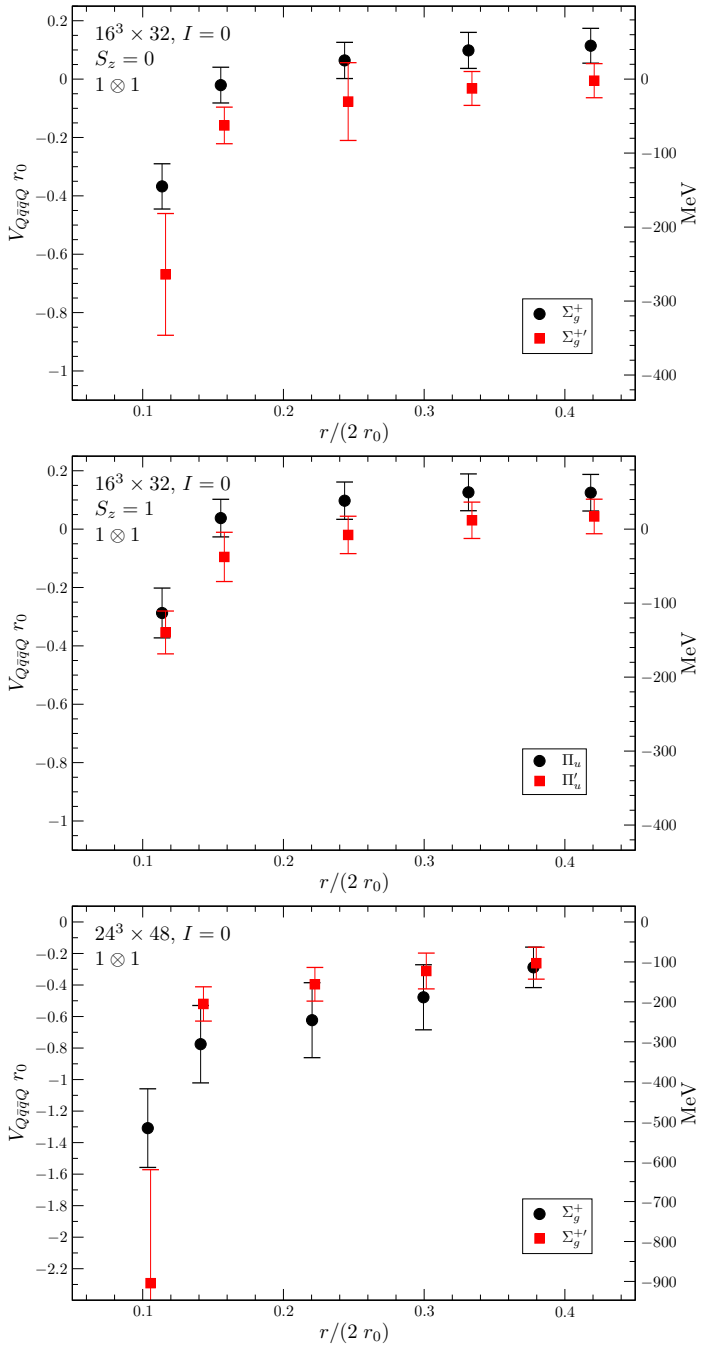

Figure D.1: The intermeson potential $V_{\mathcal{B}_1\mathcal{B}_2}(r)$ in the isoscalar channel for the combination $\mathbb{1} \otimes \mathbb{1}$. From top to bottom we show the coarse lattice for $S_z = 0$, $S_z = 1$ and the fine lattice. Black circles, red squares and blue triangles mark the ground, the first and the second excited states respectively. Full symbols indicate the chosen energy levels.

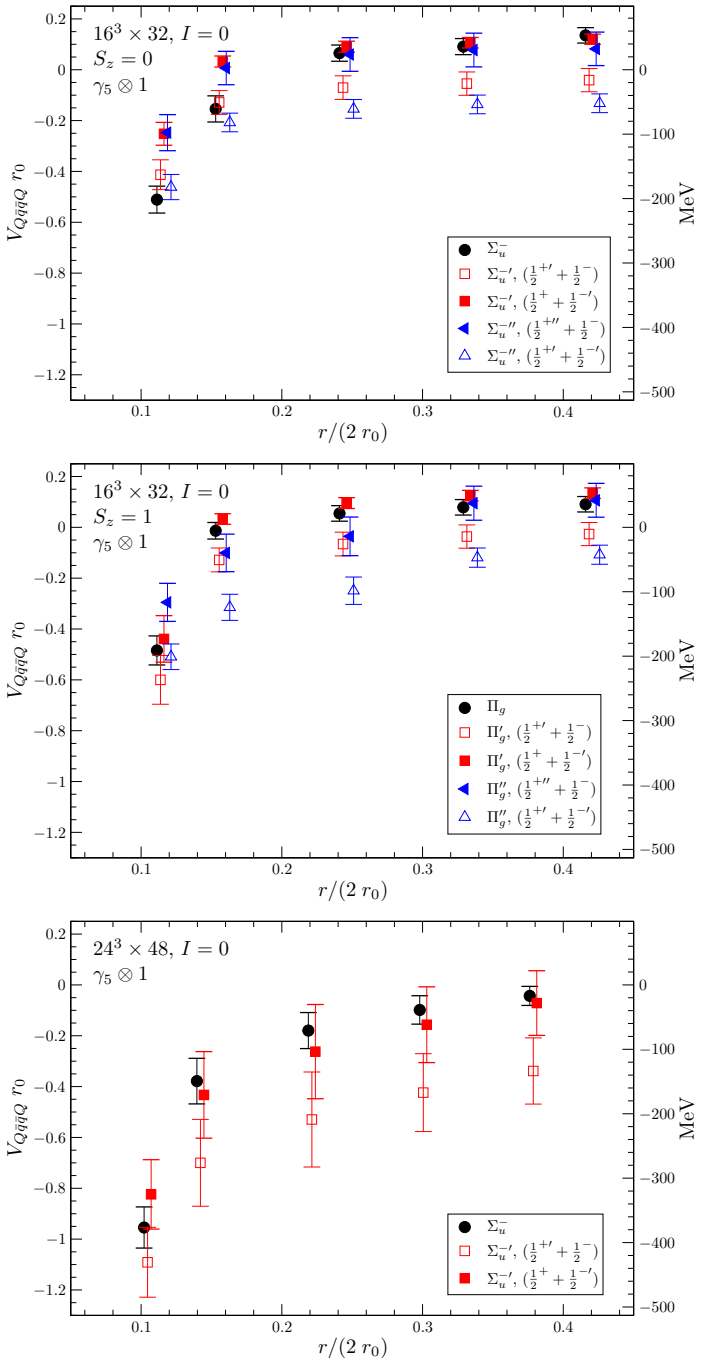

Figure D.2: The intermeson potential $V_{\mathcal{B}_1\mathcal{B}_2}(r)$ in the isoscalar channel for the combination $\gamma_5 \otimes \mathbb{1}$. From top to bottom we show the coarse lattice for $S_z = 0$, $S_z = 1$ and the fine lattice. Black circles, red squares and blue triangles mark the ground, the first and the second excited states respectively. Full symbols indicate the chosen energy levels.

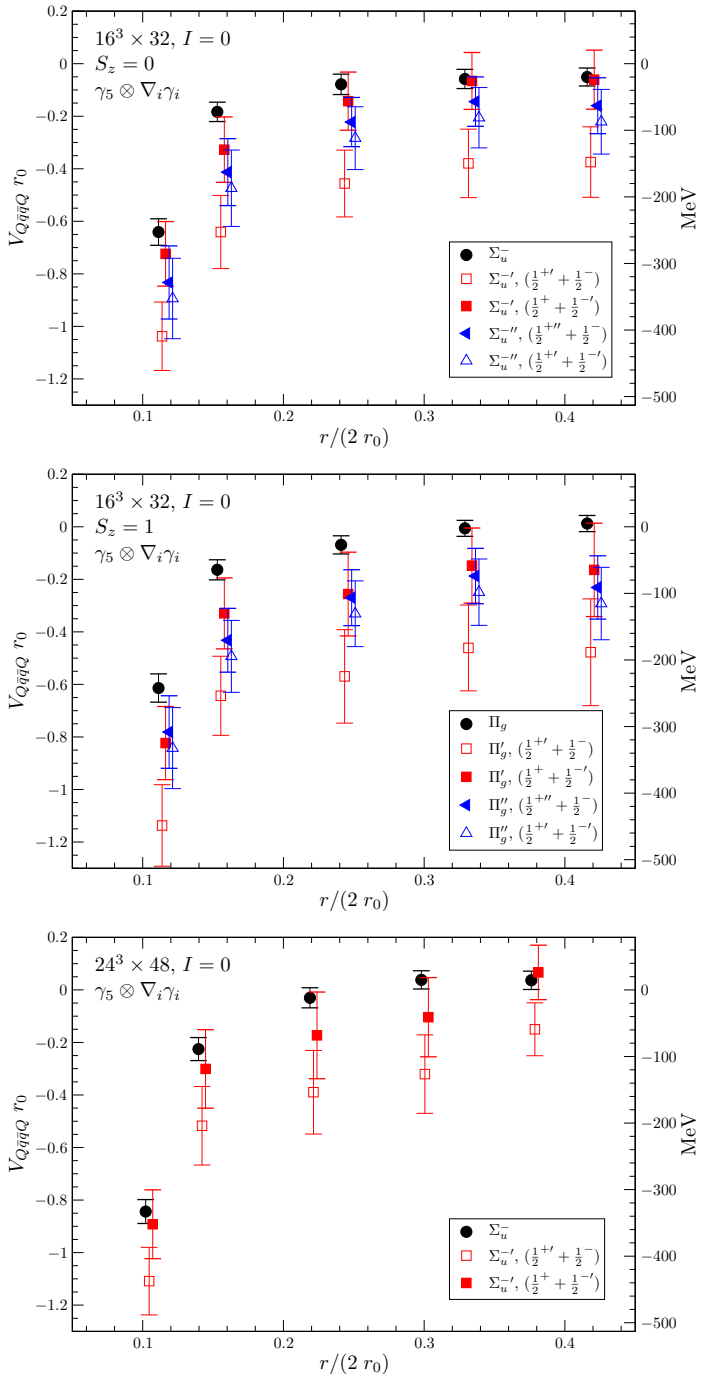

Figure D.3: The intermeson potential $V_{\mathcal{B}_1\mathcal{B}_2}(r)$ in the isoscalar channel for the combination $\gamma_5 \otimes \nabla_i \gamma_i$. From top to bottom we show the coarse lattice for $S_z = 0$, $S_z = 1$ and the fine lattice. Black circles, red squares and blue triangles mark the ground, the first and the second excited states respectively. Full symbols indicate the chosen energy levels.

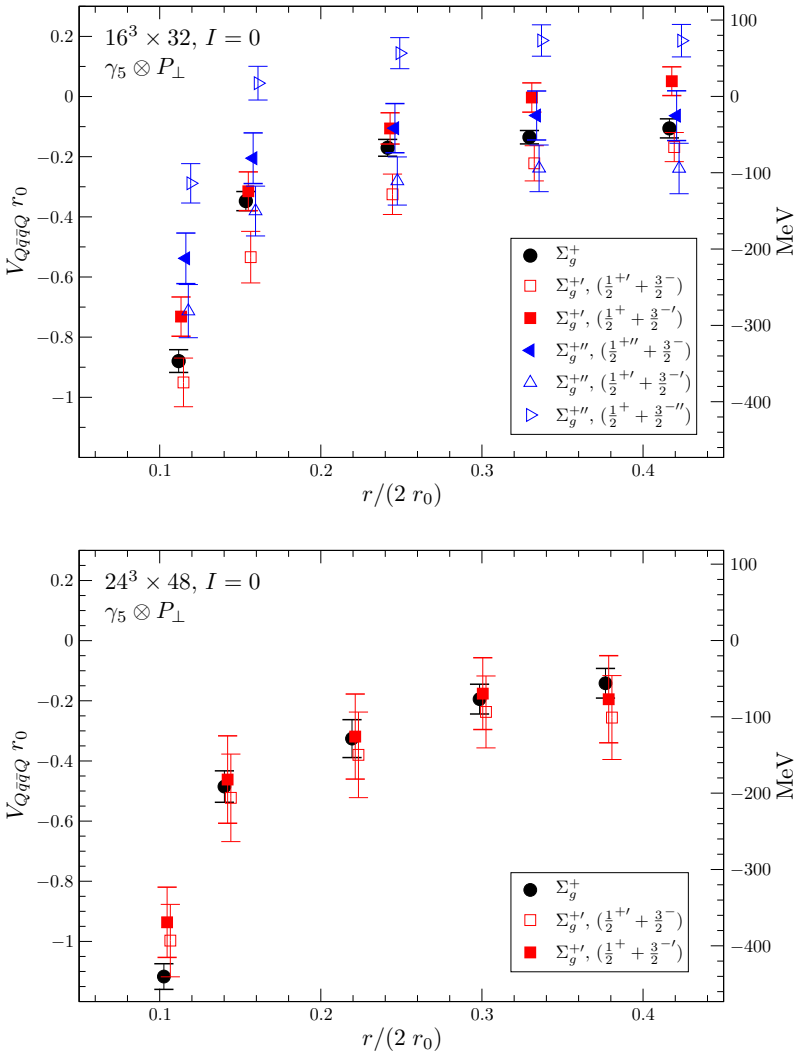

Figure D.4: The intermeson potential $V_{\mathcal{B}_1\mathcal{B}_2}(r)$ in the isoscalar channel for the combination $\gamma_5 \otimes P_\perp$. From top to bottom we show the coarse lattice for $S_z = 0$, $S_z = 1$ and the fine lattice. Black circles, red squares and blue triangles mark the ground, the first and the second excited states respectively. Full symbols indicate the chosen energy levels.

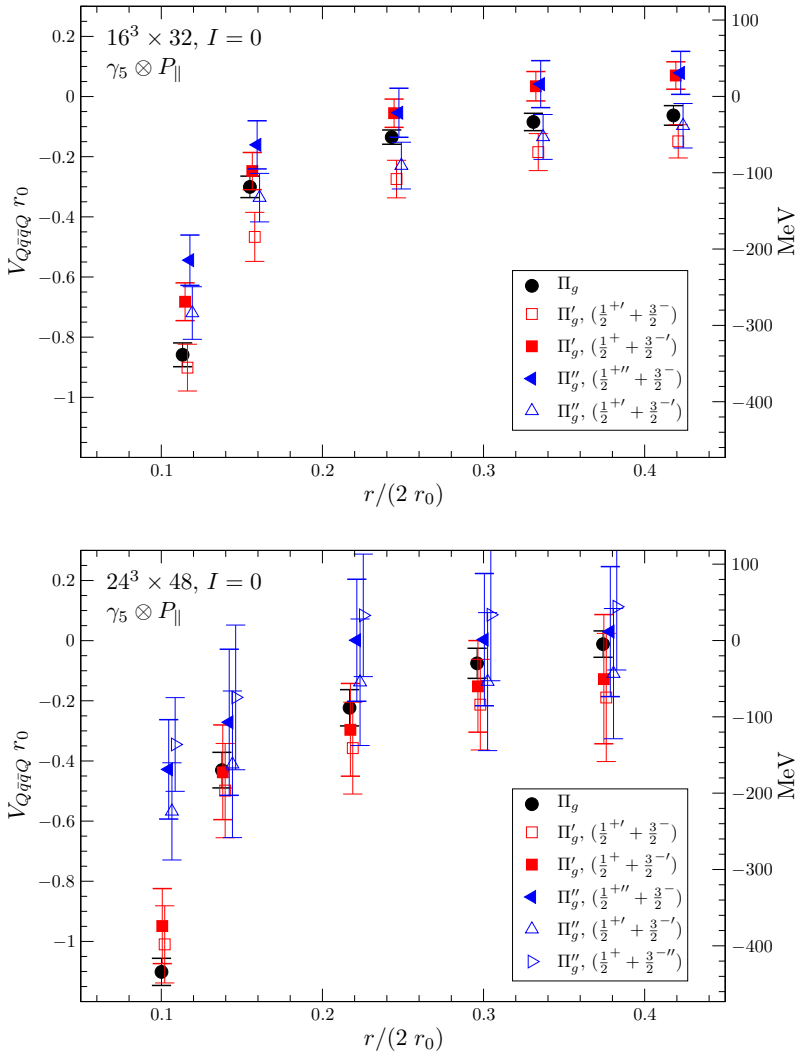

Figure D.5: The intermeson potential $V_{\mathcal{B}_1\mathcal{B}_2}(r)$ in the isoscalar channel for the combination $\gamma_5 \otimes P_\parallel$. From top to bottom we show the coarse lattice for $S_z = 0$, $S_z = 1$ and the fine lattice. Black circles, red squares and blue triangles mark the ground, the first and the second excited states respectively. Full symbols indicate the chosen energy levels.

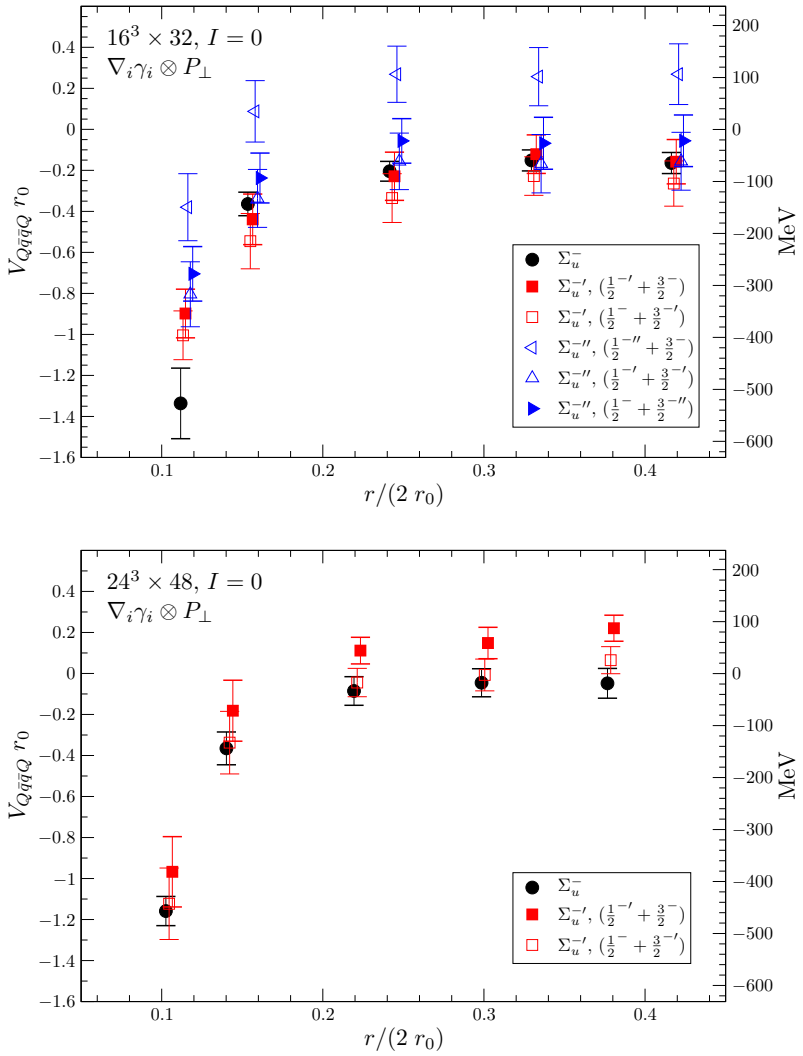

Figure D.6: The intermeson potential $V_{\mathcal{B}_1\mathcal{B}_2}(r)$ in the isoscalar channel for the combination $\nabla_i \gamma_i \otimes P_\perp$. From top to bottom we show the coarse lattice for $S_z = 0$, $S_z = 1$ and the fine lattice. Black circles, red squares and blue triangles mark the ground, the first and the second excited states respectively. Full symbols indicate the chosen energy levels.

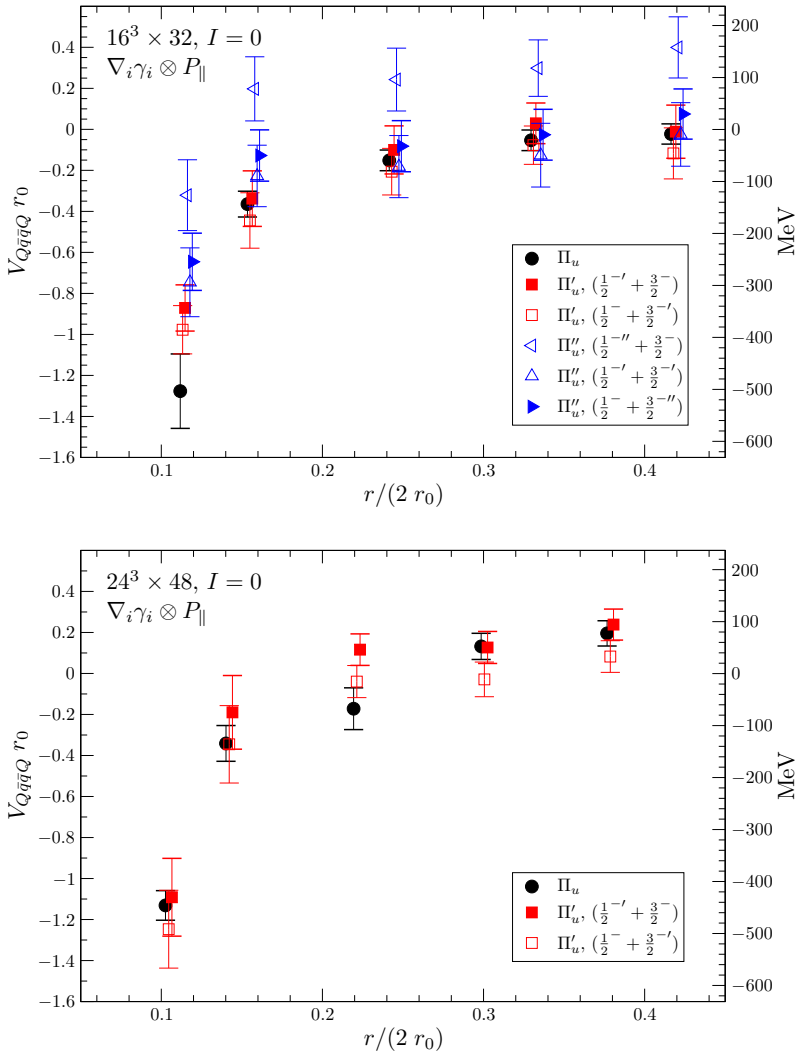

Figure D.7: The intermeson potential $V_{\mathcal{B}_1\mathcal{B}_2}(r)$ in the isoscalar channel for the combination $\nabla_i \gamma_i \otimes P_\parallel$. From top to bottom we show the coarse lattice for $S_z = 0$, $S_z = 1$ and the fine lattice. Black circles, red squares and blue triangles mark the ground, the first and the second excited states respectively. Full symbols indicate the chosen energy levels.

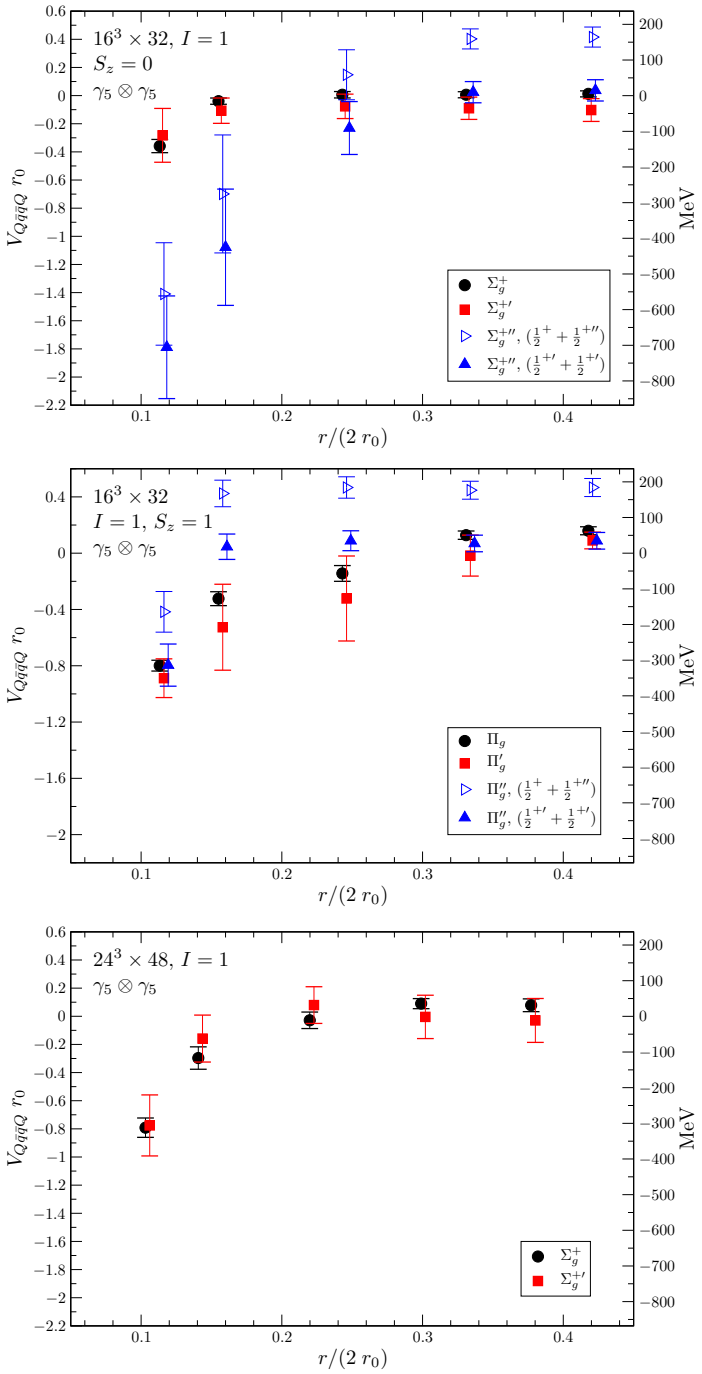

Figure D.8: The intermeson potential $V_{\mathcal{B}_1\mathcal{B}_2}(r)$ in the isovector channel for the combination $\gamma_5 \otimes \gamma_5$. From top to bottom we show the coarse lattice for $S_z = 0$, $S_z = 1$ and the fine lattice. Black circles, red squares and blue triangles mark the ground, the first and the second excited states respectively. Full symbols indicate the chosen energy levels.

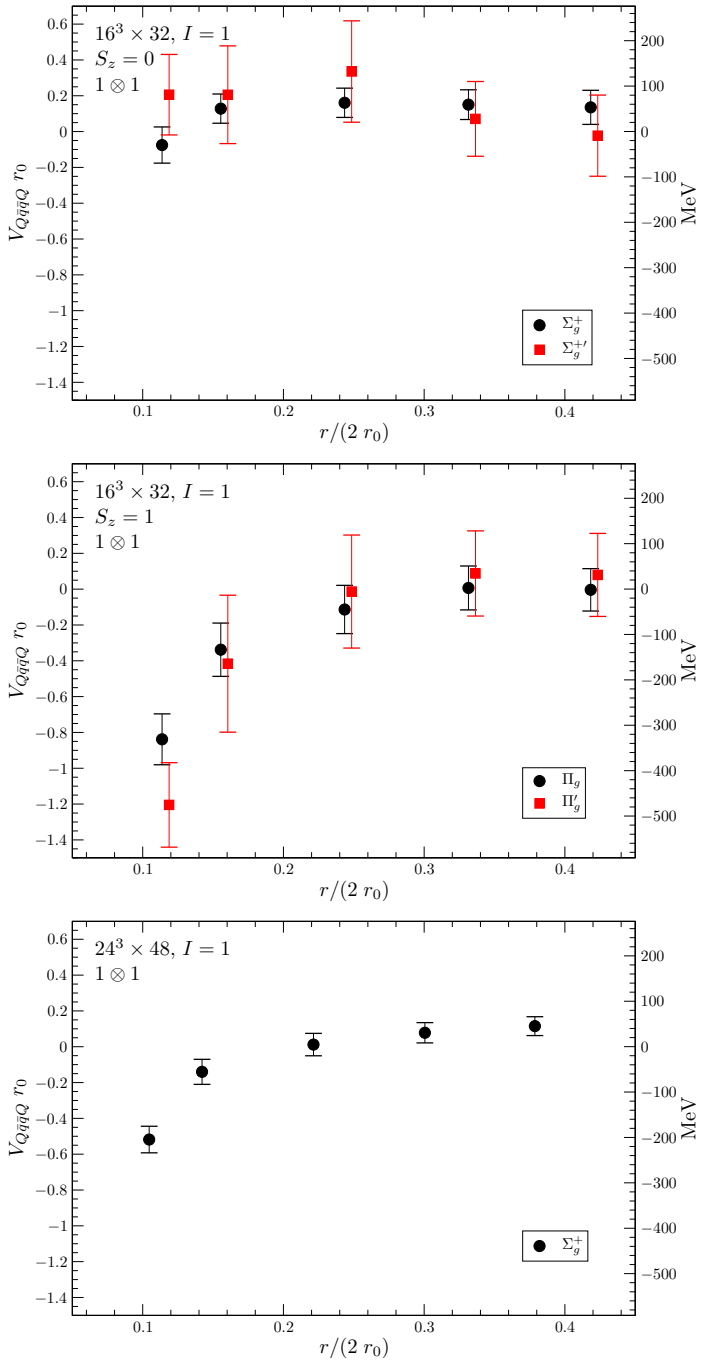

Figure D.9: The intermeson potential $V_{\mathcal{B}_1\mathcal{B}_2}(r)$ in the isovector channel for the combination $\mathbb{1} \otimes \mathbb{1}$. From top to bottom we show the coarse lattice for $S_z = 0$, $S_z = 1$ and the fine lattice. Black circles, red squares and blue triangles mark the ground, the first and the second excited states respectively. Full symbols indicate the chosen energy levels.

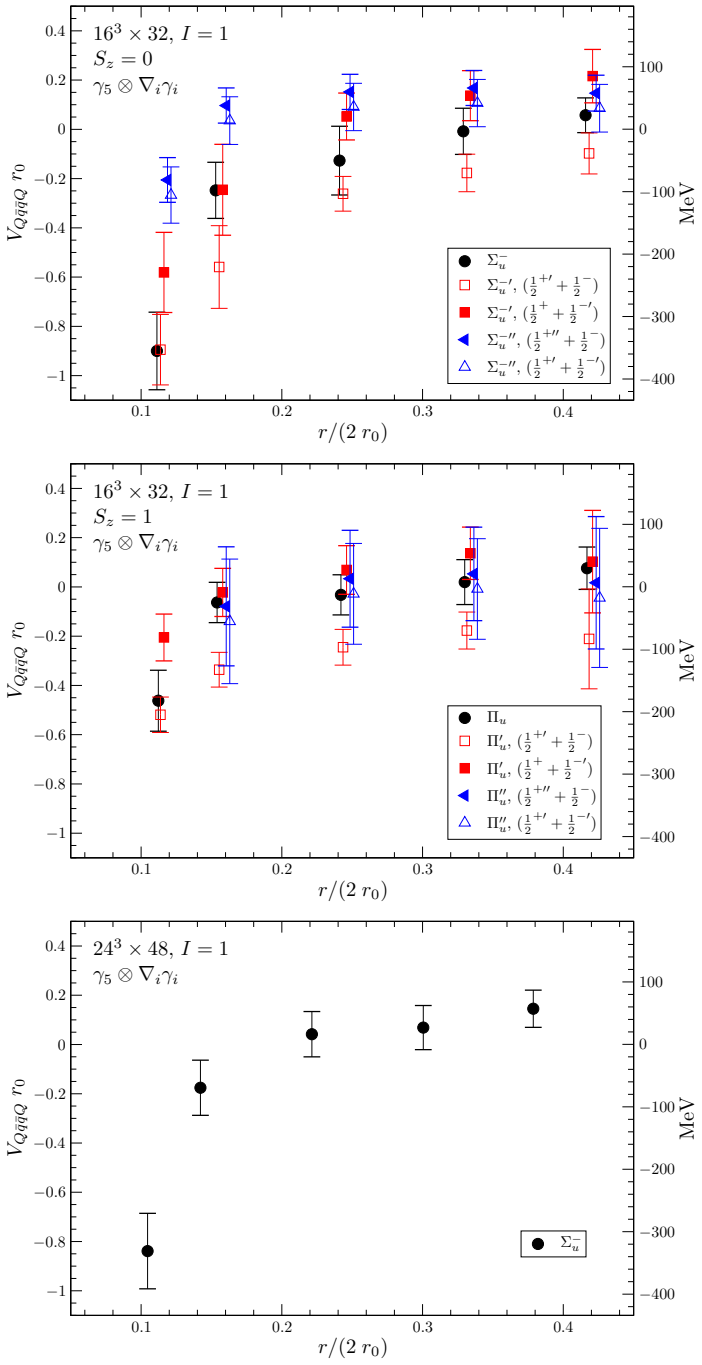

Figure D.10: The intermeson potential $V_{\mathcal{B}_1\mathcal{B}_2}(r)$ in the isovector channel for the combination $\gamma_5 \otimes \nabla_i \gamma_i$. From top to bottom we show the coarse lattice for $S_z = 0$, $S_z = 1$ and the fine lattice. Black circles, red squares and blue triangles mark the ground, the first and the second excited states respectively. Full symbols indicate the chosen energy levels.

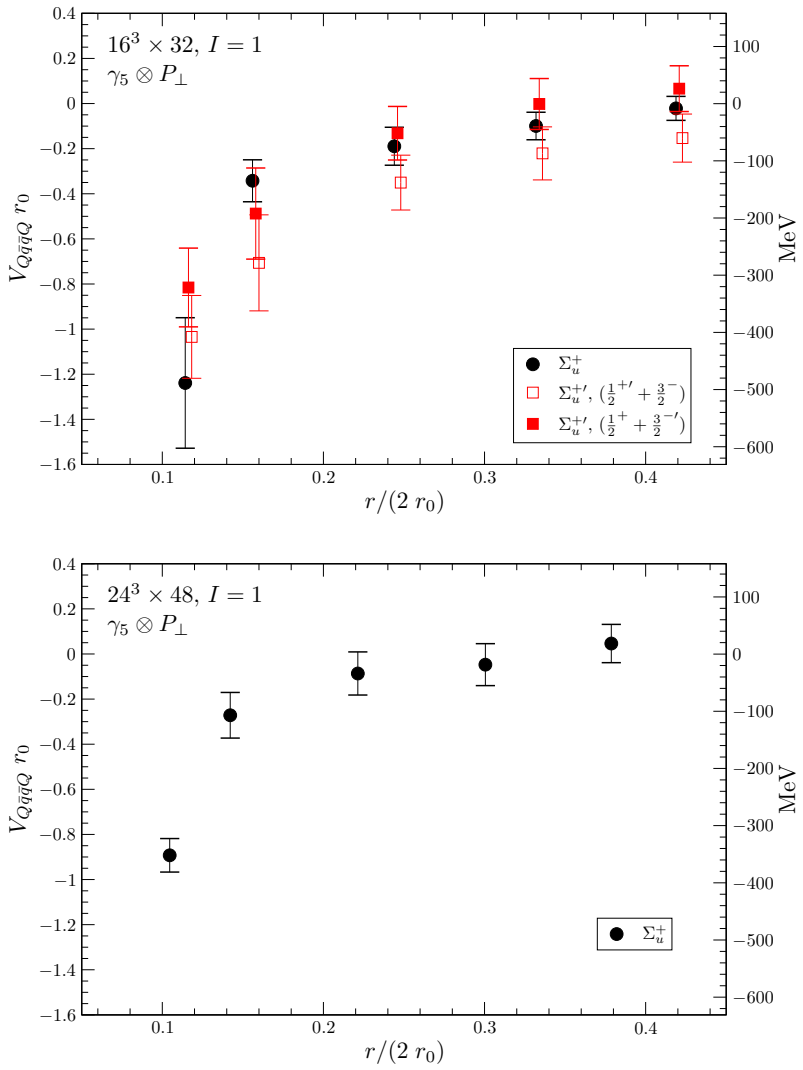

Figure D.11: The intermeson potential $V_{\mathcal{B}_1\mathcal{B}_2}(r)$ in the isovector channel for the combination $\gamma_5 \otimes P_\perp$. From top to bottom we show the coarse lattice for $S_z = 0$, $S_z = 1$ and the fine lattice. Black circles, red squares and blue triangles mark the ground, the first and the second excited states respectively. Full symbols indicate the chosen energy levels.

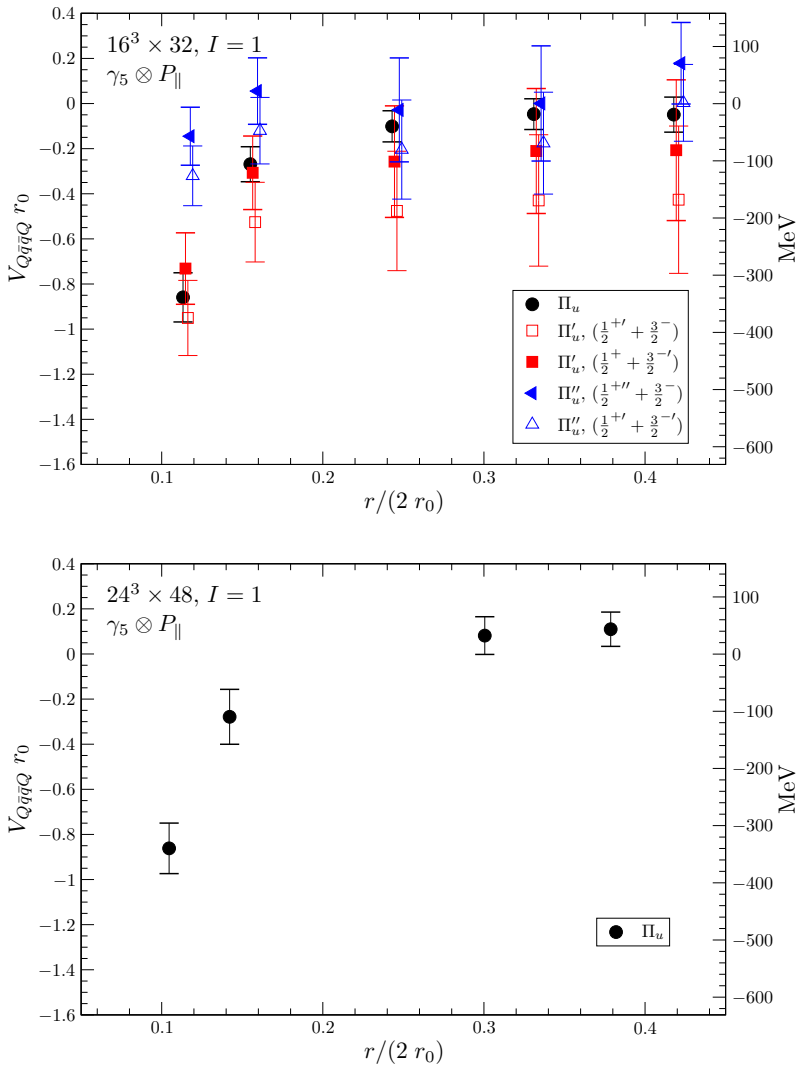

Figure D.12: The intermeson potential $V_{\mathcal{B}_1\mathcal{B}_2}(r)$ in the isovector channel for the combination $\gamma_5 \otimes P_\parallel$. From top to bottom we show the coarse lattice for $S_z = 0$, $S_z = 1$ and the fine lattice. Black circles, red squares and blue triangles mark the ground, the first and the second excited states respectively. Full symbols indicate the chosen energy levels.

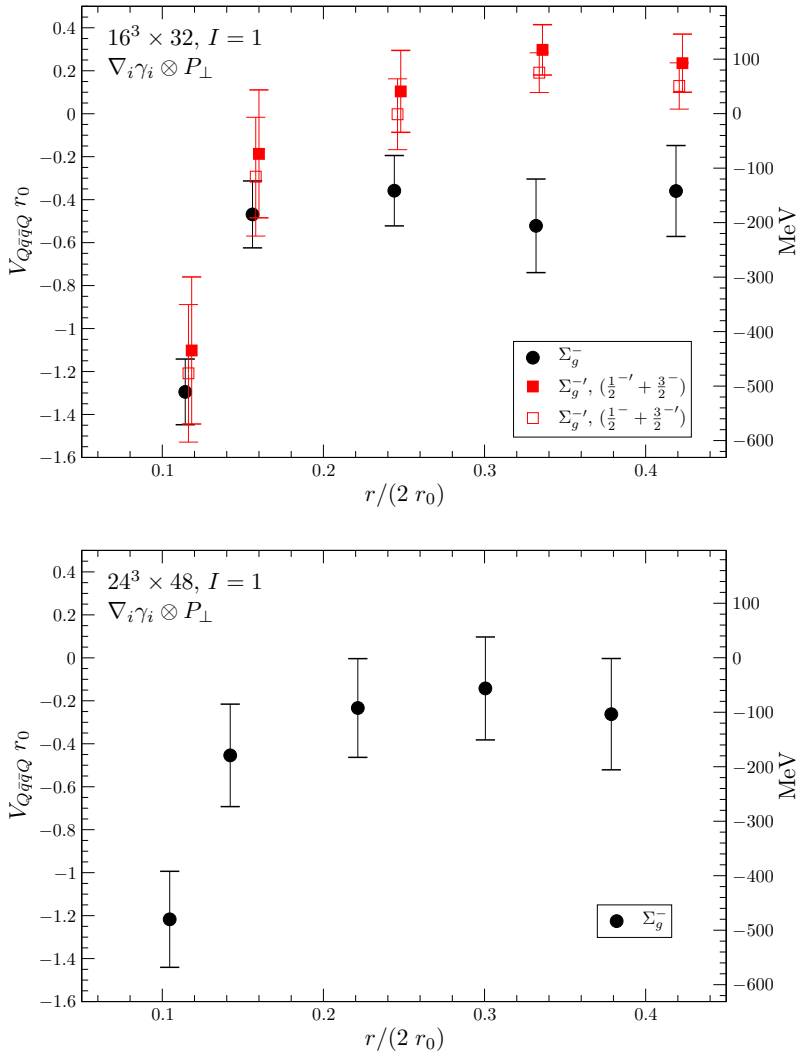

Figure D.13: The intermeson potential $V_{\mathcal{B}_1\mathcal{B}_2}(r)$ in the isovector channel for the combination $\nabla_i \gamma_i \otimes P_\perp$. From top to bottom we show the coarse lattice for $S_z = 0$, $S_z = 1$ and the fine lattice. Black circles, red squares and blue triangles mark the ground, the first and the second excited states respectively. Full symbols indicate the chosen energy levels.

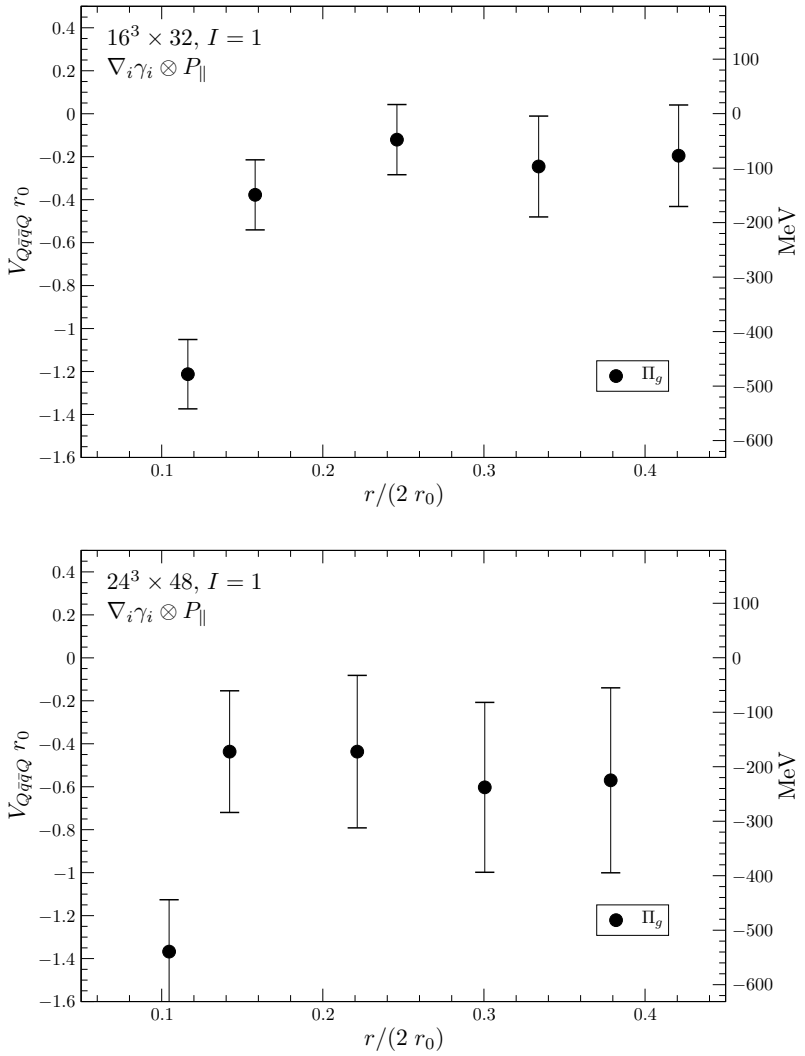

Figure D.14: The intermeson potential $V_{\mathcal{B}_1\mathcal{B}_2}(r)$ in the isovector channel for the combination $\nabla_i \gamma_i \otimes P_\parallel$. From top to bottom we show the coarse lattice for $S_z = 0$, $S_z = 1$ and the fine lattice. Black circles, red squares and blue triangles mark the ground, the first and the second excited states respectively. Full symbols indicate the chosen energy levels.

D.2 $\mathcal{B}\overline{\mathcal{B}}$ Meson-Antimeson States

In this section we present the $\mathcal{B}\overline{\mathcal{B}}$ meson-antimeson energy levels for the operator combinations that were not shown in section 7.3.2 and section 7.3.3 respectively. From figure D.15 to figure D.21 we display the operator combinations $\mathbb{1} \otimes \mathbb{1}$, $\gamma_5 \otimes \mathbb{1}$, $\gamma_5 \otimes \nabla_i \gamma_i$, $\gamma_5 \otimes P_\perp$, $\gamma_5 \otimes P_\parallel$, $\nabla_i \gamma_i \otimes P_\perp$ and $\nabla_i \gamma_i \otimes P_\parallel$ in the isovector $I = 1$ channel and in figure D.22 the operator combinations $\mathbb{1} \otimes \mathbb{1}$ and $\gamma_5 \otimes \nabla_i \gamma_i$ in the isosinglet $I = 0$ channel where we projected the static-light meson spins to $S_z = 1$.

The layout for the following figures is the same as in figure 7.20 of section 7.3.2 for instance. We display the meson-antimeson masses as a function of the static quark-antiquark separation r in fm. Ground states are labeled as black circles, first excited states as red squares and second excited states as blue diamonds. For very large distances, the expected limit is given by the sum of the corresponding static-light $\mathcal{B}$ mesons. These are represented by the solid lines, where their widths indicate the jackknife errors. In addition green triangles denote the static quark potential $V_{Q\overline{Q}}$ plus various light mesons that have the appropriate quantum numbers. In cases where we performed the spin projection we display the $\mathcal{B}\overline{\mathcal{B}}$ energy levels on our coarse lattice for $S_z = 0$ in the upper plot and for $S_z = 1$ in the intermediate plot, while the lower plot shows our fine lattice results. In the other cases where we did not perform the spin projection the upper plot of the figures shows the coarse lattice results and the lower plot those from the fine lattice.

In general we find the expected $r \to \infty$ limit in all channels for the observed operator combinations at intermediate distances of $r \approx 0.4$ fm. At short distances however, it is hard to decide whether we see substantial attractive forces between the static-light meson-antimeson pairs or bound states between the static quark potential and additional light mesons. This holds for all the following operator combinations. The reason is, that states consisting of the $Q\overline{Q}$ static potential and appropriate scalar mesons have the same quantum numbers as the $\mathcal{B}\overline{\mathcal{B}}$ states.

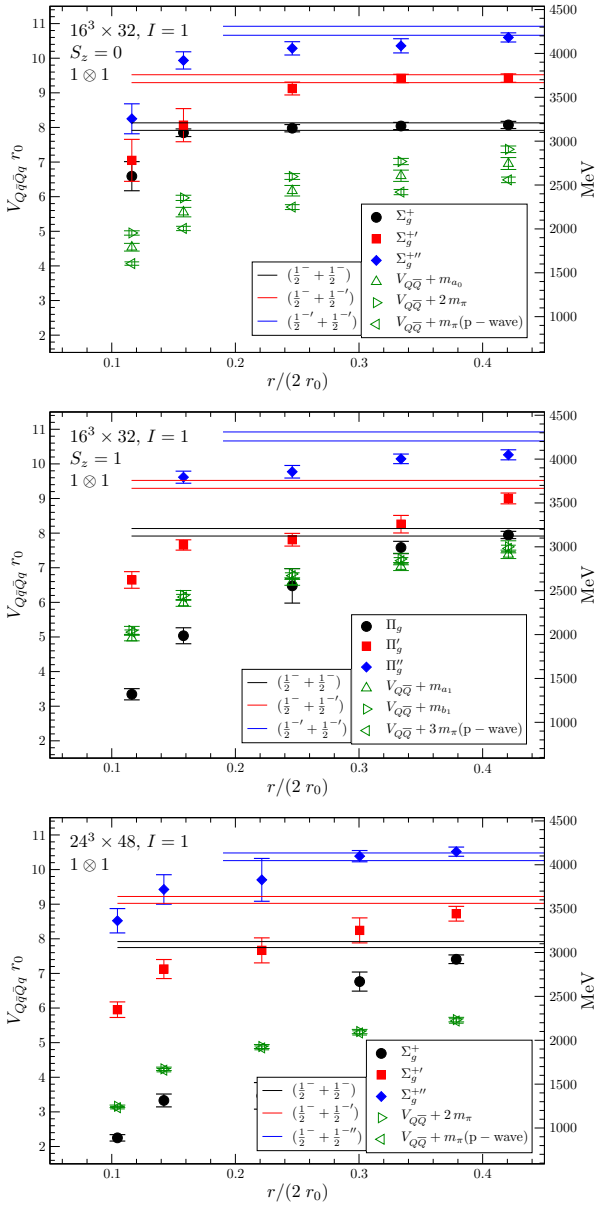

Figure D.15: The $\mathcal{B}\overline{\mathcal{B}}$ meson-antimeson masses for the combination $\mathbb{1} \otimes \mathbb{1}$ in the isovector channel. From top to bottom we show the coarse lattice for $S_z = 0$, $S_z = 1$ and the fine lattice. Black circles, red squares and blue diamonds mark the ground, the first and the second excited states respectively while the green triangles label the static $Q\overline{Q}$ potential plus various light mesons. The horizontal lines represent the sum of the corresponding static-light $\mathcal{B}$ mesons, the expected $r \to \infty$ limit, where their widths indicate the jackknife errors.

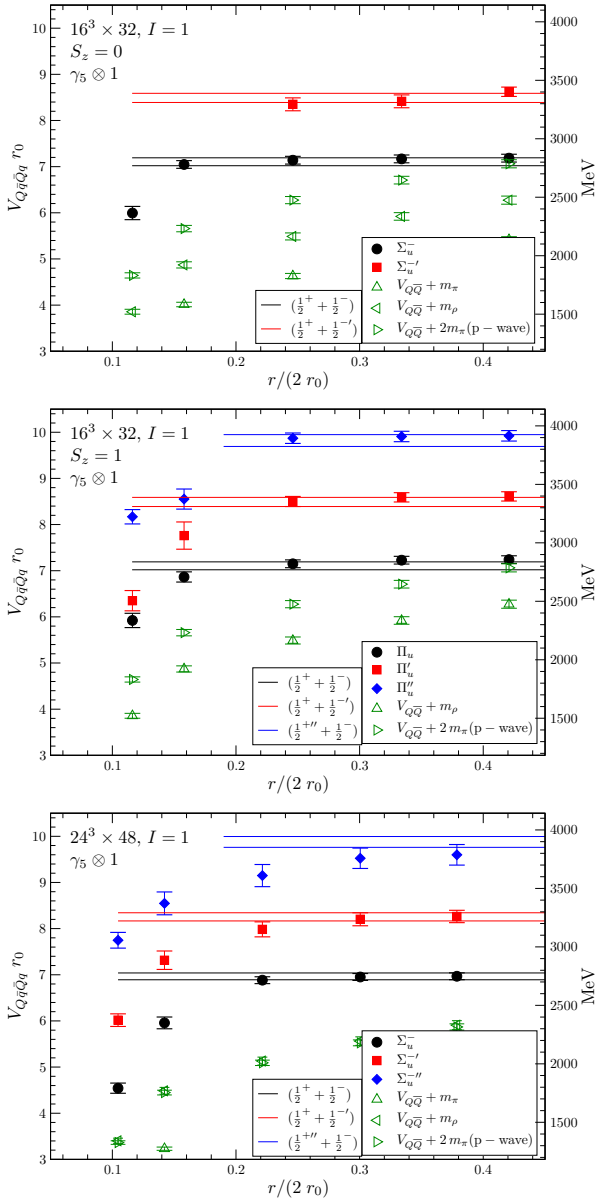

Figure D.16: The $\mathcal{B}\overline{\mathcal{B}}$ meson-antimeson masses for the combination $\gamma_5 \otimes \mathbb{1}$ in the isovector channel. From top to bottom we show the coarse lattice for $S_z = 0$, $S_z = 1$ and the fine lattice. Black circles, red squares and blue diamonds mark the ground, the first and the second excited states respectively while the green triangles label the static $Q\overline{Q}$ potential plus various light mesons. The horizontal lines represent the sum of the corresponding static-light $\mathcal{B}$ mesons, the expected $r \to \infty$ limit, where their widths indicate the jackknife errors.

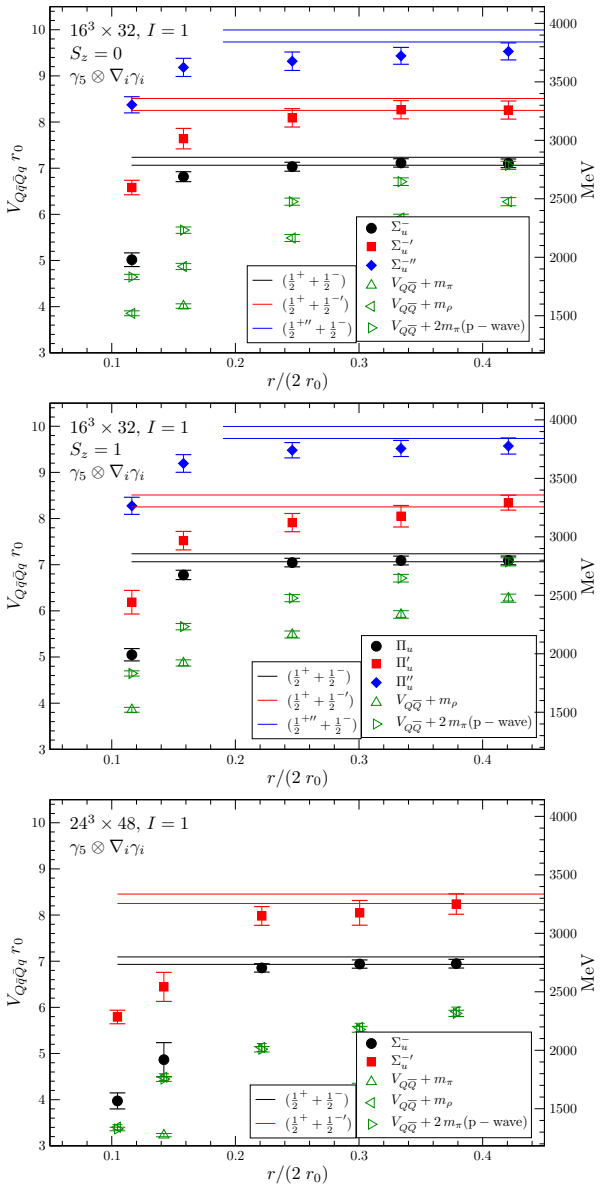

Figure D.17: The $\mathcal{B}\overline{\mathcal{B}}$ meson-antimeson masses for the combination $\gamma_5 \otimes \nabla_i \gamma_i$ in the isovector channel. From top to bottom we show the coarse lattice for $S_z = 0$, $S_z = 1$ and the fine lattice. Black circles, red squares and blue diamonds mark the ground, the first and the second excited states respectively while the green triangles label the static $Q\overline{Q}$ potential plus various light mesons. The horizontal lines represent the sum of the corresponding static-light $\mathcal{B}$ mesons, the expected $r \to \infty$ limit, where their widths indicate the jackknife errors.

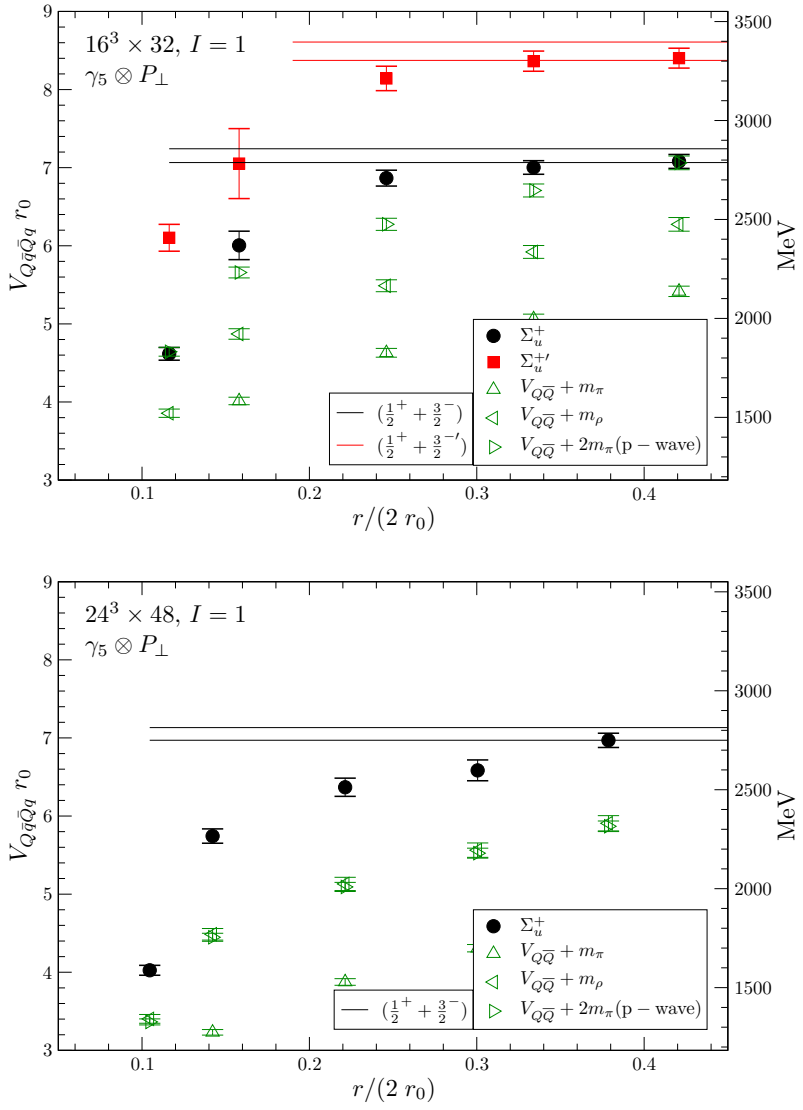

Figure D.18: The $\mathcal{B}\overline{\mathcal{B}}$ meson-antimeson masses for the combination $\gamma_5 \otimes P_\perp$ in the isovector channel. From top to bottom we show the coarse lattice for $S_z = 0$, $S_z = 1$ and the fine lattice. Black circles, red squares and blue diamonds mark the ground, the first and the second excited states respectively while the green triangles label the static $Q\overline{Q}$ potential plus various light mesons. The horizontal lines represent the sum of the corresponding static-light $\mathcal{B}$ mesons, the expected $r \to \infty$ limit, where their widths indicate the jackknife errors.

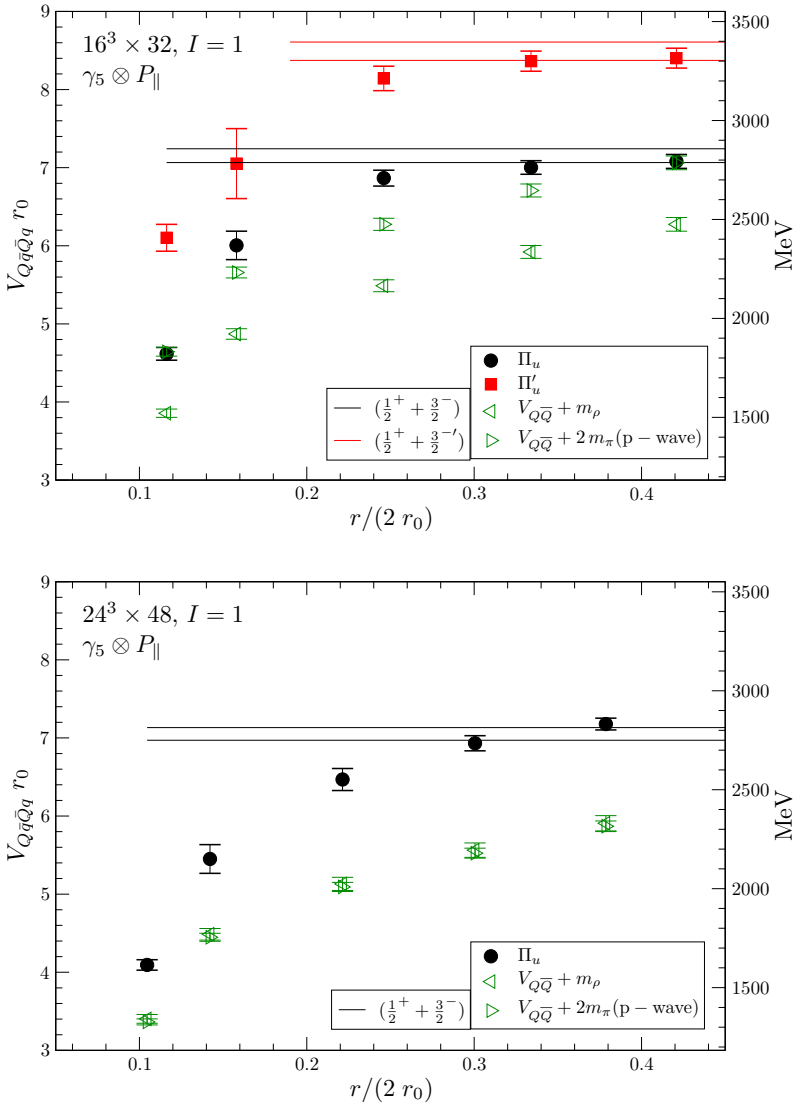

Figure D.19: The $\mathcal{B}\overline{\mathcal{B}}$ meson-antimeson masses for the combination $\gamma_5 \otimes P_\parallel$ in the isovector channel. From top to bottom we show the coarse lattice for $S_z = 0$, $S_z = 1$ and the fine lattice. Black circles, red squares and blue diamonds mark the ground, the first and the second excited states respectively while the green triangles label the static $Q\overline{Q}$ potential plus various light mesons. The horizontal lines represent the sum of the corresponding static-light $\mathcal{B}$ mesons, the expected $r \to \infty$ limit, where their widths indicate the jackknife errors.

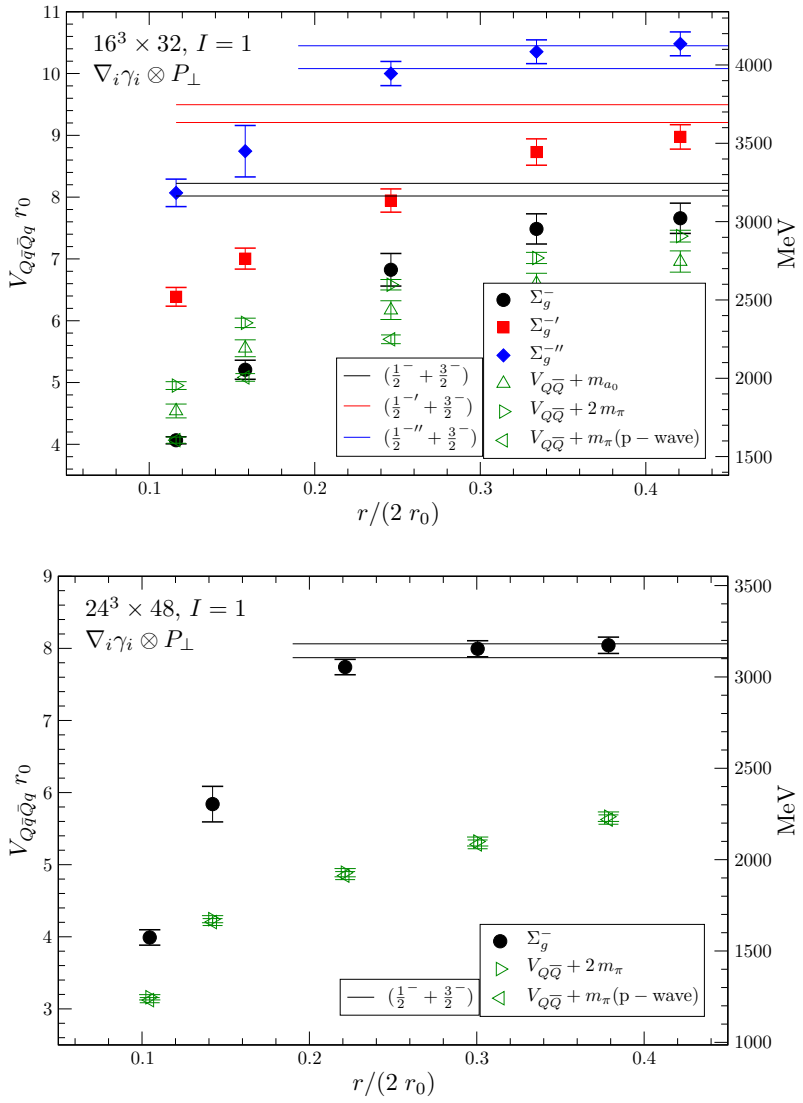

Figure D.20: The $\mathcal{B}\overline{\mathcal{B}}$ meson-antimeson masses for the combination $\nabla_i \gamma_i \otimes P_\perp$ in the isovector channel. From top to bottom we show the coarse lattice for $S_z = 0$, $S_z = 1$ and the fine lattice. Black circles, red squares and blue diamonds mark the ground, the first and the second excited states respectively while the green triangles label the static $Q\overline{Q}$ potential plus various light mesons. The horizontal lines represent the sum of the corresponding static-light $\mathcal{B}$ mesons, the expected $r \to \infty$ limit, where their widths indicate the jackknife errors.

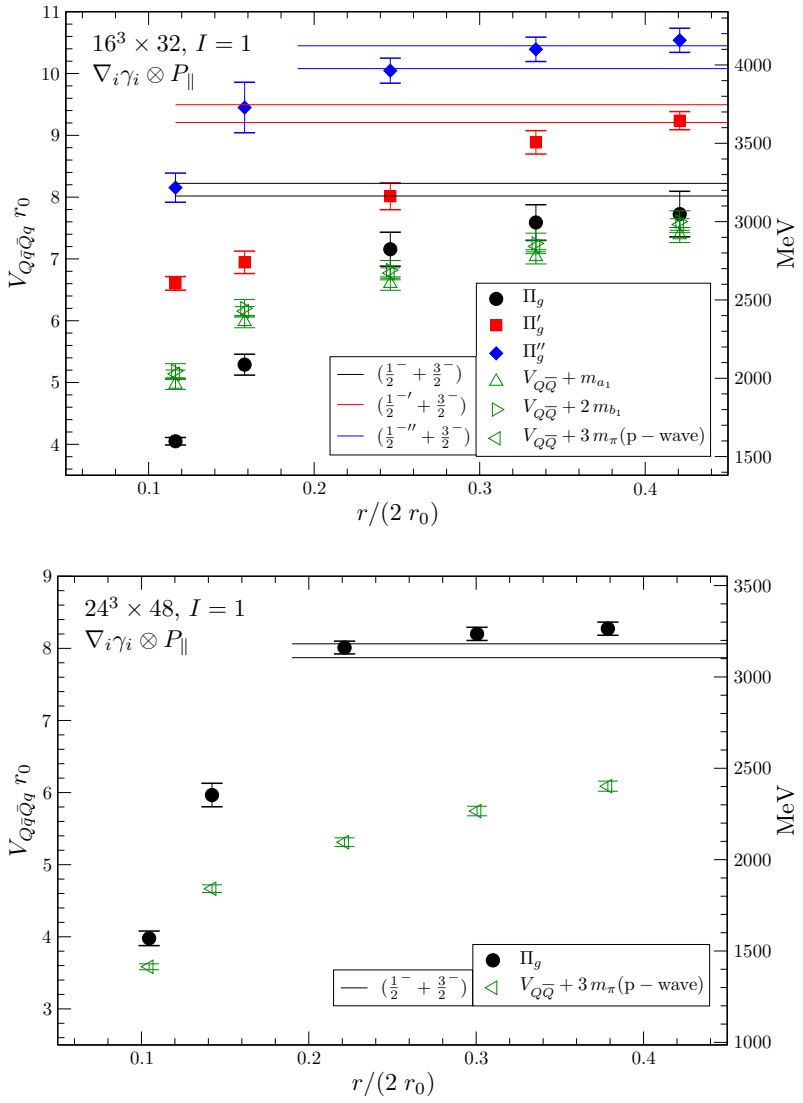

Figure D.21: The $\mathcal{B}\overline{\mathcal{B}}$ meson-antimeson masses for the combination $\nabla_i \gamma_i \otimes P_\parallel$ in the isovector channel. From top to bottom we show the coarse lattice for $S_z = 0$, $S_z = 1$ and the fine lattice. Black circles, red squares and blue diamonds mark the ground, the first and the second excited states respectively while the green triangles label the static $Q\overline{Q}$ potential plus various light mesons. The horizontal lines represent the sum of the corresponding static-light $\mathcal{B}$ mesons, the expected $r \to \infty$ limit, where their widths indicate the jackknife errors.

Isoscalar Meson-Antimesons

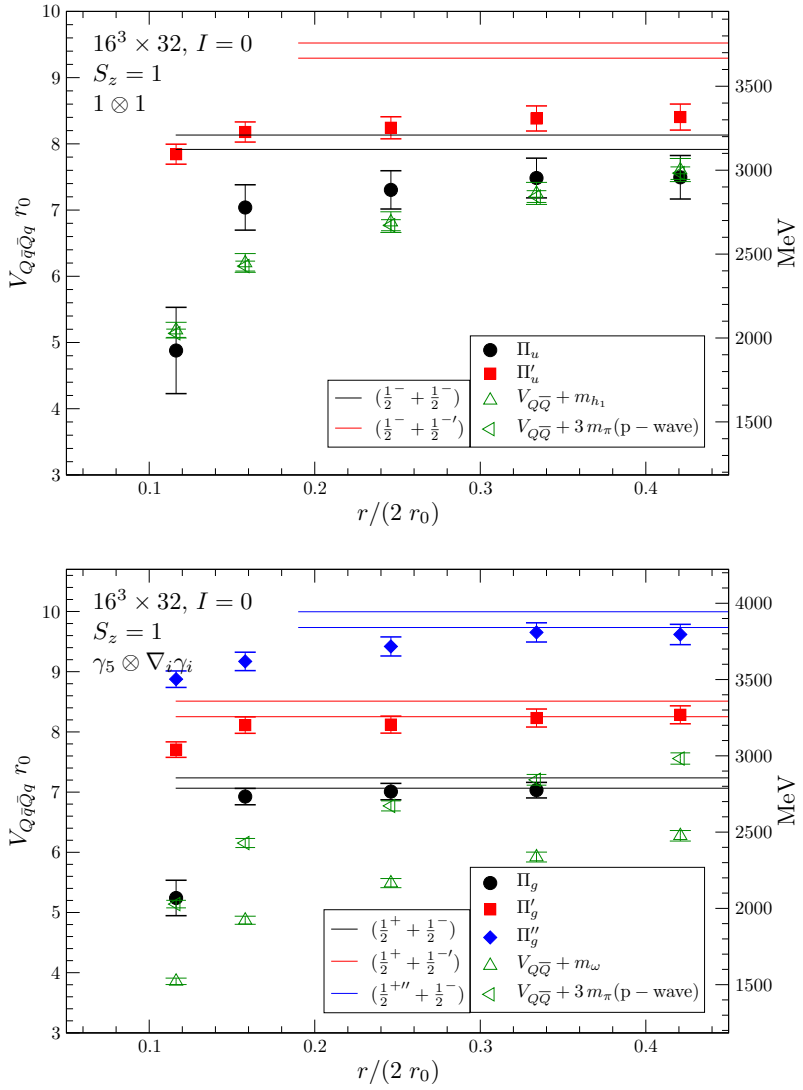

Figure D.22: The $\mathcal{B}\overline{\mathcal{B}}$ meson-antimeson masses on our coarse lattice for the operator combination $\mathbb{1} \otimes \mathbb{1}$ (upper plot) and $\gamma_5 \otimes \nabla_i \gamma_i$ (lower plot) for $I = 0$ and $S_z = 1$. Black circles, red squares and blue diamonds mark the ground, the first and the second excited state respectively while the green triangles label the $Q\overline{Q}$ static potential plus various light mesons. The horizontal lines represent the sum of the corresponding static-light $\mathcal{B}$ mesons, where their widths indicate the jackknife errors.

Bibliography

[1] G. Flügge and P. Jenni, "Der Large Hadron Collider," *Physik Journal* **Februar** (2006).

[2] R. Klanner and T. Schörner-Sadenius, "Verstehen wir die starke Kraft?," *Physik Journal* **May** (2006).

[3] M. Gell-Mann, "A schematic model of baryons and mesons," *Phys. Lett.* **8** (1964) 214–215.

[4] G. Zweig, "An SU(3) model for strong interaction symmetry and its breaking,". CERN-TH-401.

[5] G. Zweig, "An SU(3) model for strong interaction symmetry and its breaking. 2,". CERN-TH-412.

[6] H. J. Rothe, "Lattice gauge theories: An introduction," *World Sci. Lect. Notes Phys.* **74** (2005) 1–605.

[7] J. E. Augustin *et al.*, [SLAC-SP-017 Collaboration], "Discovery of a narrow resonance in e^+e^- annihilation," *Phys. Rev. Lett.* **33** (1974) 1406–1408.

[8] J. J. Aubert *et al.*, [E598 Collaboration], "Experimental observation of a heavy particle J," *Phys. Rev. Lett.* **33** (1974) 1404–1406.

[9] D. J. Gross and F. Wilczek, "Ultraviolet behavior of nonabelian gauge theories," *Phys. Rev. Lett.* **30** (1973) 1343–1346.

[10] H. D. Politzer, "Reliable perturbative results for strong interactions?," *Phys. Rev. Lett.* **30** (1973) 1346–1349.

[11] M. Creutz, "Monte Carlo study of quantized SU(2) gauge theory," *Phys. Rev.* **D21** (1980) 2308–2315.

[12] A. V. Manohar and M. B. Wise, "Heavy quark physics," *Camb. Monogr. Part. Phys. Nucl. Phys. Cosmol.* **10** (2000) 1–191.

[13] A. S. Kronfeld, "Heavy quarks and lattice QCD," *Nucl. Phys. Proc. Suppl.* **129** (2004) 46–59, arXiv:hep-lat/0310063.

[14] E. S. Swanson, "The new heavy mesons: A status report," *Phys.Rept.* **429** (2006) 243–305, arXiv:hep-ph/0601110 [hep-ph].

[15] S. Godfrey and S. L. Olsen, "The exotic XYZ charmonium-like mesons," *Ann.Rev.Nucl.Part.Sci.* **58** (2008) 51–73, arXiv:0801.3867 [hep-ph].

[16] G. S. Bali, S. Collins, and C. Ehmann, "Charmonium spectroscopy and mixing with light quark and open charm states from $n_F = 2$ lattice QCD," arXiv:1110.2381 [hep-lat].

[17] S. Choi *et al.*, [Belle Collaboration], "Observation of a narrow charmonium - like state in exclusive $B^{\pm} \to K^{\pm}\pi^{+}\pi^{-}J/\psi$ decays," *Phys.Rev.Lett.* **91** (2003) 262001, arXiv:hep-ex/0309032 [hep-ex].

[18] D. Acosta *et al.*, [CDF II Collaboration], "Observation of the narrow state $X(3872) \to J/\psi\pi^{+}\pi^{-}$ in $\bar{p}p$ collisions at $\sqrt{s} = 1.96$ TeV," *Phys.Rev.Lett.* **93** (2004) 072001, arXiv:hep-ex/0312021 [hep-ex].

[19] V. Abazov *et al.*, [D0 Collaboration], "Observation and properties of the $X(3872)$ decaying to $J/\psi\pi^{+}\pi^{-}$ in $p\bar{p}$ collisions at $\sqrt{s} = 1.96$ TeV," *Phys.Rev.Lett.* **93** (2004) 162002, arXiv:hep-ex/0405004 [hep-ex].

[20] B. Aubert *et al.*, [BABAR Collaboration], "Study of the $B \to J/\psi K^{-}\pi^{+}\pi^{-}$ decay and measurement of the $B \to X(3872)K^{-}$ branching fraction," *Phys.Rev.* **D71** (2005) 071103, arXiv:hep-ex/0406022 [hep-ex].

[21] M. Voloshin and L. Okun, "Hadron molecules and charmonium atom," *JETP Lett.* **23** (1976) 333–336.

[22] A. De Rujula, H. Georgi, and S. Glashow, "Molecular charmonium: A new spectroscopy?," *Phys.Rev.Lett.* **38** (1977) 317.

[23] E. S. Swanson, "Short range structure in the $X(3872)$," *Phys.Lett.* **B588** (2004) 189–195, arXiv:hep-ph/0311229 [hep-ph].

[24] F. E. Close and P. R. Page, "The $D^{*0}\overline{D}^{0}$ threshold resonance," *Phys.Lett.* **B578** (2004) 119–123, arXiv:hep-ph/0309253 [hep-ph].

[25] M. Voloshin, "Interference and binding effects in decays of possible molecular component of $X(3872)$," *Phys.Lett.* **B579** (2004) 316–320, arXiv:hep-ph/0309307 [hep-ph].

[26] L. Maiani, F. Piccinini, A. Polosa, and V. Riquer, "Diquark-antidiquarks with hidden or open charm and the nature of $X(3872)$," *Phys.Rev.* **D71** (2005) 014028, arXiv:hep-ph/0412098 [hep-ph].

[27] D. Ebert, R. Faustov, and V. Galkin, "Masses of heavy tetraquarks in the relativistic quark model," *Phys.Lett.* **B634** (2006) 214–219, arXiv:hep-ph/0512230 [hep-ph].

[28] B. A. Li, "Is $X(3872)$ a possible candidate of hybrid meson," *Phys.Lett.* **B605** (2005) 306–310, arXiv:hep-ph/0410264 [hep-ph].

[29] S. Choi *et al.*, [BELLE Collaboration Collaboration], "Observation of a resonance-like structure in the $\pi^{\pm}\psi'$ mass distribution in exclusive $B \to K\pi^{\pm}\psi'$ decays," *Phys.Rev.Lett.* **100** (2008) 142001, arXiv:0708.1790 [hep-ex]. 12 pages, 4 figures, submitted to the 2007 Lepton-Photon Symposium, Daegu, Korea.

[30] C. Meng and K.-T. Chao, "$Z^{+}(4430)$ as a resonance in the $D_1(D_1')D^{*}$ channel," arXiv:0708.4222 [hep-ph].

[31] S. H. Lee, A. Mihara, F. S. Navarra, and M. Nielsen, "QCD sum rules study of the meson $Z^{+}(4430)$," *Phys.Lett.* **B661** (2008) 28–32, arXiv:0710.1029 [hep-ph].

[32] X. Liu, Y.-R. Liu, W.-Z. Deng, and S.-L. Zhu, "Is $Z^{+}(4430)$ a loosely bound molecular state?," *Phys.Rev.* **D77** (2008) 034003, arXiv:0711.0494 [hep-ph].

[33] L. Maiani, A. Polosa, and V. Riquer, "The charged $Z(4433)$: Towards a new spectroscopy," arXiv:0708.3997 [hep-ph]. 3 pages.

[34] G. Bali and M. Hetzenegger, "Potentials between pairs of static-light mesons," arXiv:1111.2222 [hep-lat].

[35] L. H. Ryder, "Quantum Field Theory,". Cambridge, Uk: Univ. Pr. (1985) 443p.

[36] M. E. Peskin and D. V. Schroeder, "An introduction to Quantum Field Theory,". Reading, USA: Addison-Wesley (1995) 842 p.

[37] C. Gattringer and C. B. Lang, "Quantum Chromodynamics on the lattice (an introductory presentation),". Springer-Verlag, (2009).

[38] C. Itzykson and J. B. Zuber, "Quantum Field Theory,". New York, USA: Mcgraw-hill (1980) 705 P.(International Series In Pure and Applied Physics).

[39] C. Hagen, "Improved hadronic measurements and spectral sums on the lattice,". 2008, PhD thesis.

[40] D. Hierl, "Lattice Quantum Chromodynamics with approximately chiral fermions,". 2008, PhD thesis.

[41] C. Ehmann, "A lattice QCD calculation of the charmonium spectrum,". 2010, PhD thesis.

[42] J. H. Rohrwild, "Renormalization and applications of baryon distribution amplitudes in QCD,". 2009, PhD thesis.

[43] J. Goldstone, A. Salam, and S. Weinberg, "Broken symmetries," *Phys. Rev.* **127** (1962) 965–970.

[44] X. Liao and T. Manke, "Excited charmonium spectrum from anisotropic lattices," `arXiv:hep-lat/0210030`.

[45] T. Burch, "Study of spin dependent masses and configuration mixings in heavyquarkonia and hybrids using lattice nonrelativistic quantum chromodynamics,". UMI-30-89920.

[46] G. S. Bali, "QCD forces and heavy quark bound states," *Phys. Rept.* **343** (2001) 1–136, `arXiv:hep-ph/0001312`.

[47] A. Chodos, R. L. Jaffe, K. Johnson, C. B. Thorn, and V. F. Weisskopf, "A new extended model of hadrons," *Phys. Rev.* **D9** (1974) 3471–3495.

[48] P. Hasenfratz and J. Kuti, "The Quark Bag Model," *Phys. Rept.* **40** (1978) 75–179.

[49] N. Isgur and J. E. Paton, "A Flux Tube Model for hadrons," *Phys. Lett.* **B124** (1983) 247.

[50] T. A. DeGrand, R. L. Jaffe, K. Johnson, and J. E. Kiskis, "Masses and other parameters of the light hadrons," *Phys. Rev.* **D12** (1975) 2060.

[51] J. B. Kogut, D. K. Sinclair, and L. Susskind, "A quantitative approach to low-energy Quantum Chromodynamics," *Nucl. Phys.* **B114** (1976) 199.

[52] T. Barnes, "Exotic mesons, theory and experiment," *Acta Phys. Polon.* **B31** (2000) 2545–2556, `arXiv:hep-ph/0007296`.

[53] T. Barnes, "Hybrid baryons: A brief review," `arXiv:nucl-th/0009011`.

[54] W. Pauli and F. Villars, "On the invariant regularization in relativistic quantum theory," *Rev. Mod. Phys.* **21** (1949) 434–444.

[55] G. 't Hooft and M. J. G. Veltman, "Regularization and renormalization of gauge fields," *Nucl. Phys.* **B44** (1972) 189–213.

[56] C. G. Bollini and J. J. Giambiagi, "Lowest order divergent graphs in nu-dimensional space," *Phys. Lett.* **B40** (1972) 566–568.

[57] G. 't Hooft, "Dimensional regularization and the renormalization group," *Nucl. Phys.* **B61** (1973) 455–468.

[58] T. DeGrand and C. E. Detar, "Lattice methods for Quantum Chromodynamics,". New Jersey, USA: World Scientific (2006) 345 p.

[59] M. Creutz, "Quarks, gluons and lattices,". Cambridge, Uk: Univ. Pr. (1983) 169 P. (Cambridge Monographs On Mathematical Physics).

[60] I. Montvay and G. Munster, "Quantum fields on a lattice,". Cambridge, UK: Univ. Pr. (1994) 491 p. (Cambridge Monographs On Mathematical Physics).

[61] S. Schäfer, "Chiral symmetry and hadronic measurements on the lattice,". 2002, PhD thesis.

[62] T. Kaltenbrunner, "Renormalization of three-quark operators for the nucleon distribution amplitude,". 2008, PhD thesis.

[63] N. Warkentin, "Nucleaon wave function from lattice QCD,". 2008, PhD thesis.

[64] K. G. Wilson, "Quarks and strings on a lattice,". New Phenomena In Subnuclear Physics. Part A. Proceedings of the First Half of the 1975 International School of Subnuclear Physics, Erice, Sicily, July 11 - August 1, 1975, ed. A. Zichichi, Plenum Press, New York, 1977, p. 69, CLNS-321.

[65] H. B. Nielsen and M. Ninomiya, "Absence of neutrinos on a lattice. 1. Proof by homotopy theory," *Nucl. Phys.* **B185** (1981) 20.

[66] H. B. Nielsen and M. Ninomiya, "Absence of neutrinos on a lattice. 2. Intuitive topological proof," *Nucl. Phys.* **B193** (1981) 173.

[67] P. H. Ginsparg and K. G. Wilson, "A remnant of chiral symmetry on the lattice," *Phys. Rev.* **D25** (1982) 2649.

[68] D. B. Kaplan, "A method for simulating chiral fermions on the lattice," *Phys. Lett.* **B288** (1992) 342–347, `arXiv:hep-lat/9206013`.

[69] Y. Shamir, "Chiral fermions from lattice boundaries," *Nucl. Phys.* **B406** (1993) 90–106, `arXiv:hep-lat/9303005`.

[70] R. Narayanan and H. Neuberger, "Chiral fermions on the lattice," *Phys. Rev. Lett.* **71** (1993) 3251–3254, `arXiv:hep-lat/9308011`.

[71] R. Narayanan and H. Neuberger, "A construction of lattice chiral gauge theories," *Nucl. Phys.* **B443** (1995) 305–385, `arXiv:hep-th/9411108`.

[72] P. Hasenfratz, "Prospects for perfect actions," *Nucl. Phys. Proc. Suppl.* **63** (1998) 53–58, `arXiv:hep-lat/9709110`.

[73] C. Gattringer, "A new approach to Ginsparg-Wilson fermions," *Phys. Rev.* **D63** (2001) 114501, `arXiv:hep-lat/0003005`.

[74] C. Gattringer, I. Hip, and C. B. Lang, "Approximate Ginsparg-Wilson fermions: A first test," *Nucl. Phys.* **B597** (2001) 451–474, `arXiv:hep-lat/0007042`.

[75] K. G. Wilson, "Confinement of quarks," *Phys. Rev.* **D10** (1974) 2445–2459.

[76] M. Lüscher and P. Weisz, "On-shell improved lattice gauge theories," *Commun. Math. Phys.* **97** (1985) 59.

[77] G. Curci, P. Menotti, and G. Paffuti, "Symanzik's improved lagrangian for lattice gauge theory," *Phys. Lett.* **B130** (1983) 205.

[78] K. Symanzik, "Continuum limit and improved action in lattice theories. 1. Principles and phi**4 Theory," *Nucl. Phys.* **B226** (1983) 187.

[79] B. Sheikholeslami and R. Wohlert, "Improved continuum limit lattice action for QCD with Wilson fermions," *Nucl. Phys.* **B259** (1985) 572.

[80] K. Symanzik, "Schrodinger representation and Casimir effect in renormalizable Quantum Field Theory," *Nucl. Phys.* **B190** (1981) 1.

[81] M. Luscher, R. Sommer, P. Weisz, and U. Wolff, "A precise determination of the running coupling in the SU(3) Yang-Mills theory," *Nucl. Phys.* **B413** (1994) 481–502, arXiv:hep-lat/9309005.

[82] M. Lüscher, S. Sint, R. Sommer, P. Weisz, and U. Wolff, "Non-perturbative O(a) improvement of lattice QCD," *Nucl. Phys.* **B491** (1997) 323–343, arXiv:hep-lat/9609035.

[83] R. G. Edwards, U. M. Heller, and T. R. Klassen, "The effectiveness of non-perturbative O(a) improvement in lattice QCD," *Phys. Rev. Lett.* **80** (1998) 3448–3451, arXiv:hep-lat/9711052.

[84] R. Sommer, "Non-perturbative QCD: Renormalization, O(a)-improvement and matching to heavy quark effective theory," arXiv:hep-lat/0611020.

[85] N. Metropolis, A. W. Rosenbluth, M. N. Rosenbluth, A. H. Teller, and E. Teller, "Equation of state calculations by fast computing machines," *J. Chem. Phys.* **21** (1953) 1087–1092.

[86] S. Duane, A. D. Kennedy, B. J. Pendleton, and D. Roweth, "Hybrid Monte Carlo," *Phys. Lett.* **B195** (1987) 216–222.

[87] R. Sommer, "A New way to set the energy scale in lattice gauge theories and its applications to the static force and alpha-s in SU(2) Yang-Mills theory," *Nucl. Phys.* **B411** (1994) 839–854, arXiv:hep-lat/9310022.

[88] M. Guagnelli, R. Sommer, and H. Wittig, [ALPHA Collaboration], "Precision computation of a low-energy reference scale in quenched lattice QCD," *Nucl. Phys.* **B535** (1998) 389–402, arXiv:hep-lat/9806005.

[89] J. Najjar *et al.*, [QCDSF Collaboration]. in preparation.

[90] D. Pleiter, "ukQCDSF database interface." `http://www-zeuthen.desy.de/~pleiter/ukqcdsf/qdbget.html`.

[91] D. Brommel *et al.*, [QCDSF/UKQCD Collaboration], "The pion form factor from lattice QCD with two dynamical flavours," *Eur. Phys. J.* **C51** (2007) 335–345, `arXiv:hep-lat/0608021`.

[92] J. Najjar, "Static-static-light baryonic potentials from lattice QCD,". diploma thesis.

[93] G. S. Bali, H. Neff, T. Duessel, T. Lippert, and K. Schilling, [SESAM Collaboration], "Observation of string breaking in QCD," *Phys. Rev.* **D71** (2005) 114513, `arXiv:hep-lat/0505012`.

[94] C. Michael, "Adjoint sources in lattice gauge theory," *Nucl. Phys.* **B259** (1985) 58.

[95] M. Lüscher and U. Wolff, "How To calculate the elastic scattering matrix in two- dimensional quantum field theories by numerical simulation," *Nucl. Phys.* **B339** (1990) 222–252.

[96] Y. Chen *et al.*, "The Sequential Empirical Bayes Method: An adaptive constrained-curve fitting algorithm for lattice QCD," `arXiv:hep-lat/0405001`.

[97] K. Sasaki, S. Sasaki, T. Hatsuda, and M. Asakawa, "Excited nucleon spectrum from lattice QCD with maximum entropy method," *Nucl. Phys. Proc. Suppl.* **129** (2004) 212–214, `arXiv:hep-lat/0309177`.

[98] T. Burch *et al.*, "Excited hadrons on the lattice: Mesons," *Phys. Rev.* **D73** (2006) 094505, `arXiv:hep-lat/0601026`.

[99] T. Burch *et al.*, "Excited hadrons on the lattice: Baryons," *Phys. Rev.* **D74** (2006) 014504, `arXiv:hep-lat/0604019`.

[100] T. Burch, C. Hagen, M. Hetzenegger, and A. Schafer, "Low and high spin mesons from $N_f = 2$ Clover-Wilson lattices," *Phys. Rev.* **D79** (2009) 114503, `arXiv:0903.2358 [hep-lat]`.

[101] T. Burch, C. Ehmann, C. Hagen, M. Hetzenegger, and A. Schäfer, "Excited mesons on dynamical clover-Wilson lattices," arXiv:arXiv:0709.0664 [hep-lat].

[102] T. Burch, C. Gattringer, L. Y. Glozman, C. Hagen, and C. B. Lang, "Variational method for lattice spectroscopy with ghosts," *Phys. Rev.* **D73** (2006) 017502, arXiv:hep-lat/0511054.

[103] S. Sasaki, T. Blum, and S. Ohta, "A lattice study of the nucleon excited states with domain wall fermions," *Phys. Rev.* **D65** (2002) 074503, arXiv:hep-lat/0102010.

[104] D. Brommel *et al.*, [Bern-Graz-Regensburg Collaboration], "Excited nucleons with chirally improved fermions," *Phys. Rev.* **D69** (2004) 094513, arXiv:hep-ph/0307073.

[105] J. Najjar and G. Bali, "Static-static-light baryonic potentials," *PoS* **LAT2009** (2009) 089, arXiv:0910.2824 [hep-lat].

[106] W. E. Caswell and G. P. Lepage, "Effective lagrangians for bound state problems in QED, QCD, and other field theories," *Phys. Lett.* **B167** (1986) 437.

[107] G. P. Lepage, L. Magnea, C. Nakhleh, U. Magnea, and K. Hornbostel, "Improved nonrelativistic QCD for heavy quark physics," *Phys. Rev.* **D46** (1992) 4052–4067, arXiv:hep-lat/9205007.

[108] E. Eichten, "Heavy quarks on the lattice," *Nucl. Phys. Proc. Suppl.* **4** (1988) 170.

[109] E. Eichten and B. R. Hill, "An effective field theory for the calculation of matrix elements involving heavy quarks," *Phys. Lett.* **B234** (1990) 511.

[110] E. Eichten and B. R. Hill, "Renormalization of heavy - light bilinears and f(B) for Wilson Fermions," *Phys. Lett.* **B240** (1990) 193.

[111] E. Eichten and B. R. Hill, "Static effective field theory: 1/m corrections," *Phys. Lett.* **B243** (1990) 427–431.

[112] N. Isgur and M. B. Wise, "Weak decays of heavy mesons in the static quark approximation," *Phys. Lett.* **B232** (1989) 113.

[113] N. Isgur and M. B. Wise, "Weak transition form-factors between heavy mesons," *Phys. Lett.* **B237** (1990) 527.

[114] R. Barret *et al.*, "Templates for the solution of linear systems: Building blocks for iterative methods," *SIAM, Philadelphia* (1994).

[115] W. H. Press, S. A. Teukolsky, W. T. Vetterling, and B. P. Flannery, "Numerical Recipes in C, 2nd ed.," *Cambridge University Press, Cambridge, New York* (1999).

[116] H. A. van der Vorst, "Bi-CGSTAB: A fast and smoothly converging variant of Bi-CG for the solution of nonsymmetric linear systems," *SIAM Journal on Scientific and Statistical Computing* **13(2)** (1992) 631.

[117] B. Jegerlehner, "Krylov space solvers for shifted linear systems," `arXiv:hep-lat/9612014`.

[118] J. Foley *et al.*, "Practical all-to-all propagators for lattice QCD," *Comput. Phys. Commun.* **172** (2005) 145–162, `arXiv:hep-lat/0505023`.

[119] C. Michael and J. Peisa, [UKQCD Collaboration], "Maximal variance reduction for stochastic propagators with applications to the static quark spectrum," *Phys. Rev.* **D58** (1998) 034506, `arXiv:hep-lat/9802015`.

[120] G. S. Bali, S. Collins, and A. Schafer, "Effective noise reduction techniques for disconnected loops in lattice QCD," *Comput. Phys. Commun.* **181** (2010) 1570–1583, `arXiv:0910.3970 [hep-lat]`.

[121] T. Burch and C. Hagen, "Domain decomposition improvement of quark propagator estimation," *Comput. Phys. Commun.* **176** (2007) 137–145, `arXiv:hep-lat/0607029`.

[122] M. F. Hutchinson, "A stochastic estimator of the trace of the influence matrix for laplacian smoothing splines," *Communications in Statistics - Simulation and Computation* **18(3)** (1989) 1059.

[123] S.-J. Dong and K.-F. Liu, "Stochastic estimation with Z(2) noise," *Phys. Lett.* **B328** (1994) 130–136, `arXiv:hep-lat/9308015`.

[124] S. Bernardson, P. McCarty, and C. Thron, "Monte Carlo methods for estimating linear combinations of inverse matrix entries in lattice QCD," *Comput. Phys. Commun.* **78** (1993) 256–264.

[125] C. Thron, S. J. Dong, K. F. Liu, and H. P. Ying, "Pade-Z(2) estimator of determinants," *Phys. Rev.* **D57** (1998) 1642–1653, arXiv:hep-lat/9707001.

[126] S. Gusken *et al.*, "Nonsinglet axial vector couplings of the baryon octet in lattice QCD," *Phys. Lett.* **B227** (1989) 266.

[127] S. Gusken, "A study of smearing techniques for hadron correlation functions," *Nucl. Phys. Proc. Suppl.* **17** (1990) 361–364.

[128] C. Best *et al.*, "Pion and rho structure functions from lattice QCD," *Phys. Rev.* **D56** (1997) 2743–2754, arXiv:hep-lat/9703014.

[129] M. Falcioni, M. L. Paciello, G. Parisi, and B. Taglienti, "Again on SU(3) glueball mass," *Nucl. Phys.* **B251** (1985) 624–632.

[130] M. Albanese *et al.*, [APE Collaboration], "Glueball masses and string tension in lattice QCD," *Phys. Lett.* **B192** (1987) 163.

[131] A. Hasenfratz and C. Nieter, "Instanton content of the SU(3) vacuum," *Phys. Lett.* **B439** (1998) 366–372, arXiv:hep-lat/9806026.

[132] T. A. DeGrand, A. Hasenfratz, and T. G. Kovacs, "Revealing topological structure in the SU(2) vacuum," *Nucl. Phys.* **B520** (1998) 301–322, arXiv:hep-lat/9711032.

[133] C. Morningstar and M. J. Peardon, "Analytic smearing of SU(3) link variables in lattice QCD," *Phys. Rev.* **D69** (2004) 054501, arXiv:hep-lat/0311018.

[134] C. Michael and P. Pennanen, [UKQCD Collaboration], "Two heavy-light mesons on a lattice," *Phys. Rev.* **D60** (1999) 054012, arXiv:hep-lat/9901007.

[135] P. Pennanen, C. Michael, and A. M. Green, [UKQCD Collaboration], "Interactions of heavy-light mesons," *Nucl. Phys. Proc. Suppl.* **83** (2000) 200–202, arXiv:hep-lat/9908032.

[136] A. Mihaly, H. R. Fiebig, H. Markum, and K. Rabitsch, "Interactions between heavy - light mesons in lattice QCD," *Phys. Rev.* **D55** (1997) 3077–3081.

[137] C. Stewart and R. Koniuk, "Hadronic molecules in lattice QCD," *Phys. Rev.* **D57** (1998) 5581–5585, arXiv:hep-lat/9803003.

[138] A. M. Green, J. Koponen, and P. Pennanen, "A variational fit to the lattice energy of two heavy-light mesons," *Phys. Rev.* **D61** (2000) 014014, arXiv:hep-ph/9902249.

[139] M. S. Cook and H. R. Fiebig, "A lattice study of interaction mechanisms in a heavy light meson meson system," arXiv:hep-lat/0210054 [hep-lat].

[140] T. T. Takahashi, T. Doi, and H. Suganuma, "Nuclear force in lattice QCD," *AIP Conf.Proc.* **842** (2006) 249–251, arXiv:hep-lat/0601006 [hep-lat].

[141] T. Doi, T. T. Takahashi, and H. Suganuma, "Meson-meson and meson-baryon interactions in lattice QCD," *AIP Conf.Proc.* **842** (2006) 246–248, arXiv:hep-lat/0601008 [hep-lat].

[142] W. Detmold, K. Orginos, and M. J. Savage, "BB potentials in quenched lattice QCD," *Phys. Rev.* **D76** (2007) 114503, arXiv:hep-lat/0703009.

[143] M. Wagner, [the ETM Collaboration], "Forces between static-light mesons," *PoS* **LATTICE2010** (2010) 162, arXiv:1008.1538 [hep-lat].

[144] M. Wagner, [ETM Collaboration], "Static-static-light-light tetraquarks in lattice QCD," *Acta Phys. Polon. Supp.* **4** (2011) 747–752, arXiv:1103.5147 [hep-lat].

[145] G. Bali and M. Hetzenegger, "Static-light meson-meson potentials," *PoS* **LATTICE2010** (2010) 142, arXiv:1011.0571 [hep-lat].

[146] A. Ali Khan *et al.*, [QCDSF Collaboration], "Accelerating the hybrid Monte Carlo algorithm," *Phys. Lett.* **B564** (2003) 235–240, arXiv:hep-lat/0303026.

[147] R. G. Edwards and B. Joo, [SciDAC Collaboration], "The Chroma software system for lattice QCD," *Nucl. Phys. Proc. Suppl.* **140** (2005) 832, arXiv:hep-lat/0409003.

[148] C. McClendon, "Optimized lattice QCD kernels for a Pentium 4 cluster." http://www.jlab.org/~edwards/qcdapi/reports/dslash_p4.pdf, 2001. Jlab preprint, JLAB-THY-01-29.

[149] http://www.physik.uni-regensburg.de/edv/linux/cluster_rz.phtml. HPC Cluster at the University of Regensburg.

[150] N. Brambilla, S. Eidelman, B. Heltsley, R. Vogt, G. Bodwin, *et al.*, "Heavy quarkonium: progress, puzzles, and opportunities," *Eur.Phys.J.* **C71** (2011) 1534, arXiv:1010.5827 [hep-ph].

[151] S. Dubynskiy and M. B. Voloshin, "Hadro-Charmonium," *Phys. Lett.* **B666** (2008) 344–346, arXiv:0803.2224 [hep-ph].

[152] L. Lyons, "A practical guide to data analysis for physical science students,". Cambridge, Cambridge University Press (1991).

"Ahhh, diese Ruhe. Der Hypophysenlappen
im Hinterkopf geht nur noch ganz langsam,
propellert nicht mehr. Eine angenehme
Blutleere im Hinterkopf macht sich breit
und verschafft einem eine inwendige
Tranquillität."
- Gemütlichkeit -

Gerhard Polt

Danksagung

Es ist mir eine große Freude, mich an dieser Stelle bei allen zu bedanken, die direkt oder indirekt zum Gelingen dieser Arbeit beigetragen haben.

Als erstes möchte ich mich bei meinem Betreuer Prof. Dr. Gunnar Bali bedanken, der es mir ermöglicht hat in seiner Gruppe zu arbeiten. Ich bedanke mich für unzählige regelmäßige und unregelmäßige Diskussionen in denen er meine vielen Fragen beantwortet und wenn nötig meine Forschungsarbeit in die richtige Richtung gelenkt hat. Besonders schätze ich sein enormes Wissen und seine reichhaltige Erfahrung, von der ich in meiner Arbeit profitieren durfte. Ich bedanke mich dafür, dass ich meine Forschungsergebnisse auf einigen Konferenzen präsentieren durfte, insbesondere den Gitter QCD Konferenzen in den Jahren 2010 und 2011. Gunnar, ich bedanke mich sehr herzlich für deine gute väterliche Art, mit der du wesentlich zum Gelingen dieser Arbeit beigetragen hast.

Großer Dank geht auch an meine Kollegen Dr. Christian Hagen, Dr. Christian Ehmann, und Johannes Najjar mit denen ich viele Diskussionen führen durfte. Ihre Kenntnisse und Erfahrungen im Bereich Gitter QCD verhalfen mir zu einem besseren Verständnis der Theorie, deren Umsetzung in C^{++} Programmen sowie der Auswertung der Ergebnisse. Ich danke Dr. Christian Ehmann auch für die Bereitstellung einiger Graphiken, die ich in meine Arbeit integrieren durfte. Des weiteren danke ich Dr. Tommy Burch für die Betreuung meiner Diplomarbeit, für zahlreiche und fruchtbare Diskussionen sowie das

Bereitstellen seiner Analyse-Tools zur Auswertung der numerischen Berechnungen. Zudem bedanke ich mich bei Dr. Sara Collins, die mir mit ihrem fundierten Wissen auch stets geduldig meine Fragen beantwortete.

Des weiteren war es mir auch eine große Freude mit meinen Kollegen Dr. Rainer Schiel, Dr. Paula Pérez-Rubio, Dr. Stefan Solbrig, Benjamin Gläßle, Sebastian Schierenberg, Luca Castagnini, sowie der gesamten Arbeitsgruppen vom Lehrstuhl Prof. Dr. Andreas Schäfer und Prof. Dr. Vladimir Braun zusammenzuarbeiten. Stets erfuhr ich große Hilfsbereitschaft und Freundlichkeit wenn ich irgendwelche Anliegen hatte.

Auch bedanke ich mich sehr bei Monika Maschek und Heidi Decock, die ebenfalls stets ansprechbar waren, sämtliche formalen Angelegenheiten erledigen und den "Laden" durch ihr Wirken erst am Laufen halten.

Ich bedanke ich auch bei der ganzen QCDSF Kollaboration für die Berechnung und Bereitstellung der Eichkonfigurationen. Die Berechnungen der Korrelatoren wurden hauptsächlich auf Regensburgs Athene HPC Cluster durchgeführt. Ich danke Dr. Michael Hartung und allen Mitarbeitern für die Betreuung und Wartung dieses Rechenclusters.

Ich bedanke ich mich für die finanzielle Unterstützung des GSI Hochschulprogramms (RSCHAE), der Deutschen Forschungsgemeinschaft (SFB Transregio 55) und der European Union grant 238353, ITN STRONGnet.

Zudem hatte ich die Gelegenheit als Systemadministrator unserer Arbeitsgruppen viel Erfahrung mit der Betreuung von Rechenclustern und Datenspeichersystemen sammeln zu können. Somit weiß ich auch wie viel Arbeit und Mühe es kostet diese Systeme am Laufen zu halten, sowie die Wünsche der Benutzer zu erfüllen. Ich danke meinen Adminkollegen Dr. Christian Hagen, Dr. Dieter Hierl, Dr. Christian Ehmann, Dr. Stefan Solbrig, Johannes Najjer, Simone Gutzwiller sowie Alessio Burello für ihre kollegiale Zusammenarbeit und ihre täglichen Anstrengungen zur Zufriedenheit aller Benutzer. Insbesondere bedanke ich mich an dieser Stelle recht herzlich bei den vier letztgenannten Kollegen, die mir während der letzten Monate die meisten Admin-Aufgaben abgenommen haben, so dass ich mich auf meine Dissertation konzentrieren konnte.

Besondere Hochachtung gebührt Dr. Sara Collins, Dr. Christian Ehmann, Johannes Najjar, Dr. Mridupawan Deka, Dr. Jian Zhou, Dr. Stefan Solbrig, Dr. Filippo Mantovani und Nils Meyer, die stets freundlich zu mir waren, obwohl ich ihr Bürokollege war.

Recht herzlich bedanke ich mich bei all meinen Freunden und Kollegen,

die mich während meines Studiums und der Zeit meiner Promotion durch Höhen und Tiefen begleitet haben und stets zu mir gestanden sind. Besonderer Dank geht an dieser Stelle an meine lieben Freunde Johannes Najjar, Benjamin Gläßle, Raphaela Müller, Tobias Harsch, Sebastian Schierenberg, Tin Sulejmanpasic, Dr. Paula Pérez-Rubio und Alessio Burello, die für jeglichen Spaß zu haben sind. Vielen Dank für viele unvergessliche Momente. Danke Johannes, dass du "Es" so locker genommen hast, diese Arbeit Korrektur gelesen hast und ich dich immer mit meinen kleinen und großen Problemen belästigen durfte. Benjamin, ich danke dir für eine wunderschöne Zeit in Kalifornien, gemeinsame Unternehmungen und deine ehrliche Art. Danke Tobias, dass du uns deine Wohnung stets für Fußball- und Kochabende zur Verfügung stellst und so gelassen mit uns bist. Raphaela, ich schätze sehr dass du soviel Wärme und Herzlichkeit mit in unsere Physikergruppe bringst. Herzlichen Dank für all deine aufbauenden Worte, Unterstützungen und dein Mitgefühl für alle Menschen. Vielen Dank Sebastian, fürs Korrekturlesen und deinen unvergleichbaren sarkastischen Humor.

Ich möchte mich bei Sabine Rosali Brindl bedanken. Durch deine Freundschaft habe ich einen neuen Blick für diese Welt erfahren. Vielen Dank für diese Bereicherung und deine vollkommen verrückte Art des Seins.

Ich bedanke mich bei Dr. Michael Hirmer für eine wunderbare Freundschaft während unserer gemeinsamen Studienzeit.

Eine ganz herzliche Umarmung bekommt Christine Pietsch. Vielen lieben Dank für zahlreiche Tangoabende, gemeinsame Unternehmungen und Ausflüge. Ich danke dir ganz herzlich für deine Liebe und Freundschaft und schätze deine Achtsamkeit und Herzenswärme. Vielen Dank, dass du mir geholfen hast meinen Unfall so gut zu überstehen und mir so viel Lebensmut in schwierigen Situationen schenkst.

Ich bedanke mich auch bei allen Freunden und Bekannten, die ich jetzt nicht namentlich erwähnt habe.

Schließlich möchte ich mich bei meinen Eltern Edeltraud und Gerhard sowie meiner Schwester Sabine bedanken. Liebe Mama, lieber Papa, ich danke euch von Herzen für all die Unterstützung, die ihr mir die ganzen Jahre gegeben habt. Vielen lieben Dank für alles, das ihr für mich getan habt und noch für mich tut, für ein stets angenehmes Leben in Fülle und Liebe. Ohne euch wäre diese Arbeit wahrscheinlich nicht möglich gewesen.